Universität Bremen

The transitional regime of pulsatile pipe flow

Vom Fachbereich Produktionstechnik
der

UNIVERSITÄT BREMEN

zur Erlangung des Grades
Doktor-Ingenieur
genehmigte

Dissertation

von

M.Sc. Daniel Morón Montesdeoca

1. Gutachter Prof. Dr. Marc Avila
University of Bremen

2. Gutachter Prof. Dr. Philipp Schlatter
Friedrich-Alexander-University Erlangen-Nuremberg

M.Sc. Daniel Morón Montesdeoca
The transitional regime of pulsatile pipe flow
Reviewers: Prof. Dr. Marc Avila and Prof. Dr. Philipp Schlatter
Supervisor: Prof. Dr. Marc Avila

University of Bremen

Center of Applied Space Technology and Microgravity (ZARM)
Faculty of Production Engineering
Am Fallturm 2
28359 and Bremen
Doctoral viva on September 2nd, 2024

Acknowledgments

There is a huge number of people I should thank for this thesis.

First and foremost, my supervisor Prof. Marc Avila. I am grateful that he decided to give me the opportunity to come to Bremen and work with him and the rest of the group during the past four years. I am very thankful for the outstanding amount of things he has taught me, the amount of good papers he has recommended me, and the challenges he has pushed me to do. I am extremely lucky that he trusted me with this work, that he, with patience, has put up with my not so clean way of doing things, as he showed me how to improve them, and has motivated me to try my own ideas. Thank you, for everything.

I would like to thank Dr. Daniel Feldmann, for sharing with me his deep knowledge on all the topics related with fluid mechanics and CFD; for exercising with me his patience; for showing me how to better write my results and produce my figures; and specially for teaching me that, sometimes, it is worth it to spend a couple of more minutes so the work is not a 9 out of 10 but a 10 out of 10. I am still practicing this last one.

I would also like to thank all of the members of the fluids simulation and modeling research group, that have come and go with the years. Specially Carlos Plana and Alberto Vela-Martín. Dr. Plana helped me to get up to speed with the `nsPipe` code, and was always ready, with extremely good arguments, to challenge my perhaps too crazy ideas. Dr. Vela-Martín got me interested in many research areas, showed me how to code in `C-CUDA` and taught me to always have questions, specially with my own work. I am extremely grateful to the two of them for the amount of hours we spent talking about science, life and all sort of stuff, both at work, but also outside. I would like to also mention the new batch of excellent and bright PhD students in the group, Patrick, Mehdi and Larissa. They are extremely lucky to have one-another and to get rid of me soon.

Most of this project has been done as part of a DFG research unit, with members in other German, Austrian and Swiss universities, that are here gratefully acknowledged. The project has been funded with two DFG grants: AV 120/6-1 and 349558021. Computational resources were partially provided by the North German Supercomputing Alliance (HLRN), which are also gratefully acknowledged.

I am also thankful to Prof. Jiménez for hosting us on June 2023, in his excellent turbulence workshop. In the past years I have met many incredibly intelligent and valuable people in conferences and meetings, like Dr. P. Encinar and many others that have contributed with ideas and questions to this work, and who I would like to also thank here. These conferences and meetings have also

allowed me to reconnect with past colleagues and professors. This includes my old Bsc. and Msc. theses supervisors, Oscar and Manolo, who I am always happy to see in these conferences, and to whom I am incredibly grateful for recommending me to Prof. Avila.

I would also like to thank the rest of my friends and family. The former for being there in the past years, specially during the pandemic in online format. The latter for their support. Specially my parents, Luis and Margarita, whose hard work made it possible in the first place that I am here writing this lines, and that have always been supportive with whatever I choose to be/do. To my sister Paula who is always available for a quick call and chat. And also to my two grandfathers, Jose Luis and Pepe, who were there for the beginning of this thesis, but unfortunately not for its end.

Last but not least I would like to thank my new family, Andrea. Again, thank you for putting up with me everyday, for having always a smile in your face and an unwavering trust on me. I am happy that you chose me for this adventure we now simply call a life together, and for spending with me these past years in Bremen. I am looking forward to what our future holds.

Abstract

The presence of turbulence in the circulatory system is thought to lead to cardiovascular diseases. Despite its importance, turbulence transition in cardiovascular flows is not well understood. In particular, it is unclear which one of the numerous complex features of blood flow (unsteady driving, rheology, flexible walls, complex geometry...) is the dominant one in terms of turbulence transition. The main aim of this thesis is to single out the effects of one of these features: the unsteady driving of the flow.

Specifically, the case of a pulsatile driven, Newtonian fluid, in a rigid smooth pipe of circular cross-section is considered, referred to as pulsatile pipe flow. Two main questions are investigated: whether and how laminar pulsatile pipe flows transition to turbulence, and how turbulence behaves once triggered. Pulsatile pipe flows in the transitional regime, with a mean $1000 \lesssim Re \lesssim 3000$, are considered. Apart from single harmonic pulsations, different waveforms are considered, including waveforms relevant for physiological flows.

By combining linear transient growth and stability analyses, it is demonstrated that, at intermediate pulsation frequencies $(4 \lesssim Wo \lesssim 20)$ and moderate to high pulsation amplitudes $(0.5 \lesssim A \lesssim 3)$, the laminar pulsatile pipe flow is highly susceptible to large disturbance amplification. Coincidentally the blood flow in the human aorta falls in this parameter regime. The underlying mechanisms related to this susceptibility are identified, and their dependence with respect to the flow parameters explored. Additionally, it is shown that, specific features of the driving waveform can enhance these mechanisms. In particular, bulk velocities with steep acceleration/deceleration phases and, counter-intuitively, with longer low velocity phases promote turbulence transition.

The turbulence behavior in this broad parametric space is studied with the use of a large number of direct numerical simulations. As part of this thesis a new `C-CUDA` code was developed in order to perform fast direct numerical simulations. The code outperforms state-of-the-art `CPU` codes in terms of computing time and computing resources. With the use of a causal analysis, it is shown that turbulence production increases due to the same mechanisms that render the flow susceptible to transition. Finally, a reduced-order model is developed to approximate the behavior of turbulence in pulsatile pipe flow reasonably well.

In sum, this thesis describes the way the flow is more likely to transition to turbulence in this parametric regime, and the behavior of turbulence once triggered. The results presented here suggest that blood flow in the larger arteries is susceptible to transition due to the pulsatile beating of our hearts alone.

Abstract (German)

Es wird oft vermutet, dass das Vorhandensein von Turbulenz im Blutkreislauf zu Herz-Kreislauferkrankungen führen kann. Trotz der Bedeutung des Turbulenzüberganges in kardiovaskulären Strömungen, ist dieser jedoch nur wenig verstanden. Insbesondere ist unklar, welcher der zahlreichen komplexen Merkmale von Blutströmungen (instationäre Antrieb, Rheologie, flexible Wände, komplexe Geometrie usw.) für den Turbulenzübergang maßgeblich ist. Das Hauptziel dieser Doktorarbeit ist es, die Auswirkungen eines dieser Merkmale herauszuarbeiten: den instationären Antrieb der Strömung.
Konkret wird der Fall eines pulsierend angetriebenen Newtonschen Fluids in einem starren und glatten Rohr mit kreisförmigem Querschnitt betrachtet. Dieser Fall wird als pulsierende Rohrströmung bezeichnet wird. Zwei Hauptfragen werden untersucht: ob und wie laminare pulsierende Rohrströmungen in Turbulenz übergehen und wie sich Turbulenz verhält, sobald sie ausgelöst wurde. Dafür werden pulsierende Rohrströmungen im Übergangsbereich mit einem Mittelwert von $1000 \lesssim Re \lesssim 3000$ betrachtet. Abgesehen von harmonischen Pulsationen mit einer einzigen Frequenz, werden verschiedene Wellenformen betrachtet, darunter solche, die für physiologische Strömungen relevant sind.
Durch die Kombination von linearen transienten Wachstums- und Stabilitätsanalysen wird gezeigt, dass die laminare pulsierende Rohrströmung bei mittleren Pulsationsfrequenzen von $(4 \lesssim Wo \lesssim 20)$ und mäßigen bis hohen Pulsationsamplituden $(0.5 \lesssim A \lesssim 3)$ besonders anfällig für große Störungsverstürkungen ist. Zufälligerweise fällt die Blutströmung in der menschlichen Aorta in diesen Parameterbereich. Die dieser Anfälligkeit zugrunde liegenden Mechanismen werden identifiziert und ihre Abhängigkeit von den Strömungsparametern untersucht. Außerdem wird gezeigt, dass bestimmte Merkmale der treibenden Wellenform diese Mechanismen verstärken können. Insbesondere steile Beschleunigungs-/Verzögerungsphasen der mittleren Geschwindigkeit und - kontraintuitiv - längere Phasen niedriger Geschwindigkeit begünstigen den Turbulenzübergang.
Das Turbulenzverhalten in diesem breiten Parameterraum wird mit Hilfe einer großen Anzahl direkter numerischer Simulationen untersucht. Im Rahmen dieser Arbeit wurde ein neuer `C-CUDA` Code entwickelt, mit dem schnelle direkte numerische Simulationen durchgeführt werden können. Der Code übertrifft den Stand der Technik in Bezug auf Rechenzeit und Rechenressourcen. Mit Hilfe einer Kausalanalyse wird gezeigt, dass die Turbulenzerzeugung durch dieselben Mechanismen zunimmt, die die Strömung für den Übergang anfällig machen. Schließlich wird ein Modell reduzierter Ordnung entwickelt, das das Verhalten von Turbulenzen in pulsierenden Rohrströmungen recht gut approximiert.
Insgesamt wird in dieser Arbeit beschrieben, wie die Strömung in diesem Parameterbereich eher in Turbulenz übergeht und wie sich die Turbulenz verhält, sobald sie ausgelöst wurde. Die hier vorgestellten Ergebnisse deuten darauf hin, dass der Blutfluss in den größeren Arterien allein durch das pulsierende Schlagen unseres Herzens anfällig für einen Turbulenzübergang ist.

Contents

1 Introduction

Human kind has always been fascinated by the behavior of the skies, rivers and oceans. Proof of that, is the prevalence and importance of sky, river and ocean deities in pretty much every religious pantheon, like: Enlil for the Mesopotamian, Zeus and Poseidon for the Greek or Thor for the Norse. However, it was not spiritual beliefs, but rather fluid dynamics knowledge what allowed our ancestors to navigate the seas and the oceans by harnessing wind power with sails. It was the knowledge of sea currents, what allowed Columbus to re-discover (what we know today as) the American continent. And it was the use of fluid dynamics what allowed the Wright brothers to perform the first manned controlled flight a little bit more than a century ago. In sum, humankind has learned for millennia how to predict and even influence fluid mechanics. This knowledge has greatly impacted our history, and fueled innovations that have taken societies to new technological advances. But, there are still many aspects of fluid dynamics that we still do not understand.

Fig. 1.1.: Airbus A320 flying over the Atlantic ocean and turbulent clouds. The photo was taken on the 22nd of December of 2021.

A major open problem is turbulence. To start with, turbulence does not have a clear definition. Instead, it is identified according to a series of characteristics [Pop00; Dav15]. The two most important ones are that turbulence is chaotic, and that it displays a wide range of motion scales. The first means that, infinitesimal changes in the initial conditions have large effects in the subsequent motions, and the second that, the velocity field fluctuates in a wide range of magnitudes in time and space. These characteristics make turbulence extremely difficult to predict and highly dependent on the initial conditions and the geometry of the flow. Despite the difficulty to study turbulent flows, there is an urgent need to improve our understanding of turbulence, from how flows become turbulent (the problem of turbulence transition) to how turbulence behaves once triggered. After all, turbulent flows are related with increased friction, and therefore, with energy losses. Some estimates

suggest that turbulence is behind the 10% of the yearly energy losses worldwide [Blo18]. Moreover, turbulence plays an important role in other physical set-ups that are of great scientific interest. It plays a major role in weather prediction, and in larger scale phenomena like solar ejections or accretion disks of black holes [Dav15; BH98].

Turbulence also has a direct impact on our health. The presence of turbulence, or at least irregular flow patterns, in cardiovascular flows has been long linked with cardiovascular diseases [FH64; CG05; GN10]. The reason is that, irregular flow patterns, and/or turbulence, exert additional shear stresses locally, which can lead to the formation of injuries in large arteries [MAI99] and eventually serious health issues like aneurysms. Despite its importance, it is still not clear how turbulence emerges and behaves in cardiovascular flows. There are several reasons for this:

1. The flow behavior in the larger arteries is difficult to measure, specially in in-vivo experiments [Gül+18; Cor+21].
2. According to the typical parameters observed in cardiovascular flows (more on this below) they lay in the transitional regime [Bür+12; Les+10; Sta+11]. In this regime, flows can either be laminar (ordered and predictable), turbulent (disordered and unpredictable) or intermittently transition between the two.
3. Cardiovascular flows are extremely complex. The flow is influenced by patient specific physiological traits, by blood rheology, by the geometric complexity of the cardiovascular network [Gül+18], by fluid-structure interactions between the vessel walls and the flow [RB20]; and by the unsteady driving force of the pumping heart, see fig. 1.2.

The main motivation of this thesis is to determine if flows in the larger arteries may be susceptible to transition or not, and if they are, how turbulence behaves once triggered. The idea is to consider a highly simplified model of cardiovascular flows: the ideal case of a Newtonian fluid in a smooth, straight, rigid and cylindrical pipe, thereby ignoring all the complex features of cardiovascular flows, except for the unsteady driving of the flow. With this simplification, I can focus on just one characteristic, analyze it in detail and achieve a deep understanding on the most important effects the unsteady driving has. Future studies can benefit from this thesis, and combine my results with their analyses of other features: such as rheology, fluid-structure interactions or the effect of the geometry.

There are several reasons to consider the unsteady driving and not other complex features. Here I name three. First, our understanding on turbulence transition and behavior in pipe flow driven at a steady rate has greatly improved in the last century, see Avila *et al.* [ABH23] for a recent review. The idea is to exploit this knowledge and extend it to unsteadily driven flows. Second, flows driven with time-dependent forces are ubiquitous. Two examples are: the weather system that is driven mostly by a time dependent solar radiation [AO18], and turbulence in flapping wings [CL16]. Third, in larger vessels, other effects like rheology or the geometric complexity are expected to play a smaller role. In the next section, I justify the reasons to ignore them and to ignore the compliance wall effects.

1.1 From cardiovascular to pulsatile pipe flow

Blood is a complex fluid, that shows shear-thinning, viscoelastic and other Non-Newtonian behaviors [Ber+21]. Moreover, it is heterogeneous, and carries, apart from other cells, red blood cells, that conform $40-45\%$ of the total blood volume. Red blood cells vibrate, move and interact with each other, forming stacked structures like rouleaux, see fig. 1.2 (center), that increase the friction forces

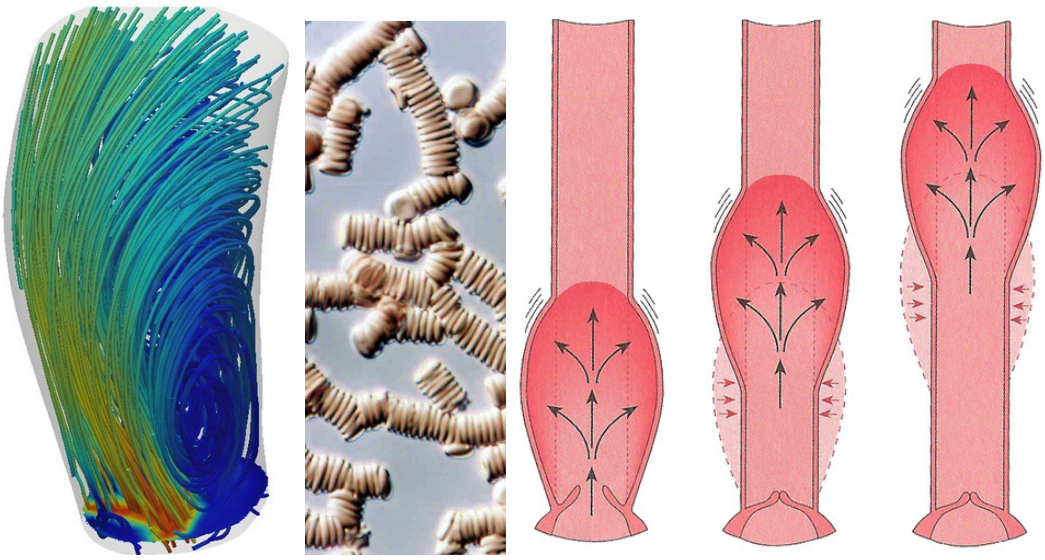

Fig. 1.2.: Three examples of complex features of cardiovascular flows. First on the left: flow trajectories measured in a model of a human aorta with stenosis by the group of M. Holzner [HZ]. Second on the left: rouleaux structures formed by stacked red blood cells [Bäu+99]. To the right: the Windkessel effect: the flow deforms the aorta, that stores some volume of fluid during the heart systole and then releases it during diastole [MZJ18].

in the flow [Bäu+99]. These structures have yield stresses and can be broken down by the flow, releasing energy and momentum carried by the red blood cells. Unfortunately, currently we do not have the computer capabilities to model all these complex multiscale features, let alone model them together with the fluid movement. Fortunately, in the larger vessels, these features are expected to play a small role [Kar+14] and are typically considered as part of the viscous effects. Moreover, the observed velocity of blood in the larger arteries is small enough to assume that compressible effects are negligible [Bür+12]. Therefore, here, and in the rest of my thesis, I only consider incompressible flows of Newtonian fluids.

The aorta is the vessel where turbulence is expected to be more prominent [CL13], since blood flow in the aorta has the highest flow velocity observed in the circulatory system. The human aorta can be split in different sections: the ascending aorta, the aortic arch, the descending aorta and the supraceliac aorta. (See a representation of the human aorta at the end of this chapter in figure 1.10). The most critical section, in terms of cardiovascular diseases, is the descending aorta [Mal+16]. Incidentally this section is relatively straight, that is why I model it as a straight pipe. Also, although the descending aorta has a certain roughness, that worsens with age and diseases [XT10; Sco+20], here I model it as a smooth pipe. In order to consider the effect of geometric imperfections in turbulence transition, at some point of this thesis I model the effect of individual roughness elements at the wall, see §2.1.5.

Note that the endothelial cells that cover the vessel walls can actually freely move and adapt to the flow [FBF20]. This behavior is ignored in this thesis, and the flow is assumed to vanish at the walls. Another geometric feature, here ignored, is the flow bifurcations in the aorta. I understand that both features should be considered in future analyses, as they have an impact on the boundary conditions and behavior of the flow as a whole. I also assume the flow to be fully developed at the pipe inlet. This is not the case for cardiovascular flows [Ha+16], and future analysis should consider the effect of different inlet conditions.

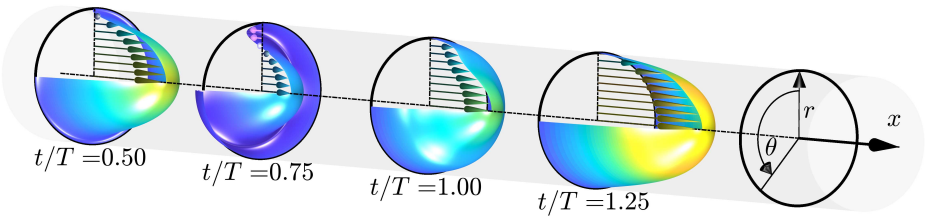

Fig. 1.3.: Geometric definition of the problem. The rigid pipe of circular cross-section is represented with a grey surface. The cylindrical coordinates of the problem are: x as the axial and stream-wise direction, θ is the azimuthal direction and r the radial and wall normal direction. Find with surfaces and arrows the instantaneous laminar profiles of a pulsatile pipe flow at Reynolds number (see eq. (1.9)) $Re = 2000$, Womersley number (see eq. (1.17)) $Wo = 11$ and pulsation amplitude (see eq. (1.16)) $A = 1$, at different phases of the period. Brighter colors mean higher u_x axial velocities.

Lastly, it is widely known that fluid-structure interactions between the flexible vessel walls and blood flow are of major importance in arterial flows. In fact, as blood travels from the heart to the smaller vessels, the Windkessel effect dampens the harmonic components of the flow, and makes it steady [MZJ18], see fig. 1.2(right). The aorta is a flexible vessel and its stiffness depends on gender, age and health [Mal+16]. Stiffer aortas have been associated with cardiovascular diseases, as they are suspected to affect the behavior of the flow and stresses at the wall. Despite its importance, it is currently extremely difficult to correctly model fluid-structure interactions, specially if other features like the unsteady driving are considered. Here I adopt a bottom-top approach and ignore the fluid-structure interaction effects on transition. I believe that, by obtaining a deep understanding on the effects of the unsteady driving, future analysis can build up from my results and extend the analysis to pulsatile flows bounded by flexible walls.

In this thesis, pulsatile pipe flow refers to the incompressible flow of a Newtonian fluid in a smooth, straight and cylindrical pipe driven with a time dependent bulk velocity. See a graphical representation of the problem considered here in figure 1.3.

The rest of the chapter is organized as follows. First a methodology to study shear flows is presented, §1.2. Then, a short survey on methods to study turbulence transition and turbulence in shear flows §1.3 & 1.4 is included. The description then offers a state of the art analysis of transition and turbulence behavior in pulsatile pipe flows §1.5. At the end of the chapter, §1.6 the questions addressed in this thesis are clearly stated together with a short description of the rest of the chapters.

1.2 A methodology to study fluid dynamics

The physics discipline of fluid dynamics is fortunate enough to have a successfully tested and clearly defined set of equations of motion: the Navier–Stokes equations. Here I quickly go over the philosophy by which these equations were originally derived.

Firstly, the fluid is assumed as a continuum. Therefore, a property ϕ of the fluid, like the velocity $\boldsymbol{u}$ or the density ρ, is described as a field. This means that, the property is assigned a unique value at each position $\boldsymbol{x}$ and time t, $\phi(\boldsymbol{x}, t)$.

Just as a quick word about notation, in this thesis, bold quantities denote vectors. For instance, in cylindrical coordinates the position is defined as $\boldsymbol{x} = [r, \theta, x]$ and the velocity as $\boldsymbol{u} = [u_r, u_\theta, u_x]$. The vorticity field is defined as

$$\boldsymbol{\omega} = \nabla \times \boldsymbol{u}. \tag{1.1}$$

Take an infinitesimally small lump of fluid. The movement of the lump of fluid is affected by body forces $\boldsymbol{f_B}$ and surface forces $\boldsymbol{f_S}$. By invoking Newton's second law, the linear momentum of the lump is governed by:

$$\frac{\mathrm{D}\left(\rho \boldsymbol{u}\right)}{\mathrm{D}t} = \boldsymbol{f_B} + \boldsymbol{f_S}, \tag{1.2}$$

where

$$\frac{\mathrm{D}\bullet}{\mathrm{D}t} = \frac{\partial \bullet}{\partial t} + \boldsymbol{u} \cdot \left(\nabla \bullet\right), \tag{1.3}$$

is the material derivative. The body forces act on the whole volume of the fluid lump, and can be for instance gravity or magnetic forces. The surface forces can be further split between pressure forces and friction forces. The latter, that we know as viscous forces, have a molecular origin and must be modeled [Dav15]. Here I model the viscous forces as linearly proportional to the shear rate, what is known as a Newtonian fluid. The constant of proportionality is the viscosity ν, that is an emergent property of the fluid. It quantifies the molecular interactions that result in the macroscopic friction (viscous) forces of the flow.

Together with Newton's second law, the fluid lump must also satisfy mass and energy conservation. From these conditions, two additional equations can be defined, that, together with Newtons second law and a model for the fluid, allow for the study of the fluid energy, density and velocity evolution.

The first to define such a model was Euler [Eul52]. Instead of modeling the friction forces of the fluid, he ignored them all-together and obtained (what we now know as) the Euler equations. Much later, Navier and Stokes used the Newtonian fluid model for the viscous forces, and obtained a set of second-order in space, and first order in time, non-linear partial-differential equations that we know today as the Navier–Stokes equations (NSE). The accuracy of the NSE has been proven time and time again comparing experiments and theory/simulations. They are the most successful model we currently have to study fluid dynamics.

In this thesis the incompressible flow of a Newtonian fluid with density ρ and kinematic viscosity ν in a pipe with circular cross section, driven with a pulsatile bulk velocity constraint, is studied. The linear momentum of the flow is governed by the NSE:

$$\frac{\partial \boldsymbol{u}}{\partial t} + \left(\boldsymbol{u} \cdot \nabla\right) \boldsymbol{u} = -\nabla \cdot p + \nu \boldsymbol{\nabla^2 u} + \frac{1}{\rho} \boldsymbol{f_B}, \tag{1.4}$$

where $p = P/\rho$ is a modified pressure; and $\boldsymbol{f_B}$ is any body force acting on the flow. The flow velocity must also satisfy the divergence free condition:

$$\nabla \cdot \boldsymbol{u} = 0. \tag{1.5}$$

Despite coming from simple physical principles (mass and linear momentum conservation) the NSE are extremely difficult to solve. In order to effectively use them, they are either simplified, or

numerically integrated. By this I mean that the NSE are discretized in space, and are integrated at discrete time steps using time-marching algorithms. In the past, human calculators were used to perform this integration. Nowadays, we write numerical codes that run in computers and that do the calculations for us. Direct Numerical Simulations (DNS) refer to the numerical integration of the full NSE, without the inclusion of (turbulent) models or other simplifications to the equations.

Computational Fluid Dynamics (CFD) is an active research area that seeks to improve the accuracy and the efficiency of numerical codes to numerically solve fluid dynamic problems. As part of this thesis I developed a `C-CUDA` code that runs in Graphical Processing Units `GPUs` to numerically integrate the shear flow in a rigid, straight, smooth and cylindrical pipe. The code outperforms existing `CPU` codes for similar (in terms of spent energy) computational resources, with the same accuracy. It has allowed me to perform DNS on a broad parametric space in a fast way. Find more about the methods and the code in Chapter 2.

1.2.1 Statistically steady pipe flow

In the following sections, the case of statistically steady pipe flow (SSPF), i.e. pipe flow driven in a steady manner, is given a special attention. This is because, as I show in this thesis, the transitional regime of pulsatile pipe flow is very similar to the transitional regime of SSPF in a broad parametric regime. Moreover, it was the problem of transition to turbulence in pipe flow what originally motivated most of the studies on turbulence transition.

In the case of laminar pipe flow, the velocity $\boldsymbol{U} = [0, 0, U_{HP}(r)]$ has only a stream-wise component, that is only radially dependent. This unidirectional velocity field is known as the Hagen-Poiseuille flow, and it has an analytical solution. Let U be the time-averaged bulk velocity and D the diameter of the pipe, the Hagen-Poiseuille profile is given as:

$$U_{HP}(r) = 2U\left(1 - \left(\frac{2r}{D}\right)^2\right). \tag{1.6}$$

The mean shear of the laminar profile is defined as the derivative of the velocity profile with respect to the (radial) wall-normal direction: $\frac{\mathrm{d}U_{HP}}{\mathrm{d}r}$.

Note that in the case of a flow in a pipe with length L_x, the bulk velocity is defined as:

$$u_b = \langle u_x \rangle_V = \frac{4}{\pi D^2 L_x}\int_0^{2\pi}\int_0^{D/2} \boldsymbol{u}\cdot\boldsymbol{e_x} r\mathrm{d}r\mathrm{d}\theta\mathrm{d}x, \tag{1.7}$$

where $\boldsymbol{e_x}$ is the unit vector in the (axial) stream-wise direction. The time averaged bulk velocity can be computed as:

$$U = \langle u_b \rangle_t = \frac{1}{t}\int_0^t u_b \mathrm{d}t. \tag{1.8}$$

Angled brackets denote averaging with respect to one or more spatial directions, time or pulsation phase. In this case V stands for the pipe volume and t for time.

I will use the time-averaged bulk velocity and pipe diameter as the characteristic velocity and length of the flow in the rest of my thesis.

1.3 Turbulence transition in shear flows

Flows with a mean velocity that is predominantly one-dimensional, are known as shear flows [Dav15]. They are usually related with the presence of a force and/or a boundary condition, like a wall, that result in a mean shear in the flow. Several canonical flows are shear flows, such as channel, Taylor-Couette, boundary layer or, the main focus of this thesis, pipe flow.

In this section I review the mechanisms by which shear flows transition to turbulence, and the main methods to study transition.

1.3.1 Reynolds experiment

The famous experiments of Reynolds [Rey83] kick-started the study of turbulence transition 140 years ago. In his experiments, Reynolds observed how, at low bulk velocities, pipe flow remained ordered and 'featureless' (what we now know as laminar). As he increased the bulk velocity of the flow, he noticed that some 'flashes' of disordered flow were intermittently triggered. At these velocities, the flow remained ordered (laminar) except for the regions with turbulent flashes. We now know this regime as the transitional regime. By increasing the velocity, after a certain value, the flashes elongated rapidly and contaminated the whole pipe with disordered flow, what we know today as fully turbulent flow. His experiments raised many questions about turbulence transition that took more than a century to solve [ABH23], and others that have not been answered yet.

Reynolds found that, what regime to expect: laminar, transitional or turbulent, depends on a single non-dimensional parameter:

$$Re = \frac{UD}{\nu}, \tag{1.9}$$

that we know today as the Reynolds number.

The Reynolds number compares the viscous forces with the inertial (advective) forces of the flow. It can also be understood as a ratio of time scales. The numerator represents a viscous time scale in the form D^2/ν and the denominator the advective time scale D/U. This means that, if $Re \gg 1$ the averaged inertia processes on the flow occur much faster than the averaged viscous processes.

Reynolds identified that at low Re the flow in the pipe is always laminar. As he increased the velocity, and thus Re, the flow becomes transitional and at some point turbulent at $Re \gtrsim 2000$. Reynolds was unable to accurately determine the critical Re_c of pipe flow and suggested that would be around $Re_c \approx 2000$. The critical Reynolds number sets the boundary between turbulent flow at $Re > Re_c$ and laminar flow at $Re < Re_c$. The critical Reynolds number of pipe flow was determined almost 130 years after Reynolds experiment by Avila *et al.* [Avi+11], and it is now fixed at $Re_c \simeq 2040$,

1.3.2 Supercritical transition (modal growth)

After Reynolds experiments, many researchers suspected that, at a sufficiently high Re, laminar pipe flow becomes unstable. In that case, infinitesimal perturbations in the experimental set up, instead of decaying, grow in magnitude, saturate and trigger turbulence in the flow. In order to check if infinitesimal perturbations do grow in magnitude, researchers studied the linear stability of shear flows [Eck10].

In the framework of linear stability, first a given solution/state of the system is selected. In the case of shear flows this usually corresponds to the laminar profile $\boldsymbol{U}$. Then, the equations of motion are used to describe the behavior of perturbations around this equilibrium condition. The perturbations are assumed to be infinitesimally small, and therefore, the equations of motion can be linearized about the equilibrium condition. In the case of a steady $\boldsymbol{U}$, this results in a linear problem with the form:

$$\frac{\partial \boldsymbol{u'}}{\partial t} = \mathrm{A}\boldsymbol{u'}, \tag{1.10}$$

where $\boldsymbol{u'}$ is the velocity perturbation, and A a linear operator on $\boldsymbol{u'}$, that depends on $\boldsymbol{U}$ and Re. In the case of fluid dynamics, the operator A corresponds to the linearized NSE about the laminar profile $\boldsymbol{U}$ (more about this in §3.1). If the real part of any of the eigenvalues of A is positive, perturbations can grow exponentially in magnitude. This is commonly referred to as modal growth of perturbations, as they exponentially grow through linear instabilities. Here modal refers to the mode defined by the eigenvector of the unstable eigenvalue.

Perturbations that exponentially grow at some point will reach a magnitude big enough to trigger non-linear effects and then turbulence. This kind of transition is known as supercritical.

Determining the eigenvalues of the operator A is a difficult task, specially without the use of numerical methods. Therefore, some researchers tried to develop formulas or expressions that could indicate whether a laminar flow is unstable or not. Rayleigh considered the case of inviscid flows. Using the Euler equations, and for Cartesian coordinates, he determined that, a necessary condition for a laminar profile to be inviscidly unstable is that it must have at least an inflection point [Ray95]. Inflection points are positions in the laminar profile where the mean shear is maximum or minimum. Later Fjørtoft [Fjø50] found that this condition applies only if there is a single inflection point in the flow profile, and only if it satisfies a certain condition, see §4.2.1 for more details. Indeed, the presence of inflection points has been historically linked with turbulence transition. A notable example is the Kelvin-Helmholtz instability, that is related with the existence of inflection points in the flow profile [PHC78]. In the case of cylindrical coordinate, there exists an equivalent condition also related with the existance of inflection points [BG62].

However most laminar shear flows, like the parabolic Hagen-Poiseuille profile, do not have inflection points, but still transition to turbulence at finite Re. To determine the stability of most shear flows, one needs to inevitably take into account the viscous effects and obtain the eigenvalues of the operator A in equation (1.10). One can find in the literature the critical Re at which several canonical flows become unstable. Two notable examples are: plane Poiseuille flow $Re_c \geq 5772.2$ and the Blasius boundary layer flow, with $Re_c \geq 519.4$ (table 3.1 in Schmid & Henningson[SH00]). In the case of boundary layer flow, at sufficiently high Re the laminar profile becomes susceptible to the growth of a certain type of perturbations, Tollmien-Schlichting waves [Tol35; Sch33], no matter how small they initially are. They grow, saturate and lead to a supercritical turbulence transition.

Even after considering viscous effects, the Hagen-Poiseuille profile is linearly stable, at least up to $Re \approx \mathcal{O}\left(10^7\right)$ [MT03], while transition is observed at $Re \approx 2000$. This is also observed in plane Couette flow that, despite being linearly stable, transitions to turbulence at finite Re [DHB92]. Other shear flows typically experience turbulence transition at Re far lower than what their corresponding linear stability analysis suggests like channel flow [Cha02] or the Blasius boundary layer flow [BSH04]. Obviously the linear stability theory is not able to explain transition in all of these cases.

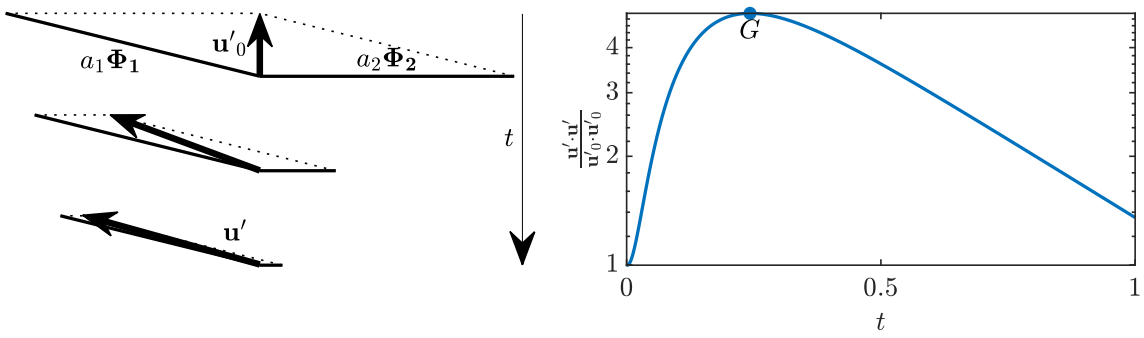

Fig. 1.4.: Graphical representation of non-modal growth due to the superposition of two non-orthogonal vectors. To the left, from top to bottom, the time evolution of the perturbation velocity. To the right the energy growth. Results correspond to $\boldsymbol{u'}(t) = a_1\mathbf{\Phi_1}\exp(\lambda_1 t) + a_2\mathbf{\Phi_2}\exp(\lambda_2 t)$ for $a_1 = a_2 = 1$, $\lambda_1 = -1$, $\lambda_2 = -10$, $\mathbf{\Phi_1} = (-3, 1)$ and $\mathbf{\Phi_2} = (3, 0)$.

1.3.3 Subcritical transition (non-modal growth)

The failure of the linear stability analysis to explain transition to turbulence seemed to contradict the theoretical works of Orr and others. They had established that the only way perturbations can grow on top of a laminar profile is through linear mechanisms [SH00]. Yet, tiny perturbations grow and trigger turbulence in flows that are stable, and they do so without the presence of (linear) instabilities. What was wrong: the theory or the experimental evidence?

It turns out that, for most shear flows, the A operator in equation (1.10) is non-normal. This means that the eigenvalues of A do not need to be orthogonal to one another. This has a profound impact on the growth of perturbations on top of the laminar profile, and it is best understood with an example.

Let me consider a profile without linear instabilities. In that case, the eigenvalues of the corresponding operator A in equation (1.10) have a negative real part $\Re(\lambda_j) < 0$. For the sake of simplicity I will assume that all the eigenvalues are real valued. Let me order the eigenvalues according to their real part so: $\lambda_{j>2} < \lambda_2 < \lambda_1 < 0$, and let $\mathbf{\Phi}_j$ be the corresponding eigenvectors. The time evolution of any perturbation with initial magnitude $\boldsymbol{u'}_0$, can be described as:

$$\boldsymbol{u'}(t) = \sum_j a_j \mathbf{\Phi_j} \exp(\lambda_j t), \tag{1.11}$$

where a_j depend on the shape of the initial condition. The value of the perturbation can be approximated with the two leading eigenvalues as:

$$\boldsymbol{u'}(t) \approx a_1\mathbf{\Phi_1}\exp(\lambda_1 t) + a_2\mathbf{\Phi_2}\exp(\lambda_2 t). \tag{1.12}$$

Since both eigenvalues are smaller than 0, the flow is stable, and the magnitude of perturbations will asymptotically decay. However, if the angle between the two eigenvalues is bigger than $90°$, see top-left of figure 1.4, and for certain initial conditions, perturbations can in fact grow in magnitude during finite times and then decay. See in the figure how, while $\mathbf{\Phi}_1\exp(\lambda_1 t)$ and $\mathbf{\Phi}_2\exp(\lambda_2 t)$ decrease in magnitude, the magnitude of $\boldsymbol{u'}$, represented by the length of the vector, actually

increases transiently. See in figure 1.4 (right), how the energy of the perturbation grows until it reaches a maximum usually denoted as :

$$G = \max_t \frac{\boldsymbol{u'}(t) \cdot \boldsymbol{u'}(t)}{\boldsymbol{u'}_0 \cdot \boldsymbol{u'}_0}, \tag{1.13}$$

and then quickly decays. In the case of sear flows, the maximum energy growth G of perturbations scales algebraically with Re: $G \propto Re^2$ [SH00].

Using this linear mechanism, perturbations can grow on top of laminar flows for finite times. This type of growth is referred to as non-modal or transient growth, as it does not come from modal instabilities of the laminar profile and is only found during finite time spans. Perturbations that have a sufficiently big magnitude grow through this mechanism and at some point trigger non-linear effects and turbulence. This type of transition is known as subcritical transition, as it is inevitably related with the initial magnitude of the perturbation. The minimal (initial) magnitude the perturbations need to trigger turbulence is known as the 'minimal seed', [PK10; Che+11] and it is an active area of research in transition to turbulence. Usually, the higher the Re is, the smaller in magnitude the minimal seed becomes. It must also be noted that some perturbations are more likely than others to trigger turbulence, *i.e.* reach a higher G for the same initial magnitude. The determination of which perturbations are optimal, for which kind of flows, is also an open research area.

Interestingly, Reynolds hypothesis for turbulence transition was close to this phenomena. He wrote:

> *'This showed that the steady motion was unstable for large disturbances long before the critical velocity was reached . [...] But the fact that in some conditions it [the laminar flow] will break down for a large disturbance, while it is stable for a smaller disturbance shows that there is a certain residual stability so long as the disturbances do not exceed a given amount' (Reynolds 1883 [Rey83]).*

Basically, Reynolds suspected that transition in pipe flow does not happen due to linear instabilities, but due to sufficiently large perturbations.

In summary, it is due to transient non-modal growth, and not due to modal instabilities, that pipe flow transitions to turbulence [Col65]. Perturbations can grow on top of the laminar profile thanks to non-modal mechanisms. If the initial energy of the perturbation and Re are high enough, perturbations will grow and eventually trigger turbulence. In the case of pipe flow, the optimal perturbation is a pair of stream-wise constant vortices [SH94]. See a representation of the stream-wise constant perturbation in figure 1.5. Note that the non-modal growth is a linear mechanism, which does not contradict the theoretical works of Orr and others.

Mechanisms for non-modal growth

Some of the linear mechanisms behind non-modal growth are found in several shear flows. Here we mention the two most important ones:

- **Lift-up**. This type of mechanism is found in the case of perturbations that have velocities perpendicular to the shear of the laminar profile. The perturbations extract energy from the shear and energize stream-wise perturbations [EP75]. If the perturbation velocity is in the wall normal direction, this mechanism is called the **lift-up** mechanism, see fig. 1.5.

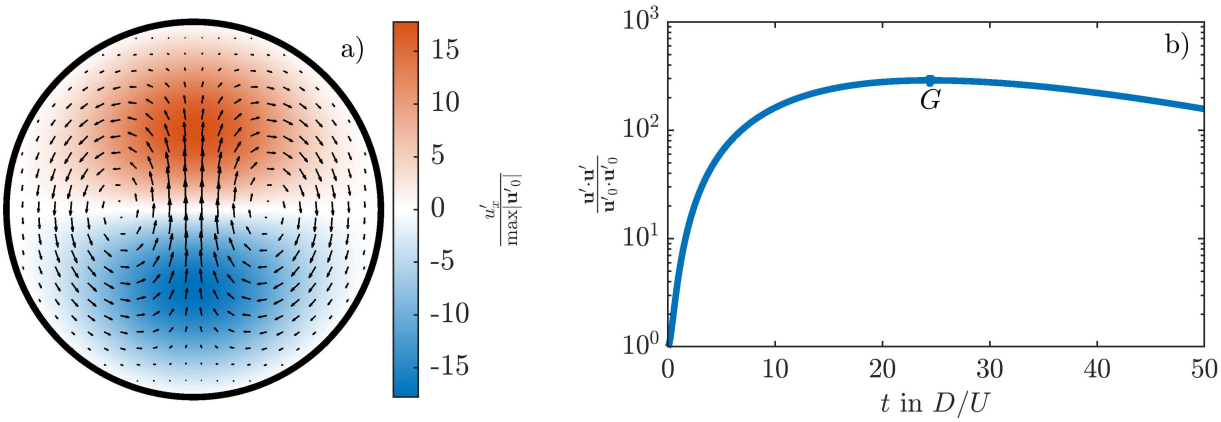

Fig. 1.5.: (a) cross section view of the optimal stream-wise coherent perturbation in SSPF at $Re = 2000$. The snapshot corresponds to the instant of time where the energy of the perturbation is maximum. With colors the axial perturbation velocity normalized with the perturbation velocity at $t = 0$. (b) the energy growth of the perturbation with respect to time.

- **Orr-mechanism**. This mechanism is found in perturbations that are initially backwards-leaning with respect to the shear of the laminar profile. These perturbations are tilted forward, until they are normal to the mean shear. This happens by the action of continuity, and releases high cross-shear velocities when the perturbations are finally normal to the mean shear [Orr07; Cha+16].

How to determine the non-modal growth

In the literature one finds several methods to obtain the perturbations that yield the maximal non-modal, also known as transient, growth. The majority of the methods share a similar idea: to solve an optimization problem and obtain the initial $\boldsymbol{u'}_0$ that maximizes G in equation (1.13). They differ in the type of constraints they impose to the problem.

One method imposes that the perturbation $\boldsymbol{u'}$ evolves according to the linearized NSE [BBS08; XSA21]. This is the method I use in this thesis to compute the optimal perturbations on top of pulsatile pipe flow. The method is relatively fast and robust, which allows me to compute the optimal perturbation at several flow parameters. More on this, in Chapters 3 & 4. Unfortunately the method does not allow for the calculation of the minimal seed, as perturbations here are assumed to be infinitesimally small. To obtain the minimal seed one needs to consider the full non-linear NSE.

Another method imposes that the perturbation $\boldsymbol{u'}$ evolves according to the NSE [Ker18]. This method is able to compute the minimal seed for turbulence transition. It is, however, much more computationally expensive and not that robust.

In the recent years, a new method called the optimally time-dependent modes [BS16] has also been used to compute the optimal perturbation on top of time dependent flows. Instead of solving the optimization problem, the method generates a time-evolving orthonormal basis, capable of identifying transient growth and instabilities in a time-evolving flow. Recently this framework has been successfully applied to pulsatile Poiseuille flow [Ker+21] and time dependent solutions of Boundary Layer flows [Ben+23]. The first optimally dependent mode actually corresponds to the optimal perturbation of the flow obtained with the first optimization problem described above. As drawbacks, this method does not return the minimal seed, it can be computationally costly and more importantly, apart from the first mode, the rest of modes do not have a physical interpretation.

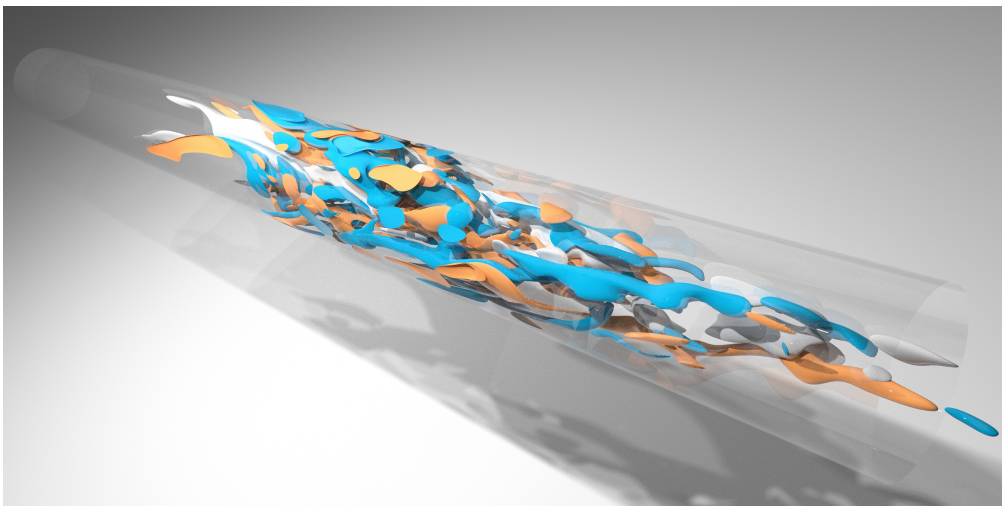

Fig. 1.6.: Visualization of a turbulent puff in a direct numerical simulation of statistically steady pipe flow at $Re = 2000$. Grey denotes low axial velocity streaks with $-0.4U$ with respect to the Hagen-Poiseuille profile and in red/blue positive/negative axial vorticity with $\pm 3U/D$.

1.4 Turbulence in shear flows

Independently of the type of growth of perturbations, modal or non-modal, once they reach a sufficiently high magnitude, they trigger non-linear effects and if Re is high enough, turbulence. As mentioned above, in the turbulent regime, the flow is organized in multiple scales of motion and is also chaotic and unpredictable. These characteristics make turbulence extremely difficult to study.

Historically turbulence has been studied with the use of statistics. This is because, despite being seemingly random, the statistics of turbulence are reproducible between shear flows and experimental realizations (the NSE are deterministic but result in chaotic dynamics). A notable example of this is the famous *log-law* of the wall. At sufficiently high Re, the mean stream-wise velocity profile attains a universal form, that is independent on Re. Instead, it scales with the shear at the wall. The *log-law* of the wall only has one parameter, that, when correctly fitted, perfectly reproduces the mean profile of several wall bounded flows at high Re. This, (and other universal statistic results), indicate that there may exist some dominant dynamics of turbulence behind its complicated behavior, that we still do not know of [Dav15]. One of the main goals of modern fundamental turbulence research, is the identification of these underlying dynamics.

Apart from the use of simple statistics, in this thesis I use two additional methods to study the behavior of turbulence in pulsatile pipe flow: the study of coherent structures and low-order models. The former focuses in persistent structures of the flow, as they are believed to be the cause of persistent turbulent dynamics. The latter tries to define models as simple as possible, that are able to explain the main dynamics of turbulence. In what follows I describe them both in more detail.

1.4.1 Coherence in turbulent flows

Coherent structures are local solutions of the flow, that are intense enough to evolve on their own and are not greatly affected by the rest of flow structures [Jim18]. The study of persistent structures in wall-bounded flows dates back to the works of Townsend [Tow61]. He already noted the importance eddies have on the behavior of the flow. Eddies can be understood as a sort of coherent structures. However, it is difficult to find a concrete definition of what an eddy is, and I

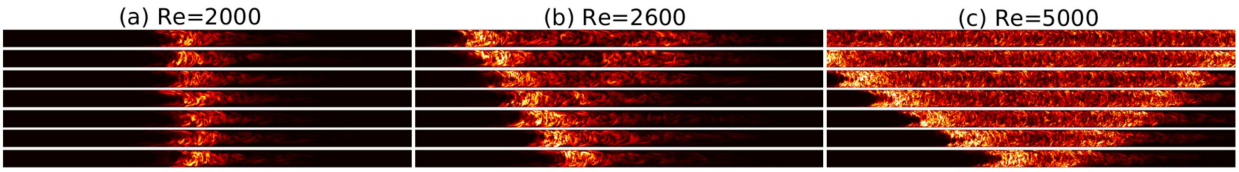

Fig. 1.7.: Visualization of the temporal evolution of turbulent puffs and slugs in SSPF, extracted from figure 1 from Song *et al.* [Son+17]. In (a) a puff at $Re = 2000$, in (b) a slug at $Re = 2600$ and in (c) a slug at $Re = 5000$. The flow is from left to right and turbulence is visualized by the cross-section kinetic energy $u_r^2 + u_\theta^2$ with respect to a reference frame moving at the averaged upstream and downstream front speed. Dark areas correspond to small fluctuations and bright areas to large fluctuations. The vertical length scale (radial) is scaled by a factor of 2 for better visualization. Time evolves in the upward direction and panels are separated by $10D/U$ in (a,c) and by $100D/U$ in (b), where U is the time-averaged bulk velocity, and D the pipe diameter.

will not try to come up with one here. Roughly, eddies are vortical structures that persist during relatively long times in the flow [Dav15].

Another classical example of coherent structures are velocity streaks. Streaks are flow structures, that have an streamwise velocity smaller (or larger) than the mean one. They tend to be relatively long, and persist for relatively long times. Because of this, their presence has a big impact on the local dynamics and dominates them during certain times. Streaks are usually linked with the presence of stream-wise vortices. The interaction between streaks and vortices is the main ingredient of a coherent motion observed in all wall-bounded turbulent flows: the wall-cycle. The wall cycle is a self-sustaining process [JM91; JP99], that can be understood as a coherent motion. The cycle starts with the development of velocity streaks due to (allegedly) linear mechanisms (more on this later). At some point the streaks meander, and result in vortical bursts that release high levels of turbulent kinetic energy. The mechanisms by which the cycle restarts are currently unknown, and are actively researched.

1.4.2 Turbulent puffs in pipe flow

When linearly stable flows first transition to turbulence, they do so in the form of localized turbulent patches that remain coherent (with approximately a constant length and magnitude) for asymptotically long times. Examples are: spiral turbulence in the Taylor Couette flow [Col65; Mes+09; Fel+23], stripes in plane-Poiseuille and plane-Couette flow [AHA86; BT05] and turbulent puffs in pipe flow [WC73]. See an example of a turbulent puff in figure 1.6 and in figure 1.7a. These structures can be understood as localized wall cycles, that are advected at a certain velocity with respect to the bulk of the flow. In what follows I describe the behavior of puffs in pipe flow in more detail.

Puffs exhibit a variety of chaotic behaviors. The probability to observe one behavior, and not others, depends on Re. Puffs are more likely to randomly decay at low $Re \lesssim 2040$, split at $2040 \lesssim Re \lesssim 2250$ or elongate into slugs at $Re \gtrsim 2250$ [ABH23]. Slugs are turbulent structures that have a similar upstream front to puffs [Son+17] but that elongate until they fill the pipe with turbulence, see fig 1.7b and c.

See an example of random puff decay at $Re = 1900$ in figure 1.8. At this Re puffs decay at seemingly unpredictable times, as seen in figure 1.8a. Even though all of the puffs in the figure are initialized with similar instantaneous states, they show radically different times of decay. The probability that a

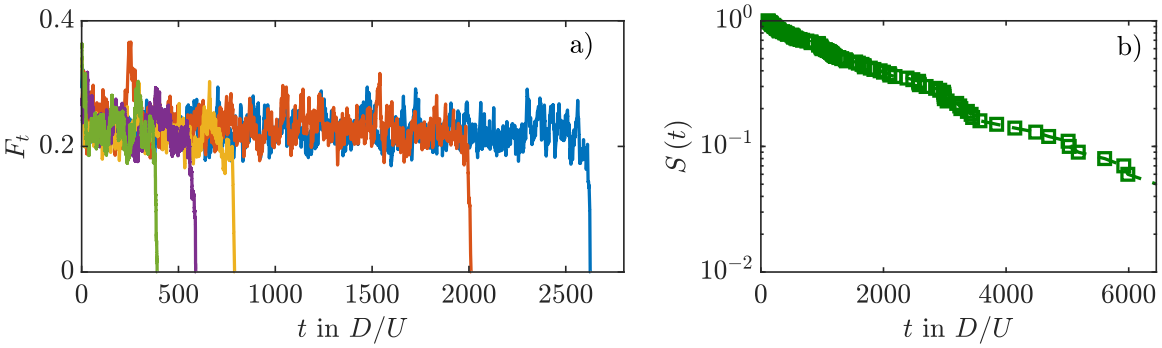

Fig. 1.8.: Decay of turbulent puffs in SSPF at $Re = 1900$. (a) the temporal evolution of turbulent fraction is shown, where $F_t = 1$ corresponds to fully turbulent flow, $F_t = 0$ to fully laminar. The results correspond to 5 different DNS in $L_x = 50D$ long pipes. Each simulation is initialized with a different instantaneous puff. Puffs may persist for significant time before abruptly decaying to laminar flow. (b) probability of puff survival at $Re = 1900$ collected from 100 independent simulations. It corresponds to the probability to observe a puff survive for a time t or longer. The figure is adapted from figure 8 in Avila *et al.* [ABH23].

puff survives for a time t or longer after being initialized at $t = 0$, follows an exponential distribution as shown in figure 1.8b.

In SSPF, puffs (slugs) move (and elongate) at a certain upstream (and downstream) front speed c_u (and c_d) that also depends on Re. The exact mechanisms by which turbulent puffs decay, split or elongate are still un-clear.

1.4.3 Models of turbulence in wall-bounded flows

Historically, researchers have looked for reduced-order models that can explain the main dynamics of turbulent flows. They can be divided between linear and non-linear models.

Many phenomena in the wall cycle can be explained with linear mechanisms [Jim13]. For example Encinar *et al.* [EJ20] showed that the bursts of turbulence in the wall cycle, are mainly due to the Orr mechanism. This mechanism happens at a time scale set by the local mean shear.

Also Lozano *et al.* [LD+21] recently studied the effect linear mechanisms have on turbulence survival. They performed causal analysis where they modified the flow field in order to sequentially eliminate the effects of: linear-instabilities of the streaks, lift-up and Orr mechanisms on the turbulent flow. They showed how linear instabilities play almost no role on turbulence survival, and that, out of the lift-up and the Orr-mechanism, the latter is more important. In this thesis I perform a similar causal analysis, and show that at some flow parameters, and in contrast to their results, localized turbulence actively makes use of instabilities in the flow to survive.

Recently the use of machine learning methods to obtain reduced order models of turbulent flows has gained popularity. Some examples are Dynamic Mode Decomposition [Sch10] or Sparse Non-linear Dynamic identification algorithms [BPK16]. However, their successful application to (relatively) high Re flows is still limited.

Other researchers have developed non-linear models to describe particular dynamics of turbulence. A classic example is the Lorenz model [Lor63], that corresponds to a model of turbulent natural

convection. In the case of transitional flows, Baggett *et al.* [BDT95] developed a simple model to explain transition and turbulence survival due to non-modal effects. Additionally, Moehlis *et al.* [MFE04] developed a reduced-order model of transitional Walaffe flow (the flow between two free-slip walls subjected to a sinusoidal force). The model is able to reproduce the transient chaos behavior (random decays) observed in transitional shear flows (like puffs in pipe flow at $Re \lesssim 2040$).

1.4.4 Model of puffs in steady pipe flow

One of the most successful reduced-order models of turbulence is the one proposed by Barkley *et al.* [Bar11a; Bar11b; Bar+15; Bar16] for puffs in pipe flow. This model is further referred to as the Barkley Model (BM) and it is briefly introduced in the following paragraphs, and explained in detail in Appendix A.

The BM is able to reproduce the front speeds of turbulent puffs and slugs in SSPF. The model considers only two one-dimensional, time-dependent variables, $q(x,t)$ and $u(x,t)$, whose evolution is described by two non-linearly coupled advection-diffusion-reaction equations. These equations are inspired by, but not derived from, the Navier–Stokes equations. The variable q represents the turbulence intensity, and u the state of the local mean shear of the flow, at each axial location x and time t. The key feature of the BM is the non-linear interaction between u and q. The turbulence intensity q takes advantage of the mean shear u to grow. However, in the axial locations where $q > 0$, the local mean shear is reduced [Hof+10; Küh+18], and in turn, adversely affects the growth of q. When fitted correctly, the model returns the turbulent front speeds c_u and c_d of turbulent structures in SSPF with high accuracy in a broad Re regime [Bar+15; Son+17; CXS22]. The remarkable success of this model has motivated some researchers to use it to study puffs split dynamics, [FG22], or even turbulence transition of non-Newtonian pipe flow [Rom+21].

The question still remains of, to what extent, the assumptions and simplifications of the BM are correct, and if it can be easily adapted to similar flow set ups, such us the pipe flow driven at an unsteady flow rate studied in this thesis. In Chapter 7 I extend the BM to the case of pulsatile pipe flow.

1.5 Pulsatile pipe flow

The bulk velocity of a pulsatile pipe flow with a generic waveform, and non-dimensionalized with the time averaged bulk velocity U, is defined as:

$$u_b(t) = 1 + \sum_{n=1}^{\infty} a_n \cos(n \cdot 2\pi f \cdot t) + \sum_{n=1}^{\infty} b_n \sin(n \cdot 2\pi f \cdot t), \tag{1.14}$$

where a_n and b_n are the Fourier coefficients of the pulsation and f the frequency of the pulsation. In the case of a single harmonic pulsation, the bulk velocity is defined as:

$$u_b(t) = 1 + A \sin(2\pi f \cdot t) \tag{1.15}$$

being

$$A = \max(u_b) - 1, \tag{1.16}$$

the amplitude of the pulsation. Apart from the waveform of the pulsation, *i.e.* either the combination of a_n and b_n or the amplitude A, pulsatile pipe flow depends on two dimensionless parameters, the Reynolds number and the Womersley number. Re is computed using U, and the pipe diameter D, see equation (1.9). The Womersley number compares the viscous time scale with the characteristic time scale of the pulsation:

$$Wo = \frac{D}{2}\sqrt{\frac{2\pi f}{\nu}}. \tag{1.17}$$

It also defines the Stokes boundary layer thickness as $\delta_S \propto \frac{1}{Wo}$. The Stokes boundary layer thickness sets the normal distance from the wall that separates the Stokes layer (close to the wall) dominated by viscous forces, from the layer (away from the wall) dominated by the inertia of the pulsation.

The pulsation period is defined as $T = 1/f$. In advective time units $(d(U)$, the length of the period is:

$$T = \frac{\pi Re}{2Wo^2}. \tag{1.18}$$

Additionally, an instantaneous $Re_i\,(t)$ can be defined as:

$$Re_i\,(t) = u_b\,(t)\,Re, \tag{1.19}$$

and a maximum $Re_{\max}$ as:

$$Re_{\max} = \max\,(u_b)\,Re = (1 + A)\,Re. \tag{1.20}$$

As it was firstly obtained by [Sex30; Wom55] in the case of laminar flow, pulsatile pipe flow has an analytical solution, the Sexl-Womersley (SW) velocity profile $\boldsymbol{U} = [0, 0, U_{SW}\,(r, t)]$. In that case, the flow has only an axial component, that is radial and time dependent $U_{SW}\,(r, t)$. See a representation of the SW profile at a given Re, Wo and A, and different phases of the period in figure 1.3. See additional SW profiles in Appendix B. In this thesis I study transition to turbulence of the SW profile and the behavior of turbulence once triggered.

In what follows I summarize the existing knowledge about transition and the transitional regime of pulsatile pipe flow. Apart from some notable exceptions [BV18; Sca+23] most research on transition in pulsatile pipe flow has mainly focused on harmonic pulsations, eq (1.15). Studies with single harmonic pulsations can be classified between those that consider small-to-moderate A and those that consider higher A.

1.5.1 Small-to-moderate amplitudes

At small-to-moderate $A \lesssim 0.4$, the critical Re_c was initially suspected to scale with Wo and A. Peacock *et al.* [Pea+98] performed measurements for a broad range of flow parameters, and determined that $Re_c = 1220\,Wo^{0.42}A^{0.17}/(1 + A)$. However, others [Sar66; SH86; Tri+12] showed that at large Wo, Re_c actually reaches an asymptotic value. Despite reaching the same conclusion, all of these studies reported different asymptotic Re_c as Wo increased.

These discrepancies were eventually explained in the experimental and numerical studies of Xu *et al.* [Xu+17; XA18]. They identified that, the differences in Re_c observed by all the previous studies, were due to the type of perturbations they used to trigger turbulence in the flow. For instance, Stettler

[SH86] and Trip [Tri+12] continuously perturbed the flow, while Sarpkaya [Sar66] introduced impulsive perturbations.

Xu *et al.* also offered a convincing explanation on how pulsatile pipe flows at $A \lesssim 0.4$ transition to turbulence. Transition occurs due to finite amplitude perturbations as in SSPF. During the phases of the period where $Re_i \gtrsim 1600$, the perturbations can trigger a turbulent puff, whose behavior depends on the pulsation frequency. At high $Wo \gtrsim 20$ (independently of A) puffs do not have enough time to adapt to the fast harmonic driving [XA18], and their behavior is identical to the one found in SSPF. At low $Wo \lesssim 4$ the behavior is quasi-steady, and the puff dynamics depend on the instantaneous Reynolds number [Xu+17]. At intermediate $5 \lesssim Wo \lesssim 19$, the behavior of puffs smoothly transitions between the two limiting cases described above.

1.5.2 Moderate-to-high amplitudes

At higher $A \geq 0.5$, transition in pulsatile pipe flow shows a different behavior.

Thomas *et al.* [Tho+11] studied the problem from a linear stability point of view. They performed Floquet stability analysis on pulsatile pipe flows at many Re, Wo and A. The Floquet stability analysis is similar to the linear stability analysis presented in equation (1.10). In this case the operator A corresponds to the linearized Navier-Stokes equations integrated over 1 pulsation period. A periodic flow is Floquet stable if, after one pulsation period, all infinitesimal perturbations on top of it decay. In their study they only considered axisymmetric perturbations to the flow. They identified that only at extremely high $A \gtrsim 10$ the corresponding SW profile is unstable at $Re \lesssim 1000$. They also reported that Wo has a small effect on turbulence transition. However, later experiments by Xu *et al.* [Xu+20] exhibited turbulence transition at $Re \approx 800$ and $A \gtrsim 1$, with a strong dependence on Wo.

Specifically Xu *et al.* [Xu+20] reported transition in the form of localized sudden bursts at intermediate $Wo \approx 6$ and small $Re \approx 800$, see fig. 1.4. These bursts appeared periodically in every deceleration phase $\left(\frac{\mathrm{d}u_b}{\mathrm{d}t} < 0\right)$ and were attributed to small geometric imperfections in the experimental set-up. Initially, the bursts exhibit a helical shape that collapses and evolves into a localized turbulent spot. The turbulent spot first expands in the axial direction and is later advected by the mean flow before it is finally dampened during the acceleration phase $\left(\frac{\mathrm{d}u_b}{\mathrm{d}t} > 0\right)$. Xu *et al.* [XSA21] linked these bursts to a family of non-modal helical perturbations. They performed transient growth analysis at different combinations of Re, Wo and A and showed that for $Re \geq 800$ and $A \geq 0.5$ at least two different types of perturbations are able to grow on top of the laminar SW profile. Depending on Wo, one grows more than the other. At $Wo \lesssim 4$ or $Wo \gtrsim 20$, the optimal perturbation is the pair of stream-wise-constant vortices, as in SSPF [SH94]. At $5 \lesssim Wo \lesssim 19$, on the other hand, helical perturbations exhibit the highest energy growth (G). While stream-wise vortex perturbations exhibit only algebraic scaling with Re ($G \propto Re^2$, [SH00]), helical perturbations exhibit an exponential scaling ($G \propto e^{aRe}$, [XSA21]). This exponential scaling renders helical perturbations more dangerous (in terms of turbulence transition) than the stream-wise vortices at some Wo and A [PS21]. Initially Xu *et al.* [XSA21] linked the growth of helical perturbations with an Orr mechanism. But non-modal mechanisms, by definition, do not grow exponentially as described above in §1.3.3. The reason for the outstanding growth of helical perturbations have not been identified yet.

At certain combinations of Wo and A, the SW profile exhibits inflection points [Tru06; Mia+17; Neb19]. Remember that inflection points are usually linked with flow instabilities [Stu82]. At high Wo, the SW profile changes quickly and perturbations do not have enough time to take advantage of these instabilities to grow. Kerczek [KD74] reached a similar conclusion for a similar study in Stokes layer flow. However, at lower Wo, the SW profile evolves slower and perturbations have

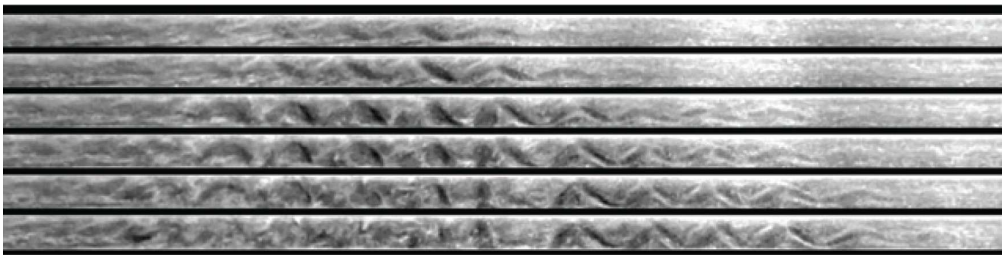

Fig. 1.9.: Visualization of transition to turbulence in pulsatile pipe flow, extracted from Xu *et al.* [Xu+20]. The figure shows the evolution of the helical instability at $(Re, Wo, A) = (2200, 5.6, 0.85)$ from a tiny geometric disturbance close to the wall. Even though the flow is from left (upstream) to right (downstream), the helical wave spreads downstream as well as upstream. The snapshots correspond to equispaced phases of the period from $t/T = 0.625$ at the top to $t/T = 0.75$ at the bottom.

enough time to take advantage of the inflection points to grow. This was first suggested by Cowley *et al.* [Cow87] and recently demonstrated by Nebauer *et al.* [Neb19]. Following these ideas, Kern *et al.* [Ker+21] recently connected the growth of optimal time dependent modes to the presence and characteristics of inflection points in (plane) pulsatile Poiseuille flow. However, a relationship between the inflection points and the growth of the helical perturbations in pulsatile pipe flow has not been shown yet.

The pulsation waveform

In most applications, pipe flows exhibit a bulk velocity with multiple harmonics, resulting in multiple non-zero coefficients (a_n, b_n) in eq. (1.14). This introduces additional control parameters to the problem, as the transition scenario depends on all the non-zero a_n and b_n that define the waveform of the pulsation. This new parametric space has been largely unexplored. Experiments on turbulence transition for non-single harmonic pulsations show that waveforms with longer deceleration phases have an earlier onset of transition, whereas steeper accelerations delay it [BV18]. Despite these interesting results, there is still a huge range of waveform characteristics (including cardiovascular-like waveforms) that have not been studied in detail yet.

Another question concerns the dynamics after the flow transitions to turbulence. In the experiments and numerical simulations of Xu *et al.* [Xu+20; XSA21], they observe how the helical instability is able to trigger turbulence during some phases of the period, that then quickly decays after a single pulsation. Whether this behavior is found at other flow parameters or not, it is still unknown. Recent studies have also shown how pulsatile pipe flows driven with physiological-like waveforms can result in a reduction of the energy input to achieve a mean net flux [Sca+23], compared to the corresponding SSPF case. To this day, broad parametric regimes of pulsatile pipe flow remain largely unexplored.

1.6 Objectives of the thesis

The scope of this thesis is the transitional regime of pulsatile pipe flows, at $1000 \lesssim Re \lesssim 3000$, $3 \lesssim Wo \lesssim 21$, at different pulsation amplitudes and for different pulsation waveform. All the cases considered here correspond to moderate-to-high amplitudes $A \gtrsim 0.5$ with little or no reverse bulk flow $\min(u_b) \approx 0$. Note that the parametric space considered here is relevant for cardiovascular flows, as combinations of these flow parameters are found in different sections of blood flow in the human aorta, see figure 1.10 and table 1.1. The objective of the thesis is two-fold.

First, the transition mechanisms of pulsatile pipe flows at these flow parameters will be studied. To that end, transient growth and stability analyses will be combined, to identify the features that make some pulsatile pipe flows more susceptible to transition than others. Here, and for the first time, not only single harmonic pulsations will be considered, but also pulsations with multiple harmonics.

Second, the behavior of turbulence once triggered will be studied. To that end, a large number of direct numerical simulations (DNS) of different pulsatile pipe flows, will be performed. Again, not only single harmonic pulsations will be considered, but also multiple harmonic pulsations, including, cases with a physiological-like pulsation. In order to understand the dynamics by which turbulence survives at some flow parameters, causal analyses are performed. At the end of the thesis, the low-order Barkley model (BM) of turbulence in transitional SSPF is extended to the pulsatile case.

1.6.1 Outline of the thesis

The rest of the thesis is organized as follows.

- Find in Chapter 2 the mathematical models used in this thesis and the numerical methods used to perform DNS of pulsatile pipe flows. As part of this thesis a new `C-CUDA` code was developed to perform fast and efficient simulations. Find a description of the code also there.
- Chapter 3 includes a description of the methods to numerically perform the transient growth and stability analyses.
- Chapter 4 includes the results of the transient growth and stability analyses.
- Find in Chapter 5 the results of different pulsatile pipe flows DNS. In this chapter, several strategies to trigger turbulence in pulsatile pipe flow are studied, together with the behavior of turbulence once it is triggered.
- In Chapter 6 a causal analysis is performed to show that, the mechanism that makes some pulsatile pipe flows more susceptible to transition, is also related with the survival of turbulence once it is triggered.
- Find in Chapter 7 a description on how the original BM is extended to pulsatile pipe flow using the lessons learned in the previous chapters. The chapter describes the new model and the results of the model compared with the numerical simulations presented in Chapter 5.
- Chapter 8 includes the main conclusions of the thesis together with an outlook.

At the end of the thesis a series of Appendixes are added to complement the information discussed in the main chapters.

- Appendix A includes a description of the original BM for SSPF.
- Appendix B has a catalogue of figures with the SW profile at different flow parameters, and the results of the corresponding linear stability.
- Appendix C includes a description on how we estimate the grid in our DNS, together with the list of DNS analyzed in this thesis.
- Appendixes D & E expand on the methods and results of my causal analysis.
- Appendix F includes a list of Peer-Reviewed papers related with this thesis.
- Appendix G includes a list of student bachelor thesis related to this thesis.

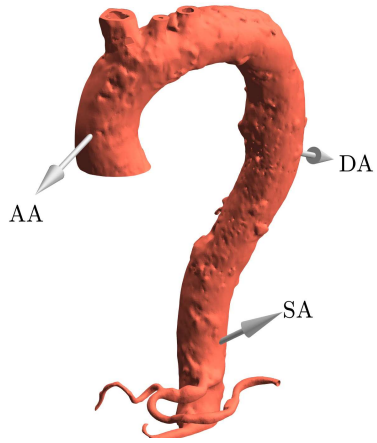

Fig. 1.10.: Human aorta.

Tab. 1.1.: Typical flow parameters for individuals in unstressed conditions, in different sections of the aorta according to Les *et al.* [Les+10] and Stalder *et al.* [Sta+11]. AA stands for ascending aorta, DA for descending aorta and SA for supraceliac aorta.

	AA	DA	SA
Re	1000-1500	1100-1400	700-900
$Re_{\max}$	3300-4800	3630-4620	2310-2970
Wo	15-18	10-14	5.3-7.5

2 Mathematical formulation and DNS numerical methods

Find in this chapter first a short description of the mathematical formulation used in this thesis. This includes the way the bulk velocity is defined and also how the effect of geometric defects at the wall are modeled in DNS.

In the second part of this chapter, §2.2 and following sections, the description of the methods used in this thesis to numerically integrate the Navier–Stokes equations (NSE), eq. (2.3), are described. All the methods are implemented in an open-source, pseudo-spectral code **nsPipe** [Ló+20] which is also described here. As part of this thesis, a new C-CUDA GPU-version of **nsPipe** was developed. A detailed explanation of the new GPU-**nsPipe** is included in this chapter, together with its validation and performance verification.

2.1 Mathematical models

Find in this section more details on the NSE presented in equation (1.4), and the method by which they are discretized in this thesis. The methods by which the bulk velocity and the effect of geometric defects in the pipe wall are defined are also shown.

2.1.1 Pressure-velocity coupling

The pressure p in the NSE, see equation (1.4), does not act as a thermodynamic pressure, but as a dynamic pressure and it is another unknown of the flow. Here, the pressure is actually a Lagrange multiplier, that is meant to make sure the divergence free condition is satisfied at all positions in the flow $\boldsymbol{x}$.

By taking the divergence of equation (1.4), and invoking $\nabla \cdot \boldsymbol{u} = 0$ one can obtain a Poisson equation for the pressure as:

$$\nabla^2 p = -\nabla \cdot [(\boldsymbol{u} \cdot \nabla)\, \boldsymbol{u}]\,. \tag{2.1}$$

See section 2.4.3 for a description of the boundary conditions.

2.1.2 Non-dimensionalization

In this thesis, a rigid circular cross section pipe with diameter D (and radius $R = D/2$) is considered. All the variables in the problem are rendered non-dimensional with the pipe diameter D, the time averaged bulk velocity of the laminar profile U and the fluid density ρ_f. The incompressible NSE take the form:

$$\rho_f \frac{U^2}{D}\frac{\partial \hat{\boldsymbol{u}}}{\partial \hat{t}} + \rho_f \frac{U^2}{D}\left(\hat{\boldsymbol{u}}\cdot\hat{\nabla}\right)\hat{\boldsymbol{u}} = -\rho_f \frac{U^2}{D}\hat{\nabla}\cdot\hat{p} + \rho_f \frac{U^2}{D}\frac{1}{Re}\hat{\boldsymbol{\nabla}}^{\mathbf{2}}\hat{\boldsymbol{u}} + \rho_f \frac{U^2}{D}\hat{\boldsymbol{f}}_{\boldsymbol{B}}, \tag{2.2}$$

where $Re = \frac{UD}{\nu}$, and variables with a hat are non-dimensional. One can eliminate $\rho_f \frac{U^2}{D}$ from the above equation and obtain the non-dimensional NSE as:

$$\frac{\partial \boldsymbol{u}}{\partial t} + (\boldsymbol{u}\cdot\nabla)\boldsymbol{u} = -\nabla\cdot p + \frac{1}{Re}\boldsymbol{\nabla}^{\mathbf{2}}\boldsymbol{u} + f_p(t)\,\boldsymbol{e}_x + \boldsymbol{f}_b, \text{ and } \nabla\cdot\boldsymbol{u} = 0, \tag{2.3}$$

where the upper hat has been dropped from the notation. In the rest of this thesis only non-dimensional quantities are considered, unless stated otherwise.

Here the body force $\boldsymbol{f_B} = f_p(t)\,\boldsymbol{e}_x + \boldsymbol{f}_b$ has been split between the driving pressure gradient $f_p(t)\,\boldsymbol{e}_x$, and any other body force acting on the flow defined as $\boldsymbol{f}_b$. Note that, the unitary vector $\boldsymbol{e}_x$ defines the stream-wise direction.

2.1.3 Cylindrical coordinates

The problem here is considered in cylindrical coordinates: (r, θ, x), where r is the radial and at the same time wall normal direction, x is the axial and at the same time stream-wise direction, and θ the azimuthal direction.

In cylindrical coordinates, the NSE take the following form for each velocity component:

$$\begin{aligned}\frac{\partial u_r}{\partial t} + u_r\frac{\partial u_r}{\partial r} + \frac{u_\theta}{r}\frac{\partial u_r}{\partial \theta} - \frac{u_\theta^2}{r} + u_x\frac{\partial u_r}{\partial x} &= -\frac{\partial p}{\partial r}\\ &+ \frac{1}{Re}\left[\frac{\partial}{\partial r}\left(\frac{1}{r}\frac{\partial}{\partial r}(r u_r)\right) + \frac{1}{r^2}\frac{\partial^2 u_r}{\partial \theta^2} + \frac{\partial^2 u_r}{\partial x^2} - \frac{2}{r^2}\frac{\partial u_\theta}{\partial \theta}\right] + \boldsymbol{f}_b\cdot\boldsymbol{e}_r,\end{aligned}$$

$$\begin{aligned}\frac{\partial u_\theta}{\partial t} + u_r\frac{\partial u_\theta}{\partial r} + \frac{u_\theta}{r}\frac{\partial u_\theta}{\partial \theta} + \frac{u_\theta u_r}{r} + u_x\frac{\partial u_\theta}{\partial x} &= -\frac{1}{r}\frac{\partial p}{\partial \theta}\\ &+ \frac{1}{Re}\left[\frac{\partial}{\partial r}\left(\frac{1}{r}\frac{\partial}{\partial r}(r u_\theta)\right) + \frac{1}{r^2}\frac{\partial^2 u_\theta}{\partial \theta^2} + \frac{\partial^2 u_\theta}{\partial x^2} + \frac{2}{r^2}\frac{\partial u_r}{\partial \theta}\right] + \boldsymbol{f}_b\cdot\boldsymbol{e}_\theta, \text{ and}\end{aligned}$$

$$\frac{\partial u_x}{\partial t} + u_r\frac{\partial u_x}{\partial r} + \frac{u_\theta}{r}\frac{\partial u_x}{\partial \theta} + u_x\frac{\partial u_x}{\partial x} = -\frac{\partial p}{\partial x} + \frac{1}{Re}\left[\frac{1}{r}\frac{\partial}{\partial r}\left(r\frac{\partial u_x}{\partial r}\right) + \frac{1}{r^2}\frac{\partial^2 u_x}{\partial \theta^2} + \frac{\partial^2 u_x}{\partial x^2}\right] + f_p + \boldsymbol{f}_b\cdot\boldsymbol{e}_x.$$

The continuity equation takes the form:

$$\frac{1}{r}\frac{\partial}{\partial r}(r u_r) + \frac{1}{r}\frac{\partial u_\theta}{\partial \theta} + \frac{\partial u_x}{\partial x} = 0. \tag{2.4}$$

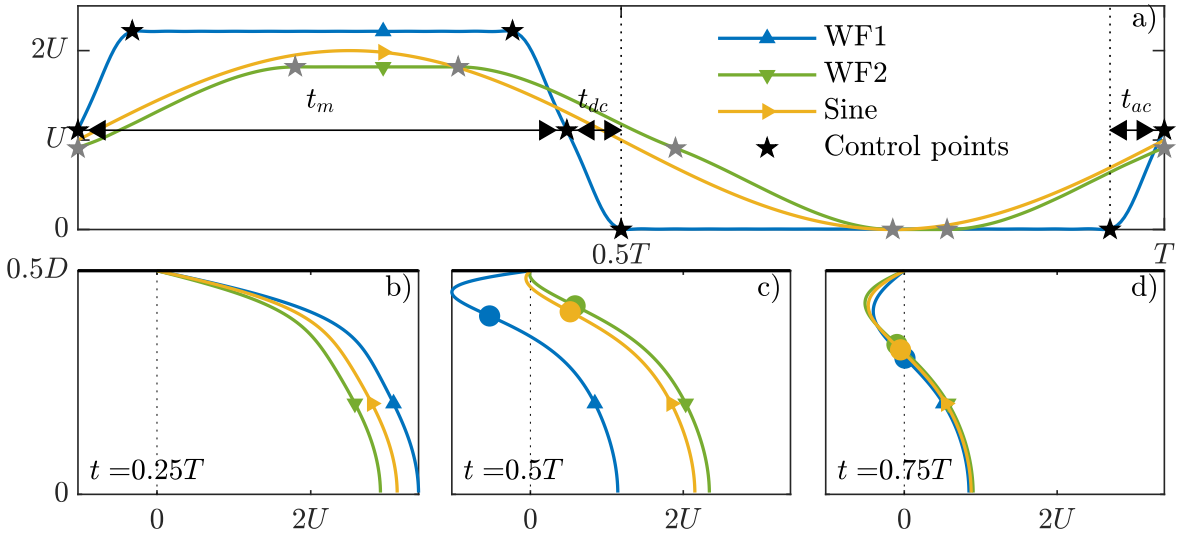

Fig. 2.1.: Definition of three bulk velocity waveform and corresponding laminar flow profiles. In the top panel, the black stars denote the 6 control points which define the waveform 1 (WF1), with $t_{ac} = t_{dc} = 0.05$ and $t_m = 0.45$; in blue a 30 Fourier mode approximation of the corresponding spline. The grey stars denote the 6 points which define the waveform 2 (WF2), with $t_{ac} = t_{dc} = 0.2$ and $t_m = 0.55$; in green a 30 Fourier mode approximation of the spline. In yellow a single harmonic sine wave pulsation with $A = 1$. In the bottom three panels, the laminar profiles for the three waveform defined in the top panel are shown at three instants of time. Filled points denote the position and existence of inflection points in the laminar profile.

2.1.4 *Definition of the bulk velocity*

The driving pressure gradient $f_p(t)$ in equation (2.3) can either be constant, or time dependent. In the latter case, it is set to adjust the bulk velocity of the flow so at each time step the desired bulk velocity is obtained. As described in §1.6, in this thesis single harmonic and multiple harmonic pulsations at $A \in [0, 1]$ are considered. In the case of multiple harmonic pulsations, a certain type of waveform is designed.

The waveform is designed so the bulk velocity is never negative, and has a minimum $\min(u_b(t)) = 0$. This is inspired by cardiovascular flows, where the minimum bulk velocity is close to zero in the larger vessels [Bür+12]. Although the bulk velocity is always positive, locally the velocity profile can have negative axial velocities, as shown in fig. 2.1c. Apart from this constraint, the waveform is designed so its acceleration and deceleration slopes, and its time symmetry, can be controlled with a limited number of parameters.

Six control points (black or grey stars in figure 2.1a) are defined in time. They represent the *skeleton* of the waveform. Their horizontal position is controlled by 3 parameters t_{ac}, t_{dc} and t_m. They are understood as the length in time of certain phases of the period, and are described in detail below.

All the waveform shapes have an acceleration phase with a slope that is set by the parameter t_{ac}. Note that the total time the bulk velocity stays in the acceleration phase is $2t_{ac}$. The bulk velocity then remains in a high velocity phase $u_b = \max(u_b(t))$ for a the time span $t_m - t_{ac} - t_{dc}$. Then the pulsation enters a deceleration phase $\left(\frac{\partial u_b}{\partial t} < 0\right)$, whose slope is set by the parameter t_{dc}, so that the total time the pulsation decelerates is $2t_{dc}$. Finally the bulk velocity remains in a low velocity

phase where $u_b \equiv 0$ for the rest of the pulsation period ($T - t_m - t_{ac} - t_{dc}$). The last parameter ($0 < t_m < T$) defines how symmetric the waveform is with respect to time. This, together with the minimum bulk velocity constraint $\min(u_b(t)) = 0$ in turn indirectly sets the maximum $Re_{\max}$ of the flow as

$$Re_{\max} = Re\frac{T}{t_m}. \tag{2.5}$$

At $t_m = \frac{1}{2}$, the waveform is symmetric and stays the same fraction of time in the high and low velocity phases. Since the minimum velocity is $u_b = 0$, for this case $Re_{\max} = 2Re$. As $t_m \to 0$ the time the flow stays in a high velocity phase decreases and $Re_{\max}$ increases.

The parameters t_{ac}, t_{dc} and t_m are non-dimensional, normalized in terms of T so they are always within t_{ac}, t_{dc}, $t_m \in [0, 1]$. They are connected with one another such that

$$t_m + t_{ac} + t_{dc} < 1,\ t_{ac} < 0.5 \text{ and } t_{dc} < 0.5. \tag{2.6}$$

The velocity at each of the control points (black or grey stars in figure 2.1a) is then determined so the time-averaged bulk velocity is equal to U. The velocities at the points are then embedded in a smooth spline, using a monotone piecewise cubic Hermite interpolating polynomial [FC80]. The spline is then fitted using $N_F = 30$ Fourier modes to obtain a periodic pulsation.

2.1.5 Model geometric defects close to the pipe wall

At some point in the thesis, the effect of geometric disturbances close to the wall are studied. Inspired by the work of Marensi *et al.* [Mar+20], this is done, not by changing the geometry of the problem, but by using body forces to model the effect of disturbances close to the wall. The body force takes the form:

$$\boldsymbol{f_b}(r, \theta, x, t) = -A_b \cdot f_b(r, \theta, x) \cdot \boldsymbol{u}(r, \theta, x, t). \tag{2.7}$$

It acts against the velocity field $\boldsymbol{u}$ and is localized in the radial, azimuthal, and axial direction by

$$f_b(r, \theta, x) = f(r) \cdot g(\theta, x) \cdot h(x) \text{ with} \tag{2.8}$$

$$f(r) = \frac{1}{2} + \frac{1}{\pi}\arctan(S_r(r - r_0)), \tag{2.9}$$

$$g(\theta, x) = \frac{1}{\pi}\left(\arctan(S_\theta(\theta - \pi(\theta_0(x) - l_\theta))) - \arctan(S_\theta(\theta - \pi(\theta_0(x) + l_\theta)))\right), \tag{2.10}$$

$$h(x) = \frac{1}{\pi}\left(\arctan\left(S_x\left(x - x_0 + \frac{l_x}{2}\right)\right) - \arctan\left(S_x\left(x - x_0 - \frac{l_x}{2}\right)\right)\right) \text{ and} \tag{2.11}$$

$$\theta_0(x) = 1 + 2\Delta\theta\frac{(x - x_0)}{l_x}. \tag{2.12}$$

These localization functions are bounded by $f_b \in [0, 1]$ and satisfy the constraints: $\max(f) = 1$, $\min(f) = 0$, $\max(g) = 1$, $\min(g) = 0$, $\max(h) = 1$, and $\min(h) = 0$; the perturbation amplitude is given by A_b.

Due to the big parametric space in hand, three simple body force set-ups are designed. The first set-up is an axisymmetric force that models the effect of a small circumferential contraction, similar to a weak stenosis in blood vessels or imperfect pipe joints in laboratory experiments. See the geometry of this disturbance in figure 2.2a.

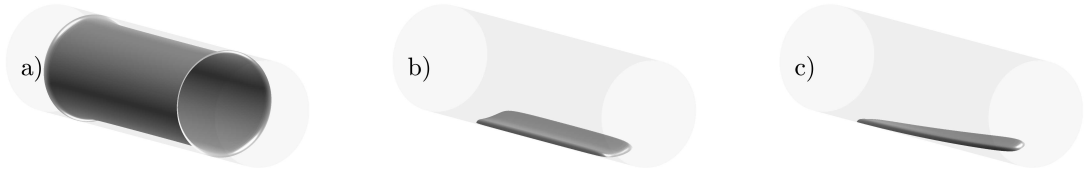

Fig. 2.2.: Geometric representation of the perturbation force ($\boldsymbol{f_b}$, eq. (2.7)) in terms of iso-surfaces (black) of the localization function for $f_b = 0.5$. (**a**) Axisymmetric contraction. (**b**) localized bump. (**c**) Tilted bump. See table 2.1 for details. The direction of the mean bulk flow is always from left to right.

Tab. 2.1.: Parameters to control the body force term in equation (2.7) to model the effect of geometric perturbations: Magnitude (A_b), slope (S), size (l), and location in the radial (r), azimuthal (θ), and axial (x) direction. Geometric representations of the perturbations are shown in figure 2.2.

	$\boldsymbol{A_b}$	$\boldsymbol{S_x}$ in $\frac{\mathbf{1}}{\boldsymbol{D}}$	$\boldsymbol{l_x}$ in $\boldsymbol{D}$	$\boldsymbol{x_0}$ in $\boldsymbol{D}$	$\boldsymbol{S_r}$ in $\frac{\mathbf{1}}{\boldsymbol{D}}$	$\boldsymbol{r_0}$ in $\boldsymbol{D}$	$\boldsymbol{S_\theta}$	$\boldsymbol{l_\theta}$	$\boldsymbol{\Delta\theta}$
Contraction	0.25	4	2.5	10	100	0.45	20	≥ 1	0
Bump	0.25	4	2.5	10	100	0.45	20	0.25	0
Tilted Bump	0.25	4	2.5	10	100	0.45	20	0.0625	0.1

The second set-up is a highly localized force that approximates the effect of a single bump or an individual roughness element, see fig. 2.2b. The third set-up is also a highly localized force that approximates the effect of a single bump or an individual roughness element, but this time, it is tilted with respect to the axial direction, see fig. 2.2c. The parameters defining the perturbations are given in table 2.1.

2.2 Spatial discretization

In `nsPipe` the NSE are treated in cylindrical coordinates, see §2.1.3. The axial and azimuthal directions x and θ are treated as periodic, and are discretized using a Fourier-Galerkin method. The code employs high order finite-differences in the (in-homogeneous) wall-normal (radial) direction r. In this section the Fourier-Galerkin method and the discretization of the radial direction r are described.

2.2.1 Fourier spectral methods

In the Fourier-Galerkin method, any variable f is approximated as a truncated series of harmonic functions:

$$f\left(r,\theta,x,t\right) \approx \sum_{k=-K/2}^{K/2-1} \sum_{m=-M/2}^{M/2-1} \hat{f}_{k,m}\left(r,t\right) e^{ikk_0 x + imm_0\theta}, \tag{2.13}$$

where, $k = 1, 2, ...$ and $m = 1, 2, ...$ are the axial and azimuthal wavenumbers, k_0 and m_0 the axial and azimuthal first harmonics, and $\hat{f}_{k,m}$ the spectral coefficients. In the rest of the manuscript, $m_0 = 1$ and $k_0 = \frac{2\pi}{L_x}$, where L_x is the length of the pipe in diameters. Also, the axial and azimuthal number of modes are denoted as $N_x = K/2$ and $N_\theta = M/2$.

The spectral coefficients can be obtained with a Discrete Fourier Transform (DFT):

$$\hat{f}_{k,m}(r,t) = \frac{1}{M_\theta M_x} \sum_{j_\theta=0}^{M_\theta-1} \sum_{j_x=0}^{M_x-1} f(r, \theta_{j_\theta}, x_{j_x}, t)\, e^{-ik\frac{2\pi j_x}{M_x} - im\frac{2\pi j_\theta}{M_\theta}}, \tag{2.14}$$

where M_θ and M_x are the azimuthal and axial discrete points where the function is evaluated in physical space. The axial discrete points x_j are computed as: $k_0 x_j = \frac{2\pi j_x}{M_x}$ and the azimuthal discrete points θ_j as $m_0\theta_j = \frac{2\pi j_\theta}{M_\theta}$, where $j_x = 0, 1, ..., M_x - 1$ and $j_\theta = 0, 1, ..., M_\theta - 1$.

Find in the rest of this section a series of issues one needs to consider when using Fourier-Galerkin methods. The description is done for a one dimensional variable $f(x)$, defined in the periodic domain $0 \leq x \leq 2\pi$, but can be extended to the two dimensional case in eq.(2.13).

Convergence of the Fourier Transform

Let the one dimensional variable $f(x)$ be discretized as:

$$f(x) \approx \sum_{k=-N/2}^{N/2-1} \hat{f}_k e^{ikx}. \tag{2.15}$$

Invoking Parseval identity:

$$\int_0^{2\pi} f^2 \mathrm{d}x = 2\pi \sum_k^\infty \hat{f}_k^2, \tag{2.16}$$

the error ϵ_N of approximating f using a truncated Fourier series can be shown to be:

$$\epsilon_N^2 = \int_0^{2\pi} f^2 \mathrm{d}x - 2\pi \sum_{|k|<N/2} \hat{f}_k^2 = 2\pi \sum_{|k|\geq N/2} \hat{f}_k^2. \tag{2.17}$$

This error is dominated by the spectral coefficient of $|k| \equiv N/2$. As long as f is continuous, this coefficient can be computed as:

$$2\pi\hat{f}_{N/2} = \int_0^{2\pi} f e^{-iNx/2} \mathrm{d}x = \frac{-2}{iN}\left[f(2\pi) - f(0)\right] e^{-iNx/2} + \frac{2}{iN}\int_0^{2\pi} \frac{\mathrm{d}f}{\mathrm{d}x} e^{-iNx/2} \mathrm{d}x. \tag{2.18}$$

If f is periodic, $f(2\pi) = f(0)$. One can apply this formula recursively as long as the derivative $\frac{\mathrm{d}^h f}{\mathrm{d}x^h}$ is continuous and periodic. At the end, the error of the discretization can be shown to be:

$$\epsilon_N \propto (N/2)^{-H} \left| \frac{\mathrm{d}^H f}{\mathrm{d}x^H} \right|, \tag{2.19}$$

where H is the last continuous and periodic derivative of f. The error thus, depends on how smooth f is [Pey02]. In case f is infinitely differentiable, the convergence of the method is better than any exponent, what is known as infinite convergence or spectral.

Fast-Fourier transform (FFT)

The Fast Fourier transform (FFT) computes the DFT (and corresponding inverse Fourier transform) in an outstandingly fast and efficient way. The algorithm takes advantage of the symmetries of the Fourier Transform to speed up the computations. Note that, to compute the coefficients $\hat{f}_k$, a

simple DFT performs of the order of $\mathcal{O}\left(N^2\right)$ operations, while the FFT needs only $\mathcal{O}\left(2\log_2\left(N\right)N\right)$ operations. Find here the main ideas behind this outstanding speed-up of the calculations.

Let the variable f be discretized in $x_j = \frac{2\pi j}{N}$ discrete points in physical space. The spectral coefficient $\hat{f}_k$ can be computed as:

$$\hat{f}_k = \frac{1}{N}\sum_{j=0}^{N-1} f_j \exp\left(-i\frac{2\pi}{N}kj\right). \tag{2.20}$$

Firstly, the FFT takes advantage of the odd/even symmetry between the points j:

$$\hat{f}_k = \frac{1}{N}\left\{\sum_{m=0}^{N/2-1} f_{2m}\exp\left[-i\frac{2\pi}{N/2}km\right] + \sum_{m=0}^{N/2-1} f_{2m+1}\exp\left[-i\frac{2\pi}{N/2}k\left(m+\frac{1}{2}\right)\right]\right\}, \tag{2.21}$$

where

$$\exp\left[-i\frac{2\pi}{N/2}k\left(m+\frac{1}{2}\right)\right] = \exp\left[-i\frac{2\pi}{N}k\right]\exp\left[-i\frac{2\pi}{N/2}km\right]. \tag{2.22}$$

Let

$$C_k = \exp\left[-i\frac{2\pi}{N}k\right], \tag{2.23}$$

then

$$\hat{f}_k = \frac{1}{N}\left\{\sum_{m=0}^{N/2-1}\left(f_{2m} + C_k f_{2m+1}\right)\exp\left[-i\frac{2\pi}{N/2}km\right]\right\}. \tag{2.24}$$

Secondly, the FFT takes advantage of the odd/even symmetry between the modes k. Note that if $k \geq N/2$, one can write $k = N/2 + r$, and find:

$$\exp\left[-i\frac{2\pi}{N/2}m\left(\frac{N}{2}+r\right)\right] = \exp\left[-i2\pi m\right]\exp\left[-i\frac{2\pi}{N/2}mr\right]. \tag{2.25}$$

Note that $\exp\left[-i2\pi m\right] = 1$, which means that for $k \geq N/2$: $\hat{f}_k = \hat{f}_{k-N/2}$.

The FFT takes advantage of this two ideas to construct a recursive algorithm, that goes from computing the first pair of $N = 2$ modes, to $N > 2$. There are more advanced versions of the FFT, that speed up the calculations even when N is not a multiple of 2. The `CPU` and `GPU` versions of **`nsPipe`** use open-access FFT algorithms to perform FFT and IFFT.

Pseudo-spectral method

Spectral methods are really convenient for linear problems. The orthogonal properties of the Fourier decomposition allow for a fast parallelization of the problem. However, in the case of non-linear problems one must take care of a particular issue. Find below a one dimensional example.

Let

$$f\left(x\right) = g\left(x\right)h\left(x\right), \tag{2.26}$$

being g and h:

$$g(x) \approx \sum_{m=-N/2}^{N/2-1} \hat{g}_m e^{imx} \quad \text{and} \quad h(x) \approx \sum_{n=-N/2}^{N/2-1} \hat{h}_n e^{inx}, \tag{2.27}$$

in spectral space one finds:

$$\hat{f}_k = \sum_{m+n=k} \hat{g}_m \hat{h}_n. \tag{2.28}$$

In order to evaluate the product in equation (2.28) for every k, one needs to perform a total of $\mathcal{O}(N^2)$ operations. If instead, one performs the product 2.26 in N physical discrete points, the total number of operations is $\mathcal{O}(N)$. Thus, in the case of spectral methods, the computation of non-linear terms in spectral space, is much more expensive than for methods that consider the variables in physical space.

In order to avoid this problem one can use a hybrid pseudo-spectral algorithm [Boy01]. In this algorithm all the linear operations are performed in spectral space, while the non-linear terms are evaluated in physical space. Every time one needs to compute a nonlinear term, the algorithm performs an IFFT to go from spectral to physical space $\hat{f} \rightarrow f$. Then, it evaluates the nonlinear product in N physical points. After the product is computed, the algorithm performs a FFT to go back from physical to spectral space $f \rightarrow \hat{f}$. If one performs the inverse and direct Fourier transforms using a Fast Fourier transform algorithm, the total number of operations to compute the nonlinear terms is of order $\mathcal{O}((1 + 2\log_2(N))N)$, and not the $\mathcal{O}(N^2)$ operations required for a purely spectral method.

The code `nsPipe` uses this pseudo-spectral approach to compute the non-linear terms in the NSE. There is however one last problem one must address when using pseudo-spectral methods, the problem of aliasing.

Aliasing

Aliasing is a type of error that takes place when one uses a sampling frequency smaller than the frequencies in the signal being processed. This results in day-to-day phenomena like the eye-perception of the blades of an helicopter rotating in the opposite direction to their actual rotating sense. See an example of aliasing in figure 2.3. In the figure, the signal of angular frequency ω is being sampled with a frequency $\omega/9$. The resultant sampled frequency is then of $\omega/9$, even though it does not exist in the actual data. In general, two trigonometric functions $e^{ik_1 x}$ and $e^{ik_2 x}$, sampled at the same discrete points $x_j = \frac{2\pi j}{N}$, appear to be equal when $k_2 - k_1 = m_c N$ for $m_c = 0, \pm 1, \pm 2, ...$

This error is also found in pseudo-spectral methods, as described below for the one dimensional example. Say one wants to compute the product (2.26), but the variables g and h are discretized with an spectral method. One can perform an inverse Fourier transform and obtain the physical value of g and h at N discrete x_j points. Then the product is computed as:

$$f(x_j) = g(x_j)\, h(x_j), \tag{2.29}$$

at N discrete locations x_j.

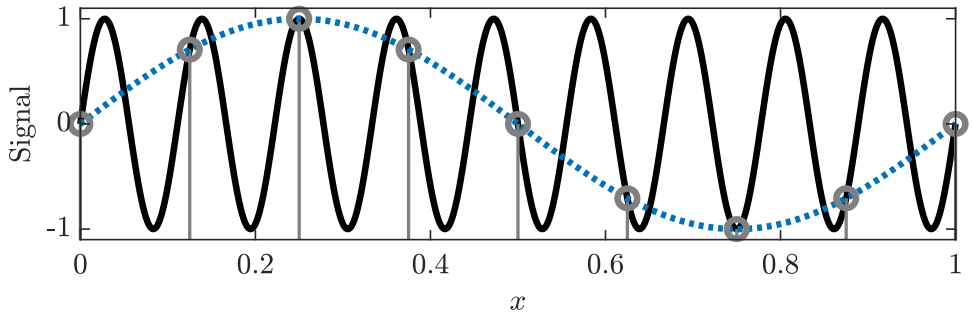

Fig. 2.3.: Example of aliasing error. The solid black line is the signal to be sampled. The vertical grey lines and open circles represent the discrete points at which the original signal is sampled. The dotted blue line represents the resultant sampled signal.

Let:

$$\hat{f}_k = \frac{1}{N}\sum_{j=0}^{N-1} f(x)\, e^{-ikx_j} \tag{2.30}$$

$$= \frac{1}{N}\sum_{j=0}^{N-1} \left[g(x)\, h(x)\right] e^{-ikx_j} \tag{2.31}$$

$$= \frac{1}{N}\sum_{j=0}^{N-1} \left[\left(\sum_{m=-N/2}^{N/2-1} \hat{g}_m e^{imx_j}\right)\left(\sum_{n=-N/2}^{N/2-1} \hat{h}_n e^{inx_j}\right)\right] e^{-ikx_j}, \tag{2.32}$$

this returns:

$$\hat{f}_k = \sum_{m+n=k} \hat{g}_m \hat{h}_n + \sum_{m+n=k\pm N} \hat{g}_m \hat{h}_n, \tag{2.33}$$

where the second sum is the aliasing error of sampling the original signal with N discrete points. This error will always appear whenever one tries to sample a signal with a discrete number of physical points/sampling frequencies. Pseudo-spectral methods either ignore this error, or avoid its effects by using a technique called padding.

Padding

Before performing the product (2.26), the variables g and h are computed as:

$$g(x) \approx \sum_{m=-J/2}^{J/2-1} \tilde{g}_m e^{imx} \quad \text{and} \quad h(x) \approx \sum_{n=-J/2}^{J/2-1} \tilde{h}_n e^{inx}, \tag{2.34}$$

where $J > N$ and:

$$\tilde{g}_m = \begin{cases} \hat{g}_m & |m| \leq N/2 \\ 0 & \text{otherwise} \end{cases} \quad \text{and} \quad \tilde{h}_n = \begin{cases} \hat{h}_n & |n| \leq N/2 \\ 0 & \text{otherwise.} \end{cases} \tag{2.35}$$

The variables g and h are then interpolated to J physical points, and the product (2.26) computed in this J points. The spectral coefficients of f are then computed as:

$$\tilde{f}_k = \frac{1}{J}\sum_{j=0}^{J-1} f_j \exp\left(-i\frac{2\pi}{N}kj\right), \tag{2.36}$$

which can be shown to be equivalent to:

$$\tilde{f}_k = \sum_{m+n=k} \tilde{g}_m\tilde{h}_n + \sum_{m+n=k\pm J} \tilde{g}_m\tilde{h}_n. \tag{2.37}$$

Since the spectral coefficients of f will be padded back so the code only retains all $|k| \leq N/2$, the number of points J must be chosen so, for all $|k| \leq N/2$:

$$|J| > |m+n-k|\,. \tag{2.38}$$

According to the formulation, the worst case scenario corresponds to $m = n = -N/2$ and $k = N/2-1$. Therefore:

$$J \geq \frac{3N}{2}. \tag{2.39}$$

This means that, if everytime one goes from spectral to physical space, one interpolates in J and not on $2N$ physical points, one will push the aliasing error to modes $|k| > N/2$. These modes are in any case ignored by the code, effectively removing the aliasing error from the modes of interest $|k| \leq N/2$. This strategy is usually referred to as padding and the 3/2 rule.

Symmetry of the Fourier transform

The Fourier transform of a real signal results in symmetric Fourier modes. Let $k \in [-N/2, N/2-1]$, and $\hat{f}_k$ be the Fourier coefficients that result from the one dimensional Fourier transform of the real signal f. It can be shown that $\hat{f}_k = \hat{f}^{\dagger}_{-k}$ where the dagger stands for complex number conjugate.

In the case of a two-dimensional FT like equation (2.13), one can choose which direction to transform first. This way one can reduce the total number of Fourier modes considered in the discretization to one half, by reducing by one half the modes considered in one of the two directions.

In the original `CPU` code, the variables are firstly Fourier transformed in θ when a transform is performed. This means that the total number of modes consider is of $m_f = (N_\theta + 1) \times 2N_x$. In the new `GPU` code, the variables are firstly Fourier transformed in x. This means that the number of modes considered is of $m_f = (N_x + 1) \times 2N_\theta$.

2.2.2 Radial discretization

The code **`nsPipe`** discretizes the inhomogeneous radial direction r using N_r discrete radial points. The discrete points are not uniformly distributed in the radial direction. They are clustered close the wall as shown in figure 2.4. The code does this by initially distributing the points as Chebyshev collocation points:

$$r_j = \cos\left(\frac{\pi j}{2N_r - 1}\right), \tag{2.40}$$

and later employing a relaxation to define more points away from the wall.

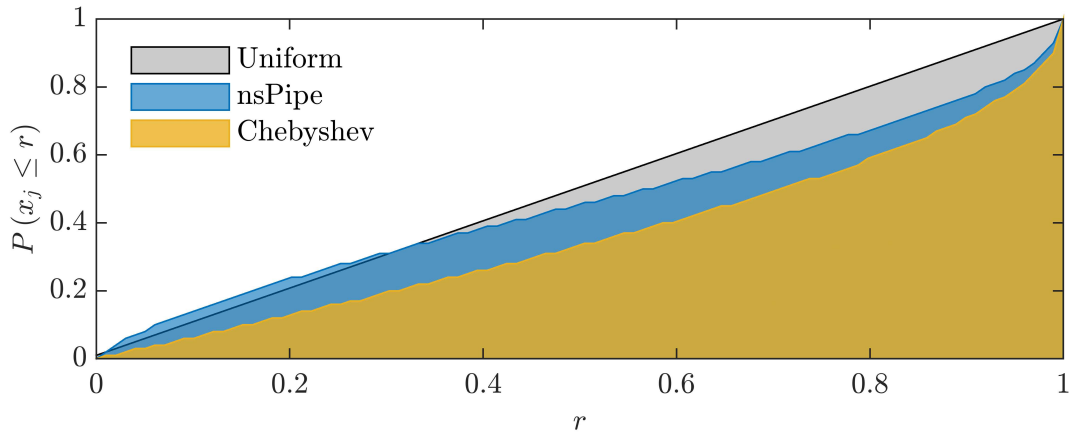

Fig. 2.4.: Cumulative distribution of radial grid points r_j for three different discretizations methods. The vertical axis represents the percentage of the total number of points clustered at locations $r_j \leq r$. In black, the case of uniformly distributed radial points. In yellow a grid with Chebyshev collocation points. In blue the discretization in `nsPipe`.

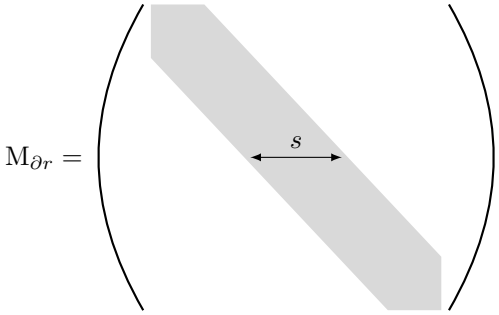

Fig. 2.5.: Banded structure of the radial derivative matrix. Kindly provided by Dr. Plana [PT22].

The radial derivatives are computed using high order finite differences. In order to compute the coefficients for the finite difference derivatives, also known as the weights, the strategy described in Fornberg [For88] is used. The method uses a recursive approach based on Lagrange polynomials, and computes the weights for stencils of arbitrary sizes and non-homogeneous grids. Here, only the final recursive expression is given. For a more detailed explanation see Fornberg [For88].

The coefficient $c^k_{i,j}$ corresponds to the weight of the i grid point, in a j stencil, to approximate the derivative of order k. Starting with $c^0_{0,0} = 1$, and assuming that any undefined coefficient is 0, any arbitrary coefficient can be computed as:

$$c^k_{i,j} = \begin{cases} \left[\frac{\prod_{l=0}^{j-2}(r_{j-1}-r_l)}{\prod_{l=0}^{j-1}(r_j-r_l)}\right]\left(kc^{k-1}_{i-1,j-1} - r_{j-1}c^k_{i-1,j-1}\right) & \text{for } i = j \\ \frac{1}{r_j-r_i}\left(r_j c^k_{i,j-1} - kc^{k-1}_{i,j-1}\right) & \text{otherwise.} \end{cases} \tag{2.41}$$

In this thesis, a stencil $s = 7$ is considered in the `GPU` code, and a stencil $s = 9$ in the `CPU` code. This results in diagonal banded matrices as shown in figure 2.5 which are computed at the beginning of the simulation, and efficiently stored as sparse. To compute the radial derivatives one only needs to perform a matrix vector multiplication. Say f is a one dimensional variable discretized at j radial

locations, and vector $\boldsymbol{f}$ has all these values stored. The vector with the value of the radial derivative of f evaluated at each radial location is then:

$$\frac{\partial \boldsymbol{f}}{\partial r} = \mathrm{M}_{\partial r} \boldsymbol{f}. \tag{2.42}$$

2.3 Numerical integration

In this section the numerical integration algorithm is described.

2.3.1 Characteristic magnitudes in the code

It is important to note that, in **nsPipe**, the variables are non-dimensionalized with the fluid density $\rho_f = 1$, with the pipe radius $R = D/2$ and the center-line velocity of the Hagen-Poiseuille flow profile $u_c = 2U$. This means that the characteristic time of the code defined as $t_c = R/u_c$ actually corresponds to $t_c = 0.25D/U$ advective time units.

2.3.2 Discretization of the momentum equation

Let the superscript n denote the time step, Δt the time step size, and c be a constant $c \in [0, 1]$; in **nsPipe** the NSE are discretized using a Crank-Nicolson method:

$$\begin{aligned}\frac{\boldsymbol{u}^{n+1} - \boldsymbol{u}^n}{\Delta t} &= -c\left(\boldsymbol{u}^{n+1} \cdot \nabla\right)\boldsymbol{u}^{n+1} - (1-c)\left(\boldsymbol{u}^n \cdot \nabla\right)\boldsymbol{u}^n - \nabla p^{n+1} \\ &+ \frac{1}{Re}\left[c\boldsymbol{\nabla^2}\boldsymbol{u}^{n+1} + (1-c)\boldsymbol{\nabla^2}\boldsymbol{u}^n\right] + c\boldsymbol{f_p}^{n+1} + (1-c)\boldsymbol{f_p}^n + c\boldsymbol{f_b}^{n+1} + (1-c)\boldsymbol{f_b}^n,\end{aligned}$$

where $\boldsymbol{f}_b$ is any body force acting on the flow, $\boldsymbol{f_p} = f_p(t)\,\boldsymbol{e}_x$ the driving pressure gradient of the flow, and

$$\nabla \cdot \boldsymbol{u}^n = \nabla \cdot \boldsymbol{u}^{n+1} = 0. \tag{2.43}$$

Due to the presence of the non-linear term $\left(\boldsymbol{u}^{n+1} \cdot \nabla\right)\boldsymbol{u}^{n+1}$ and pressure ∇p^{n+1} the above equation needs to be iteratively solved in order to obtain the new velocity field $\boldsymbol{u}^{n+1}$. The code **nsPipe** uses a predictor-corrector algorithm to do so in a numerically efficient way.

Below I describe the predictor-corrector method in more detail. In the description I use as notation:

$$\mathbf{N_u}^* \equiv -\left(\boldsymbol{u}^* \cdot \nabla\right)\boldsymbol{u}^* + \boldsymbol{f_p}^* + \boldsymbol{f_b}^*, \tag{2.44}$$

$$\mathbf{rhs}^* \equiv \mathbf{N_u}^* + \left[\frac{1}{\Delta t} + \frac{1-c}{Re}\boldsymbol{\nabla^2}\right]\boldsymbol{u}^n, \text{ and} \tag{2.45}$$

$$\mathrm{X} \equiv \left[\frac{1}{\Delta t} - \frac{c}{Re}\boldsymbol{\nabla^2}\right]. \tag{2.46}$$

The asterisk $*$ can either correspond to n, $n+1$ or an intermediate step of the integration k.

2.3.3 *Predictor-corrector time-stepping algorithm*

The predictor-corrector algorithm integrates the NSE in two steps. In the first step, during the predictor, it computes an intermediate velocity field $\boldsymbol{u}^k$, for $k = 1$, as a guess to the actual velocity field $\boldsymbol{u}^{n+1}$. Then, during the corrector step, it iterates and obtains new $\boldsymbol{u}^{k+1}$ velocity fields to improve the original guess $\boldsymbol{u}^k$. At each iteration step it checks the error between the current $\boldsymbol{u}^{k+1}$ and past $\boldsymbol{u}^k$ guess. If the error is small enough it stops the iteration and sets $\boldsymbol{u}^{n+1} = \boldsymbol{u}^{k+1}$.

Predictor step

The nonlinear term ${\mathbf{N_u}}^n$ in equation (2.44) is computed using $\boldsymbol{u}^n$. With the non-linear term, the term $\mathbf{rhs}^n$ in equation (2.45) is then computed by setting $* \equiv n$.

With $\mathbf{rhs}^n$, an intermediate pressure p^k is obtained by solving the Poisson equation:

$$\nabla^2 p^k = \nabla \cdot \mathbf{rhs}^n, \tag{2.47}$$

with a Neumann boundary condition at the wall:

$$\left.\frac{\partial p^k}{\partial r}\right|_{r=R} = 0. \tag{2.48}$$

The first guess (prediction) of the new velocity field $\boldsymbol{u}^k$ is then computed by solving the Helmholtz problem:

$$\mathrm{X}\boldsymbol{u}^k = \mathbf{rhs}^n - \nabla p^k, \tag{2.49}$$

for each velocity component. The velocity field is solved so it is zero at the pipe wall. Finally, as shown later in §2.4.3 and 2.4.4 the boundary condition of the pressure at the wall are corrected, and the mass flux imposed (if needed).

The code then iterates on the guessed velocities $\boldsymbol{u}^k$ in the corrector step.

Corrector step

At each iteration of the corrector step, a new nonlinear term ${\mathbf{N_u}}^k$ is computed, eq. (2.44), using the velocity field $\boldsymbol{u}^k$. This nonlinear term is subsequently used to compute:

$${\mathbf{N_u}}^{k+1} = c{\mathbf{N_u}}^k + (1-c)\,{\mathbf{N_u}}^n. \tag{2.50}$$

With the new guess on ${\mathbf{N_u}}^{k+1}$ the term $\mathbf{rhs}^{k+1}$ in equation (2.45) is obtained after setting $* \equiv k+1$.

With $\mathbf{rhs}^{k+1}$, a new intermediate pressure p^{k+1} is obtained by solving again the Poisson equation:

$$\nabla^2 p^{k+1} = \nabla \cdot \mathbf{rhs}^{k+1}, \tag{2.51}$$

with again, the Neumann boundary condition at the wall:

$$\left.\frac{\partial p^{k+1}}{\partial r}\right|_{r=R} = 0. \tag{2.52}$$

A new velocity field $\boldsymbol{u}^{k+1}$ is then computed by solving the Helmholtz problem:

$$\mathrm{X}\boldsymbol{u}^{k+1} = \mathbf{rhs}^{k+1} - \nabla p^{k+1}, \tag{2.53}$$

for each velocity component. The velocity field is solved so it is zero at the pipe wall. Afterwards, the boundary condition at the wall and the mass flux are adjusted.

The algorithm then computes the error between the new guess $\boldsymbol{u}^{k+1}$ and the previous one $\boldsymbol{u}^{k}$ as:

$$err = \frac{d_2}{d_1}, \tag{2.54}$$

where

$$d_1 = \max\left\{\max\left[\left(u_x^k\right)^2\right], \max\left[\left(u_\theta^k\right)^2\right], \max\left[\left(u_r^k\right)^2\right]\right\}, \text{ and} \tag{2.55}$$

$$d_2 = \max\left\{\max\left[\left(u_x^{k+1} - u_x^k\right)^2\right], \max\left[\left(u_\theta^{k+1} - u_\theta^k\right)^2\right], \max\left[\left(u_r^{k+1} - u_r^k\right)^2\right]\right\}. \tag{2.56}$$

If the error is higher or equal to a certain tolerance, $err \geq tol$, the code sets $\boldsymbol{u}^k = \boldsymbol{u}^{k+1}$ and continues iterating. If the error is smaller, then the code sets $\boldsymbol{u}^{n+1} = \boldsymbol{u}^{k+1}$, finishes the iteration and the integration of the current time step $n+1$.

Integration parameters

In this work the integration parameters c and tol have been set to $c = 0.51$ and $tol = 5e-5$.

2.4 Building blocks of the algorithm

In this section, some steps/aspects performed by `nsPipe` during the integration of the NSE are described in detail. Find a work-flow of the integration algorithm in figure 2.7.

2.4.1 Variable time step

At each point of the domain $\boldsymbol{x}$ the Courant number is computed as:

$$\mathbf{CFL}\left(\boldsymbol{x}\right) = |\boldsymbol{u}|\,\frac{\Delta t}{|\Delta \boldsymbol{x}|}. \tag{2.57}$$

In the `CPU` version of the `nsPipe` code, the time step size is adjusted, so the Courant number is always smaller than $\mathbf{CFL} \leq 0.2$ in the whole domain.

2.4.2 Change of variables

In cylindrical coordinates, the radial and azimuthal velocities are coupled through the vector Laplacian operator:

$$\boldsymbol{\nabla^2 u} \cdot \boldsymbol{e}_r = \nabla^2 u_r - \frac{2}{r^2}\frac{\partial u_\theta}{\partial \theta} - \frac{u_r}{r^2}, \tag{2.58}$$

$$\boldsymbol{\nabla^2 u} \cdot \boldsymbol{e}_\theta = \nabla^2 u_\theta + \frac{2}{r^2}\frac{\partial u_r}{\partial \theta} - \frac{u_\theta}{r^2}, \tag{2.59}$$

$$\boldsymbol{\nabla^2 u} \cdot \boldsymbol{e}_x = \nabla^2 u_x, \tag{2.60}$$

where ∇^2 is the Laplacian operator in cylindrical coordinates defined as:

$$\nabla^2 f = \frac{1}{r}\frac{\partial f}{\partial r} + \frac{\partial^2 f}{\partial r^2} + \frac{1}{r^2}\frac{\partial^2 f}{\partial \theta^2} + \frac{\partial^2 f}{\partial x^2} \tag{2.61}$$

The vector Laplacian can be decoupled in spectral space [BCN82]:

$$u_\pm = u_r \pm i u_\theta. \tag{2.62}$$

With the use of this transformation, the vector Laplacian operator of $u_\pm$ is:

$$\nabla^2_\pm u_\pm = \nabla^2 u_\pm - \frac{u_\pm}{r^2} \pm \frac{2i}{r^2}\frac{\partial u_\pm}{\partial \theta}. \tag{2.63}$$

The original variables can be computed as:

$$u_r = \frac{1}{2}\left(u_+ + u_-\right), \quad \text{and} \quad u_\theta = -\frac{i}{2}\left(u_+ - u_-\right). \tag{2.64}$$

By performing this variable change, the equations to compute the cross-section velocities can be decoupled, speeding up the numerical integration.

2.4.3 Boundary conditions

In the `nsPipe` formulation the axial and azimuthal directions are treated as periodic directions. In the radial direction boundary conditions must be set at the pipe center-line and pipe wall.

Pipe center-line: parity condition

In order to impose boundary conditions at the pipe center-line, the code uses the method proposed by Trefthen [Tre00]. The idea is to expand the radial coordinate from $r \in (0, 1]$ to $r \in [-1, 1]$. Note that in this new domain there exists an equivalence between data points in the domain since the coordinate:

$$\boldsymbol{r}\left(r, \theta, x\right) \equiv \boldsymbol{r}\left(-r, \pi + \theta, x\right). \tag{2.65}$$

All the variables in the problem must have a unique value at each physical coordinate, independently of the sense of r. This imposes a condition to the fields also in spectral space as:

$$\begin{array}{ll} \hat{f}_m\left(r, m\right) = -\hat{f}_m\left(-r, m\right) & \text{if } m \text{ is odd} \\ \hat{f}_m\left(r, m\right) = \hat{f}_m\left(-r, m\right) & \text{if } m \text{ is even.} \end{array} \tag{2.66}$$

The code takes advantage of this parity conditions, to calculate the radial derivatives close to the pipe center-line.

Let $\hat{\boldsymbol{f}}_m\left(r\right)$ be a vector that contains all the discrete spectral coefficients of azimuthal wavenumber m in the $2N_r$ grid, where $r \in [-1, 1]$. The derivative of $\hat{\boldsymbol{f}}_m\left(r\right)$ can be computed through a matrix-vector multiplication, as shown in figure 2.6, where $\mathrm{M}_{\partial r}$ is now a $2N_r \times 2N_r$ matrix. One can split the

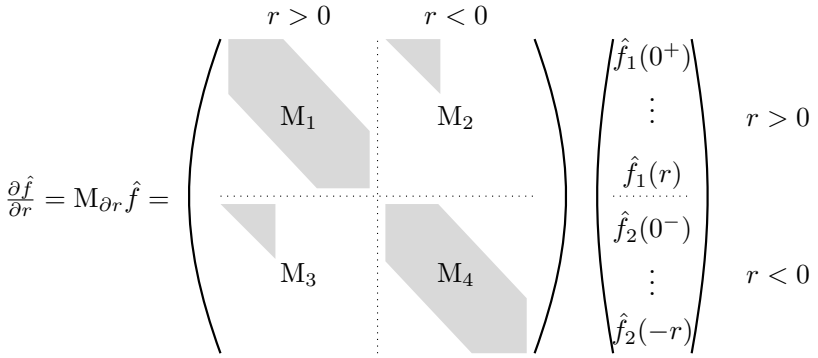

Fig. 2.6.: Decomposition of the radial derivation matrix according to the parity condition, kindly provided by Dr. Plana [PT22].

vector $\hat{\boldsymbol{f}}_m(r)$ in two parts: $\hat{\boldsymbol{f}}_{m,1}$ for $r > 0$ and $\hat{\boldsymbol{f}}_{m,2}$ for $r < 0$. Conversely the matrix can be splitted in 4 sub-matrices M_1, M_2, M_3 and M_4. From (2.66), $\hat{\boldsymbol{f}}_{m,2} = \pm\hat{\boldsymbol{f}}_{m,1}$, and from the symmetry of the problem $\mathrm{M}_1 + \mathrm{M}_2 = \mathrm{M}_3 + \mathrm{M}_4$. The calculation of the derivative can then be simplified to:

$$\begin{aligned} \frac{\partial \hat{f}_m}{\partial r} &= (\mathrm{M}_1 - a\mathrm{M}_2)\,\hat{f}_m \quad \text{if } m \text{ is odd} \\ \frac{\partial \hat{f}_m}{\partial r} &= (\mathrm{M}_1 + a\mathrm{M}_2)\,\hat{f}_m \quad \text{if } m \text{ is even.} \end{aligned} \tag{2.67}$$

where the constant a depends on the variable f and can be $a = \pm 1$. The axial velocity and pressure fields are even functions in r, as for instance $u_x(r, \theta, x) = u_x(-r, \pi + \theta, x)$. In this case $a = 1$. The radial and azimuthal velocity fields are odd functions in r, as for instance $u_r(r, \theta, x) = -u_r(-r, \pi + \theta, x)$. In this case $a = -1$.

In order to compute higher order derivatives, note that the derivative of an odd function in r is an even function in r, and conversely, the derivative of an even function in r is an odd function in r.

Pipe wall: influence matrix

At the pipe wall the code imposes a zero-velocity boundary condition. Regarding the pressure, at each predictor step, and corrector iteration, a Poisson problem is solved in order to compute p, see eq. (2.47) and (2.51). As mentioned earlier the Poisson equation is solved with Neumann boundary conditions at the wall:

$$\left.\frac{\partial p}{\partial r}\right|_{r=R} = 0. \tag{2.68}$$

But this boundary condition is unrealistic, and the resultant pressure field does not correspond to the actual pressure field of an incompressible flow, specially close to the wall [Rem06].

In order to avoid this error, `nsPipe` implements an influence matrix method [KS80; KS84; Wil17]. The idea is to perform an additional step during the time integration, after solving the Helmholtz problem, see eq. (2.49) and (2.53). In this new step a better boundary condition to the pressure field is imposed, and additionally, the incompressible condition in the flow close to the wall improved. Find below a quick description of the method.

Let $\boldsymbol{u}^*$ be the resultant velocity field after solving the Helmholtz problem in eq. (2.49) or eq. (2.53), and p^* the corresponding pressure field, the one obtained in a previous step by solving eq. (2.47) or eq. (2.51) with the unrealistic Neumann boundary condition in eq. (2.68). The velocity field

satisfies zero velocity at the wall, but, due to the unrealistic pressure field p^*, it is not guaranteed that it satisfies the incompressibility condition $\nabla \cdot \boldsymbol{u} = 0$ at all points in the flow, and in particular close to the pipe wall. The velocity and pressure fields are corrected with:

$$\boldsymbol{u}^\ddagger = \boldsymbol{u}^* + a_4 \boldsymbol{u}' + \sum_{j=1}^{3} a_j \boldsymbol{u}_j'', \text{ and } p^\ddagger = p^* + \frac{a_4}{\Delta t} p', \tag{2.69}$$

where a_j are tuning parameters that must be determined, so the improved velocity field $\boldsymbol{u}^\ddagger$ complies with the incompressible and zero velocity conditions at the wall:

$$\nabla \cdot \boldsymbol{u}^\ddagger\Big|_{r=R} = 0, \text{ and } \boldsymbol{u}^\ddagger\Big|_{r=R} = 0. \tag{2.70}$$

The auxiliary velocity fields $\boldsymbol{u}_j''$ are computed by solving:

$$\mathrm{X}\boldsymbol{u}_j'' = 0, \tag{2.71}$$

with different boundary conditions:

$$\begin{array}{l} (u_+'', u_-'', u_x'')\big|_{r=R} = (1,0,0)\,, \quad \text{if } j = 1, \\ (u_+'', u_-'', u_x'')\big|_{r=R} = (0,1,0)\,, \quad \text{if } j = 2, \\ (u_+'', u_-'', u_x'')\big|_{r=R} = (0,0,i)\,, \quad \text{if } j = 3. \end{array} \tag{2.72}$$

The pseudo-pressure field p' is computed by solving the Poisson equation:

$$\nabla^2 p' = 0, \tag{2.73}$$

with the boundary condition:

$$\frac{\partial p'}{\partial r}\Big|_{r=R} = 1. \tag{2.74}$$

And the corresponding velocity as:

$$\boldsymbol{u}' = -\nabla p'. \tag{2.75}$$

As a side note, if one multiplies the above equation by X, one can obtain:

$$\mathrm{X}\boldsymbol{u}' = -\mathrm{X}\left(\nabla p'\right) = c\frac{\nabla^2}{Re}\left(\nabla p'\right) - \frac{\nabla p'}{\Delta t} = c\frac{\nabla}{Re}\left(\nabla^2 p'\right) - \frac{\nabla p'}{\Delta t}, \tag{2.76}$$

and, since $\nabla^2 p' = 0$, then:

$$\mathrm{X}\boldsymbol{u}' = -\frac{\nabla p'}{\Delta t}. \tag{2.77}$$

By imposing the boundary condition in eq. (2.70), to the improved velocity in eq. (2.69), one finds:

$$0 = \boldsymbol{u}^*|_{r=R} + a_4\, \boldsymbol{u}'|_{r=R} + \sum_{j=1}^{3} a_j\, \boldsymbol{u}_j''\Big|_{r=R}, \text{ and} \tag{2.78}$$

$$0 = (\nabla \cdot \boldsymbol{u}^*)_{r=R} + a_4\, (\nabla \cdot \boldsymbol{u}')_{r=R} + \sum_{j=1}^{3} a_j \left(\nabla \cdot \boldsymbol{u}_j''\right)_{r=R}, \tag{2.79}$$

that corresponds to a system of 4 equations with 4 unknowns, a_j for $j = 1, 2, 3, 4$. This system can be written as:

$$A\boldsymbol{a} = \boldsymbol{g} \rightarrow \begin{bmatrix} 1 & 0 & 0 & u'_+ \\ 0 & 1 & 0 & u'_- \\ 0 & 0 & i & u'_x \\ \nabla \cdot \boldsymbol{u}_1'' & \nabla \cdot \boldsymbol{u}_2'' & \nabla \cdot \boldsymbol{u}_3'' & \nabla \cdot \boldsymbol{u}_4'' \end{bmatrix}_{r=R} \cdot \begin{bmatrix} a_1 \\ a_2 \\ a_3 \\ a_4 \end{bmatrix} = \begin{bmatrix} -u_+^* \\ -u_-^* \\ -u_x^* \\ -\nabla \cdot \boldsymbol{u}^* \end{bmatrix}_{r=R} \tag{2.80}$$

where A is the so-called influence matrix. By inverting the influence matrix, one can obtain the coefficients a_j, that allow $\boldsymbol{u}^\ddagger$ to satisfy the zero velocity and incompressible conditions at the wall at each time step. Note that at points different to the wall, the velocity $\boldsymbol{u}^\ddagger$ can still have a certain divergence $\left(\nabla \cdot \boldsymbol{u}^\ddagger\right)\Big|_{r<R} \neq 0$.

As a final note, if one multiplies equation (2.69) by X one obtains:

$$\mathrm{X}\boldsymbol{u}^\ddagger = \mathrm{X}\boldsymbol{u}^* + a_4\, \mathrm{X}\boldsymbol{u}' + \sum_{j=1}^{3} a_j\, \mathrm{X}\boldsymbol{u}_j'' = \mathrm{X}\boldsymbol{u}^* + a_4\, \mathrm{X}\boldsymbol{u}'. \tag{2.81}$$

If $* = k+1$, and invoking eq. (2.77) one finds an evolution equation of $\boldsymbol{u}^\ddagger$ as:

$$\mathrm{X}\boldsymbol{u}^\ddagger = \mathbf{rhs}^{k+1} - \nabla p^{k+1} - a_4 \frac{\nabla p'}{\Delta t} = \mathbf{rhs}^{k+1} - \nabla p^\ddagger, \tag{2.82}$$

which represents a complementary equation to eq. (2.53), and where $p^\ddagger$ is the actual pressure field in the flow.

2.4.4 Pulsatile driving of the flow

In the case of an axially periodic pipe flow, there are two strategies to model the driving of the flow: to either impose a pressure gradient or to impose a desired bulk velocity. Both methods consider the use of an axial body force (pressure gradient) $\boldsymbol{f_p} = f_p\,(t)\, \boldsymbol{e}_x$.

Option 1: prescribed pressure gradient

A caveat of imposing the pressure gradient is that the bulk velocity of the flow becomes an output of the simulation, and not an input. If the turbulent fraction increases in the pipe, the mean bulk velocity and/or the waveform of the bulk velocity will change.

The strategy to implement it in the code is simple: the driving force $\boldsymbol{f_p} = f_p\,(t)\, \boldsymbol{e}_x$ is set by the user when $\mathbf{N_u}^*$ is computed in eq. (2.44).

Option 2: prescribed bulk velocity

A caveat of imposing the bulk velocity is that the pressure gradient will become an output and not an input of the simulation. In this thesis this second option is used unless stated otherwise.

In order to impose a pre-defined bulk velocity, `nsPipe` takes advantage of the iterations in the predictor and the corrector steps to adjust the bulk velocity to machine precision. It does so by following several steps.

1. In the initialization phase of the code, the auxiliary axial velocity profile $u_{aux}(r)$ is computed as the resultant velocity from an unit axial impulse:

$$\mathrm{X}\left[0,0,u_{aux}\right]=\left[0,0,1\right]. \tag{2.83}$$

   Together with this velocity profile, an auxiliary bulk velocity u_a is computed as:

$$u_a=\langle u_{aux}\rangle_V=\frac{1}{L_x\pi R^2}\int_0^{L_x}\int_0^{2\pi}\int_0^{R}u_{aux}r\mathrm{d}r\mathrm{d}\theta\mathrm{d}x. \tag{2.84}$$

2. Before solving the Helmholtz problems in equations (2.49) and (2.53), the code computes a guess of the driving pressure gradient as the balance to the mean viscous stresses at the wall:

$$\tilde{f}_p(t)=\frac{-1}{L_x\pi R^2}\int_0^{L_x}\int_0^{2\pi}\int_0^{R}\frac{1}{Re}\left.\frac{\partial u_x^*}{\partial r}\right|_{r=R}r\mathrm{d}r\mathrm{d}\theta\mathrm{d}x, \tag{2.85}$$

   where $*=k$ or $*=k+1$. It plugs this guess of the driving force in the term $\mathbf{N_u}^*$ computed in eq. (2.44).

3. After solving the Helmholtz problem, and adjusting the boundary conditions of $\boldsymbol{u}^*$, the current bulk velocity u_c is computed as:

$$u_c=\frac{1}{L_x\pi R^2}\int_0^{L_x}\int_0^{2\pi}\int_0^{R}u_x^{\ddagger}r\mathrm{d}r\mathrm{d}\theta\mathrm{d}x. \tag{2.86}$$

   Note that at this stage, probably $u_c\neq u_b(t^n)$ being u_b^* the desired bulk velocity at time step $*$.

4. A correction to the bulk velocity is then computed as:

$$\beta^*=\frac{u_b^*-u_c}{u_a}. \tag{2.87}$$

   And the axial velocity at $*=k$ or $*=k+1$ is corrected as:

$$u_x^*=u_x^{\ddagger}+\beta^*\cdot u_{aux}(r). \tag{2.88}$$

As a final note, if one multiplies equation (2.88) by X, and by setting $*=k+1$, one arrives at:

$$\mathrm{X}\boldsymbol{u}^{k+1}=\mathrm{X}\boldsymbol{u}^{\ddagger}+\beta^{k+1}\boldsymbol{e}_x. \tag{2.89}$$

By plugging equation (2.82) one finds

$$\mathrm{X}\boldsymbol{u}^{k+1}=\mathbf{rhs}^{k+1}-\nabla p^{\ddagger}+\beta^{k+1}\boldsymbol{e}_x, \tag{2.90}$$

which represents a complementary equation to eq. (2.53). After invoking the definition of **rhs** in equation (2.45), it is easy to check that the actual pressure gradient driving the flow is equal to:

$$f_p(t) = \tilde{f}_p(t) + \beta(t), \tag{2.91}$$

and it is indirectly computed by the code at each discrete time step.

2.4.5 Solving the Poisson and Helmholtz problems

It can be shown that, for each Fourier mode, the solution of the discretized Poisson and Helmholtz problem reduces to a one dimensional (radial) problem, which is solved by inverting a diagonal matrix, similar to the matrix shown in fig. 2.5. For the case of the Helmholtz problem, by invoking the change of variables explained in §2.4.2, the three velocity components can be decoupled. Therefore, instead of one, three Helmholtz problems can be solved, one for each velocity component, to obtain the velocity field of the corresponding Fourier mode.

In the case of the `CPU` code, the system of equations are solved using open-access C libraries. In the case of the `GPU` code, with an in-house programmed LU decomposition.

2.5 Parallelization strategies

Note that, in all the operations described in §2.3, §2.4, and in fig. 2.7, except for the times where the nonlinear term $\mathbf{N_u}^*$, (2.44), is computed, the velocity and pressure fields are discretized in spectral space. This means that, any linear operation on the velocity or pressure fields can be computed for each Fourier mode independently of the others. Even the computation of the non-linear term $\mathbf{N_u}^*$ is performed at each discrete point independently of the others. In sum, the above described algorithm is highly susceptible to parallelization. In this section, the strategies followed in the `CPU` and `GPU` code are described.

2.5.1 `CPU` code

In the original **`nsPipe`** code the parallelization is performed with an hybrid method. It combines shared-memory parallel programming using OpenMP (Open MultiProcessing) and distributed-memory parallel programming using `MPI` (Message Passing Interface). Using `MPI` the program can be distributed in multiple nodes. At each node the OpenMP allows for parallelized execution of certain operations.

Find in this section a description of the main ideas behind these strategies, and the way they are implemented in the code. For a more detailed description the reader is referred to more detailed references [HW10; PT22].

Shared-memory parallel programming (OpenMP)

In OpenMP some `CPU`s perform operations on a common shared memory space. All of them have access to the full memory. OpenMP is rarely working all the time. Instead it is only initiated during certain operations. When an OpenMP instance starts, a single thread, called the *master thread* performs the operations in a serial way, until the order to execute in parallel is reached. There, parallel threads are spawned and execute the subsequent instructions concurrently. When the

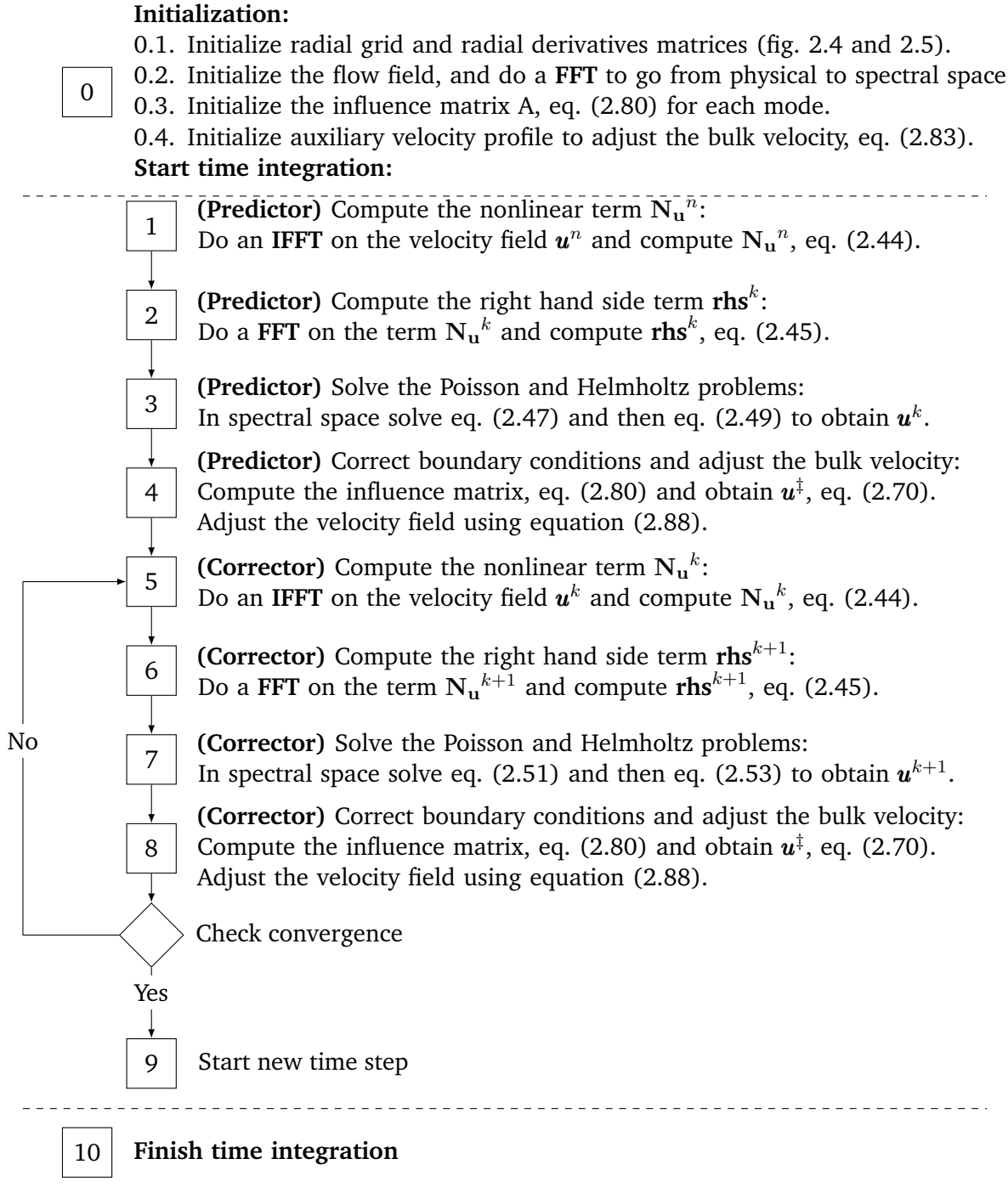

Fig. 2.7.: Description of the code and the time-stepping algorithm.

parallel region finishes, the threads are terminated. They send the information to the *master thread*, which continues the execution until the OpenMP is called off.

Distributed-memory parallel programming (MPI)

In MPI, the total memory of the program is distributed among a series of CPUs, which run their version of the program independently to one another. This means that the variables are distributed among the CPUs and the portion of the variable that is in one CPU cannot be accessed by the other CPUs unless the CPUs exchange information. This can be done through MPI standard messages, that can go from simple point-to-point communication, to broadcast to all CPUs at once.

Distribution of memory among CPUs

The total number of data points in spectral space in the CPU code is equal to the product of $m_f = (N_\theta + 1)\, 2N_x$ Fourier modes and N_r radial points. In physical space the total number of points is equal to, after padding, $m_p = N_r \cdot (3N_\theta + 1) \cdot (3N_x + 1)$. Both in spectral and physical space the data points have to be distributed among the N_c MPI CPUs.

In spectral space, each CPU has stored $n_f = \frac{m_f}{N_c}$ Fourier modes, and the corresponding radial points. This means that each CPU is able to operate only on n_f modes. Each CPU can then compute all the radial derivatives and even invert the Poisson and Helmholtz problems for all the n_f modes, without needing to communicate with the other CPUs.

In order to perform the IFFT operation, the information of all the m_f modes are needed for each radial position. In order to go to physical space, the code performs a global transpose on the memory of each CPU. After this operation, now the CPUs have the information of all m_f modes at $n_r = \frac{N_r}{N_c}$ radial positions. Now each CPU can efficiently perform the IFFT of the corresponding n_r radial points. Then it can compute the nonlinear term in the $n_p = n_r \cdot (3N_\theta + 1) \cdot (3N_x + 1)$ physical points, and subsequently perform a FFT and a global transposition to set the code back to its spectral space standard.

Using this approach, the number of radial points must be a multiple of the number of processors N_c, and $N_c \leq n_r$. This second limitation is alleviated by the code using the hybrid OpenMP-MPI architecture, allowing, in physical space, for the concurrent work of OpenMP threads doing different tasks.

2.5.2 GPU code

In the case of the GPU code, the parallelization is performed with the use of CUDA kernels.

Every time a linear operation is performed by the code, that does not correspond to a solution of the Poisson or Helmholtz problem, each thread of the GPU card is assigned to one Fourier mode and one radial position. That thread performs the linear operation on the mode and the radial location, independently of the rest.

The same is done for the computation of the nonlinear term $\mathbf{N_u}^*$ in eq. (2.44). Each thread is assigned a discrete point in the domain, and computes $\mathbf{N_u}^*$ at that point and independently to the rest.

In order to solve the Poisson and Helmholtz problems, one thread is assigned to each Fourier mode. The thread then reads all the radial points of that particular mode, and inverts the corresponding matrix. Find more details of the new GPU code in the following section

Tab. 2.2.: Performance of the GPU code compared with the performance of the CPU code. The code has been tested for two different grids, described in the three first columns, with the number of physical radial N_r, azimuthal M_θ and axial M_x points. The third column denotes the total memory required to run the code in the GPU, for each grid size. The rest of the columns denote the computing time of performing a time step in ms, averaged over 1000 time steps. The GPU used is an A100 80GB (fifth column). The CPU code (sixth to ninth columns) is run with different numbers of Xeon 8360Y processors. A single processor has 36 cores. The test was performed by Markus Rampp who is here gratefully acknowledged.

N_r	M_θ	M_x	Memory GPU	GPU	2x36	4x36	8x36	16x36
48	96	768	2GB	8.65	40.15	22.37	14.16	8.923
96	240	5760	30GB	397.45	2302.66	1230.55	649.68	372.28

2.6 Details of the GPU-nsPipe code

2.6.1 Code functionalities

The user can select the stencil-length of the finite-difference scheme, being the default a length of 7. Regarding the driving of the flow, the user can select between a prescribed or time variable driving pressure gradient.

All the relevant parameters (number of Fourier modes, radial points, time step size, Reynolds number, etc.) can be written in the `head.h` file before the code is compiled and run.

2.6.2 Code architecture and performance

In order to run the GPU-**nsPipe** code, a CUDA-capable GPU device with compute capability 2.0 (or higher), support for double-precision arithmetic and NVIDIA's CUDA toolkit are required. The GPU code runs in a massively parallel setup with thousands of GPU threads and highly efficient memory management. It relies on CUDA kernels for linear algebra and Fast-Fourier Transforms (cuFFT). An in-house algorithm is implemented to invert the Helmholtz and Poisson problems that result from the discretization of the velocity and pressure equations respectively.

This GPU version runs on single GPU devices, although there are plans to further develop it for hybrid MPI-GPU applications. Currently the maximum size of the case to be run is limited by the amount of memory of the GPU.

The performance of the code was tested by comparing the computing time per time step of the GPU code with the computing time of the CPU code for different grids and number of CPUs. Note that all the cases have the same stencil s of radial points. See the main results of this comparison in table 2.2. There is an outstanding speed-up of the GPU code compared with the original **nsPipe** code run in 72, 144 or 288 cores. Only by running the CPU **nsPipe** code in 566 or more cores, both codes reach the same level of performance. Note that, this will require at least 16 CPUs or more, while the CUDA code needs a single GPU. In sum, the GPU code results in a much faster code than the CPU code.

Another limitation of the GPU-**nsPipe** code is its dependency on NVIDIA GPU architectures. As part of the development of this code, some functionalities to port the CUDA code to other GPUs have been tested, yielding similar performance capabilities in AMD GPUs.

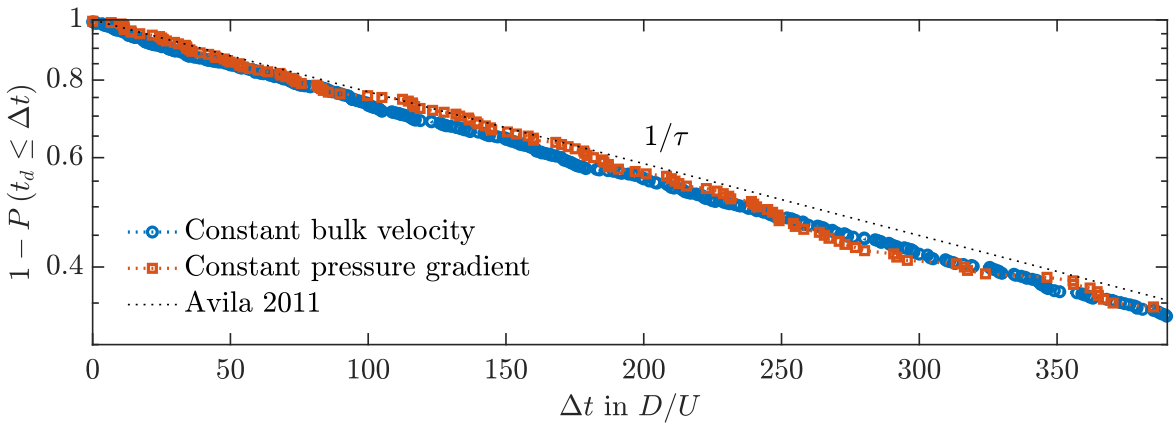

Fig. 2.8.: Lifetimes statistics of puffs in DNS using the new `C-CUDA` code in $L_x = 50D$ long pipes at $Re = 1850$. The vertical axis represents one minus the cumulative distribution function of puff decay after a time step size Δt. In blue (red) and circles (squares) cases with a constant bulk velocity (constant pressure gradient). The dotted line corresponds to the value of the exponential distribution proposed by Avila et al. [Avi+11], $1 - P_q \approx \exp(-\Delta t/\tau)$, where $\tau = \exp(\exp(0.005556 \cdot Re - 8.499))$, that fits the experimental data of Hof *et al.* [Hof+08].

2.6.3 Code validation

In order to validate the code, lifetimes statistics of puffs in SSPF at $Re = 1850$ are computed with the `GPU` code. The two versions of the `GPU` code are considered, one with constant and other with a time-dependent driving of the flow. In the case of the first version, the pressure gradient is set so, the bulk velocity is always close to $u_b \approx U$.

See in figure 2.8 the lifetime distribution of puff decay using the two versions of the code. The simulations are capped to a maximum run time of $t \leq 400D/U$. The two distributions are compared with the exponential distribution derived by Avila et al. [Avi+11], $1 - P_q \approx \exp(-\Delta t/\tau)$, where $\tau = \exp(\exp(0.005556 \cdot Re - 8.499))$, that fits the experimental data of Hof *et al.* [Hof+08]. As seen in the figure, the distributions produced by the code matches the experimental fit, independently of the method used to drive the flow.

3 Methods: Linear Stability and Transient Growth Analysis

In this thesis the stability of laminar pulsatile pipe flows is studied. Two methods are used: transient growth analysis (TGA) and linear stability analysis (LSA). They both make use of the Navier–Stokes equations linearized with respect to the laminar flow, what is referred to as the Linearized Navier–Stokes equations (LNSE). Find in this chapter the mathematical formulation behind the laminar profile and the LNSE. Find also the methods used to integrate the laminar profile and also to perform the TGA and LSA.

3.1 Mathematical formulation of the LNSE

Assuming axisymmetric and parallel flow $\boldsymbol{U} = (0, 0, U_{SW}(r,t))$, the NSE (2.3) can be simplified to the equation:

$$\frac{\partial U_{SW}}{\partial t} = f_p(t) + \frac{1}{Re}\left(\frac{\partial^2 U_{SW}}{\partial r^2} + \frac{1}{r}\frac{\partial U_{SW}}{\partial r}\right), \tag{3.1}$$

where $U_{SW}(r,t)$ is the laminar profile. As initially derived by Sexl and Womersley [Sex30; Wom55], equation (3.1) has an analytical expression, the Sexl-Womersley profile.

Let the velocity field be defined as $\boldsymbol{u} = \boldsymbol{U} + \boldsymbol{u}'$ and the pressure field as $p = p'$, where $\boldsymbol{u}'$ and p' are perturbation velocity and pressure fields. By plugging this definition in the NSE (2.3), and ignoring any body force, one finds:

$$\frac{\partial(\boldsymbol{U}+\boldsymbol{u}')}{\partial t} + \left[(\boldsymbol{U}+\boldsymbol{u}')\cdot\nabla\right](\boldsymbol{U}+\boldsymbol{u}') = -\nabla p' + \frac{1}{Re}\boldsymbol{\nabla^2}(\boldsymbol{U}+\boldsymbol{u}') + f_p(t)\,\boldsymbol{e}_x. \tag{3.2}$$

After invoking equation (3.1), the above equation simplifies to:

$$\frac{\partial \boldsymbol{u}'}{\partial t} + (\boldsymbol{U}\cdot\nabla)\boldsymbol{u}' + (\boldsymbol{u}'\cdot\nabla)\boldsymbol{U} = -\nabla p' + \frac{1}{Re}\boldsymbol{\nabla^2}\boldsymbol{u}' - (\boldsymbol{u}'\cdot\nabla)\boldsymbol{u}'. \tag{3.3}$$

Here $|\boldsymbol{u}'|$ is assumed to be small enough, so the last term $(\boldsymbol{u}'\cdot\nabla)\boldsymbol{u}'$ can be ignored. Thus the linearized Navier–Stokes equations (LNSE), on top of a laminar profile $\boldsymbol{U}$, can be written as:

$$\frac{\partial \boldsymbol{u}'}{\partial t} + (\boldsymbol{U}\cdot\nabla)\boldsymbol{u}' + (\boldsymbol{u}'\cdot\nabla)\boldsymbol{U} = -\nabla p' + \frac{1}{Re}\boldsymbol{\nabla^2}\boldsymbol{u}', \text{ and } \nabla\cdot\boldsymbol{u}' = 0. \tag{3.4}$$

3.1.1 The LNSE in cylindrical coordinates

In the case of the SW profile, and cylindrical coordinates, the LNSE take the form:

$$\frac{\partial u_r'}{\partial t} + U_{SW}\frac{\partial u_r'}{\partial x} = -\frac{\partial p'}{\partial r} + \frac{1}{Re}\left[\frac{\partial}{\partial r}\left(\frac{1}{r}\frac{\partial}{\partial r}\left(r u_r'\right)\right) + \frac{1}{r^2}\frac{\partial^2 u_r'}{\partial \theta^2} + \frac{\partial^2 u_r'}{\partial x^2} - \frac{2}{r^2}\frac{\partial u_\theta'}{\partial \theta}\right],$$

$$\frac{\partial u_\theta'}{\partial t} + U_{SW}\frac{\partial u_\theta'}{\partial x} = -\frac{1}{r}\frac{\partial p'}{\partial \theta} + \frac{1}{Re}\left[\frac{\partial}{\partial r}\left(\frac{1}{r}\frac{\partial}{\partial r}\left(r u_\theta'\right)\right) + \frac{1}{r^2}\frac{\partial^2 u_\theta'}{\partial \theta^2} + \frac{\partial^2 u_\theta'}{\partial x^2} + \frac{2}{r^2}\frac{\partial u_r'}{\partial \theta}\right], \text{ and}$$

$$\frac{\partial u_x'}{\partial t} + U_{SW}\frac{\partial u_x'}{\partial x} = -u_r'\frac{\partial U_{SW}}{\partial r} - \frac{\partial p'}{\partial x} + \frac{1}{Re}\left[\frac{1}{r}\frac{\partial}{\partial r}\left(r\frac{\partial u_x'}{\partial r}\right) + \frac{1}{r^2}\frac{\partial^2 u_x'}{\partial \theta^2} + \frac{\partial^2 u_x'}{\partial x^2}\right],$$

with:

$$\frac{1}{r}\frac{\partial}{\partial r}\left(r u_r'\right) + \frac{1}{r}\frac{\partial u_\theta'}{\partial \theta} + \frac{\partial u_x'}{\partial x} = 0. \tag{3.5}$$

3.2 Mathematical formulation of the TGA

In this thesis, the optimal perturbations $\boldsymbol{u}_0'$, that, according to the LNSE, can grow the most on top of the laminar U_{SW} profile, are determined. They are computed with a transient growth analysis (TGA). Find in this section the mathematical background behind the TGA. Note that the methods used here were developed by Barkley *et al.* [BBS08].

3.2.1 TGA as an optimization problem

The idea is to find the initial velocity field $\boldsymbol{u}_0'$ at time t_0 that results in the highest energy (E) growth

$$G\left(t_f, t_0\right) = \max_{\boldsymbol{u}'(t_0)} \frac{E\left(t_f\right)}{E\left(t_0\right)} = \frac{\left(\boldsymbol{u}'\left(t_f\right)\cdot\boldsymbol{u}'\left(t_f\right)\right)_V}{\left(\boldsymbol{u}'\left(t_0\right)\cdot\boldsymbol{u}'\left(t_0\right)\right)_V}, \tag{3.6}$$

at time t_f. Note that $(\bullet)_V$ here represents integration in the fluid domain. The velocity at time t_f can be computed as:

$$\boldsymbol{u}'\left(t_f\right) = \mathrm{A}\left(t_f, t_0\right)\boldsymbol{u}'\left(t_0\right), \tag{3.7}$$

where $\mathrm{A}\left(t_f, t_0\right)$ represents a linear operator that is equivalent to the action of integrating the LNSE in the time interval $t \in [t_0, t_f]$. The operator $\mathrm{A}\left(t_f, t_0\right)$ is also referred to as the evolution operator of the LNSE.

The TGA used in this thesis is equivalent to an optimization problem that looks for the initial flow field $\boldsymbol{u}_0'$ that maximizes G in equation (3.6), with the constraint that the behavior of $\boldsymbol{u}'$ is governed by the LNSE. The perturbation that results in the biggest G for all t_0 and t_f is called the optimal perturbation.

In the following subsections, a method to simplify and solve the above optimization problem is presented.

3.2.2 Equivalent algebraic problem to the TGA

Let the fraction in equation (3.6) be written as:

$$\frac{E\left(t_f\right)}{E\left(t_0\right)} = \frac{\left(\boldsymbol{u}'\left(t_f\right)\cdot\boldsymbol{u}'\left(t_f\right)\right)_V}{\left(\boldsymbol{u}'\left(t_0\right)\cdot\boldsymbol{u}'\left(t_0\right)\right)_V} = \frac{\left(\mathrm{A}\left(t_f,t_0\right)\boldsymbol{u}'\left(t_0\right)\cdot\mathrm{A}\left(t_f,t_0\right)\boldsymbol{u}'\left(t_0\right)\right)_V}{\left(\boldsymbol{u}'\left(t_0\right)\cdot\boldsymbol{u}'\left(t_0\right)\right)_V}, \tag{3.8}$$

one can define the numerator in the right hand side as:

$$\left(\mathrm{A}\left(t_f,t_0\right)\boldsymbol{u}'\left(t_0\right)\cdot\mathrm{A}\left(t_f,t_0\right)\boldsymbol{u}'\left(t_0\right)\right)_V \equiv \left(\boldsymbol{u}'\left(t_0\right)\cdot\mathrm{A}^*\left(t_f,t_0\right)\mathrm{A}\left(t_f,t_0\right)\boldsymbol{u}'\left(t_0\right)\right)_V, \tag{3.9}$$

where $\mathrm{A}^*\left(t_f,t_0\right)$ is the adjoint evolution operator to the LNSE in the $t\in[t_0,t_f]$ time interval, $\mathrm{A}\left(t_f,t_0\right)$, according to the L_2 inner product. See a detailed description of this operator in §3.2.3.

Let λ_j and $\boldsymbol{v}_j$ denote eigenvalues and eigenvectors of the joint operator A*A:

$$\mathrm{A}^*\left(t_f,t_0\right)\mathrm{A}\left(t_f,t_0\right)\boldsymbol{v}_j = \lambda_j\boldsymbol{v}_j, \tag{3.10}$$

it can be shown that the optimization problem in equation (3.8) is equivalent to finding the maximum eigenvalue:

$$G\left(t_f,t_0\right) = \max_{\boldsymbol{u}'(t_0)}\frac{E\left(t_f\right)}{E\left(t_0\right)} = \max_j\lambda_j. \tag{3.11}$$

This means that, in order to obtain the maximum growth G, one needs to find the maximum eigenvalue λ_j of the operator A*A. The corresponding eigenvector $\boldsymbol{v}_j$ is actually the optimal initial flow field $\boldsymbol{u}_0'$. As shown in §3.4.1 there is a simple way to compute these eigenvalues using an Arnoldi iteration. This method requires the integration of not only the LNSE but the adjoint LNSE as well. See in the following paragraphs the definition of the adjoint LNSE.

3.2.3 The adjoint LNSE

By definition, given two fields $\boldsymbol{q}$ and $\boldsymbol{q}^*$, with compact support (so they vanish at the boundaries), the adjoint operator, according to a L_2 norm, of the linear operator H, is any operator H* that satisfies

$$\left\langle\mathrm{H}\boldsymbol{q}\cdot\boldsymbol{q}^*\right\rangle = \left\langle\boldsymbol{q}\cdot\mathrm{H}^*\boldsymbol{q}^*\right\rangle, \tag{3.12}$$

where

$$\left\langle\bullet\right\rangle = \int_{t_0}^{t_f}\iiint_V \bullet \quad \mathrm{d}V\mathrm{d}t. \tag{3.13}$$

Find here the derivation of the adjoint operator A* of the LNSE, eq. (3.4) term by term. Here $\boldsymbol{q}=[\boldsymbol{u}',p']$ corresponds to the perturbation velocity $\boldsymbol{u}'$ and pressure p' fields, and $\boldsymbol{q}^*=[\boldsymbol{u}^*,p^*]$ to the corresponding velocity $\boldsymbol{u}^*$ and pressure p^* adjoint fields. Note that, axial and azimuthal periodic boundary conditions are considered, and no-slip velocity (and adjoint velocity) at the walls.

Partial time derivative

Let:

$$\int_{t_0}^{t_f} \iiint_V \frac{\partial \boldsymbol{u}'}{\partial t} \cdot \boldsymbol{u}^* \mathrm{d}V\mathrm{d}t = \int_{t_0}^{t_f} \iiint_V \frac{\partial \left(\boldsymbol{u}^* \cdot \boldsymbol{u}'\right)}{\partial t} \mathrm{d}V\mathrm{d}t - \int_{t_0}^{t_f} \iiint_V \boldsymbol{u}' \cdot \frac{\partial \boldsymbol{u}^*}{\partial t} \mathrm{d}V\mathrm{d}t, \tag{3.14}$$

where the first term in the right hand side takes the form:

$$\int_{t_0}^{t_f} \iiint_V \frac{\partial \left(\boldsymbol{u}' \cdot \boldsymbol{u}^*\right)}{\partial t} \mathrm{d}V\mathrm{d}t = \iiint_V \left[\boldsymbol{u}' \cdot \boldsymbol{u}^*\right]_{t_0}^{t_f} \mathrm{d}V = \left(\boldsymbol{u}'\left(t_f\right) \cdot \boldsymbol{u}^*\left(t_f\right)\right)_V - \left(\boldsymbol{u}'\left(t_0\right) \cdot \boldsymbol{u}^*\left(t_0\right)\right)_V. \tag{3.15}$$

By choosing suitable initial conditions this term vanishes. In particular, given that, by definition:

$$\boldsymbol{u}^*\left(t_0\right) = \mathrm{A}^* \boldsymbol{u}^*\left(t_f\right), \tag{3.16}$$

if one sets:

$$\boldsymbol{u}^*\left(t_f\right) = \mathrm{A}\boldsymbol{u}'\left(t_0\right), \tag{3.17}$$

the term reduces to 0 and then:

$$\int_{t_0}^{t_f} \iiint_V \frac{\partial \boldsymbol{u}'}{\partial t} \cdot \boldsymbol{u}^* \mathrm{d}V\mathrm{d}t = -\int_{t_0}^{t_f} \iiint_V \boldsymbol{u}' \cdot \frac{\partial \boldsymbol{u}^*}{\partial t} \mathrm{d}V\mathrm{d}t. \tag{3.18}$$

Note that here the adjoint operator of interest is the one related with $(\bullet)_V$ (volume integral), eq. (3.9), not $\langle\bullet\rangle$ (volume and time integral), eq. (3.12). In what follows, as long as the initial condition derived in equation (3.17) is satisfied for the desired combination of t_f and t_0, the adjoint operator of the operation $\langle\bullet\rangle$ is equivalent to the one of the $(\bullet)_V$ operation.

First cross-term

Given that, $\nabla \cdot \boldsymbol{U} = 0$, one can show that:

$$\nabla \cdot \left\{\boldsymbol{U} \cdot \left(\boldsymbol{u}' \cdot \boldsymbol{u}^*\right)\right\} = \left(\nabla \cdot \boldsymbol{U}\right) \cdot \left(\boldsymbol{u}' \cdot \boldsymbol{u}^*\right) + \boldsymbol{U} \cdot \left[\nabla \cdot \left(\boldsymbol{u}' \cdot \boldsymbol{u}^*\right)\right] = \boldsymbol{U} \cdot \left[\nabla \cdot \left(\boldsymbol{u}' \cdot \boldsymbol{u}^*\right)\right]. \tag{3.19}$$

Furthermore:

$$\nabla \cdot \left\{\boldsymbol{U} \cdot \left(\boldsymbol{u}' \cdot \boldsymbol{u}^*\right)\right\} = \boldsymbol{U} \cdot \left[\nabla \cdot \left(\boldsymbol{u}' \cdot \boldsymbol{u}^*\right)\right] = \left[\left(\boldsymbol{U} \cdot \nabla\right) \boldsymbol{u}'\right] \cdot \boldsymbol{u}^* + \left[\left(\boldsymbol{U} \cdot \nabla\right) \boldsymbol{u}^*\right] \cdot \boldsymbol{u}' \tag{3.20}$$

Thus:

$$\int_{t_0}^{t_f} \iiint_V \left[\left(\boldsymbol{U} \cdot \nabla\right) \boldsymbol{u}'\right] \cdot \boldsymbol{u}^* \mathrm{d}V\mathrm{d}t = \int_{t_0}^{t_f} \iiint_V \nabla \cdot \left\{\boldsymbol{U} \cdot \left(\boldsymbol{u}' \cdot \boldsymbol{u}^*\right)\right\} \mathrm{d}V\mathrm{d}t - \tag{3.21}$$

$$\int_{t_0}^{t_f} \iiint_V \left[\left(\boldsymbol{U} \cdot \nabla\right) \boldsymbol{u}^*\right] \cdot \boldsymbol{u}' \mathrm{d}V\mathrm{d}t, \tag{3.22}$$

where, by invoking the Gauss divergence theorem:

$$\int_{t_0}^{t_f} \iiint_V \nabla \cdot \left\{\boldsymbol{U} \cdot \left(\boldsymbol{u}' \cdot \boldsymbol{u}^*\right)\right\} \mathrm{d}V\mathrm{d}t = \int_{t_0}^{t_f} \iint_{\partial V} \left\{\boldsymbol{U} \cdot \left(\boldsymbol{u}' \cdot \boldsymbol{u}^*\right)\right\} \cdot \mathbf{N} \mathrm{d}S\mathrm{d}t. \tag{3.23}$$

Since the velocity fields are periodic in the axial and azimuthal directions, and they vanish at the pipe wall the surface integral in the right hand side of the above expression is equal to 0. Thus, the adjoint operator of the second term in eq. (3.4) can be shown to be:

$$\int_{t_0}^{t_f} \iiint_V \left[(\boldsymbol{U} \cdot \nabla) \boldsymbol{u}' \right] \cdot \boldsymbol{u}^* \mathrm{d}V \mathrm{d}t = - \int_{t_0}^{t_f} \iiint_V \left[(\boldsymbol{U} \cdot \nabla) \boldsymbol{u}^* \right] \cdot \boldsymbol{u}' \mathrm{d}V \mathrm{d}t. \tag{3.24}$$

Second cross-term

One can show that:

$$\left[(\boldsymbol{u}' \cdot \nabla) \boldsymbol{U} \right] \cdot \boldsymbol{u}^* = \left[(\nabla \boldsymbol{U})^T \boldsymbol{u}^* \right] \cdot \boldsymbol{u}', \tag{3.25}$$

by simply rearranging the terms. Thus:

$$\int_{t_0}^{t_f} \iiint_V \left[(\boldsymbol{u}' \cdot \nabla) \boldsymbol{U} \right] \cdot \boldsymbol{u}^* \mathrm{d}V \mathrm{d}t = \int_{t_0}^{t_f} \iiint_V \left[(\nabla \boldsymbol{U})^T \boldsymbol{u}^* \right] \cdot \boldsymbol{u}' \mathrm{d}V \mathrm{d} \tag{3.26}$$

Viscosity term

One can show, using Green's second vector identity, that:

$$\left(\boldsymbol{\nabla^2} \boldsymbol{u}' \right) \cdot \boldsymbol{u}^* = \nabla \cdot \nabla \left(\boldsymbol{u}' \cdot \boldsymbol{u}^* \right) + \left(\boldsymbol{\nabla^2} \boldsymbol{u}^* \right) \cdot \boldsymbol{u}' - 2 \nabla \cdot \left[(\boldsymbol{u}^* \cdot \nabla) \boldsymbol{u}' + \boldsymbol{u}^* \times \nabla \times \boldsymbol{u}' \right]. \tag{3.27}$$

When integrating over the volume, all the terms multiplied by the divergence are canceled at the boundaries, and the adjoint operator reduces to:

$$\int_{t_0}^{t_f} \iiint_V \left(\boldsymbol{\nabla^2} \boldsymbol{u}' \right) \cdot \boldsymbol{u}^* \mathrm{d}V \mathrm{d}t = \int_{t_0}^{t_f} \iiint_V \left(\boldsymbol{\nabla^2} \boldsymbol{u}^* \right) \cdot \boldsymbol{u}' \mathrm{d}V \mathrm{d}t. \tag{3.28}$$

The adjoint LNSE

The final adjoint equations of the operator in eq. (3.9) are defined as:

$$-\frac{\partial \boldsymbol{u}^*}{\partial t} - (\boldsymbol{U} \cdot \nabla) \boldsymbol{u}^* + (\nabla \boldsymbol{U})^T \boldsymbol{u}^* = -\nabla p^* + \frac{1}{Re} \boldsymbol{\nabla^2} \boldsymbol{u}^*, \text{ and } \nabla \cdot \boldsymbol{u}^*. \tag{3.29}$$

The adjoint LNSE in cylindrical coordinates

In the case of the SW profile, and cylindrical coordinates, the adjoint LNSE take the form:

$$-\frac{\partial u_r^*}{\partial t} - U_{SW} \frac{\partial u_r^*}{\partial x} = -u_x^* \frac{\partial U_{SW}}{\partial r} - \frac{\partial p^*}{\partial r} + \frac{1}{Re} \left[\frac{\partial}{\partial r} \left(\frac{1}{r} \frac{\partial}{\partial r} \left(r u_r^* \right) \right) + \frac{1}{r^2} \frac{\partial^2 u_r^*}{\partial \theta^2} + \frac{\partial^2 u_r^*}{\partial x^2} - \frac{2}{r^2} \frac{\partial u_\theta^*}{\partial \theta} \right],$$

$$-\frac{\partial u_\theta^*}{\partial t} - U_{SW} \frac{\partial u_\theta^*}{\partial x} = -\frac{1}{r} \frac{\partial p^*}{\partial \theta} + \frac{1}{Re} \left[\frac{\partial}{\partial r} \left(\frac{1}{r} \frac{\partial}{\partial r} \left(r u_\theta^* \right) \right) + \frac{1}{r^2} \frac{\partial^2 u_\theta^*}{\partial \theta^2} + \frac{\partial^2 u_\theta^*}{\partial x^2} + \frac{2}{r^2} \frac{\partial u_r^*}{\partial \theta} \right], \text{ and}$$

$$-\frac{\partial u_x^*}{\partial t} - U_{SW} \frac{\partial u_x^*}{\partial x} = -\frac{\partial p^*}{\partial x} + \frac{1}{Re} \left[\frac{1}{r} \frac{\partial}{\partial r} \left(r \frac{\partial u_x^*}{\partial r} \right) + \frac{1}{r^2} \frac{\partial^2 u_x^*}{\partial \theta^2} + \frac{\partial^2 u_x^*}{\partial x^2} \right],$$

with:

$$\frac{1}{r}\frac{\partial}{\partial r}\left(ru_r^*\right)+\frac{1}{r}\frac{\partial u_\theta^*}{\partial \theta}+\frac{\partial u_x^*}{\partial x}=0. \tag{3.30}$$

3.3 Numerical integration of the LNSE (and adjoint)

In this thesis, the LNSE are used in order to perform the TGA on the laminar profile, and to integrate the evolution of the optimal perturbations obtained with the TGA. Here the methods by which the LNSE, and the adjoint of the LNSE, eq. (3.29), are integrated, are described. Note that the original `MATLAB` code used in this thesis was first developed by Xu *et al.* [XSA21]. Please refer to that paper for additional information.

3.3.1 Axial and azimuthal discretization

The pressure and perturbation flow fields are discretized with a Chebyshev-Fourier-Fourier spectral method;

$$\boldsymbol{u}'=\sum^{m}\sum^{\alpha}\hat{\boldsymbol{u}}'_{m,\alpha}\left(r,t\right)\exp\left(im\theta\right)\exp\left(i\alpha x\right) \tag{3.31}$$

Here, m is the azimuthal wavenumber, and α the axial one. Note that $m\in\mathbb{Z}$ is an integer number, while $\alpha=kk_0$ is a real number, being $k\in\mathbb{Z}$ and $k_0=2\pi/L_x$.

Radial discretization

The velocity is discretized in N_r Chebyshev collocation points r_j:

$$r_j=\cos\left(\frac{\pi j}{2N_r-1}\right), \tag{3.32}$$

where $j=0,1,...,N_r$. Following Trefthen [Tre00], the profile is discretized using a Chebyshev spectral method, and it is interpolated using a N_r degree polynomial. The polynomial is chosen so it automatically satisfies the zero velocity at the pipe wall and the boundary condition at the center-line of the pipe.

Using this spectral method, any radial derivative can be computed as a matrix-vector multiplication. Let $\boldsymbol{U}_{SW}$ be a vector with the value of the laminar profile U_{SW} at the r_j discrete radial points. The derivative of the profile can be computed as:

$$\frac{\partial \boldsymbol{U}_{SW}}{\partial r}=\mathrm{M}_{\partial r}\boldsymbol{U}_{SW}, \tag{3.33}$$

where $\mathrm{M}_{\partial r}$ is a filled matrix with the derivative coefficients.

Using a Clenshaw–Curtis quadrature, the integral in the radial direction can be numerically computed as the dot product between a vector $\boldsymbol{w}$ and the integrand f:

$$a=\boldsymbol{w}\cdot\boldsymbol{f}. \tag{3.34}$$

The idea behind this quadrature is related to the inverse problem:

$$\frac{\partial \boldsymbol{u}}{\partial r} = \boldsymbol{f} \rightarrow \mathrm{M}_{\partial r}\boldsymbol{u} = \boldsymbol{f} \rightarrow \boldsymbol{u} = \mathrm{I}_{\mathrm{M}}\boldsymbol{f}. \tag{3.35}$$

Here I_{M} is the inverse matrix of $\mathrm{M}_{\partial r}$. By taking the first row of I_{M} as $\boldsymbol{w}$, and the first value of $\boldsymbol{u}$ as a, equation (3.34) is obtained.

3.3.2 Time stepping algorithm

The integration in time is performed using a second-order (AB/BDF) scheme, that is a combination of Adams–Bashforth and backward differentiation formula. The incompressibility condition is imposed using a projection method [HR98].

The perturbation velocity $\boldsymbol{u}'$, at the time step $n+1$, is computed as:

$$\frac{3\boldsymbol{u}'^{,n+1} - 4\boldsymbol{u}'^{,n} + \boldsymbol{u}'^{,n-1}}{2\Delta t} + 2\mathbf{N}_{\mathbf{u}'}{}^{n} - \mathbf{N}_{\mathbf{u}'}{}^{n-1} = -\nabla p'^{,n+1} + \frac{1}{Re}\boldsymbol{\nabla^2}\boldsymbol{u}'^{,n+1}, \text{ and } \boldsymbol{\nabla}\cdot\boldsymbol{u}'^{,n+1} = 0, \tag{3.36}$$

In the case of the LNSE:

$$\mathbf{N}_{\mathbf{u}'} = \left(U_{SW}\cdot\nabla\right)\boldsymbol{u}' + \left(\boldsymbol{u}'\cdot\nabla\right)U_{SW}, \tag{3.37}$$

and in the adjoint:

$$\mathbf{N}_{\mathbf{u}'} = -\left(U_{SW}\cdot\nabla\right)\boldsymbol{u}' + \left(\nabla U_{SW}\right)^T\boldsymbol{u}'. \tag{3.38}$$

Note that the LNSE are integrated forward in time, so $n+1$ corresponds to a time instant $t^{n+1} > t^n$. The adjoint LNSE are integrated backwards, so $n+1$ corresponds to a time instant $t^{n+1} < t^n$.

At the pipe center-line the code imposes even/odd boundary conditions depending on the azimuthal wavenumber m, and the variable of interest, as described in §2.4.3. The numerical methods used here to integrate the LNSE, also make use of other tricks during the integration, like the change of variables described in §2.4.2.

Find below a short description of the projection method used to impose the incompressibility condition to the flow. The algorithm, at its core, is based on a predictor-corrector method similar to the one described in §2.3.3.

Predictor step

In the predictor step, first a guess on the pressure is computed as:

$$\nabla^2\bar{p}'^{,n+1} = -\nabla\cdot\left[2\mathbf{N}_{\mathbf{u}'}{}^{n} - \mathbf{N}_{\mathbf{u}'}{}^{n-1}\right], \tag{3.39}$$

with boundary condition:

$$\left.\frac{\partial\bar{p}'^{,n+1}}{\partial r}\right|_{r=R} = \boldsymbol{e_r}\cdot\left\{\frac{-3\boldsymbol{u}'^{,n+1} + 4\boldsymbol{u}'^{,n} - \boldsymbol{u}'^{,n-1}}{2\Delta t} - 2\mathbf{N}_{\mathbf{u}'}{}^{n} + \mathbf{N}_{\mathbf{u}'}{}^{n-1} + \frac{1}{Re}\left[2\boldsymbol{\nabla^2}\boldsymbol{u}'^{,n} - \boldsymbol{\nabla^2}\boldsymbol{u}'^{,n-1}\right]\right\}\Bigg|_{r=R}.$$

In order to improve the stability of the code, the Laplacian operator is implemented in the form: $\boldsymbol{\nabla^2 u'} = -\nabla \times (\nabla \times \boldsymbol{u'})$. As a second step, an intermediate velocity is computed as:

$$\frac{3\mathbf{u}'^{,*} - 4\boldsymbol{u}'^{,n} + \boldsymbol{u}'^{,n-1}}{2\Delta t} + 2\mathbf{N}_{\mathbf{u}'}{}^{n} - \mathbf{N}_{\mathbf{u}'}{}^{n-1} = -\nabla \bar{p}'^{,n+1} + \frac{1}{Re}\boldsymbol{\nabla^2 u'}^{,*}, \tag{3.40}$$

which does not satisfy the incompressibility condition.

Corrector step

In the corrector step, the new velocity is solved using:

$$\frac{3\boldsymbol{u}'^{,n+1} - 3\boldsymbol{u}'^{,*}}{2\Delta t} = -\nabla\left(p'^{,n+1} - \bar{p}'^{,n+1}\right), \text{ with } \nabla \cdot \boldsymbol{u}'^{,n+1} = 0. \tag{3.41}$$

The pressure field $p'^{,n+1}$ is computed using the intermediate pseudo-pressure ϕ', computed as:

$$\nabla^2 \phi' = \nabla \cdot \boldsymbol{u}'^{,*}, \tag{3.42}$$

with Neumann boundary condition:

$$\left.\frac{\partial \phi'}{\partial r}\right|_{r=R} = 0. \tag{3.43}$$

The pressure field is then computed as:

$$p'^{,n+1} = \bar{p}'^{,n+1} + \frac{3}{2\Delta t}\phi', \tag{3.44}$$

and the velocity field:

$$\boldsymbol{u}'^{,n+1} = \boldsymbol{u}'^{,*} - \nabla \phi'. \tag{3.45}$$

This algorithm does not iterate in the corrector step.

Grid spacing

The number of radial grid points is estimated using eq. (C.13), where $Re_{\max} = (1 + A)\, Re$. The time step size is estimated by imposing a constant Courant number $\text{CFL} = 2(1 + A)U\frac{N_r \Delta t}{R} = 0.8$.

3.4 Algorithm to compute the TGA

As lengthy described in §3.2.1, in order to perform the transient growth analysis, one solves an optimization problem, to find the initial perturbation velocity field $\boldsymbol{u}'(t_0)$ that maximizes the kinetic energy of $\boldsymbol{u}'(t = t_f)$ at time t_f. After some mathematical developments, it turns out that this is equivalent to solving for the maximum eigenvalue λ_j of a matrix operator $\mathrm{A}^*\mathrm{A}$:

$$G(t_f) = \max \lambda_j \rightarrow \mathrm{A}^*\mathrm{A}\boldsymbol{v}_j = \lambda_j \boldsymbol{v}_j. \tag{3.46}$$

In order to compute the dominant eigenvalue, an Arnoldi iteration is used.

3.4.1 Arnoldi iteration

The Arnoldi iteration is an iterative method to solve for the eigenvalues of a matrix $\mathrm{M} = \mathrm{A}^*\mathrm{A}$, where $\mathrm{M}\boldsymbol{v}_j = \lambda_j \boldsymbol{v}_j$. It constructs a matrix, B, whose columns, for an initial guess $\boldsymbol{v}_0$ are:

$$\mathrm{B}_N = \left[\frac{\boldsymbol{v}_0}{\alpha_0}, \frac{\mathrm{M}\boldsymbol{v}_0}{\alpha_1}, \frac{\mathrm{M}^2\boldsymbol{v}_0}{\alpha_2}, ..., \frac{\mathrm{M}^N\boldsymbol{v}_0}{\alpha_N} \right], \tag{3.47}$$

being N the total number of Arnoldi iterations and α constants to normalize all the columns vectors.

The action of M on B_N is given by:

$$\mathrm{MB}_N = \mathrm{B}_{N+1}\mathrm{D}_N^{N+1}, \tag{3.48}$$

where the $(N+1) \times N$ matrix D_N^{N+1}, has elements $D_{ij} = \alpha_i \delta_{i,j+1}$. Here $\delta_{i,j}$ is the Kronecker delta. This is the fundamental operation in a Krylov sequence.

Then the matrices B_N and B_{N+1}, are expressed in terms of their QR decomposition:

$$\mathrm{MQ}_N\mathrm{R}_N = \mathrm{Q}_{N+1}\mathrm{R}_{N+1}\mathrm{D}_N^{N+1}, \tag{3.49}$$

where the matrix Q_N has N orthonormal columns, and R_N is a $N \times N$ upper triangular matrix. One can then define an upper Hessenberg matrix:

$$\mathrm{H}_N^{N+1} = \mathrm{R}_{N+1}\mathrm{D}_N^{N+1}\mathrm{R}_N^{-1}, \tag{3.50}$$

and find:

$$\mathrm{MQ}_N = \mathrm{Q}_{N+1}\mathrm{H}_N^{N+1}. \tag{3.51}$$

The last row in the upper Hessenberg matrix has only one non-zero element, denoted as $h^* \equiv \mathrm{H}_{N,N+1}$. Let H_N be the $N \times N$ resultant matrix, after copying all the elements of matrix H_N^{N+1}, except for the last column. If one explicitly separates the last column $\boldsymbol{q}_N$ of Q_{N+1} one obtains:

$$\mathrm{MQ}_N = \mathrm{Q}_N\mathrm{H}_N + h^*\boldsymbol{q}_N\boldsymbol{e}_N^T, \tag{3.52}$$

where $\boldsymbol{e}_N^T$ is a unit vector of length $1 \times N$. This definition is the projection of M on the reduced orthonormal basis Q_N. The term h^* represents the error of the projected H_N matrix.

Using this projection one can compute the eigenvalues $\boldsymbol{v}_j$ and eigenvectors λ_j of matrix H_N. By gathering the eigenvectors in the matrix Γ_N and the eigenvalues in the diagonal matrix Λ_N one can show that:

$$\mathrm{MQ}_N\Gamma_N = \mathrm{Q}_N\Gamma_N\Gamma_N^{-1}\mathrm{H}_N\Gamma_N + h^*\boldsymbol{q}_N\boldsymbol{e}_N^T\Gamma_N \rightarrow \mathrm{M}\Psi_N = \Psi_N\Lambda_N + h^*\boldsymbol{q}_N\boldsymbol{e}_N^T\Gamma_N. \tag{3.53}$$

Here $\Psi_N = \mathrm{Q}_N\Gamma_N = [\boldsymbol{\psi}_0, \boldsymbol{\psi}_1, ...]$ is the matrix whose columns are the normalized approximate (Ritz) eigenvectors $\boldsymbol{\psi}_j$ of M. The residual error of the eigenpar $\boldsymbol{\psi}_j$ and λ_j is exactly given by:

$$\epsilon_j = |\mathrm{M}\boldsymbol{\psi}_j - \lambda_j\boldsymbol{\psi}_j| = \left| h^*\boldsymbol{q}_N\boldsymbol{e}_N^T\boldsymbol{v}_j \right|. \tag{3.54}$$

3.4.2 Implementation of the algorithm

In the MATLAB code used in this thesis, the above method is used to compute the leading eigenvalue of the operator M = A*A. The code initializes $\boldsymbol{v}_0$, with a random and small $\mathcal{O}(10^{-20})$ velocity field. It then constructs the matrix in eq. (3.47), by repeatedly integrating forward (LNSE) and backwards (adjoint LNSE) the initial velocity field $\boldsymbol{v}_0$. Note that, the act of integrating forward, and then backwards $\boldsymbol{v}_0$, is equivalent to perform M$\boldsymbol{v}_0$. The number of Arnoldi iterations is kept to $N = 5$, unless the final error $\epsilon_j \geq tol$ is bigger than a certain tolerance. In that case the code performs more steps of the Arnoldi iteration, i.e. more for-backwards integrations.

3.4.3 The maximal growth G

In this thesis, the maximal growth G corresponds to the maximal $G(t_f)$ obtained after checking all possible combinations of t_0, t_f, m and α for a particular laminar profile. To that end, the code always iterates on all possible combinations of t_0, t_f, m and α for the selected Wo, Re and A.

3.5 Linear Stability Analysis

In this thesis the laminar profile is computed and saved at several time steps during the pulsation period. Then, each instantaneous laminar profile is plugged, as if it were steady, in the algorithm developed by Meseguer *et al.* [MT00]. The code performs a linear stability analysis, that returns a vector with the eigenvalues $\boldsymbol{\lambda}$ of the laminar profile at that time step. The maximum eigenvalue $\lambda_{\max}(t) = \max \boldsymbol{\lambda}(t)$ at each time step is saved. All the maximum eigenvalues are then treated as a continuous function in time $\lambda_{\max}(t)$ and used to study the stability of the flow during one pulsation period, as analyzed in Chapter 4.

In what follows, the main ideas of the algorithm will be presented. For more details the reader is referred to the original references [MT00; MT03].

3.5.1 Spatial discretization

The perturbation velocity is discretized with a Petrov-Galerkin projection. A Fourier Ansatz is used in the axial and azimuthal directions. In the radial direction the velocity is expanded with the use of two polynomial:

$$\boldsymbol{u}' = \sum^{m}\sum^{\alpha} \hat{\boldsymbol{u}}'_{m,\alpha}(r,t)\exp(im\theta + i\alpha x) \tag{3.55}$$

$$= \sum^{m}\sum^{\alpha}\sum_{l=0}^{L}\left[a_l^{(1)}\boldsymbol{v}_{l,m,\alpha}^{(1)}(r,t) + a_l^{(2)}\boldsymbol{v}_{l,m,\alpha}^{(2)}(r,t)\right]\exp(im\theta + i\alpha x). \tag{3.56}$$

The polynomial are chosen so the zero-divergence condition is satisfied:

$$\nabla\cdot\left[\boldsymbol{v}_{l,m,\alpha}^{(1,2)}\exp(im\theta + i\alpha x)\right] = 0. \tag{3.57}$$

The trial functions $\boldsymbol{V}$ are the solenoidal base to which the polynomial are projected. They are computed so they comply with the divergence free condition.

3.5.2 Weak formulation

The problem is defined using the weak formulation. One can write the LNSE in the form:

$$\frac{\partial \boldsymbol{u}'}{\partial t} = \mathbf{N}_{\mathbf{u}'} - \nabla p' + \frac{1}{Re}\boldsymbol{\nabla^2 u}' \rightarrow \boldsymbol{u}'_t = \mathrm{L}\,\boldsymbol{u}' - \nabla p', \tag{3.58}$$

where L are all the linear operations on the perturbation velocity. Using the weak formulation, the above equation can be written as:

$$(\boldsymbol{u}'_t, \boldsymbol{W}) = (\mathrm{L}\,\boldsymbol{u}'_t, \boldsymbol{W}) - (\nabla p', \boldsymbol{W}), \tag{3.59}$$

where $(\cdot,\cdot)$ is the inner product in the flow domain, and $\boldsymbol{W}$ are solenoidal tests functions that vanish at the pipe wall. Since $\boldsymbol{W} = 0$ at the wall, the functions are solenoidal $\nabla \cdot \boldsymbol{W} = 0$, and using periodic boundary conditions in the axial and azimuthal directions, one can show that $(\nabla p', \boldsymbol{W}) = -(p', \nabla \cdot \boldsymbol{W}) = 0$. This means that, in the weak formulation, the above problem can be simplified as:

$$(\boldsymbol{u}'_t, \boldsymbol{W}) = (\mathrm{L}\,\boldsymbol{u}'_t, \boldsymbol{W}). \tag{3.60}$$

The test functions $\boldsymbol{W}$ could be set equal to the trial functions $\boldsymbol{V}$ [MT00]. Instead $\boldsymbol{W}$ are computed as modified trial functions $\boldsymbol{V}$.

3.5.3 Implementation of the algorithm

The above method is used to compute the leading eigenvalue of the operator L, for each snapshot of the laminar profile. The code performs three loops, one in the time step of the laminar profile, other on the azimuthal wavenumber m and another on the axial wavenumber α. At each time step it computes the instantaneous maximum eigenvalue $\max(\boldsymbol{\lambda})$ out of all wavenumbers, and saves it to the function $\lambda_{\max}(t)$.

4 Results: Linear Stability and Transient Growth Analysis

In this chapter, transient growth analysis and linear stability analysis of pulsatile pipe flows driven with different pulsation waveforms and different flow parameters Re, Wo are performed. Among the inifinite combinations of flow parameters possible, here only cases at $Re \approx \mathcal{O}(10^3)$, $5 \lesssim Wo \lesssim 20$, $A \geq 0.5$ are considered. At these Re and A, and at intermediate $8 \lesssim Wo \lesssim 20$ the laminar pulsatile pipe flow $U_{SW}(r,t)$ is highly susceptible to the growth of helical perturbations [XSA21]. These perturbations are optimally triggered during the deceleration phase of the pulsation, $\frac{\mathrm{d}u_b}{\mathrm{d}t} < 0$ and show an outstanding energy growth which scales exponentially with Re, A and Wo^{-2}. Similar flow patterns have been observed in experiments [Xu+20], where they behave similar to their theoretical counterparts until they saturate and trigger turbulence.

The main focus of this chapter is the analysis of these helical perturbations. As it is described below, the mechanisms the helical perturbations use to outstandingly grow, are related to the shape of the laminar pulsatile pipe flow itself. Therefore, at the beginning of this chapter, some time is devoted to describe the laminar pulsatile pipe flow itself. Following our paper [MFA22], the causes of the helical perturbations and the effect the shape of the pulsation has on them are then explained. Part of the results in this chapter have been published there.

4.1 General characteristics of pulsatile pipe flow

In order to highlight some characteristics of laminar pulsatile pipe flow and the transient growth of perturbations on top of them, here some results of the original work of Womersley [Wom55] and Xu *et al.* [XSA21] are reproduced.

4.1.1 Sexl–Womersley profile

Laminar pulsatile pipe flow has an analytical solution, the Sexl-Womersley (SW) profile $U_{SW}(r,t)$ §3.1. As Wo increases the maximum center-line velocity of the SW profile:

$$U_c(t) = U_{SW}(r=0,t), \tag{4.1}$$

decreases, and the phase difference between the driving pressure gradient $f_p(t)$ and bulk velocity u_b increases, see fig. 4.1b.

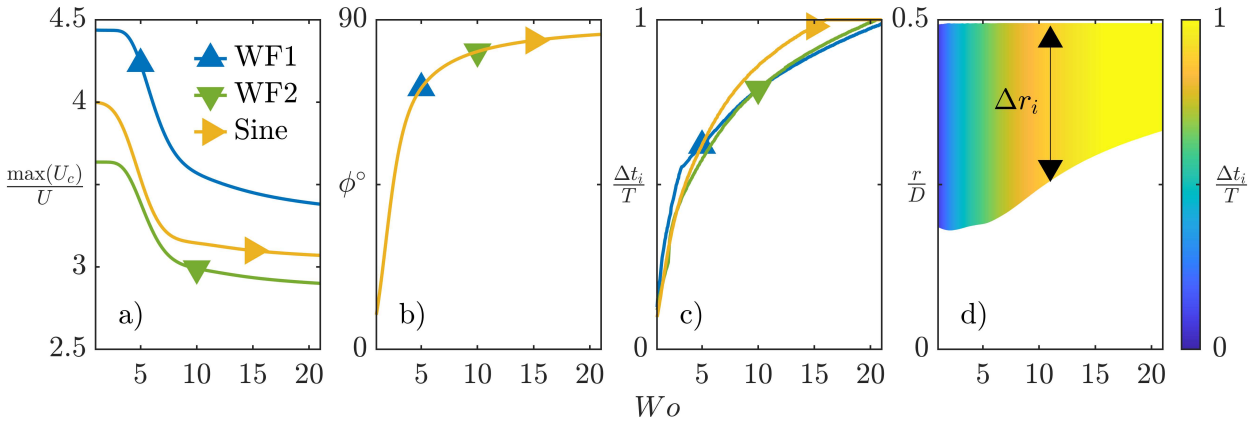

Fig. 4.1.: Characterization of the laminar pulsatile pipe flow profile U_{SW} for different pulsation waveforms (symbols) and Wo (horizontal axis). Here WF1 corresponds to a custom waveform with $t_m = 0.45$ and $t_{ac} = t_{dc} = 0.05$. WF2 corresponds to $t_m = 0.55$ and $t_{ac} = t_{dc} = 0.2$, see §2.1.4. Sine stands for a single harmonic pulsation at $A = 1$. See the waveform in fig. 2.1 and 4.3. In a), the maximum center-line velocity during the pulsation. In b) phase difference between bulk velocity $u_b\,(t)$ and the driving pressure gradient $f_p\,(t)$. In c) the total lifetime of inflection points in the laminar profile as a fraction of the pulsation period. In d) with colors, the lifetime of inflection points in the laminar profile as a fraction of the period. The area denotes all the radial positions of inflection points during a pulsation period at each Wo.

At $A = 1$ and $Wo \geq 1$, the SW profile has inflection points where:

$$\frac{\partial^2 U_{SW}}{\partial r^2} = 0, \tag{4.2}$$

that survive for a certain phase of the period $\frac{\Delta t_i}{T}$, that scales with Wo, see fig. 4.1c and d. These inflection points appear at the pipe wall during the deceleration phase of the pulsation and move radially towards the center-line of the pipe during the rest of the pulsation. How close they come to $r = 0$ depends on Wo, see fig. 4.1d.

These inflection points, as shown later, are related with the stability of the laminar pipe flow and with the growth of perturbations on top of it. By changing the pulsation waveform, one can change the radial movement and lifetime of these inflection points, see fig. 4.1c and d.

4.1.2 A word of warning regarding optimal perturbations

In this chapter the main focus is the optimal perturbations to different U_{SW} profiles. The optimal perturbation corresponds to the perturbation that can grow the most by extracting energy from the laminar flow. In the case of pulsatile pipe flow, it is optimally triggered at a given phase t_0/T, and reach maximum energy after a time t_f/T. For most of the flows considered here, this optimal perturbation corresponds to the so-called helical perturbation, see fig. 4.2. The shape of the optimal helical perturbation varies between flows. For all the cases considered here, it always has an azimuthal wavenumber $m = 1$, but its radial profile and axial wavelength α change, as described by Xu *et al.* [XSA21]. By focusing on the optimal perturbation, however, other perturbations that can also grow in pulsatile pipe flow are ignored. They are quickly mentioned here.

On the one hand, as long as $Re \approx \mathcal{O}\,(10^3)$, pulsatile pipe flows are susceptible to the growth of stream-wise constant perturbations with $m = 1$ and $\alpha = 0$, as in the case of steady pipe flow. Their growth depends on Re. See in figure 4.3 (in dashed lines) the transient growth of stream-wise

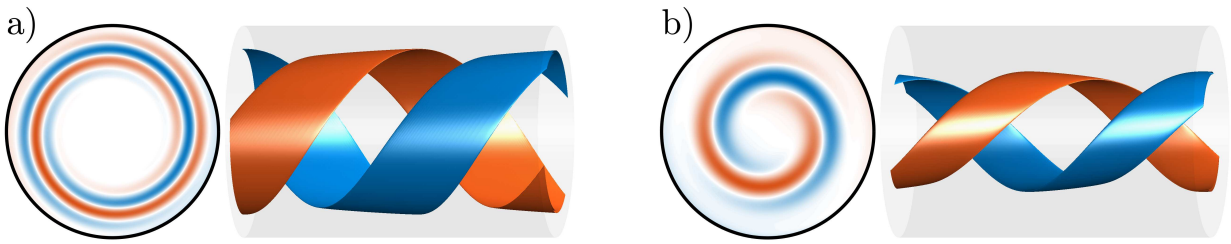

Fig. 4.2.: Isosurfaces of positive (blue) and negative (vermilion) axial vorticity ω_x of the optimal helical perturbation of a pulsatile pipe flow driven with a sine wave pulsation at $Re = 2000$, $A = 1$ and $Wo = 11$. In a) at $t_0/T = 0.5$ and in b) at $t/T = 1$. In both panels a section $x = 1.5D$ long of the pipe is shown, and the isosurface corresponds to the $\pm 0.9 \max(\omega_x)$ at that instant of time.

Tab. 4.1.: Parametric space considered for the linear stability (LSA) and transient growth (TGA) analyses: range of Reynolds (Re) and Womersley (Wo) numbers and the three parameters (t_m, t_{ac}, t_{dc}) defining the generic waveform, the total number of each parameter values ($N_{...}$) and the total number of cases (N).

Method	Re	N_{Re}	Wo	N_{Wo}	t_m	N_{t_m}	$t_{ac,dc}$	$N_{t_{ac,dc}}$	N
LSA	1000 to 4000	7	1 to 25	25	0.40 to 0.60	5	0.05 to 0.2	4	14 000
TGA	1500 to 2500	3	7 to 15	5	0.45 to 0.55	3	0.05 to 0.2	2	180

constant perturbations on top of three different pulsatile flows. At these particular Wo, Re and A the growth of these perturbations is much smaller than the helical perturbations. Note, however, that their energy decays at a much slower rate than the helical perturbation one.

On the other hand, the mechanism behind the growth of the helical perturbation, allows the growth of additional perturbations. In particular, the presence of inflection points in the profiles is related to the optimal growth of helical perturbations with $m = 1$ and $\alpha \approx 4$, but also of perturbations with $m = 2$ and $1 \lesssim \alpha \lesssim 6$. These results are not shown here.

4.2 Linear analysis

In this section, results of a large set of LSA and TGA of laminar profiles at many different combinations of Re, Wo and waveforms, as compiled in table 4.1, are shown. For $5 \leq Wo \leq 19$ all the bulk velocities show susceptibility to the development of the helical perturbations in a similar fashion to the single harmonic pulsation. According to the TGA the helical perturbation is optimally triggered during deceleration and grows during the low velocity phase, see fig. 4.3. It then reaches its maximum during, or right after, the acceleration phase for all the bulk velocities considered here.

4.2.1 Mechanism of the helical perturbation growth

The velocity profile at $Re = 2000$, $Wo = 11$ and $A = 1$, is instantaneously unstable for more than $50\,\%$ of the period. This can be seen in fig. 4.4, where the maximum real part out of all the instantaneous eigenvalues ($\lambda_{\max}$, see §3.5), is shown for this case. For most part of the acceleration phase, $\lambda_{\max}$ is constant and negative. This corresponds to the maximum eigenvalue of Hagen-Poiseuille flow at $Re = 2000$ [MT00]. However for the second half of the deceleration phase and the first half of the

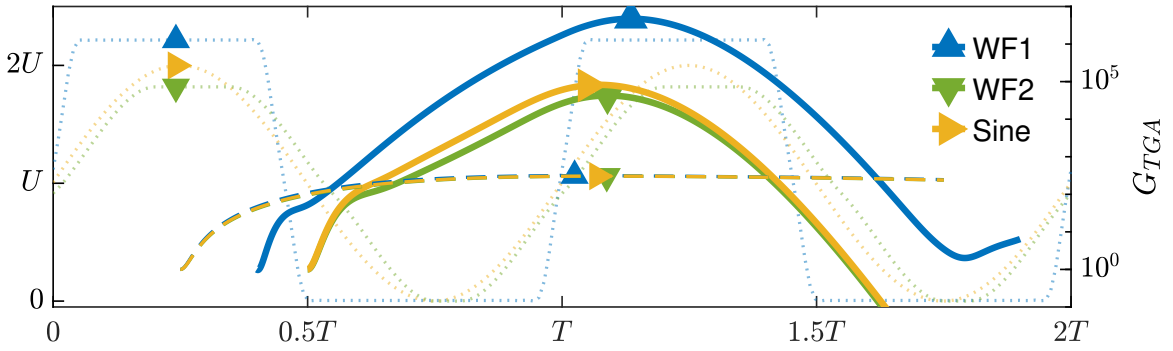

Fig. 4.3.: Energy growth of the optimal helical perturbation ($\alpha > 0$ and $m = 1$) in solid lines, and of stream-wise constant perturbations ($\alpha = 0$ and $m = 1$) in dashed lines, according to TGA for three different waveform (dotted lines) at $Re = 2000$ and $Wo = 11$.

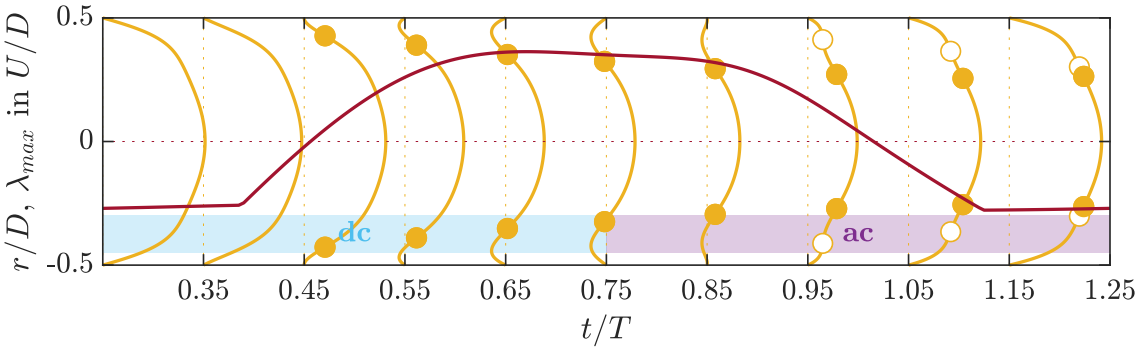

Fig. 4.4.: Laminar profile and instantaneous maximum eigenvalue $\lambda_{\max}$ according to LSA for a sine wave pulsation. In yellow the instantaneous laminar profiles U_{SW} at $Re = 2000$, $Wo = 11$ and $A = 1$. To not interfere with one another the profiles are scaled using a scalar with arbitrary units so the all time maximum is smaller than $t/T = 0.15$, since only the development of U_{SW} in time is of interest. With points find the existence and position r_i of inflection points in the profile. Filled points correspond to inflection points that also satisfy the Fjørtoft criterion locally $\frac{\partial^2 U_{SW}}{\partial r^2}\left(U_{SW} - U_{SW}\left(r_i\right)\right) < 0$. In red, the maximum real component out of all the instantaneous eigenvalues of the laminar profile $\lambda_{\max}$.

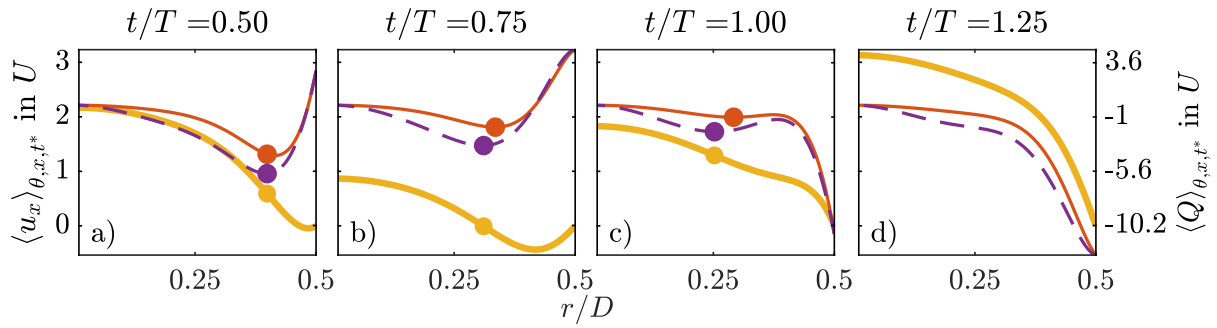

Fig. 4.5.: Laminar profile and the Q criteria, see eq. (4.4), at different phases of the pulsation period. In yellow thick lines, the instantaneous laminar profiles U_{SW} at $Re = 2100$, $Wo = 10$ and $A = 1$. With points find the existence and position r_i of inflection points in the profile that satisfy the Fjørtoft criterion locally $\frac{\partial^2 U_{SW}}{\partial r^2}\left(U_{SW} - U_{SW}\left(r_i\right)\right) < 0$. In a thinner orange line, the Q criteria, see eq. (4.4), related with the instability of the profile, for the case of $m = 1$ and $\alpha = 0$. The marker denotes the location of local minimum of Q in the interval $r \in [0, D/2)$. In a dashed purple line the criteria Q for the case $m = 1$ and $\alpha = 3.77\ 1/D$. For the sake of clarity, this last line is scaled by multiplying Q by $1 + \alpha^2 D^2$.

acceleration phase, $\lambda_{\max}$ is positive. The crossover occurs at $\frac{t}{T} \approx 0.45$, which is very close to the optimal time to trigger the helical perturbation ($\frac{t_0}{T} \approx 0.5$) found by Xu *et al.* [XSA21] based on a transient growth analysis for the same values of Re, Wo and A.

The instantaneous linear instability of the Sexl–Womersley velocity profile is related to the existence and characteristics (number or position (r_i)) of inflection points ($\frac{\partial^2 U_{SW}}{\partial r^2} = 0$) [Mia+17; Neb19]. An inflection point is regarded as inviscidly unstable, in Cartesian coordinates, when the Fjørtoft criterion:

$$\frac{\partial^2 U_{SW}}{\partial r^2}\left(U_{SW} - U_{SW}(r_i)\right) < 0, \tag{4.3}$$

is satisfied locally [SH00]. In the case of cylindrical coordinates, there is an equivalent criterion that depends on the term:

$$Q\left(r\right) = \frac{r}{m^2 + \alpha^2 r^2}\frac{\partial U_{SW}}{\partial r}. \tag{4.4}$$

A necessary condition for the profile to be unstable is that Q has a numerical minimum at some $r \neq 0$ and $r \neq R$, [BG62]. For the case of the helical perturbations considered here, with $m = 1$ and $\alpha \approx 3.7\ 1/D$, this maximum is found almost exactly at the radial location of inflection points, as seen in fig. 4.5.

Perturbations can sit on top of these inflection points and feed energy from them [Neb19]. In the following, it is shown how the helical perturbations take advantage of this mechanism to grow. To this end, the LNSE are integrated forward in time using the optimal helical perturbation according to the TGA as initial condition. Then, the production (P') and dissipation (ε') of the kinetic energy (E) contained in the perturbations are computed as

$$P' = -u_r' u_x' \frac{\partial U_{SW}}{\partial r} \quad \text{and} \quad \varepsilon' = -\frac{1}{Re}\int_V \nabla \boldsymbol{u}' : \nabla \boldsymbol{u}' \mathrm{d}V \quad \text{where} \quad \frac{\mathrm{d}E}{\mathrm{d}t} = P' + \varepsilon'. \tag{4.5}$$

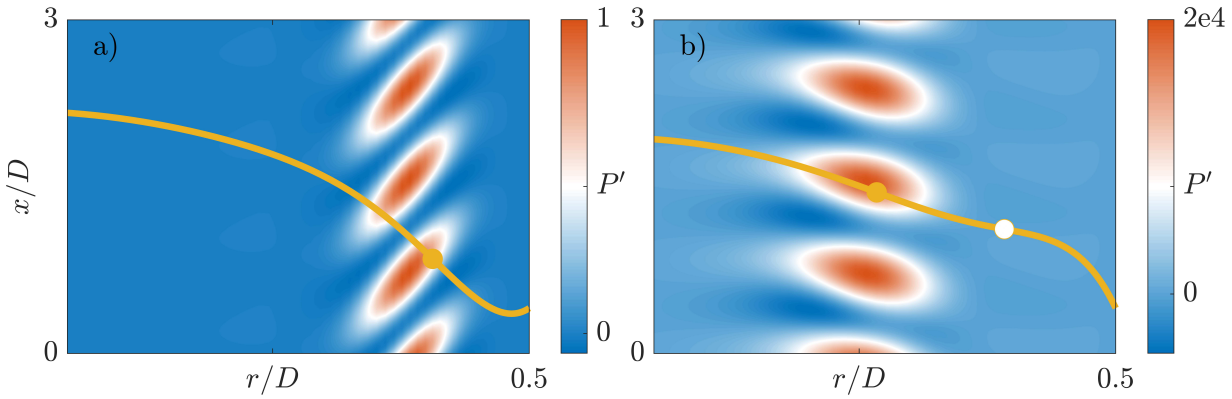

Fig. 4.6.: Link between inflection points in the Sexl–Womersley profile (U_{SW}) and production (P', see eq. (4.5)) of kinetic energy contained in the helical perturbations. Results are based on a simulation of the LNSE for a sine wave pulsation at $Re = 2000$, $Wo = 15$ with $A = 1$. Yellow lines represent $U(r,t)$ scaled in arbitrary units and dots represent existence and location (r_i) of inflection points. Filled dots additionally satisfy the Fjørtoft criterion locally. The production is normalized by the maximum value at $\frac{t_0}{T} = 0.5$, where the simulation was started. a): Mid deceleration phase at $\frac{t}{T} = 0.5$. b): Mid acceleration phase at $\frac{t}{T} = 1$.

Figure 4.6 shows how the location of strong production events of the helical perturbation attach to the radial position of the inflection points in the SW profile. This means that, the optimal helical perturbation, takes advantage of the presence and characteristics of inflection points to grow during the pulsation.

4.2.2 *Simple model for helical perturbation growth*

Pulsatile pipe flow has at least two important time scales when it comes to the evolution of perturbations. One is the advective time scale ($\frac{D}{U}$) and the other is the pulsation period ($T = \frac{\pi Re}{2Wo^2}$ in advective time units). Already Cowley *et al.* [Cow87] noted that, for sufficiently long pulsation periods (in terms of $\frac{D}{U}$), the perturbations would perceive a quasi-steady velocity profile. In that case, the perturbations would have enough time to grow on top of the instantaneous linear instability before the velocity profile changes and becomes stable again.

In view of these findings, it is hypothesised that the energy growth (G_{TGA}) observed by Xu *et al.* [XSA21], depends on how much and how long the SW velocity profile is instantaneously linearly unstable. The instability of the velocity profile, in turn, depends on the existence of inflection points that satisfy the Fjørtoft criterion [SH00; Neb19; Ker+21], as already discussed above. With these ideas in mind, from an LSA perspective, the energy growth rate should scale as

$$\frac{E_{\max}}{E_0} \propto G_{LSA} = e^{2\,\lambda_i\,T}, \tag{4.6}$$

where, λ_i is the weighted time integral

$$\lambda_i = \frac{1}{T} \int_{t_0}^{t_0+\Delta t_u} \lambda_{\max}(t)\,\mathrm{d}t, \tag{4.7}$$

for the time window Δt_u where $\lambda_{\max} > 0$. The new parameter λ_i is taken as a combined proxy for how much and how long the laminar profile U_{SW} is linearly unstable during one pulsation period.

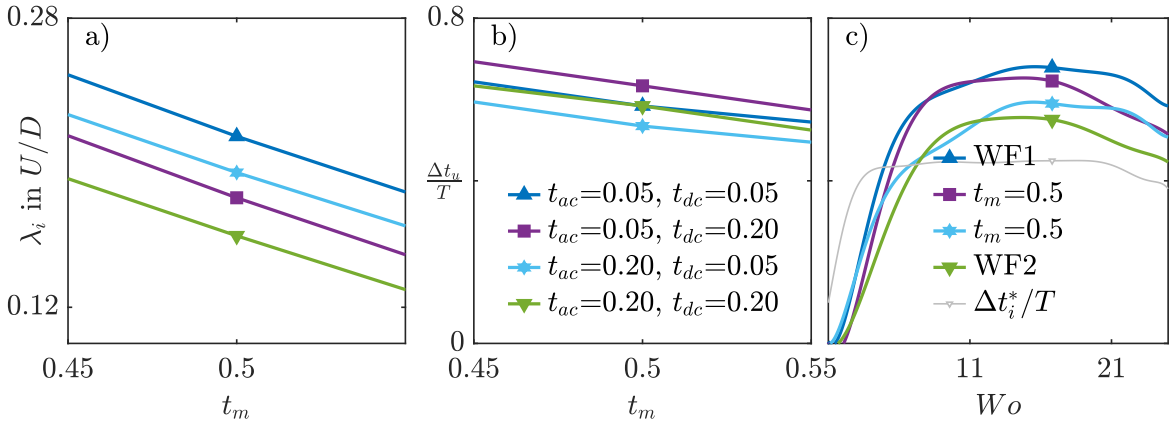

Fig. 4.7.: a) Relationship between eigenvalue proxy λ_i (see equation (4.7)) and t_m. Cases correspond to $Re = 2000$, $Wo = 11$ and different lines indicate different t_{ac} and t_{dc}. b) Δt_u or fraction of the period during which the laminar profile is instantaneously unstable for different t_m, t_{ac} and t_{dc}. c) Δt_u for different waveform with respect to Wo. The thin grey line corresponds to the total time Δt_i^* where the profile has a single inflection point that satisfies the Fjørtoft criterion.

4.3 Parametric study of helical perturbation growth

In general, the proposed eigenvalue proxy in eq. (4.7) depends on all the control parameters. Here these dependencies are studied. First its dependency with respect to the parameters that define the waveform (t_m, t_{ac} and t_{dc}) are explored, while fixing $Re = 2000$ and $Wo = 15$. Afterward, the flow parameters Re and Wo are varied. Motivated by these findings, the parametric space is massively explored and a simplified formulation from the generated data base is developed, to approximate the energy growth of a pulsatile pipe flow as a function only of the waveform and flow parameters. This formulation is finally tested with a realistic physiological waveform.

4.3.1 Dependency with respect to the waveform

The first parameter to consider is t_m, which controls the asymmetry of the waveform. The smaller t_m is, the shorter the high velocity phase (in terms of T) and the larger $Re_{\max}$ become, see eq. (2.5). From fig. 4.7a, it is clear that λ_i increases monotonically as t_m decreases. This is because a longer low velocity phase (smaller t_m) results in a longer fraction of the period Δt_u where the profile is instantaneously unstable, see fig. 4.7b. Thus the shorter t_m is the more unstable the laminar profile becomes. This conclusion is in good agreement with experimental findings of [BV18], who showed that flows with longer deceleration and longer low velocity phases are more prone to transition.

In figure 4.7a, it is also shown how λ_i depends on the other two waveform parameters. Bear in mind that t_{ac} and t_{dc} control the slope of the acceleration and the deceleration, but do not affect $Re_{\max}$. It is evident from figure 4.7a, that λ_i is inversely proportional to both parameters, implying that steeper acceleration and steeper deceleration both lead to more unstable flows. However, the sensitivity of λ_i with respect to t_{dc} is larger than the sensitivity with respect to t_{ac}. While increasing t_{ac} by a factor of four decreases λ_i by only $9\,\%$, doing the same for t_{dc} decreases λ_i by $16\,\%$.

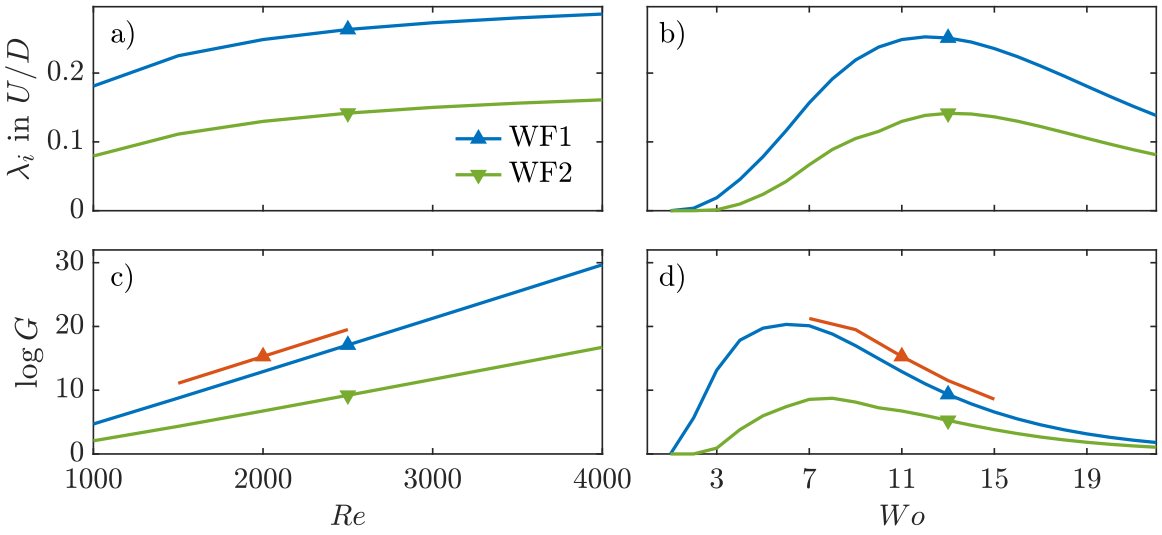

Fig. 4.8.: a) Eigenvalue proxy λ_i with respect to Re at $Wo = 11$ and two different waveform (blue/green lines). b) λ_i, equation (4.7), with respect to Wo at $Re = 2000$. c) G_{LSA}, see equation (4.6), with respect to Re at $Wo = 11$. c) G_{LSA} with respect to Wo at $Re = 2000$. Orange lines correspond to the optimal transient growth G_{TGA}. Blue and orange lines correspond to waveform 1 with $t_m = 0.45$ and $t_{ac} = t_{dc} = 0.05$, while green lines correspond to waveform 2 with $t_m = 0.55$ and $t_{ac} = t_{dc} = 0.2$.

4.3.2 *Dependency with respect to Reynolds and Womersley numbers*

The hypothesis is that G_{LSA} is proportional to the product of the period (T) and the proposed eigenvalue proxy (λ_i, eq (4.7)). Here the dependency of λ_i on Re and Wo is explored and G_{LSA} is compared with G_{TGA}, the latter obtained with a transient growth analysis.

For both waveform considered here, λ_i grows with the Reynolds number, see fig. 4.8a. At very high Re, λ_i seems to approach a given asymptotic value, which depends on the waveform.

The dependence of λ_i on the Womersley number is more complex. From $Wo \gtrsim 2$ on, $\lambda_i > 0$, see fig. 4.8b, but the exact value at which the flow becomes unstable, depends on both the Reynolds number and the waveform. Thereafter λ_i increases with Wo, until it reaches a maximum around $Wo \approx 11$. The exact location and magnitude of this maximum also depends on the Reynolds number and the waveform. If Wo is now further increased, λ_i decreases again but remains positive for all parameters considered here.

The dependence of λ_i on Wo is determined by the relationship between Δt_u and Wo, as observed when comparing figures 4.8b and 4.7c. It is the fraction of the period where the flow is unstable what dictates the value of λ_i with respect to Wo. In turn, as shown in figure 4.7c, Δt_u follows the trend of Δt_i^*. Here, Δt_i^* is the fraction of the period, where the profile has only one inflection point, that additionally satisfies the Fjørtoft criterion. Thus the presence of inflection points sets the fraction of the period where the laminar profile is unstable, which sets the level of instability λ_i.

For $Wo \gtrsim 3$ the velocity profiles exhibit inflection points for more than one quarter ($\Delta t_i^* \gtrsim \frac{T}{4}$) of the pulsation period, see fig. 4.7c. By increasing Wo ($3 \lesssim Wo \lesssim 15$), the lifespan of the inflection points (Δt_i) increases, see fig. 4.1c. The inflection points appear close to the pipe wall at the early stages of deceleration, see fig. 4.4. During the rest of the deceleration and the subsequent low velocity phase,

the inflection points move towards the pipe center-line. However, before they are able to reach the center-line, they disappear during the acceleration phase. Their movement is restricted to a radial span $\Delta r_i = \max(r_i) - \min(r_i)$ that decreases with increasing Womersley number, see fig. 4.1d. For large Wo, the evolution of the velocity profile prevents the inflection points from approaching the center line before they die. Already from $Wo \approx 11$ on, they remain in the vicinity of the pipe wall ($\min(r_i) < \frac{D}{4}$) and so do the perturbations that may grow on top of them. This in turn does not allow perturbations to access the more energetic flow in the central region of the pipe, resulting in a decreasing λ_i for $Wo > 11$, see fig. 4.8a.

In order to characterize the dependency of G_{LSA} (eq (4.6)) with respect to Re and Wo, one needs to combine the knowledge on λ_i with the effect of the pulsation period $T = \frac{\pi Re}{2Wo^2}$. For intermediate Womersley numbers, G_{LSA} grows monotonically with Re, see fig. 4.8d. At sufficiently high Reynolds numbers, λ_i is more or less constant, see fig. 4.8a, and G_{LSA} ends up following the exponential relationship between T and Re.

The combined effects of λ_i and pulsation period set the point of maximum growth at $Wo \approx 7.5$, see fig. 4.8c. Depending on the waveform or the Reynolds number, the exact position of this maximum with respect to Wo can vary slightly. Interestingly, the region close to $Wo \approx 7.5$ matches the point of maximum transient growth for a flow driven with a sine wave pulsation [XSA21], and it is close to the point of maximum growth of perturbations in pulsatile channel flow [PS17]. It is at this particular Wo, where the competing effects of shorter pulsation periods (in terms of advective time units) and higher level of average instability of the laminar profile, make the flow more susceptible for perturbations to grow.

In figure 4.8c and d it is shown that G_{LSA} approximates the optimal transient growth G_{TGA} reasonably well at several Re and Wo. This shows that the energy growth of the helical perturbation is related to the instantaneous instability of the laminar profile and confirms the initial hypothesis. It is the instantaneous instability of the laminar profile what yields the outstanding perturbation growth observed in transient growth analyses [XSA21].

Difference between energy growth in TGA and LSA

Note that G_{TGA} must always be $G_{TGA} \geq G_{LSA}$. The energy growth of perturbations according to the TGA is the combination of modal and non-modal growth, whereas the energy growth of the LSA is only modal. As discussed by Xu *et al.* [XSA21], the optimal helical perturbation in the TGA is initially tilted against the mean shear of the pulsation. See this initial tilt in figure 4.6. This tilt triggers an initial Orr like mechanism where the energy of the perturbation grows as it is tilted in favor of the mean shear.

This initial growth can be seen in figure 4.3, where there is a clear change of trend of energy growth at a time $t/T \approx 0.1$ after the perturbation has been triggered. At $Re = 2000$ and $Wo = 15$, $t = 0.1T \approx 1D/U$. The Orr mechansm time scale is equal to the time scale of the mean shear [EJ20], which in this case is indeed $\approx 1D/U$.

Tab. 4.2.: Weights (w) and biases (bi) used to fit LSA and TGA results to eqs. (4.8)–(4.10).

Case	bi_1	w_1	w_2	w_3	bi_2	w_m	w_{ac}	w_{dc}	bi_3	N
LSA	0.989	1.55	0.0059	0.1821	18.746	-17.634	-2.064	-16.38	-2.9638	14000
TGA	-0.13	1.67	0.0083	0.1925	-8.111	-16.223	-3.404	-5.491	-0.6191	180

4.3.3 A model for perturbation growth in pulsatile pipe flows

The dependency of the perturbation growth on the governing parameters is quantified by fitting the two sets of LSA and TGA results listed in table 4.1 to the expression

$$\log G_g = s \cdot \sigma \cdot Re + bi_3, \tag{4.8}$$

$$s = bi_2 + w_m \cdot t_m + w_{ac} \cdot t_{ac} + w_{dc} \cdot t_{dc}, \tag{4.9}$$

$$\sigma = \left[w_1 \left(Wo - bi_1\right) + w_2 \left(Wo - bi_1\right)^2\right] \cdot \exp\left(-w_3 Wo\right). \tag{4.10}$$

The parameter G_g is the guess on G_{LSA} or G_{TGA}. An exponential dependence on Re is assumed, motivated by figure 4.8d. Also, from the observations above, the slope of this relationship is assumed to be the product of eq. (4.9) and eq. (4.10). The function σ tries to reproduce the shape of G_{LSA} with respect to Wo that is shown in fig. 4.8c. The function s accounts for the dependency of G_g on the shape of the pulsation waveform (*i.e.* t_m, t_{ac} and t_{dc}).

Then G_g is computed by looking for the set of weights (w_i) and biases (bi_i) in eqs. (4.8)–(4.10) that minimize the error

$$\epsilon = \frac{1}{N} \sum_{n=1}^{N} \left(\log G - \log G_g\right)_n^2, \tag{4.11}$$

being N the total number of data items to fit (table 4.2). Two fits have been produced, one to the LSA results where $G = G_{LSA}$ and another to the TGA results where $G = G_{TGA}$. Each fit is initialized with the vector $\boldsymbol{x}^0$, that is filled with random guesses of weights and biases with values between zero and one. Then a gradient descent method is used to find the vector $\boldsymbol{x}^i$ that minimizes eq. (4.11). Iterations are performed until a minimum is reached. At iteration i the weights and biases are updated as

$$\boldsymbol{x}^{i+1} = \boldsymbol{x}^i - \eta \sum_{n=1}^{N} \frac{\mathrm{d}\epsilon^n}{\mathrm{d}\boldsymbol{x}^i}, \tag{4.12}$$

where η here is a *learning parameter* that is dynamically adjusted so that the error $\epsilon\left(\boldsymbol{x}^{i+1}\right) < \epsilon\left(\boldsymbol{x}^i\right)$. The case is considered as converged when the error decreases to less than 10^{-10} for consecutive iterations.

The quality of the fit is visualized in figure 4.9. The horizontal axis represents the number of the case, where the list of cases is ordered in the sense of increasing first Re, then Wo and finally t_m, t_{ac} and t_{dc} as in table 4.1. This explains why the data appears in packets of functions that look similar to the shape of the function shown in figure 4.8c.

Note that the fit performs poorer as Re increases. Re also has an effect on λ_i, as shown in figure 4.8b. But the formulation here proposed, ignores this, and other cross-dependencies, as it only considers the dependency of G on Re coming from T. Despite these differences, the error is of the order of 10^{-4} for both fits.

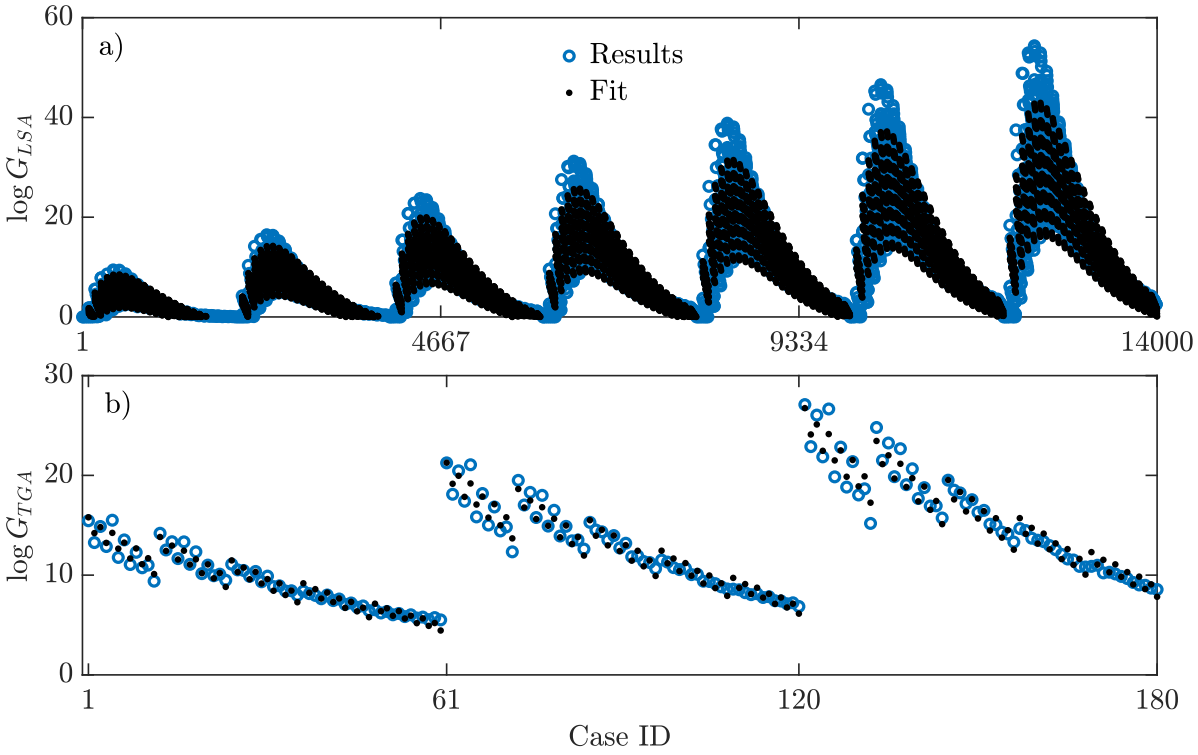

Fig. 4.9.: Results of the fit using the gradient descent method. a) Fit of G_{LSA} (see equation (4.6)) to equation (4.8). Hollow circles are individual results of the LSA for all the parameters considered, the first row of table 4.1. Black dots are the fit of the method. The horizontal axis corresponds to the number of data points in table 4.1. Each horizontal location corresponds to just one case with a given combination of Re, Wo, t_m, t_{ac} and t_{dc}. The cases are ordered in increasing sense of first Re then Wo and finally t_m, t_{ac} and t_{dc}. b) Same fit but for G_{TGA}, or the results of second row of table 4.1.

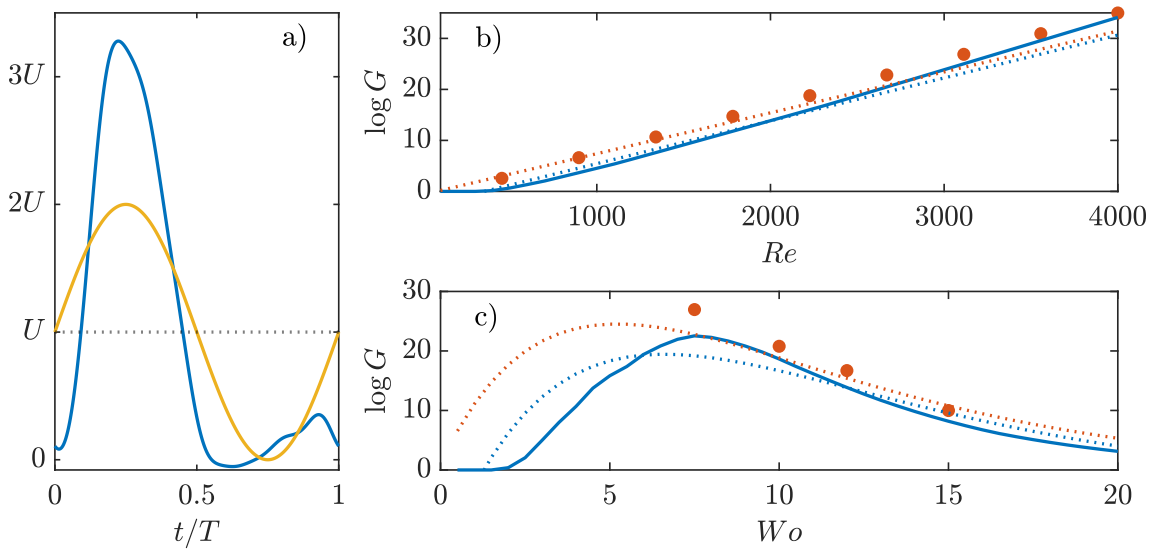

Fig. 4.10.: Results and fit of the energy growth of helical perturbations on a laminar profile driven with a physiological waveform. a) Physiological waveform defined by coefficients of table 4.3 in blue, compared with a sine wave pulsation in yellow. b) Evolution of energy growth G with Re at $Wo = 12$ for the physiological waveform. The blue solid line corresponds to G_{LSA} and the blue dotted line is a guess using the expression (4.8) with the weights in the first row of table 4.2. Filled red points correspond to TGA results and the dotted red line corresponds to a guess using the expression (4.8) with the weights in the second row of table 4.2. c) Evolution of energy growth G with respect to Wo at $Re = 2000$ for the physiological waveform. Lines and symbols correspond to the same cases as in b).

Tab. 4.3.: Fourier coefficients (a_n, b_n) used to approximate the physiological waveform [Bür+12]

$a_1 =$	-0.053	$a_5 =$	0.0368	$b_1 =$	1.4637	$b_5 =$	-0.0664
$a_2 =$	-0.7278	$a_6 =$	0.0142	$b_2 =$	-0.1712	$b_6 =$	-0.0259
$a_3 =$	-0.0957	$a_7 =$	-0.0013	$b_3 =$	-0.1905	$b_7 =$	0.00869
$a_4 =$	-0.0514	$a_8 =$	-0.0152	$b_4 =$	-0.1433	$b_8 =$	-0.00434

The final weights of the two fits (Table 4.2) show that t_m has a higher impact on the energy growth compared to t_{ac} and t_{dc}, since $|w_m| > |w_{dc}| > |w_{ac}|$. The smaller t_m, t_{ac} and t_{dc} are, the bigger the energy growth is, since $w_m < w_{ac} < w_{ac} < 0$. These fits allow us to generalize the dependency of G_{LSA} and G_{TGA} on all the control parameters for all the waveform considered here. With this tool one can infer how much helical perturbations can grow in a given pulsatile pipe flow by only knowing the waveform of the pulsation and the flow parameters (Re and Wo).

4.3.4 Physiological waveform

As a test of these observations, the behaviour of a laminar profile driven by a physiological waveform is studied. To that end a particular signal presented in the physiological study of Bürk *et al.* [Bür+12] was selected, see fig. 4.10a. In their study, they measured the mean velocity of blood flow at different sections of the aorta in several patients. I chose the signal for the descending aorta section of a young volunteer and fitted it using $N_F = 8$ Fourier modes. The resultant Fourier mode coefficients for the physiological waveform are presented in table 4.3. The corresponding waveform parameters

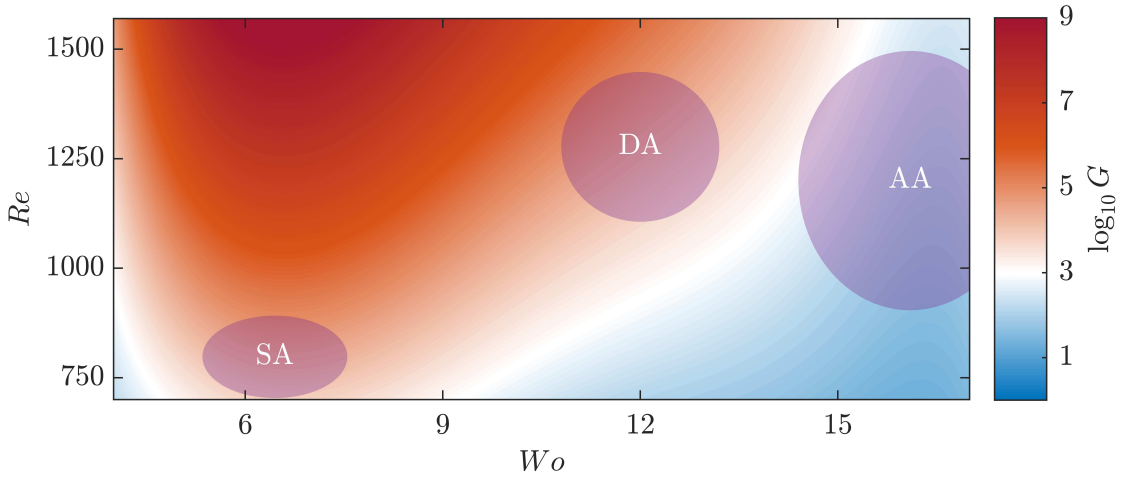

Fig. 4.11.: Energy growth G of helical perturbations on pulsatile pipe flows driven with the physiological waveform at several Re and Wo. Highlighted regions correspond to the typical flow parameter values at certain sections of the aorta [Les+10; Sta+11], gathered in table 1.1. AA stands for ascending aorta, DA for descending aorta and SA for supraceliac aorta. See figure 1.6 for a visual representation of these sections.

(t_{ac}, t_{dc} and t_m) of the physiological waveform are computed by measuring the time span between the half point of the acceleration and deceleration ($t_m \approx 0.279$). Additionally, the half length of the acceleration ($t_{ac} \approx 0.108$) and the deceleration ($t_{dc} \approx 0.141$) are measured. By introducing these parameters to expression (4.8) and using the weights listed in table 4.2, a guess of the energy growth on top of the laminar velocity profile of the physiological waveform is generated, see fig. 4.10b and c. Additionally, LSA (solid blue line) and TGA (red dots) are preformed, to probe the accuracy of the fits.

The fitting of expression (4.8) gives a good estimate of the growth of perturbations for the physiological waveform, even though the training data used to obtain the fit coefficients are for $t_m \geq 0.3$ (Table 4.1). Larger errors are found for $Wo \leq 10$ and correspond to the definition of σ in equation (4.10). Future analyses may improve this equation to better capture the behaviour at low Womersley numbers.

The TGA is extended to physiological waveform driven at flow parameters typically found in different sections of cardiovascular flow. As shown in the figure 4.11, there is a high chance of helical perturbation growth on top of pulsatile pipe flows driven with parameters and waveform found in cardiovascular flows, and at several sections of the human aorta.

4.4 Summary of the chapter

The presence of inflection points in laminar pulsatile pipe flow, at certain flow parameters, render it instantaneously unstable. If the pulsation period is long enough, in terms of advective time units, perturbations can take advantage of this instantaneous instability to transiently grow on top of it. Therefore, and despite pulsatile pipe flow is Floquet stable, perturbations can outstandingly grow during some phases of the pulsation period on top of it.

The helical perturbation happens to be the one that can grow the most on top of the inflection points. It has the shape that can take the most advantage possible of the presence and behaviour

of inflection points to grow. By changing the behaviour of the inflection points, using different pulsation waveform, one can control how unstable the flow profile is, and therefore, how much perturbations can grow on top of it. In general, the longer in time the inflection points are in the laminar profile, and the closer they get to the center-line of the pipe as they move from the wall, the higher the energy growth of the perturbations will be.

Lastly it must be noted that, despite using an instability of the flow profile, transition to turbulence due to helical perturbations is not supercritical, but subcritical. The perturbation does grow outstandingly during some phase of the pulsation period, but its energy quickly decreases during the rest of the period. As shown in figure 4.3, after one pulsation period the energy of the perturbation in smaller than the initial one. In order to trigger turbulence, the helical perturbation needs a high enough initial energy E_0 to grow to a certain energy E that is able to trigger non-linear mechanisms in the flow and then turbulence.

5 Results: DNS of pulsatile pipe flow

In this chapter the results of direct numerical simulations (DNS) of pulsatile pipe flow at different Re, Wo and harmonic pulsations are described. The parametric space considered here corresponds to the transitional regime of pulsatile pipe flow at $0.5 \leq A \lesssim 1$, and $Re \approx \mathcal{O}(10^3)$, with $Re_{\max} = (1 + A)\, Re$ in the range of $2500 \lesssim Re_{\max} \lesssim 4000$ and intermediate frequencies $6 \lesssim Wo \lesssim 20$. Different methods are used to trigger turbulence in DNS, and it is also described how turbulence behaves once triggered. As it is shown in this chapter, turbulence in pulsatile pipe flow at these flow parameters, first appears in the form of localized turbulent patches. A special attention is given to these localized structures and their behaviour depending on the flow parameters.

5.1 Trigger turbulence in pulsatile pipe flow

In order to trigger turbulence, three methods are used:

1. Some simulations are initialized with an already computed statistically steady pipe flow simulation. These simulations are referred to as DNS with IC-SSPF. In this case, the initial condition can have a puff, a slug or a fully turbulent flow.

2. Other simulations are initialized with the corresponding laminar pulsatile pipe flow profile U_{SW}. These simulations are continuously perturbed by a localized body force. These DNSs are referred to as simply DNS with a Force. As described in §2.1.5 the body force is meant to model the effect of geometric defects close to the wall, by locally decelerating the flow velocity close to the wall.

3. The majority of simulations are initialized with the corresponding laminar pulsatile pipe flow profile U_{SW} perturbed with the optimal perturbation according to the TGA described in §3.2.1. The simulations are initialized at the phase of the period t_0/T where the perturbation is optimally triggered. These DNSs are referred to as DNS with IC-SWOP. The initial perturbation is a helical perturbation, and, for reasons explained later, they are introduced localized in a given axial length and scaled to a given magnitude. All these simulations are listed in table C.1 in Appendix C.

5.1.1 DNS with IC SSPF

Firstly DNS initialized with the resultant flow field of a DNS of SSPF at $Re = 2400$ are discussed. At this Re, in SSPF, turbulence spreads in the whole pipe. The system reaches a spatio-temporal intermittent state where localized turbulent patches randomly split/elongate/decay next to laminar

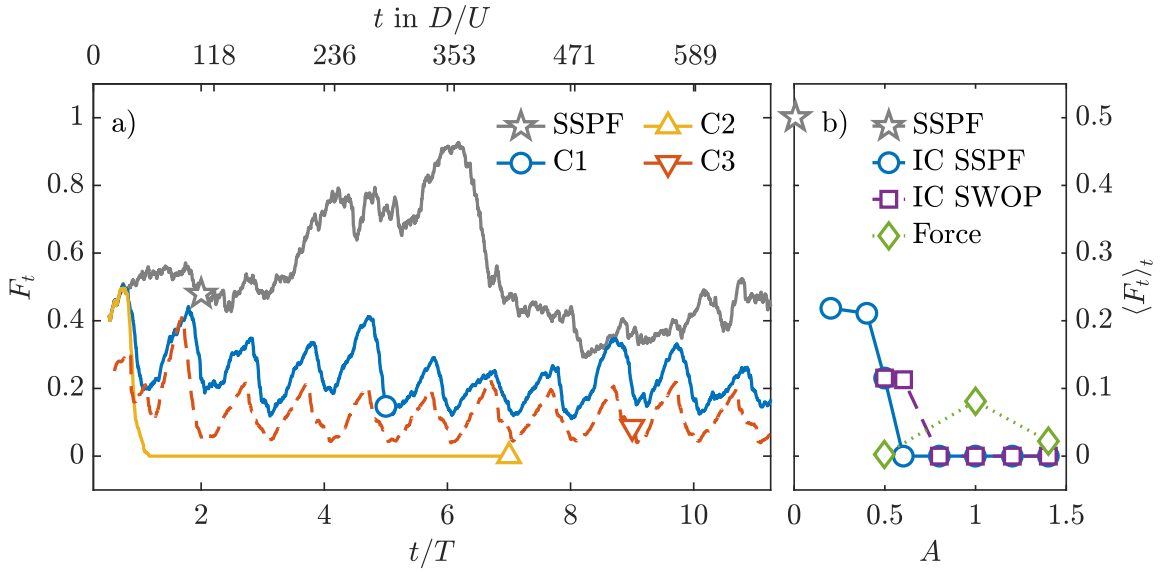

Fig. 5.1.: Turbulent fraction, eq. (5.1), based on the axial vorticity. (a) Time series of the turbulent fraction for several cases at $Re = 2400$ and $Wo = 8$ in a $L_x = 100D$ long pipe. SSPF stands for statistically steady pipe flow, or $A = 0$. C1 corresponds to a simulation with $A = 0.2$ initialized with a fully turbulent SSPF. C2 same as C1 but with $A = 0.6$. C3 corresponds to a DNS at $A = 0.6$ initialized at $t/T = 0.5$ with the corresponding U_{SW} profile and the optimal helical perturbation scaled to $|\boldsymbol{u}_0'| \approx 3e-2$ and localized in a $10D$ axial length. (b) Time averaged turbulent fraction in the 3 types of DNS explained in the main text, see section 5.1.

patches (see fig. A.5a). At this Re the turbulent fraction approaches but rarely reaches $F_t \approx 1$, see fig. 5.1. Here the turbulent fraction F_t is defined as:

$$F_t = \frac{L_t}{L_x}, \tag{5.1}$$

where L_t is the length of the pipe where $\langle \omega_x^2 \rangle_{r,\theta} \geq 0.1U^2/D^2$.

Several DNS of pulsatile pipe flow at $Re = 2400$, $Wo = 8$ and different A are initialized using this highly intermittent flow field. As shown in figure 5.1a, at this pulsation frequency, the pulsation tends to stabilize the flow. At $A = 0.2$, the intermittency of the flow decreases, as the turbulent structures tend to aggregate in individual, localized patches that are modulated in length and magnitude by the flow. By increasing A, the time averaged turbulent fraction decreases, see fig. 5.1b. At low pulsation frequencies the flow tends to behave in a quasi-steady way. This was already studied by Xu *et al.* [XA18], where they observed how localized turbulent patches elongate or decay depending on the instantaneous $Re_i\,(t) \approx u_b\,(t)\,Re$. When $Re_i \gtrsim 2250$ turbulence in pulsatile pipe flow tends to elongate, while at $Re_i \lesssim 2000$ it tends to decay. These effects manifest more prominently as A increases.

5.1.2 DNS with a localized Force

Here DNS constantly perturbed by a body force are discussed. As described in §2.1.5 the body forces are meant to model the effect of geometric defects at the wall. The body forces are proportional to $-\boldsymbol{u}$ and are localized in a small azimuthal, radial and axial section of the domain. The force acts as

a less permeable region to the flow and its magnitude is tuned so it does not trigger turbulence in SSPF at $Re \approx 2400$. At the flow parameters considered here we observe that the axisymmetric body force does not trigger turbulence. Only the azimuthally localized forces do. Since the results of both, the tilted and non-tilted body forces are similar, here we only show/discuss results of the former.

At flow parameters where the helical perturbation has an outstanding growth on top of the laminar U_{SW} profile, the body force is able to intermittently trigger turbulence. See an example of this behaviour at the end of this chapter in figure 5.11. During each deceleration phase, irregular flow patterns are triggered close to the body force. These structures grow during the low velocity phase of the period, and are then advected downstream by the flow. Depending on the flow parameters, the structures developed close to the body force can either decay or survive in the following pulsation periods.

This behaviour is also observed in experiments [Xu+20], where turbulence is intermittently triggered due to small defects at the pipe walls and then either decays or survives. This means that, even if turbulence is not able to survive for a whole pulsation period, it will be periodically triggered in the flow. As it is shown in figure 5.1 this results in a time averaged turbulent fraction $\langle F_t \rangle_t > 0$.

At $Re = 2400$ and $Wo = 8$ the effect of the body force is stronger at $A = 1$ than at $A = 0.5$ and $A = 1.4$, see fig. 5.1. At this pulsation frequency, the flow is much more instantaneously unstable at $A = 1$ than at $A = 0.5$. This explains why, at $A = 1$ the structures the body force triggers are longer in length and have a longer lifetime, than those at $A = 0.5$. At this pulsation frequency, and for the particular body force used here, at $A = 1$ the body force is able to trigger turbulent patches that survive for at least one additional period. However at $A = 1.4$ the body force triggers turbulent patches that survive for a shorter time. This explains why at $A = 1$ the time averaged turbulent fraction is higher than at $A = 1.4$.

5.1.3 DNS with IC SWOP

In our paper [FMA21] we describe DNS initialized with the correct laminar profile U_{SW} and on top of it, the corresponding optimal helical perturbation. Since at $Re = 2400$ and $Wo = 8$ only at high A the flow is susceptible to the growth of these perturbations, only cases with $A \geq 0.5$ are considered here. The perturbations are introduced axially localized in either a $10D$ or $5D$ axial section of the pipe and their magnitude is scaled to a small value $|\boldsymbol{u}'_0| \approx 3e-2$. The simulations are initialized at the optimal time t_0/T to trigger the growth of the helical perturbations.

In figure 5.2 it is shown how the helical perturbation grows, saturates and triggers turbulence in the pipe. The helical perturbation first grows in magnitude and in length until it saturates. As it saturates, it triggers low velocity streaks in the flow that disrupt the mean velocity profile. Depending on the flow parameters, once they saturate, the perturbations can either decay as they are advected by the flow, or trigger a localized turbulent structure. In the case shown in figure 5.2, at $Re = 2400$, $Wo = 11$ and $A = 1.4$, it triggers a localized turbulent patch, that is qualitatively similar to puffs typically found in SSPF: compare the structures at the back of the pipe in fig. 5.2f with fig. 1.6. These patches are then modulated in length and magnitude by the flow.

As it is shown in figure 5.1b, by initializing the DNS with the optimal perturbation, and not with the IC SSPF the lifetime of turbulence at $Re = 2400$, $Wo = 8$ and $A = 0.6$ is improved. In order to explain this phenomena, the hypothesis is that the shape of the laminar profile U_{SW} helps puffs survive the pulsation. Thus, only by initializing DNS with the corresponding laminar profile U_{SW}, and not with a highly perturbed turbulent field, can turbulence survive the pulsation at certain flow parameters. Later in the thesis this hypothesis will be demonstrated.

Unless stated otherwise, in the rest of the thesis only DNS of pulsatile pipe flow initialized with a localized helical perturbation or turbulent puff, without any body force, will be considered.

5.2 Turbulent patches in pulsatile pipe flow

Once turbulence is triggered it behaves in different ways depending on the flow parameters. At low $Re \lesssim 2000$ turbulence eventually decays. Depending on Wo and A this decay can happen earlier or later (in average). At higher $Re \gtrsim 2000$ and $0.5 \leq A \lesssim 1$, four different behaviors are observed:

1. **First elongation, then rapid decay (RaD)**: the initial helical perturbation, used to initialize the flow, first grows in length and magnitude, and then decays in less than one pulsation period (figure 5.3a). These decay events are classified as deterministic. They are different from decay events that happen (stochastically) after more than one pulsation period, which are classified in another category (3. below).

2. **Localized turbulent structures (Loc)**: the initial helical perturbation localizes in a puff, that is then modulated in length and magnitude by the pulsation and survives for long times without successfully splitting or decaying. See an example of this behaviour in figure 5.3b.

3. **Localized structures, then stochastic decay (StD)**: the initial helical perturbation localizes in structures that are modulated, in length and magnitude, by the pulsation. These structures however tend to suddenly decay after typically a short number of pulsation periods (figure 5.3c). Although here no life-time statistics are explicitly computed, these decay events happen at random times, as in pulsatile pipe flows at lower $A \leq 0.4$ [XA18] or driven with more complex waveform, §5.3. In those cases, turbulent structures decay after a random number of pulsation periods. However, different to SSPF, these decay events are more likely to happen at a particular phase of the period.

4. **Highly intermittent state (Int)**: the initial helical perturbation localizes in structures modulated by the pulsation. These structures, however, randomly split until the DNS reaches a highly intermittent state where turbulence aggregates in localized structures modulated by the pulsation and separated by laminar patches (figure 5.3d).

In this section the characteristics of these localized structures and their dependence with respect to the flow parameters will be studied.

5.2.1 Statistics of turbulent patches in pulsatile pipe flow

Here two DNS of pulsatile pipe flow at $Re = 2100$, $Wo = 11$ and either $A = 0.5$ or $A = 1$ are analyzed. In both simulations a turbulent patch remains localized and is modulated by the pulsation for long times, like in fig. 5.3b. The total time of the simulations is of $t/T \lesssim 180$ and the turbulent patches survive the whole simulation time. Phase-dependent statistics of the results are computed by splitting the pulsation period in 200 equally spaced period phases. At each time step the reference system $\hat{x}$ is changed so the upstream most part of the puff, where the axial vorticity squared is first $\langle \omega_x^2 \rangle_{r,\theta} \geq 0.1$, is located at $\hat{x} = 0$. Apart from the axial vorticity squared, the defect of center-line velocity is considered. It is defined as

$$\Delta \langle u_{x_0} \rangle_\xi = \langle u_x (r = 0, t) \rangle_\xi - U_c (t) , \tag{5.2}$$

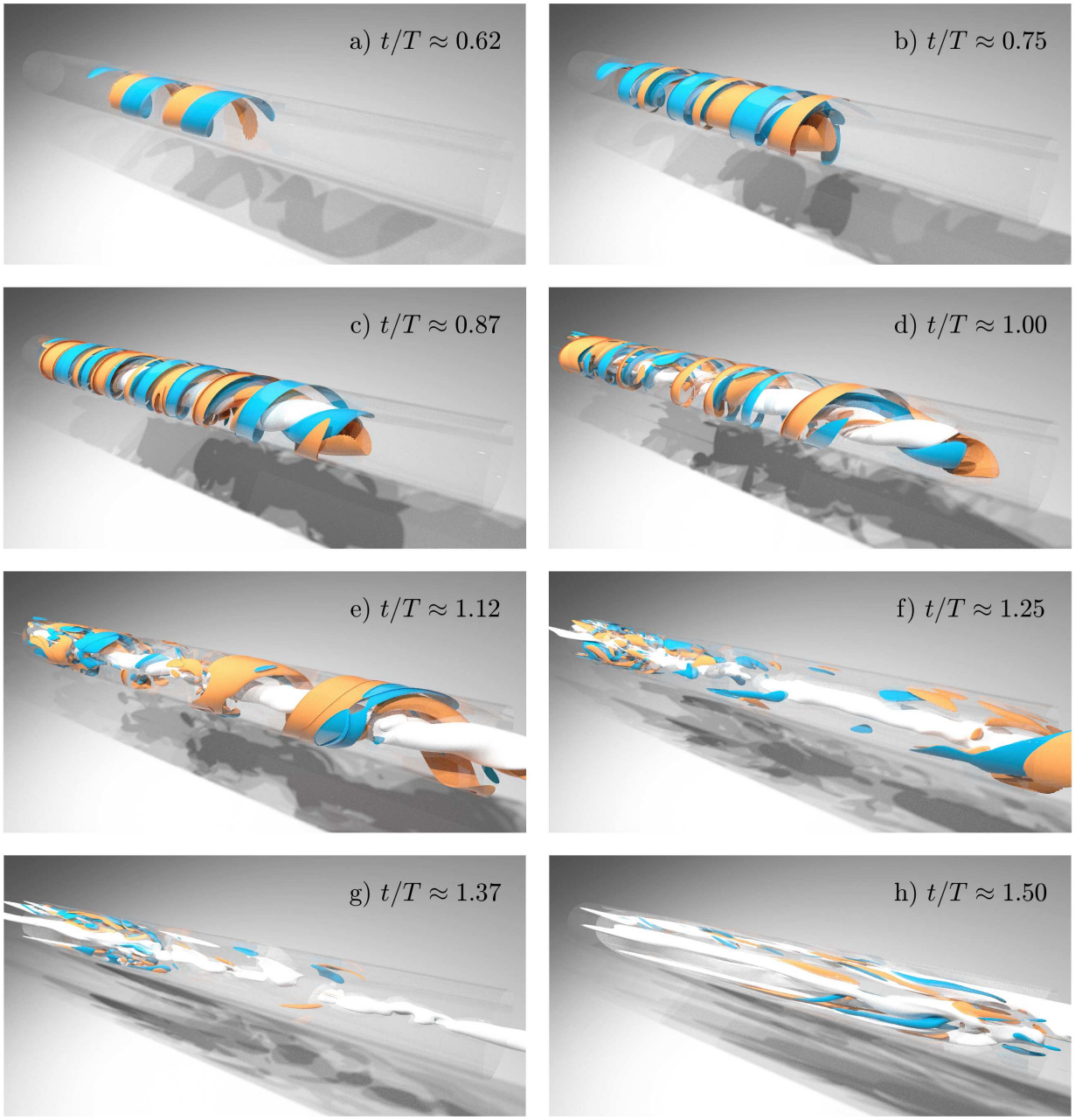

Fig. 5.2.: Evolution from a localized helical perturbation to a turbulent patch in a DNS of pulsatile pipe flow at $Re = 2400$, $Wo = 11$ and $A = 1.4$. The simulation has been initialized at $t/T = 0.5$ with the corresponding laminar U_{SW} profile, with the helical perturbation scaled to $|\boldsymbol{u}'_0| \approx 3e-2$ and localized in a $5D$ axial length. In red/blue, positive/negative axial vorticity $\omega_x = \pm 4U/D$. In grey, low axial velocity streaks $u_x - \langle u_x \rangle_{\theta,x} = -0.4U$. The images are centered with respect to the instantaneous location of the turbulent patch. The flow direction of the time-averaged bulk velocity is from left to right.

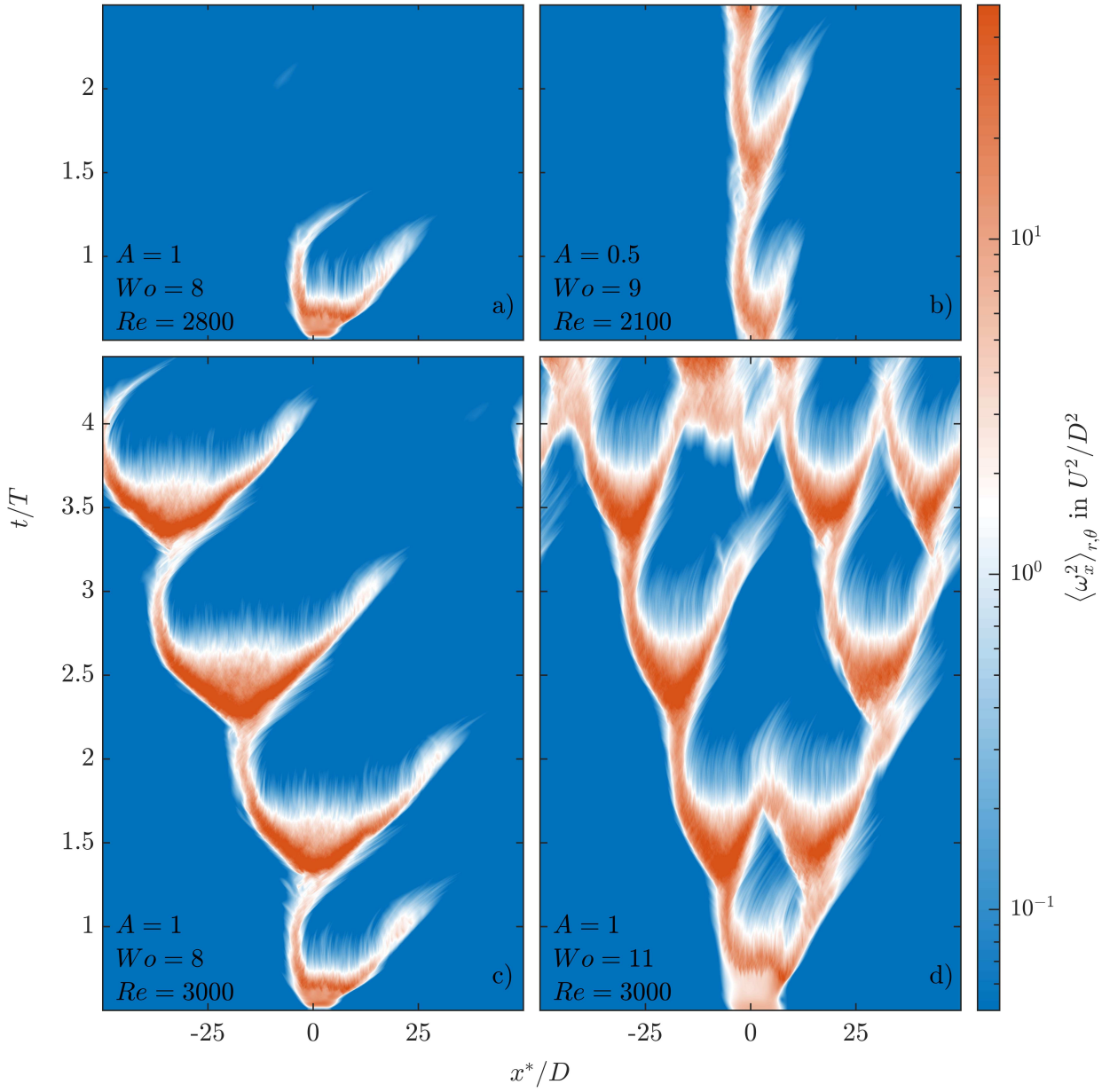

Fig. 5.3.: Space-time diagram of the cross section integral of axial vorticity squared $\langle \omega_x^2 \rangle_{r,\theta}$ of DNS in a $100D$ long pipe. The DNS are initialized with the optimal helical perturbation scaled to $|\boldsymbol{u}_0'| \approx 3e-2$ of magnitude and localized in an axial span of $5D$ [FMA21]. The diagrams are shown with respect to a moving frame x^*, moving with the bulk velocity $u_b\,(t)$. a) corresponds to $Re = 2800$, $Wo = 8$ and $A = 1$. b) corresponds to $Re = 2100$, $Wo = 9$ and $A = 0.5$. c) corresponds to $Re = 3000$, $Wo = 8$ and $A = 1$. d) corresponds to $Re = 3000$, $Wo = 11$ and $A = 1$.

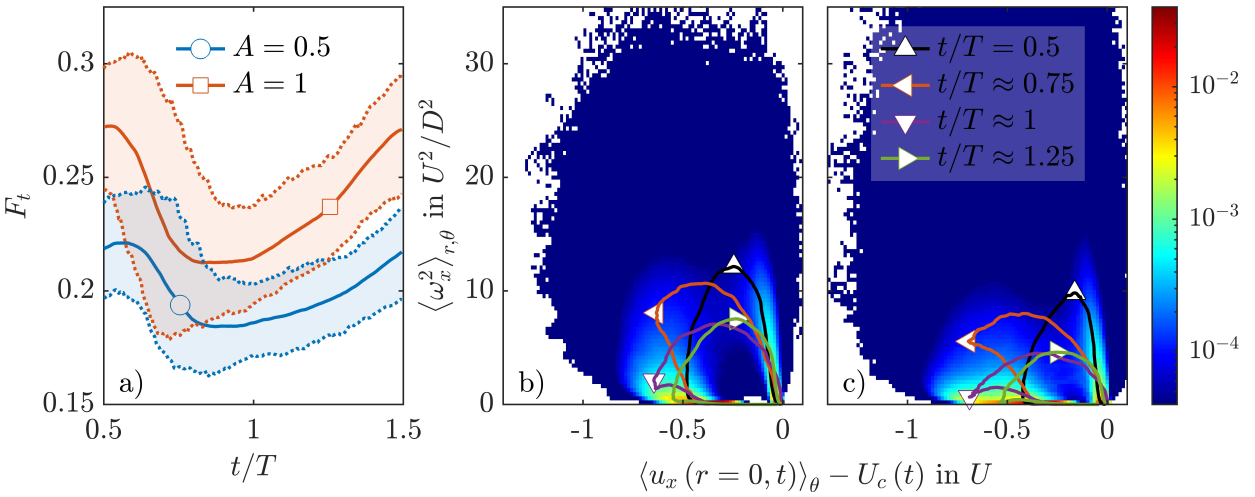

Fig. 5.4.: Statistics of turbulent patches in pulsatile pipe flow at $Re = 2100$, $Wo = 11$ and either $A = 0.5$ or $A = 1$. The results correspond to DNS in a $L_x = 100D$ long pipe initialized with the optimal perturbation scaled to $|\boldsymbol{u}_0'| \approx 3e-2$ of magnitude and localized in an axial span of $5D$ [FMA21]. a) in solid lines, the phase averaged turbulent fraction, see eq. (5.1), for $t/T \approx 180$ periods. With dotted lines find the minimum 10% and maximum 90% turbulent fraction percentiles registered in each phase of the period. b) histogram (in color) of $\langle \omega_x^2 \rangle_{r,\theta}$ versus defect of center-line velocity, see eq. (5.2), for all the simulation time at $A = 0.5$. The solid lines denote the mean $\langle \omega_x \rangle_{r,\theta}$ versus defect of center-line velocity profiles at different phases of the period. c) same as b) but at $A = 1$.

being $U_c\,(t) = U_{SW}\,(r = 0, t)$ the center-line velocity of the corresponding laminar profile. Angled brackets denote averaging with respect to ξ, being ξ any combination of spatial directions r, θ and x, as well as a fixed phase t^* of the period or time t.

In figure 5.4a phase averaged statistics of the turbulent fraction F_t are shown. Both for $A = 0.5$ and $A = 1$, the turbulent fraction is maximum at $t/T \approx 0.5$ and minimum at $t/T \approx 1$. The mean and standard deviation of turbulent fraction are higher for $A = 1$ than for $A = 0.5$ at all phases of the period.

The behaviour between $\langle \omega_x^2 \rangle_{r,\theta}$ and $\Delta \langle u_{x_0} \rangle_\theta$ in pulsatile pipe flow, see fig. 5.4b and c, and fig. 5.6, is similar to the behaviour between the cross section kinetic energy and center-line velocity in SSPF, see fig. A.2 and the works of Barkley and Song *et al.* [Bar+15; Son+17]. The presence of turbulence $\langle \omega_x^2 \rangle_{r,\theta} > 0$ disrupts the mean profile and decreases the center-line velocity $\Delta \langle u_{x_0} \rangle_\theta < 0$. The mean profiles of $\langle \omega_x^2 \rangle_{r,\theta}$ versus $\Delta \langle u_{x_0} \rangle_\theta$ look similar to those of puffs and slugs in SSPF, see fig 5.4 and 5.5. While the standard deviation of $\langle \omega_x^2 \rangle_{r,\theta}$ is higher at $A = 1$ than $A = 0.5$, both cases have a similar standard deviation of $\Delta \langle u_{x_0} \rangle_\theta$. This is also observed in the phase dependent statistics in figure 5.5.

According to the phase dependent statistics, at $t/T \approx 0.5$ turbulence reaches its highest magnitude and standard deviation, see fig. 5.5a and e and 5.6. They are both higher at $A = 1$ than at $A = 0.5$. At this phase of the period the mean $\langle \omega_x^2 \rangle_{r,\theta}$ and $\Delta \langle u_{x_0} \rangle_\theta$ profile looks similar to a turbulent puff in SSPF, see fig 5.5a and e and 5.6 compared to fig. A.2. At following phases of the period the magnitude and standard deviation of $\langle \omega_x^2 \rangle_{r,\theta}$ and $\Delta \langle u_x \rangle_{r=0,\theta}$, decrease. At $t/T \approx 0.75$ the mean $\langle \omega_x^2 \rangle_{r,\theta}$ and $\Delta \langle u_{x_0} \rangle_\theta$ profile looks similar at $A = 0.5$ to a weak slug, see fig. 5.5b, and at $A = 1$ to a strong slug, see fig. 5.5f and 5.6. At $t/T \approx 1$, turbulence intensity reaches its minimum value. At this phase of the period the mean $\langle \omega_x^2 \rangle_{r,\theta}$ and $\Delta \langle u_{x_0} \rangle_\theta$ profile looks like a decaying strong slug for

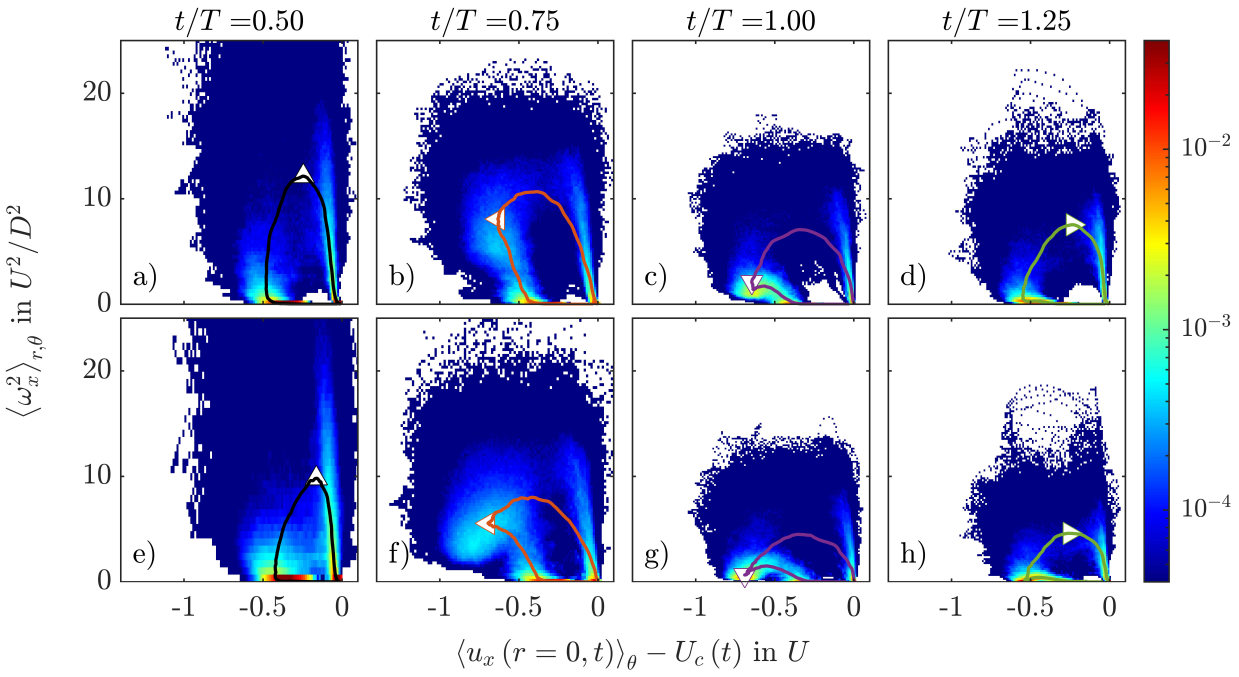

Fig. 5.5.: Histogram of $\langle\omega_x^2\rangle_{r,\theta}$ versus defect of center-line velocity, see eq. (5.2), at different phases of the period. The results correspond to DNS at $Re = 2100$, $Wo = 11$, in a $L_x = 100D$ long pipe initialized with the optimal perturbation scaled to $|\boldsymbol{u}_0'| \approx 3e-2$ of magnitude and localized in an axial span of $5D$ and with total time $t/T \approx 180$. Subplots (a,b,c,d) correspond to a DNS at $A = 0.5$; while Subplots (e,f,g,h) at $A = 1$. The phase of the period is indicated at the top of each subplot column.

both A, fig. 5.5c and g. At $t/T \approx 1.25$ the mean profile looks similar to either a puff or a strong slug of SSPF.

The localized turbulent patches observed in pulsatile pipe flow at these flow parameters, are similar to puffs and slugs of SSPF. At certain pulsation parameters, localized turbulent patches can take the form of both puffs and slugs in the duration of a single pulsation period. However these turbulent patches show unique characteristics. Firstly, they reach maximum length (F_t) and turbulence intensity at a phase of the period where their $\langle\omega_x^2\rangle_{r,\theta}$ and $\Delta\langle u_{x0}\rangle_\theta$ mean profiles look similar to a turbulent puff and not to a slug, see fig A.2. Secondly, the phase of the period at which they reach maximum turbulence intensity does not correspond to the phase of the period where the bulk velocity is maximum. In the following section this phase difference between maximum turbulence intensity and u_b is computed.

5.2.2 *Phase shift between driving and turbulence intensity*

The pulsatile bulk velocity $u_b\,(t)$ and turbulence intensity $\langle\omega_x\rangle_{r,\theta,x}\,(t)$ are harmonic functions with respect to time. See an example of these two quantities in figure 5.7. The time-averaged phase difference between the two signals, $\langle\Delta\phi\rangle_t$, is computed by projecting the time signal of $\langle\omega_x^2\rangle_{r,\theta,x}\,(t)$ to a harmonic function, and comparing its phase with the sinusoidal bulk velocity. In figure 5.8a see the resultant phase shift as an angle for all the DNS listed in tables C.1 and C.2 (Appendix C).

The phase difference between the turbulence intensity (represented by $\langle\omega_x^2\rangle_{r,\theta,x}\,(t)$) and bulk velocity is consistent with studies of small-to-moderate amplitude $A \leq 0.4$ pulsatile pipe flow [XA18], and fully turbulent pulsatile channel flows [WBH16; Liu+24]. There, they observed how the phase

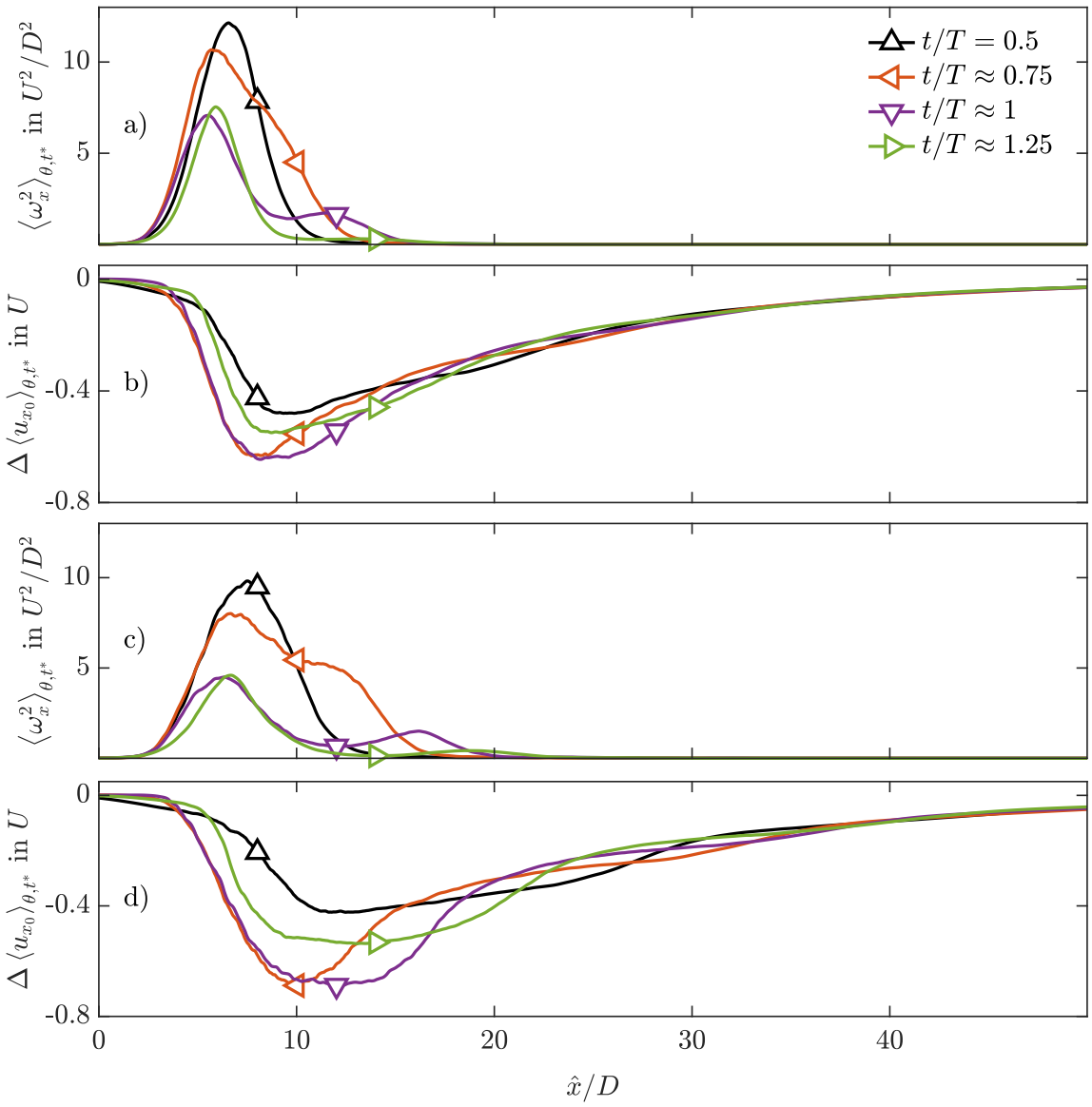

Fig. 5.6.: Phase averaged (t^*) cross section axial vorticity squared, a and c, and center-line velocity defect, b and d (see eq. (5.2)) of DNS of pulsatile pipe flow at $Re = 2100$, $Wo = 11$, $A = 0.5$, in a and b, and $A = 1$, in c and d. The results are presented with respect to a moving reference frame $\hat{x}$, such that the turbulent patch upstream front, where $\langle \omega_x^2 \rangle_{r,\theta} \geq 0.1$, always lays at $\hat{x} = 0$.

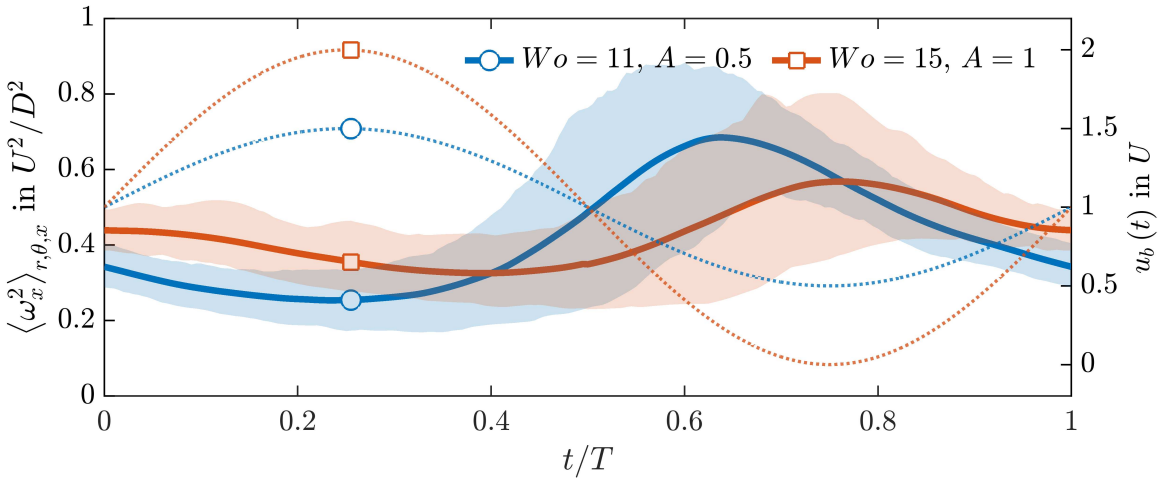

Fig. 5.7.: Time profile of $\langle \omega_x^2 \rangle_{r,\theta,x,t^*}$ (solid thick lines) compared with the bulk velocity $\bar{U}\,(t)$ (dotted lines). The shaded regions delimit the volume of data between the max/min 10% percentile of the corresponding $\langle \omega_x^2 \rangle_{r,\theta,x}\,(t^*)$ phase-dependent statistics. Blue color and circle symbols correspond to a DNS at $Re = 2100$, $Wo = 11$ and $A = 0.5$. Red color and square symbols correspond to a DNS at $Re = 2100$, $Wo = 15$ and $A = 1$.

difference increases for increasing Wo, as seen in figure 5.8a. At small $Re \approx 2100$ the phase difference saturates at $\Delta\phi \approx \frac{3\pi}{2}$. There is no apparent effect of A on $\Delta\phi$.

Note that, at high $Wo \gtrsim 20$, there is a $90°$ phase difference between the driving pressure gradient and the bulk velocity in the laminar profile [Wom55], see fig. 4.1. Thus, as the frequency increases, the turbulence intensity tends to correlate better with the driving pressure gradient, than with the bulk velocity.

5.2.3 *Front speed of localized turbulent patches*

We compute the upstream front speed c_u by tracking the upstream-most position in the turbulent patch, defined as $\langle \omega_x^2 \rangle_{r,\theta} \geq 1 \times 10^{-1}$. Since the patches tend to remain localized, for most of the cases considered here, the average upstream front speed corresponds to the averaged speed of the patch itself.

The upstream front speed, as in the case of SSPF (see fig. A.4) [Bar+15], is mainly affected by Re, see fig. 5.8b. The higher Re is, the smaller the upstream front speed becomes. According to these results, there is also a weak dependence of the front speed on the A. The upstream front speed decreases for increasing A. As Wo increases, the upstream front speed approximates the value of SSPF, as turbulence is less affected by the pulsation.

5.2.4 *Production of turbulent kinetic energy of turbulent patches*

In order to investigate the physical mechanisms by which turbulent patches survive in pulsatile pipe flow, the production of turbulent kinetic energy:

$$P_\xi = -\left\langle u_r \left(u_x - \langle u_x \rangle_\xi \right) \right\rangle_\xi \frac{\partial \langle u_x \rangle_\xi}{\partial r}, \tag{5.3}$$

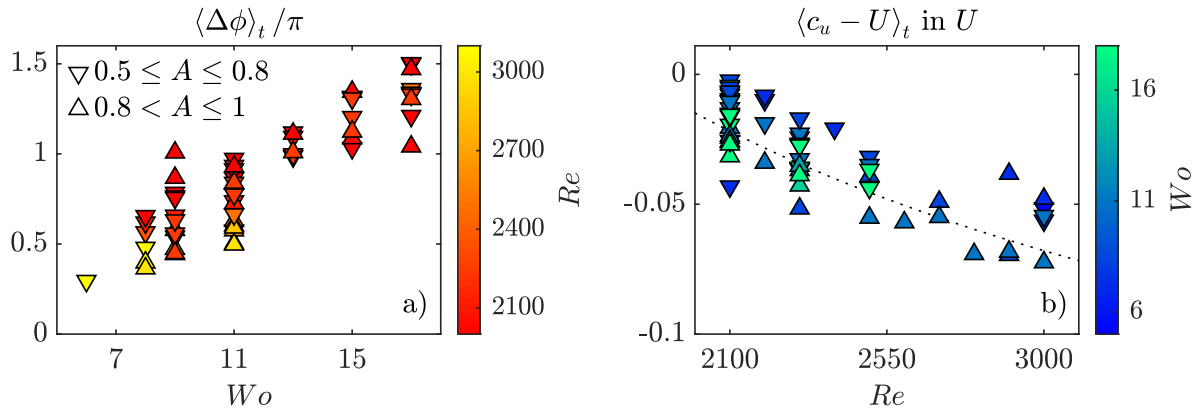

Fig. 5.8.: Effect of flow parameters on: (a) the phase difference $\Delta\phi$ between bulk velocity $\bar{U}$ and volume-averaged turbulence intensity $\langle \omega_x^2 \rangle_{r,\theta,x}(t)$; (b) upstream front speed c_u. Each marker corresponds to the time averaged value of either c_u or $\Delta\phi$ of an individual DNS of pulsatile pipe flow listed in table C.1 (and master simulations listed in table C.2). Downward (upward) pointing triangles correspond to simulations at $0.5 \leq A \leq 0.8$ ($0.8 < A \leq 1$). The face color indicates Re in subplot a) and Wo in subplot b). The dotted line in subplot b) corresponds to a fit of the upstream front speed of puffs in SSPF: $c_u - U \approx 0.28 \left[0.024 + \left(\frac{Re}{1936}\right)^{-0.528} - 1.06\right]$ in U, according to Chen *et al.* [CXS22].

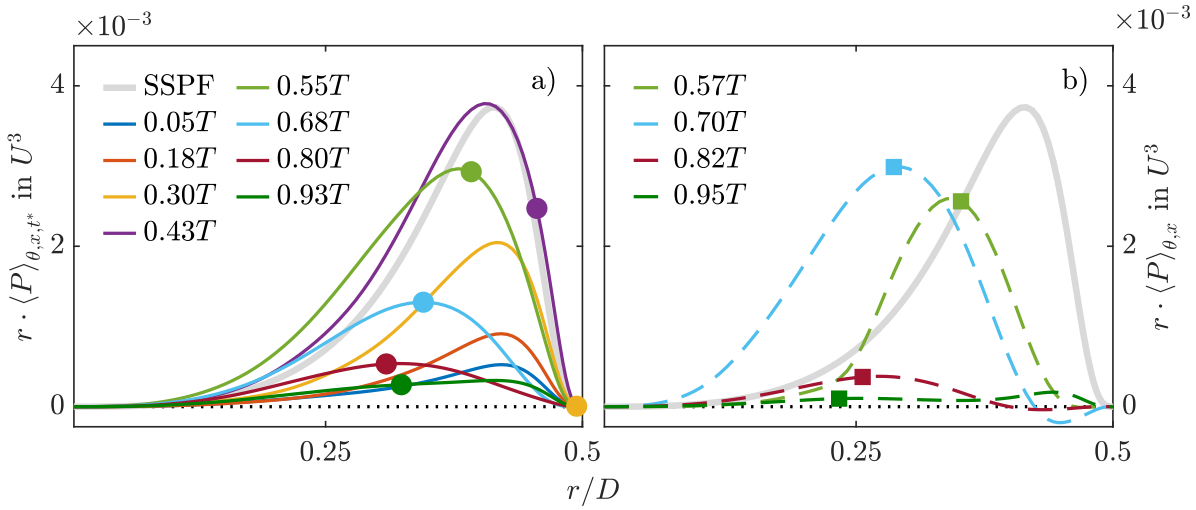

Fig. 5.9.: Production of turbulent kinetic energy at different phases of the pulsation, for two DNS of pulsatile pipe flow at $Re = 2400$ and $Wo = 8$. The simulations are performed in a $L_x = 100D$ long pipe initialized with the optimal perturbation scaled to $|\boldsymbol{u}_0'| \approx 3e-2$ of magnitude and localized in an axial span of $10D$. In a) results correspond to $A = 0.6$, and the production is averaged in the homogeneous directions and the phase of the period t^*. In b) results correspond to $A = 1$, and the production is averaged only in the homogeneous directions. Markers denote the existence and wall-normal location of inflection points in the corresponding mean profile that satisfy the Fjørtoft criterion.

is studied.

At $Re = 2400$, $Wo = 8$ and $A = 0.6$ turbulence survives for long times, as shown in fig. 5.1. In this case, peak production takes place during the early deceleration phase of the pulsation and is very similar to steady pipe flow in terms of magnitude and wall-normal distribution, see fig. 5.9a. Right after the peak in flow rate, the mean velocity profile develops an inflection point at the wall, which satisfies the Fjørtoft criterion. During the ongoing deceleration phase, the inflection point moves away from the wall and catches up with the point of peak production. Both travel together further towards the pipe center-line. Near to the minimum flow rate, the unstable inflection point loses the Fjørtoft condition and the production collapses.

At $Re = 2400$, $Wo = 8$ and $A = 1$ turbulence rapidly decays, as shown in fig. 5.1b. Here, phase averaging of turbulence production is not possible, and averaging was performed only in the homogeneous directions (θ, x), see fig. 5.9b. Again for this case, the peak production follows the movement of inflection points from the wall to the center-line of the pipe.

These results, as was first discussed in our paper [FMA21], suggest that turbulent patches take advantage of inflection points to survive the pulsation. Later in this thesis further arguments that support this hypothesis are provided.

5.3 Effect of pulsation waveform on turbulent patches

In the following section DNS results of pulsatile pipe flow driven with waveforms different from a single harmonic pulsation are discussed.

5.3.1 Generic waveform

In our paper [MFA22] we show results of DNS of pulsatile pipe flow driven with waveform whose shape we can control with the use of three parameters (see §2.1.4).

According to the TGA and LSA, the shape of the waveform has an effect on the chance of turbulence transition. Here it is checked if the waveform has an effect on turbulence behaviour and survival. Ensembles of 10 simulations of 8 different waveforms at $Re = 2000$ and $Wo = 11$ are performed. Each of the 80 simulations runs for 20 periods and is stopped if the corresponding turbulent fraction vanishes, $F_t = 0$.

Cases with smaller t_m exhibit faster growing F_t in the initial transient when compared to cases with larger t_m, see fig. 5.10. Once the perturbation has triggered turbulence at $t \gtrsim 1.5T$, the turbulent fraction remains at roughly 50%, but is clearly modulated by the pulsation in all cases. However, cases with smaller t_m reach a slightly higher turbulent fraction. Both observations are in good agreement with the stability analyses shown in Chapter 4, which predict larger energy growth for smaller t_m.

The waveform parameters have an effect on relaminarization, as shown in fig. 5.10. For large t_m only 13 out of 40 cases remain turbulent for the full 20 periods, whereas 16 out of 40 cases remain turbulent when t_m is small. Regarding the other two parameters, for large t_{dc} 17 out of 40 cases remain turbulent for the full 20 periods, whereas 12 out of 40 cases remain turbulent when t_{dc} is small. For large t_{ac} 20 out of 40 cases remain turbulent for the full 20 periods, whereas 9 out of 40 cases remain turbulent when t_{ac} is small. This suggests that both, less steep acceleration

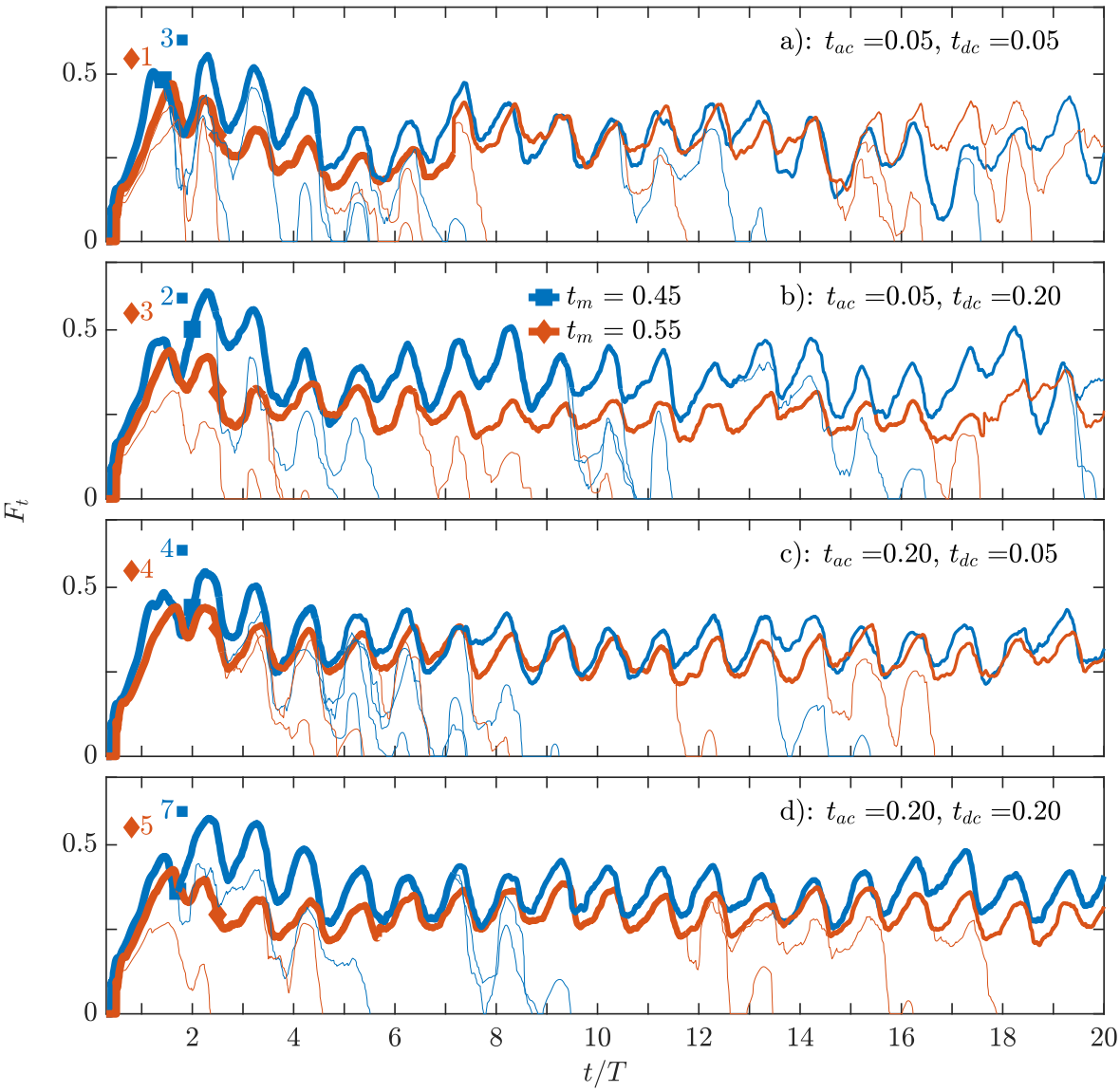

Fig. 5.10.: Turbulent fraction, see eq. (5.1), in DNS at $Re = 2000$ and $Wo = 11$. The simulations are performed in a $50D$ long pipe initialized with the helical perturbation localized in a $5D$ axial length and scaled to different initial magnitudes. Results correspond to 80 DNS: for 8 different waveform, or different t_{ac}, t_{dc} and t_m; and 10 different initial helical perturbation magnitudes in ten steps from $5e-3$ to $5e-2$. In panels find the cases with the same pair of t_{ac}, t_{dc}. The colors and symbols of the lines denote different t_m. In each panel, and for each t_m, see in a thick line the instantaneous mean turbulent fraction of the cases (out of the initial 10) that have not yet relaminarized. The thickness of the mean turbulent fraction decreases whenever one of the 10 cases relaminarizes. In thin lines, see the evolution for the cases that relaminarize at $t < 20 \cdot T$. With numbers find the number of cases where turbulence is sustained for $t \leq 20 \cdot T$.

and deceleration phases as well as long low velocity phases promote turbulence survival. Fast accelerations, on the other hand, have a strong stabilizing effect.

It is also important to mention that the decay events happen always at certain phases of the period and not in others. This was also observed for pulsatile pipe flows driven with one harmonic component, as described at the beginning of §5.2.

5.3.2 Physiological waveform

DNS of pulsatile pipe flow driven with a physiological waveform are also performed. The flow is driven at the bulk velocity measured by Bürk *et al.* [Bür+12] in the descending aorta of a young volunteer. See in fig. 4.10a the shape of this physiological waveform fitted with 8 Fourier modes. In this case two different types of DNS are performed.

DNS with a localized Force

In fig. 5.11a, b and c see DNS results of pulsatile pipe flow constantly perturbed close to the wall by a body force. The results correspond to a flow driven with a physiological waveform at $Re = 1277$ and $Wo = 12$, values typically found in the human descending aorta, see table 1.1. In the figure, one can observe the development of strong irregular flow patterns during the deceleration and low velocity phase of the pulsation. These irregular patterns develop close to the axial position of the perturbation, at the leftmost boundary of the snapshots. As time marches they detach from the perturbation, they elongate and are advected downstream by the flow. During the next deceleration phase new structures develop close to the perturbation, see fig. 5.11f, and the cycle repeats itself.

Due to the shape of the physiological waveform the structures that are developed close to perturbations on the wall tend to stay close to them as they grow in magnitude. The smaller Wo is, the shorter axial distance the structures separate from them, see figure 5.11d, e and f.

DNS with IC SWOP

Other DNS of pulsatile pipe flow driven with a physiological waveform are initialized with the optimal helical perturbation scaled and localized in a section of the pipe. In this DNS, like for the case of a single harmonic pulsation, the helix grows in length and in magnitude, saturates and triggers irregular flow patterns in the flow that survive one or more pulsation periods, depending on the flow parameters. These irregular flow patterns exert additional shear stresses:

$$\Delta\boldsymbol{\tau} = \boldsymbol{\tau} - \tau_{SW}\boldsymbol{e}_x \tag{5.4}$$

at the wall, as shown in figure 5.12. Here

$$\boldsymbol{\tau} = (0, \tau_\theta, \tau_x)\,, \tag{5.5}$$

are the shear stresses in the DNS, τ_{SW} the shear stresses of the laminar profile and $pmbe_x$ the unitary vector in the axial direction.

The results show that, even at low $Re = 1277$, pulsatile pipe flows driven with physiological waveforms, are highly susceptible to the onset of irregular flow patterns. When the flow is constantly perturbed by geometric defects close to the wall, see fig. 5.11, these irregular flow patterns will be triggered at each pulsation period. They will exert additional shear stresses in the walls, as shown in fig. 5.12, that could lead to further wall injuries or even diseases in cardiovascular vessels.

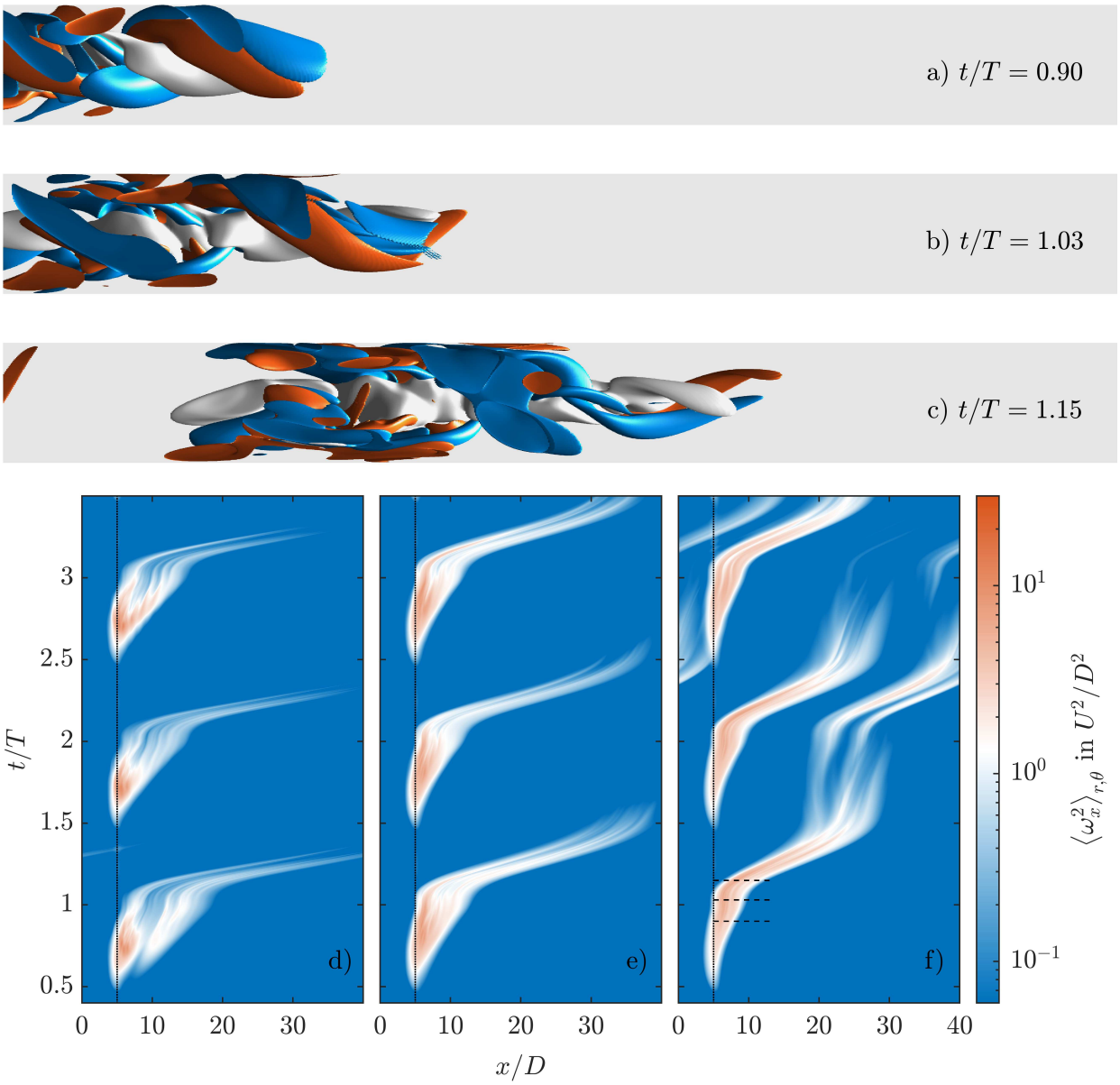

Fig. 5.11.: In a, b and c, development of irregular flow patterns in DNS of pulsatile pipe flow driven with a physiological waveform at $Re = 1277$ and $Wo = 12$. The flow is constantly perturbed by a body force close to the wall. The flow direction is from left to right and the snapshots show a $10D$ section of the pipe downstream the position of the perturbation. It is shown in red $\omega_x \approx 3U/D$, in blue $\omega_x \approx -3U/D$ and in grey low speed axial velocity streaks with $u_x - \langle u_x \rangle_{\theta,x} = -0.3 \cdot U$. In d, e, f space-time diagram of the cross section integral of axial vorticity squared. The results correspond to DNS in a $40D$ long pipe at $Re = 1277$ permanently disturbed by a body force. In d) at $Wo = 8$. In e) at $Wo = 10$. In f) at $Wo = 12$. The vertical dotted line represents the location of the geometric center of the body force. The dashed lines correspond to the position and time of the snapshots shown in a,b and c.

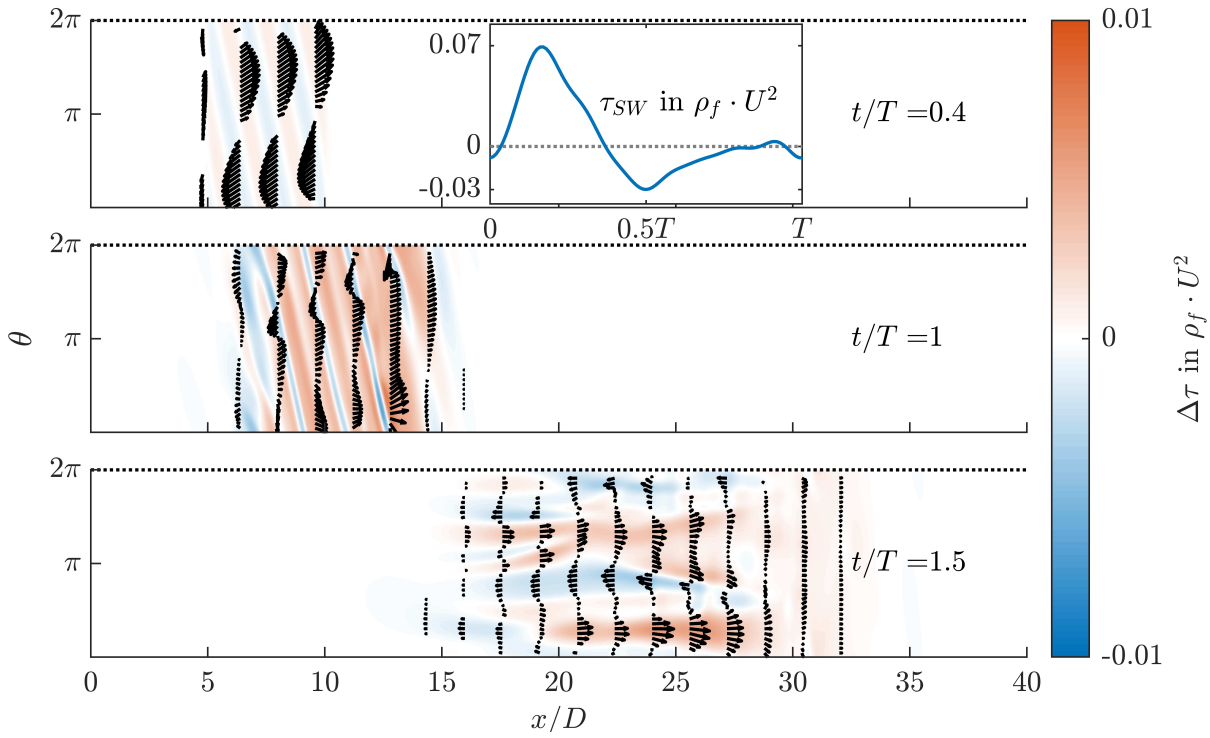

Fig. 5.12.: Additional shear stresses at the wall for a pulsatile pipe flow driven with a physiological waveform at $Re = 1277$ and $Wo = 12$ at different phases of the period. The results correspond to a DNS in a $40D$ long pipe, initialized with the corresponding laminar profile U_{SW} and the optimal helical perturbation localized in a $5D$ axial length and scaled to $|\boldsymbol{u}_0'| \approx 3e-2$ in magnitude. The arrows indicate the direction of the additional shear stresses $\Delta\boldsymbol{\tau} = \boldsymbol{\tau} - \tau_{SW}\boldsymbol{e}_x$ and the colors the difference between the shear stresses in the DNS and the laminar flow $\Delta\tau = |\vec{\tau}| - \tau_{SW}$. In the top panel see the shear stresses of the laminar U_{SW} profile with respect to time.

5.4 Summary of the chapter

In this chapter, DNS results of pulsatile pipe flow at different flow parameters were described. The parameter space has $A \geq 0.5$, and $Re \approx \mathcal{O}(10^3)$, with $Re_{\max} = (1 + A)\, Re$ in the range of $2500 \lesssim Re_{\max} \lesssim 6000$ and intermediate frequencies $6 \lesssim Wo \lesssim 20$, and different pulsation waveforms. It has been shown how turbulence can be triggered using different methods in DNS. Once turbulence is triggered its behaviour is determined by the combination of Re, Wo and A. It can either behave quasi-steadily, unaffected by the pulsation, or appear in the form of localized turbulent patches, that are heavily modulated by the pulsation. These turbulent patches are the main focus of the rest of the chapter. At the flow parameters considered here, the turbulent patches are similar to the puffs and slugs observed in SSPF. Preliminary results suggest that they actively make use of the inflection points in the quiescent laminar profile to survive the pulsation. Finally, the results of pulsatile pipe flows driven with custom and physiological waveforms are described. It is shown that, even at low $Re = 1277$ pulsatile pipe flows driven with a physiological waveform are susceptible to the trigger of irregular flow patterns that can last for more than a pulsation period. This irregular flow patterns exert additional shear stresses on the pipe walls that, in a more realistic scenario, could potentially lead to injuries or even diseases in cardiovascular flows.

6 Causal analysis of puffs in pulsatile pipe flow

A hypothesis made in Chapter 5, is that, as in SSPF, [Bar+15; Son+17; CXS22], the behavior of puffs in pulsatile pipe flow is determined by the shape of the axial velocity profile $\langle u_x \rangle_\theta (x = x_u, r, t)$ at the upstream front $x = x_u$ of the puff. In the ideal case of an extremely long pipe, and a single localized turbulent puff, the mean profile in the pipe $\langle u_x \rangle_{\theta,x} (r, t)$ approximates this profile. The idea is that puffs take advantage of two characteristics of the mean (upstream) velocity profile. One is the mean shear, as in SSPF, that, for the pulsatile case, is time-dependent. The other is the instability of the SW profile, that is linked with the presence of inflection points.

While the mean shear is related to the transient growth of stream-wise constant perturbations, like in SSPF; inflection points are related with the helical perturbation extensively explained in Chapter 4. In the previous Chapter 5 it was argued that inflection points may have an effect on turbulence once it has been triggered. However, this was not rigorously demonstrated.

In this chapter, a causal analysis is developed and performed precisely to do that. The goal is to separate the two mechanisms: the effect of the inflection points from the effect of the time varying mean shear. Inspired by the ideas of Tuerke *et al.* [TJ13], DNS are performed with an imposed time varying artificial mean profile without inflection points. The transient growth of perturbations on top of these artificial profiles are studied. Then, the behaviour of puffs in DNS with artificial mean profiles without inflection points are studied.

6.1 Methods

Following Vela-Martín [VM21], and references therein, for different combinations of Re, Wo and A, pairs of DNS that run parallel to each other are performed. Each pair of simulations is initialized with the same localized turbulent patch, and while one of them is a full DNS of pulsatile pipe flow that runs independently of the other, known as the master; the second DNS, known as the slave, uses the information of the master to modify some of its characteristics. While in Vela-Martín [VM21] the slave copies some small scales of the master, here the slave simulation uses the instantaneous mean profile of the master $U_M = \langle u_x \rangle_{\theta,x} (r, t)$ to generate its instantaneous mean profile $U_S (r, t)$.

The artificial profiles $U_S (r, t)$ are designed according to a series of constraints. In this section, first these requirements are described, followed by the methods by which the $U_S (r, t)$ profiles are generated. Finally the changes to numerical methods to compute and also impose the artificial profiles in DNS are shortly described.

6.1.1 Requirements of the slave mean profile

Four requirements are enforced to the instantaneous U_S. Firstly, they must comply with the no-slip boundary condition and vanish at the wall:

$$U_S\left(r=R,t\right)=0. \tag{6.1}$$

Secondly, the bulk velocity u_{b_S} of the profile,

$$u_{b_S}\left(t\right)=\frac{2}{R^2}\int_0^R U_S r\mathrm{d}r, \tag{6.2}$$

must be time dependent, and it is set equal to:

$$u_{b_S}\left(t\right)=\sqrt{\frac{3E_L\left(t\right)}{2}}, \tag{6.3}$$

being:

$$E_L\left(t\right)=\frac{1}{\pi R^2}\int_0^{2\pi}\int_0^R \frac{1}{2}U_{SW}^2 r\mathrm{d}r\mathrm{d}\theta, \tag{6.4}$$

the kinetic energy of the laminar pulsatile pipe flow $U_{SW}\left(r,t\right)$. With this condition one ensures that the energy of the profile is equal or smaller than the corresponding laminar U_{SW} profile. Thirdly, the average shear:

$$S=\frac{2}{R^2}\int_0^R \frac{1}{2}\left(\frac{\partial U_S}{\partial r}\right)^2 r\mathrm{d}r, \tag{6.5}$$

of the profile must be minimum. Given conditions (6.1) and (6.3), by minimizing S, one obtains profiles whose shear monotonically decreases from the wall to the center-line of the pipe.

The parabolic profile:

$$U_{S_0}\left(r,t\right)=2u_{b_S}\left(t\right)\left(1-\left(\frac{r}{R}\right)^2\right), \tag{6.6}$$

whose energy is exactly $E_L\left(t\right)$, complies with these three initial requirements. For $R=1$, and dropping the time dependence of u_{b_S} and E_L, one finds:

$$\int_0^1 U_{S_0}^2 r\mathrm{d}r=4u_{b_S}^2\int_0^1\left(1-r^2\right)^2 r\mathrm{d}r=4u_{b_S}^2\left[\frac{r^2}{2}-\frac{2r^4}{4}+\frac{r^6}{6}\right]_0^1=\frac{4u_{b_S}^2}{6}=E_L. \tag{6.7}$$

The profile U_{S_0} does not have the same bulk velocity as the corresponding laminar pulsatile pipe flow $u_b\left(t\right)$. As it is shown in Appendix D, for the parameters considered here, this error is relatively small.

As a final requirement, the slave mean profile must have the same energy as the master profile:

$$\frac{2}{R^2}\int_0^R \frac{1}{2}U_S^2 r\mathrm{d}r=E_M\left(t\right)=\frac{2}{R^2}\int_0^R \frac{1}{2}\left\langle u_x\right\rangle_{\theta,x}^2 r\mathrm{d}r. \tag{6.8}$$

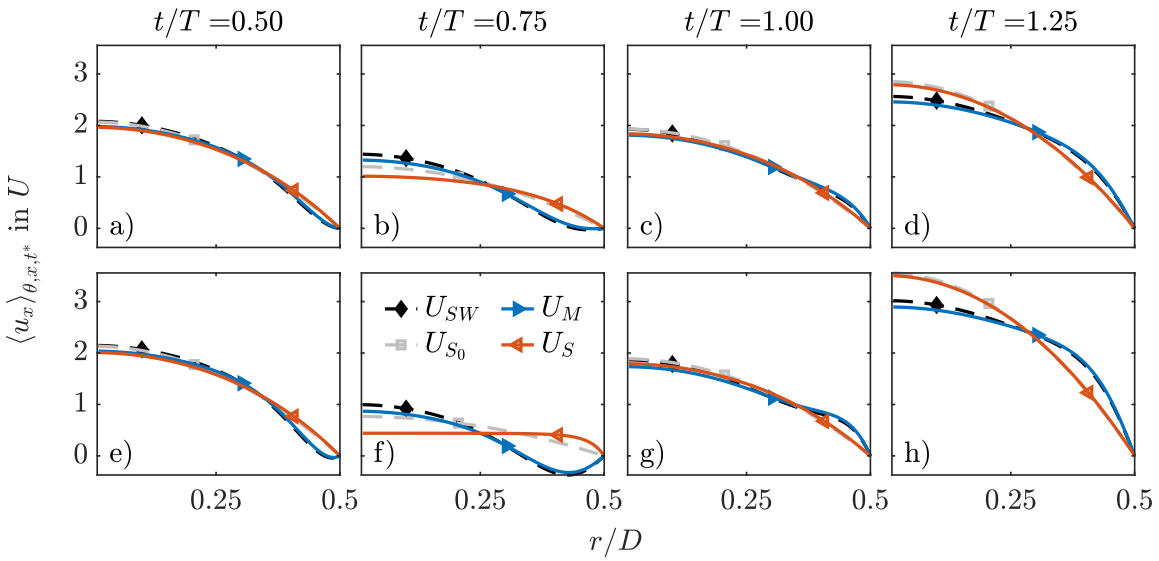

Fig. 6.1.: Phase (ϕ) averaged mean profiles of master (M) and slave (S) simulations at $Re = 2100$, $Wo = 11$, $A = 0.5$ (a,b,c,d) and $A = 0.9$ (e,f,g,h). The phase of the period is indicated at the top of each subplot column.

If $E_M \equiv E_L$, the flow in the master simulation is laminar, $U_S \equiv U_{S_0}$, and the energy of the slave mean profile will be maximum. Otherwise $E_M < E_L$ and, as it is shown in fig. 6.1, the resultant U_S is blunted. A blunted mean profile is related with a decrease in turbulence production as described by Kühnen *et al.* [Küh+18] and a reduced transient growth of perturbations.

The four conditions (6.1), (6.3), (6.5) and (6.8) define the artificial profiles. In what follows it is shown how the profiles are actually computed.

6.1.2 *Method of small variations*

Conditions (6.3)–(6.8) can be mathematically written in a functional:

$$\mathcal{S} = 2\int_0^R \mathcal{L}\left(r, U_S, U_S'\right) \mathrm{d}r, \tag{6.9}$$

to be minimized, being $U_S' = \frac{\partial U_S}{\partial r}$,

$$\mathcal{L} = \frac{1}{2}U_S'^2 r + \lambda_L\left(U_S r - \frac{u_{b_S}}{2R}\right) + \mu_L\left(\frac{1}{2}U_S^2 r - \frac{E_M}{2R}\right) \tag{6.10}$$

the Lagrangian, and λ_L and μ_L two Lagrange multipliers. In what follows, the time dependence of u_{b_S}, E_M, U_S and therefore $\mathcal{L}$, λ_L and μ_L in the notation are dropped for clarity. As part of his Bachelor thesis José Cela París, see Appendix G, derived an equation to obtain the profile U_S from the optimization of the Lagrangian $\mathcal{L}$. His derivation is reproduced below.

From the method of small variations, one can find the function U_S that minimizes $\mathcal{L}$ by solving the Euler-Lagrange equation:

$$\frac{\partial \mathcal{L}}{\partial U_S} - \frac{\partial}{\partial r}\frac{\partial \mathcal{L}}{\partial U_S'} = 0. \tag{6.11}$$

In this case, one finds:

$$\lambda_L r + \mu_L U_S r - \frac{\partial}{\partial r}\left(r U_S'\right) = 0, \tag{6.12}$$

that, after rearranging, results in the partial differential equation:

$$\frac{\partial^2 U_S}{\partial r^2} + \frac{1}{r}\frac{\partial U_S}{\partial r} - \mu_L U_S = \lambda_L, \tag{6.13}$$

with the boundary condition (6.1):

$$U_S\left(r = R\right) = 0. \tag{6.14}$$

The homogeneous part of equation (6.13) can be turned into a modified Bessel's equation of order 0:

$$r^2\frac{\partial^2 U_S}{\partial r^2} + r\frac{\partial U_S}{\partial r} - \mu_L U_S r^2 = 0, \tag{6.15}$$

being the modified Bessel's equation of order ν_B:

$$x^2 y'' + xy' - \left(a^2 x^2 + \nu_B^2\right) y = 0, \tag{6.16}$$

with solution

$$y\left(x\right) = AI_{\nu_B}\left(ax\right) + BK_{\nu_B}\left(ax\right). \tag{6.17}$$

Here I_{ν_B} and K_{ν_B} are the modified Bessel functions of order ν_B, of the first and second kind, and A and B integration constants. After comparing equation (6.15) with (6.17), $a = \sqrt{\mu_L}$ and $\nu_B = 0$. The solution is written as:

$$U_S = AI_0\left(\sqrt{\mu_L}r\right) + BK_0\left(\sqrt{\mu_L}r\right). \tag{6.18}$$

Since K_0 diverges at $r = 0$, $B = 0$. Regarding the particular solution, the constant $U_S = C$:

$$-\mu_L C = \lambda_L \rightarrow C = -\frac{\lambda_L}{\mu_L}, \tag{6.19}$$

is tried, yielding

$$U_S = AI_0\left(\sqrt{\mu_L}r\right) - \frac{\lambda_L}{\mu_L}. \tag{6.20}$$

One can determine the constant A from the boundary condition, at $r = R \equiv 1$, and find:

$$U_S = \frac{\lambda_L}{\mu_L}\left(\frac{I_0\left(\sqrt{\mu_L}r\right)}{I_0\left(\sqrt{\mu_L}\right)} - 1\right). \tag{6.21}$$

The two Lagrangian multipliers in equation (6.21) must be tuned so the slave profile complies with conditions (6.3):

$$2\int_0^1 U_S r\mathrm{d}r = u_{b_S} = \sqrt{\frac{3E_L}{2}}, \tag{6.22}$$

and (6.8):

$$2\int_0^1 \frac{1}{2}U_S^2 r\mathrm{d}r = E_M. \tag{6.23}$$

A Newton-Raphson method is used at each time step, to find the values of λ_L and μ_L that comply with the desired instantaneous u_{b_S} and E_M. In the event of $E_M \equiv E_L$ one recovers from equation (6.21), $U_S \equiv U_{S_0}$, the parabolic profile. See in figure 6.1 the instantaneous U_S, U_{S_0} and corresponding U_M, U_{SW} profiles at $Re = 2100$, $Wo = 11$, $A = 0.5$ and $A = 0.9$ computed using this method. The artificial profiles are also time dependent but, while U_M and U_{SW} have inflection points for some phases of the period, in U_S and U_{S_0} there are none.

6.1.3 Numerical methods

Here pairs of master-slave DNS of pulsatile pipe flows at different Re, Wo and A are performed. Find in Appendix C all the simulations performed here, and their corresponding grid. Each pair of simulations are initialized with the same velocity field with a localized turbulent puff of a previous master DNS. In order to initialize each pair of simulations, a previously computed case, with a similar Re, Wo and A is used.

In order to integrate simultaneously the master and slave simulations, a new version of the new `GPU-nsPipe` (see §2.5.2) code was developed. The code performs the following sub-steps during each time step:

1. The master simulation is integrated one time step.
2. Using the instantaneous mean profile $U_M = \langle u_x \rangle_{\theta,x}$ of the master, it computes the instantaneous energy E_M, see eq. (6.8). In the pseudo-spectral code, $U_M = \langle u_x \rangle_{\theta,x}$, corresponds to the $(0,0)$ Fourier mode of the axial velocity.
3. Using the corresponding laminar pulsatile pipe flow kinetic energy E_L it computes the desired u_{b_S}, see eq. (6.3).
4. It uses a Newton-Raphson method to compute the U_S profile, eq. (6.21), that complies with the desired u_{b_S} and E_M.
5. It overwrites the mean profile of the slave simulation and imposes U_S instead. (In the code, it overwrites the $(0,0)$ Fourier mode of the axial velocity of the slave simulation.)
6. It integrates one time step the slave simulation, ignoring the evolution of its mean profile.

The pipe length

The artificial profiles U_S will highly depend on the selected length of the pipe L_x. For an infinitely long pipe $L_x \to \infty$, with a single localized turbulent puff, the mean profile of the master simulation will tend to the laminar profile $\langle u_x \rangle_{\theta,x} \to U_{SW}$. This means that the energy of the mean profile $E_M \to E_L$ and therefore $U_S \to U_{S_0}$. The Newton-Raphson method works better as long as $E_M \approx E_L$.

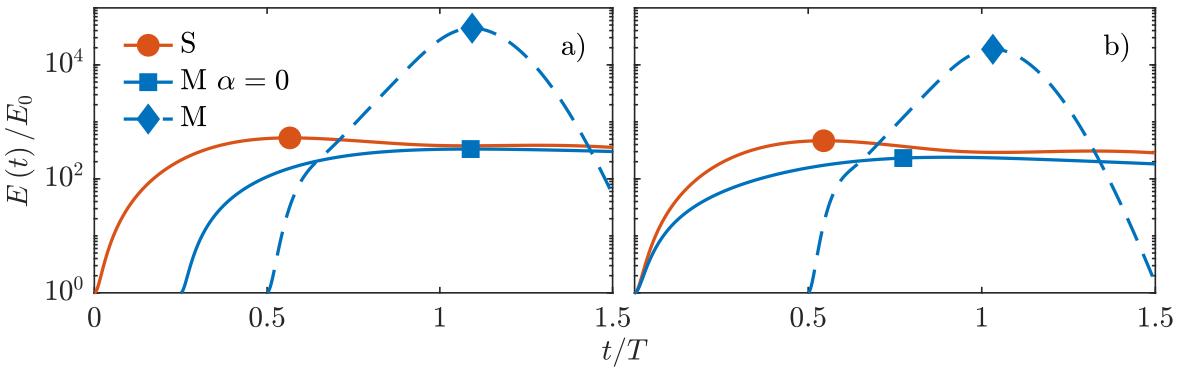

Fig. 6.2.: Energy growth of perturbations on top of master (M) and slave (S) profiles at $Re = 2100$, $A = 0.9$ and $Wo = 11$ according to TGA. Line styles correspond to different perturbations: solid and red, to the optimal perturbation on top of the slave (S) profile; solid and blue to the optimal streamwise-constant perturbation with $\alpha = 0$ on top of the master (M) profile; dashed to the optimal perturbation on top of the master (M) profile for any perturbation shape. In a) for the case of laminar pipe flow, where the master mean profile corresponds to U_{SW} and the slave to U_{S_0}. In b) for master-slave DNS in a $L_x = 100D$ long pipe using the phase averaged mean profiles of master and slave respectively.

However the computational cost increases as the length of the pipe increases. A good compromise is found, by setting a length of $L_x = 100D$.

6.2 Transient growth analysis of the laminar slave profiles

In this section the transient growth of perturbations on top of the slave mean profiles when $E_M \equiv E_L$ and $U_S = U_{S_0}$, eq. (6.6), is assessed. The analysis considers the parametric regime $Re \geq 2100$, $8 < Wo < 20$ and $0 < A < 1$. Find the instantaneous U_{S_0} profiles of two combinations of Re, Wo and A, at several phases in the period in figure 6.1. Find the U_{S_0} profiles for additional Re, Wo and A in Appendix D.

The maximum transient growth of perturbations on top of different $U_{S_0}(r,t)$ profiles using the methods described in Chapter 3 [MFA22; XSA21] have been computed. The analysis is limited to two particular types of perturbations: stream-wise constant perturbations with axial $\alpha = 0$ and azimuthal $m = 1$ wavenumbers; and helical perturbations with $\alpha > 0$ and $m = 1$. Here, the radial shape of the optimal perturbations is not shown, as the main interest is to check whether the slave profiles are highly susceptible to the growth of helical perturbations with $\alpha > 0$ and $m = 1$ or not. The optimal time where to trigger the perturbations, which is always around $t_0 \approx T/2$, and when the perturbations reach the highest G, t_f, are also not analyzed. The energy growth corresponds to the maximum G observed during one pulsation period after t_0.

In figure 6.2a the maximum transient growth of any perturbation on top of U_{S_0} (red solid lines) and perturbations with with $\alpha = 0$ and $m = 1$ on top of the U_{SW} profiles (blue solid lines) are compared. It turns out that, for all the parameters considered here, in the case of the slave profiles, the perturbations that attain a highest energy growth have $\alpha = 0$ and $m = 1$. These perturbations grow due to non-modal mechanisms, and their transient growth scales algebraically with Re. They behave the same way as the optimal perturbation to trigger turbulence in SSPF, and they are solely

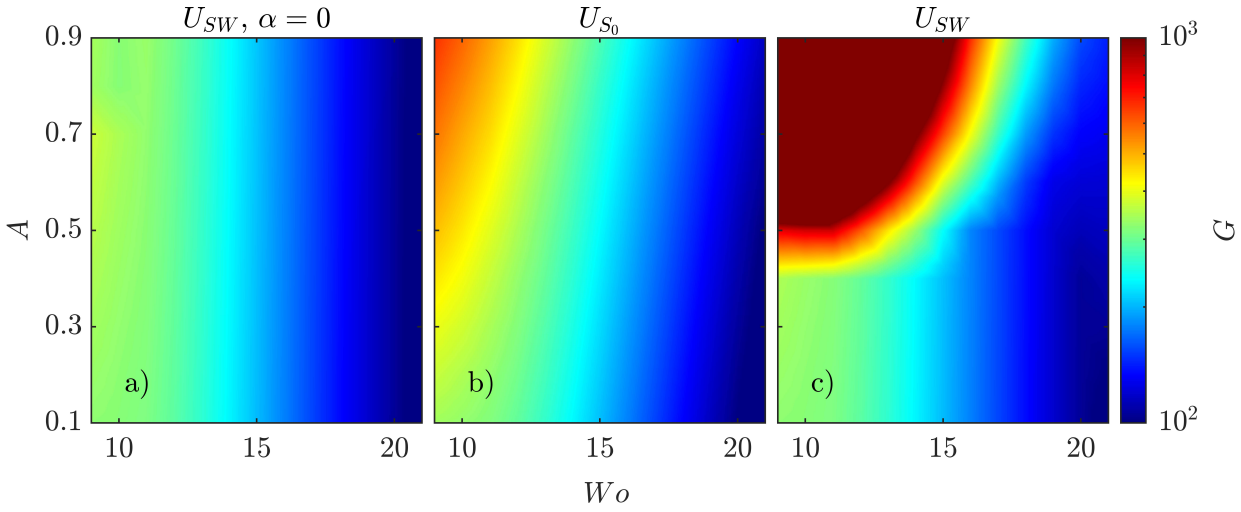

Fig. 6.3.: Maximum transient growth of perturbations on top of master U_{SW} and slave U_{S_0} laminar profiles at $Re = 2100$ and different Wo and A. In a), the maximum energy growth of perturbations with $\alpha = 0$ on top of U_{SW} profiles. In b) the maximum energy growth of any perturbation $\alpha \geq 0$ on top of U_{S_0} profiles. In c) the maximum energy growth of any perturbation $\alpha \geq 0$ on top of U_{S_0} profiles. The maximum growth G is capped to $G \leq 1e3$ in the figure for clarity.

related with the mean shear and not with the existence of inflection points. The transient growth of perturbations with $\alpha = 0$, on top of the U_{S_0} and U_{SW} profiles are almost identical, as seen in fig. 6.2a.

In figure 6.2a see also the maximum transient growth of perturbations with $\alpha > 0$ and $m = 1$ on top of the U_{SW} profile at $Re = 2100$, $Wo = 11$ and $A = 0.9$. As shown in Chapter 4, at certain $A \gtrsim 0.3$ and Wo, the laminar U_{SW} profile is susceptible to the growth of helical perturbations. This growth is related with the existence of inflection points in the U_{SW} profile, as extensively discussed in Chapter 4 and can be much higher than the growth of stream-wise constant perturbations.

In figure 6.3 the maximum transient growth of perturbations in a bigger parametric space is shown. The parameter regimes where the growth of helical perturbations ($\alpha > 0$ and $m = 1$) is higher than the growth of stream-wise constant perturbations ($\alpha = 0$ and $m = 1$) on top of U_{SW} profiles can be clearly identified, see fig. 6.3a and c. Note that in the figure the actual growth G is capped to a maximum of $G \leq 1e3$ for clarity. The growth of stream-wise constant perturbations in the U_{SW} and U_{S_0} profiles are almost identical for all the parameters considered here, except at high $A \gtrsim 0.3$. At these A, perturbations in the artificial profiles are able to grow slightly more than in the corresponding U_{SW} profiles. For all the U_{S_0} profiles considered here, the energy growth of stream-wise constant perturbations with $\alpha = 0$ is always bigger than the energy growth of helical perturbations with $\alpha > 0$. As expected, profiles without inflection points are not susceptible to the outstanding growth of helical perturbations.

6.3 Master and slave DNS

In this section the results of pairs of master–slave simulations listed in table C.2 are presented. First, the results of statistically steady pipe flow (SSPF) at $Re = 2100$ are described, and then of master-slave simulations at different Re, Wo and A.

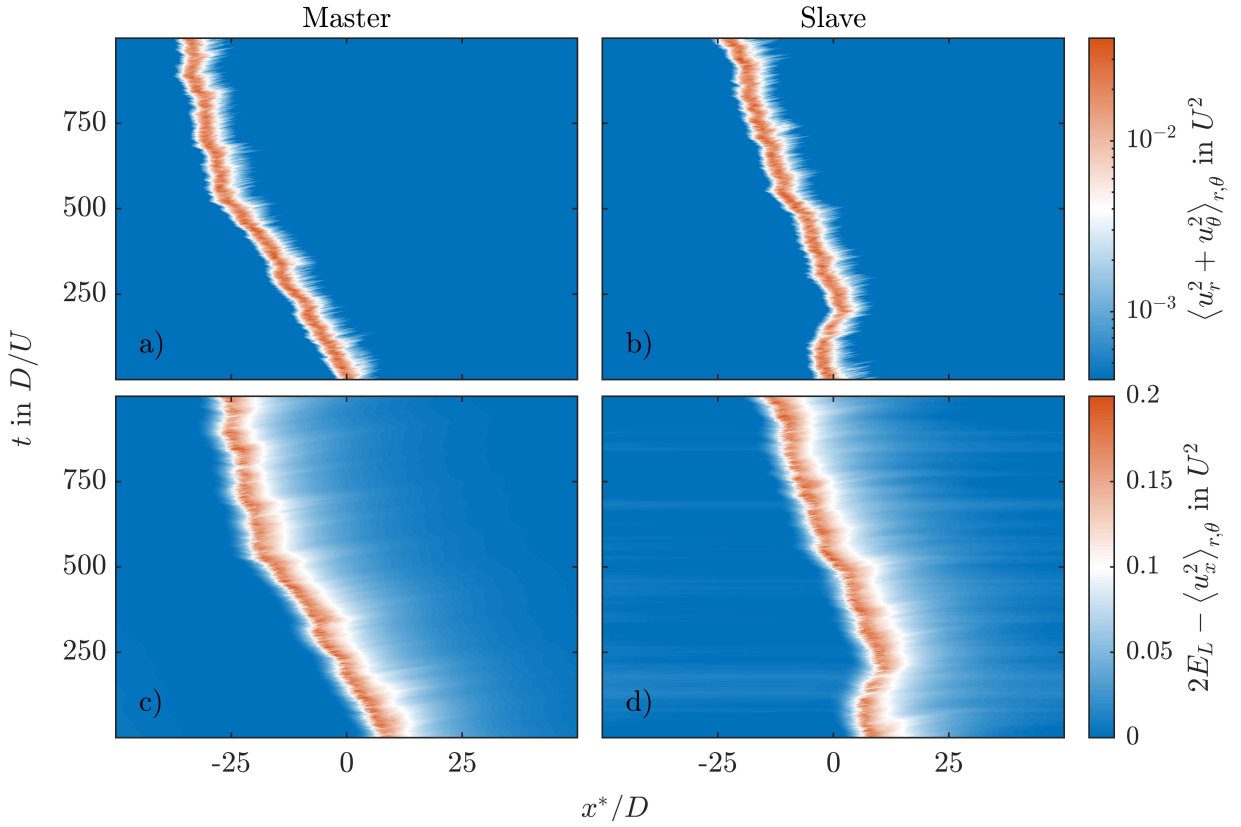

Fig. 6.4.: Space-time diagram of the cross section integral of cross section kinetic energy (a,b), and deficit of stream-wise kinetic energy, compared with the laminar kinetic energy E_L (c,d). The results correspond to a pair of master-slave DNS in a $L_x = 100D$ long pipe at $Re = 2100$ and $A = 0$, initialized with a localized turbulent puff. The results are plotted with respect to a moving reference frame, moving at the bulk velocity $u_b = U$. In a) and c) for the master simulation, in b) and d) for the slave simulation.

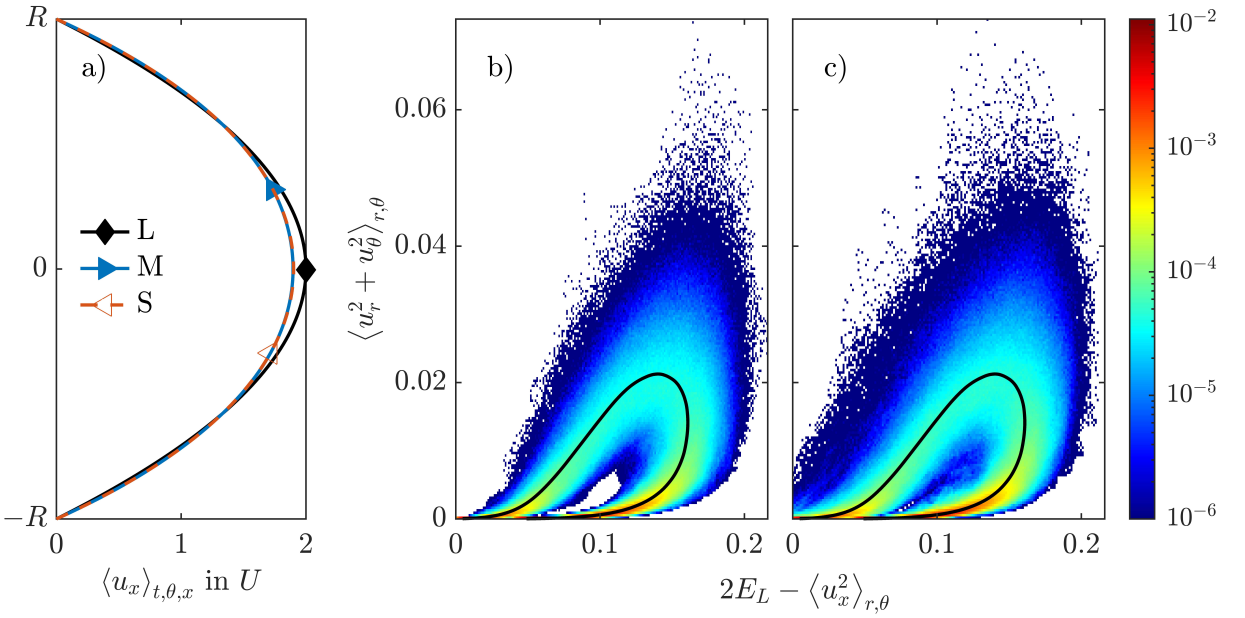

Fig. 6.5.: Comparison between master and slave SSPF DNS in a $L_x = 100D$ long pipe at $Re = 2100$. In a) the mean profile of the master (M), slave (S) and laminar (L) cases. In b) histogram of the cross section integral of cross-section kinetic energy, and stream-wise kinetic energy compared with the laminar kinetic energy E_L for the master simulation. In a black line find the mean cross-section vs stream-wise kinetic energy profile. In c), same as b), but for the slave simulation.

6.3.1 Master-slave simulations of SSPF

In the case of SSPF at $Re = 2100$, as shown in figure 6.4, there are no qualitative differences between the cross-section averaged cross-section kinetic energy of the master and slave simulations. The puffs even share almost identical upstream and downstream front speeds. For this pair of simulations the statistics of axial and cross section kinetic energies are compared. In both simulations, both energies are bounded by similar maximum and minimum values, and even share an almost identical mean behaviour, see fig. 6.5b and c.

These results show that, as long as turbulent puffs remain localized, and the mean profile of the master simulation remains similar to a parabolic profile, see fig. 6.5a, the behaviour of turbulence in the master and slave simulations is almost identical. Moreover, no additional or spurious dynamics are introduced in the slave simulations after artificially imposing the slave profiles.

6.3.2 Master-slave simulations of pulsatile pipe flow

Here pairs of master-slave simulations of pulsatile pipe flow at different Re, Wo and $A > 0$, are analyzed. For all the cases considered here, turbulence remains localized and modulated by the flow in the master DNS, as shown in figure 6.6a and c.

The phase-averaged mean profiles of master and slave DNS are computed, see fig. 6.1, and a TGA is performed on top of them. As shown in figure 6.2b, for simulations in a $L_x = 100D$ long pipe, similar transient growth characteristics are observed as in the laminar case, fig. 6.2a. This means that, even after imposing a constraint on how blunt the artificial profiles are, the master and slave mean profiles still allow a similar growth of perturbations with $\alpha = 0$. The slave mean profiles, and

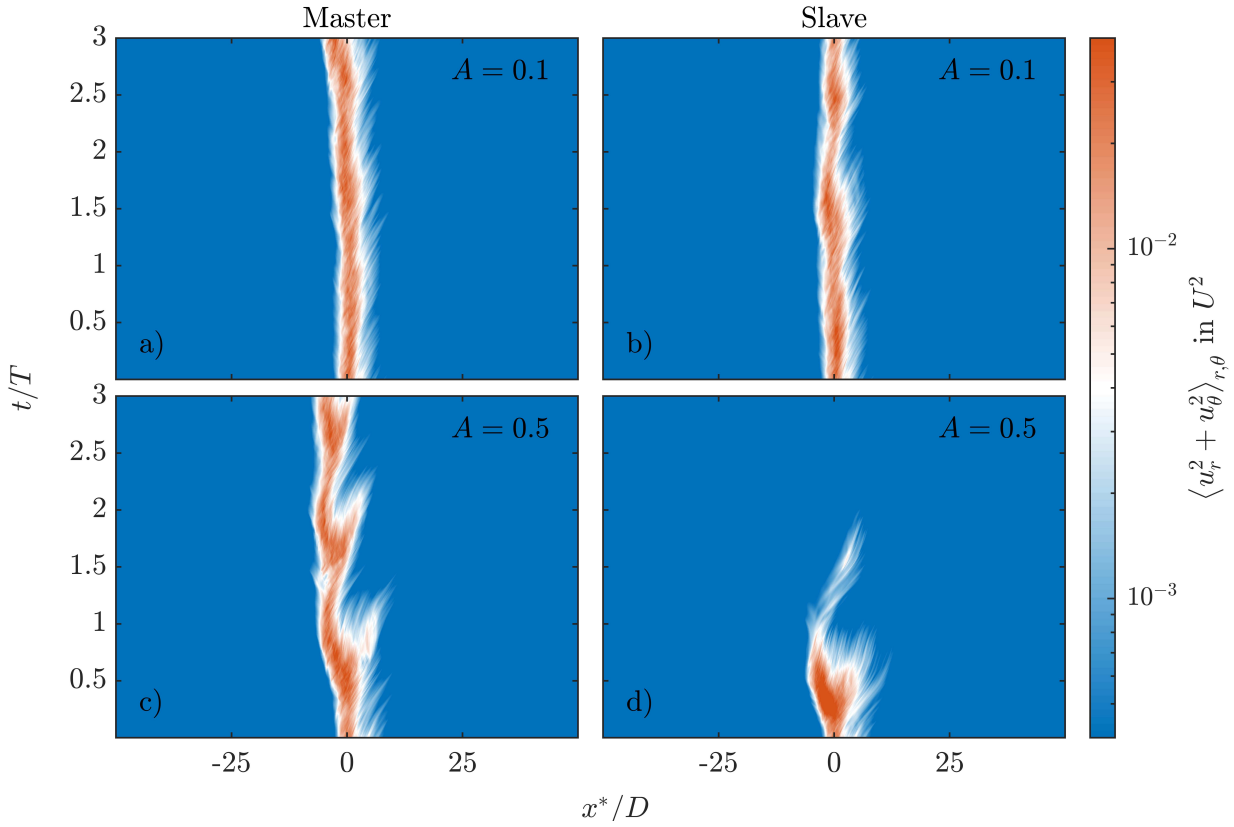

Fig. 6.6.: Space-time diagram of the cross section integral of cross-section kinetic energy, in DNS at $Re = 2100$ and $Wo = 11$. In a) and b) at $A = 0.1$ and in c) and d) at $A = 0.5$. The results correspond to two pairs of master-slave DNS in a $L_x = 100D$ long pipe initialized with a localized turbulent puff. The results are plotted with respect to a moving reference frame moving at the bulk velocity $u_b = U$. a) and c) correspond to master simulations, b) and d) to slave simulations.

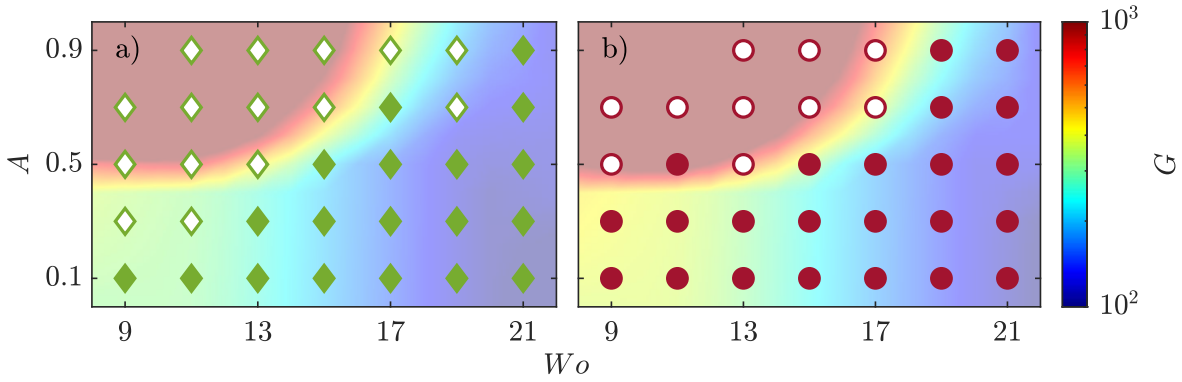

Fig. 6.7.: Survive or decay behaviors of turbulent puffs in individual pairs of master-slave DNS at different Wo and A, in a) at $Re = 2100$, in b) at $Re = 2300$. The results correspond to DNS in a $L_x = 100D$ long pipe initialized with a localized turbulent puff. Symbols (open and closed) denote pairs of DNS whose master simulation has puffs that survive for long times. Open symbols indicate pairs of DNS whose slave simulation has puffs that decay at $t \leq t_d = 120D/U$. The background color represents the maximum transient growth of perturbations on top of the corresponding laminar profile U_{SW} as in figure 6.3c.

different to the master mean profiles, are less susceptible to the growth of helical perturbations with $\alpha > 0$ than to perturbations with $\alpha = 0$.

For all the cases considered here, one observes two distinct behaviors in the master-slave simulations. On the one hand, there are slave simulations that show quick puff decay, in less than 3 pulsation periods. The corresponding laminar profiles U_{SW} of these slave simulations, are highly susceptible to the growth of helical perturbations. An example of this behaviour is shown in figure 6.6c and d. At $A = 0.5$ and $Wo = 11$ the profile is susceptible to the growth of helical perturbations, as seen in fig. 6.3c. While the master simulation has a localized puff that survives for a long time, fig. 6.6c, the puff in the slave simulation decays in less than two pulsation periods, fig. 6.6d.

On the other hand, there are simulations where there is no qualitative difference between master and slave simulations. These simulations correspond to cases whose laminar pipe flow are not susceptible to the growth of helical perturbations. For example, at $A = 0.1$ and $Wo = 11$, see fig. 6.6a and b, both the slave and master profiles are not susceptible to the growth of helical perturbations, fig. 6.2b. At these parameters, puffs survive for asymptotically long times for both, slave and master simulations. See additional results of master-slave DNS pairs in Appendix E.

In order to compare all the master-slave DNS pairs, an heuristic threshold $t_d = 120D/U$ is set. The master-slave pairs are classified according to this threshold: between pairs whose slave simulation shows a decay event before the threshold and those which do not. See in figure 6.7 a graphic representation of this classification for two different Re and different combinations of A and Wo. Symbols denote individual master-slave DNS pairs, whose master simulation shows puffs survive for long times. Hollow symbols indicate slave simulations that show puff decay at $t \leq t_d$. There is a clear boundary between cases that show quick puff decay in the slave simulations and those which do not. This boundary, in the A and Wo parametric space is very similar to the boundary between pulsatile pipe flows which are more susceptible to the helical perturbation than those that are more susceptible to the stream-wise constant perturbation, see fig. 6.3c.

At $A \gtrsim 0.5$ and $8 \lesssim Wo \lesssim 17$ pulsatile pipe flows are highly susceptible to helical perturbations, fig. 6.3c. As seen in fig. 6.7, at these flow parameters, by suppressing the inflection points, puffs quickly decay. At $A \lesssim 0.3$ and/or $Wo \gtrsim 20$, the growth of the helical perturbations is smaller than that of stream-wise constant perturbations. At these flow parameters, erasing the inflection points has no effect on the lifetime of turbulent puffs. This result further supports that, at several Re, Wo and A, as soon as puffs cannot make use of the inflection points to survive, they quickly decay.

6.4 Summary of the chapter

In this chapter a causal analysis of pulsatile pipe flows is performed, in order to study the effect inflection points have on turbulence survival. The key idea was to separate the effect of inflection points from the effect of the mean shear. DNS with imposed mean profiles without inflection points are performed and their behaviour compared with full DNS. At flow parameters where the presence of inflection points cause a huge transient growth of perturbations, removing the inflection points cause a rapid turbulence decay.

The analysis shows that at certain $2100 \lesssim Re \lesssim 2500$, $9 \lesssim Wo \lesssim 17$ and $A \gtrsim 0.3$ puffs actively make use of the shape of the mean profile of pulsatile pipe flow, and in particular of inflection points, to survive. At these parameter regime, and different to statistically steady pipe flow, the effect of the mean shear alone is not able to sustain puffs.

7 Model for puffs and slugs in pulsatile pipe flow

In this chapter the BM of steady pipe flow is extended to single harmonic pulsatile pipe flows at $2100 \leq Re \leq 3000$, $Wo \gtrsim 5$ and $0.5 \leq A \leq 1$. The objective is to extend the original model with the minimum number of changes possible, so it can reproduce the behaviour of turbulent patches at these flow parameters. The resultant Extended Barkley Model (EBM) returns to the original BM when $A = 0$.

The chapter is organized as follows. Firstly, a short introduction to the original BM model is included. Secondly, the changes proposed are described. Thirdly, the results of EBM compared with results of individual DNS of pulsatile pipe flow are shown. Finally the limitations of the extended model are discussed.

7.1 The original BM

The BM describes the evolution of two scalar variables, $q(x,t)$ and $u(x,t)$. The variable q represents the turbulence intensity, and u the state of the local mean shear of the flow, at each axial location x and time t. The main idea of the BM is the non-linear interaction between u and q. Turbulence intensity q takes advantage of the mean shear u to grow. However, in the axial locations where $q > 0$, the local mean shear is reduced [Hof+10; Küh+18], and in turn, adversely affects the growth of q.

The variable q is always either $q = 0$, which corresponds to laminar flow, or $q > 0$, which corresponds to non-laminar (turbulent) flow. As a proxy to the state of the mean shear, u corresponds to the local center-line velocity of the pipe. When the center-line velocity is maximum, $u \equiv U_c$, the flow is locally laminar and the value of the parabolic (laminar) profile $U_c = 2$ is recovered. Otherwise, when the flow is locally turbulent $q > 0$, the center-line velocity is $u < U_c$, since the velocity profile is blunted.

Find a detailed description of the BM in Appendix A.

7.2 Derivation of the EBM

The core idea of the EBM is the same as in the original BM: the non-linear interaction between the turbulence intensity q and the mean shear u. As in the BM, in the EBM u corresponds to the center-line velocity, as a proxy to the state of the local mean shear. The instantaneous laminar profile

of pulsatile pipe flow is much more complex than the simple parabolic profile of steady pipe flow, specially at high $A \geq 0.5$, see Appendix B. For these complex profiles, the shape of its shear can not be described with a single variable u like in the case of steady pipe flow. Here it is assumed that at moderate to high amplitudes $0.5 \lesssim A \lesssim 1$ the state of the mean shear can be approximated with the center-line velocity and an additional parameter, without the need to include new variables in the model. As in Appendix A with the BM, in this section the EBM is described from its local to its spatially extended dynamics.

7.2.1 Local dynamics of the mean shear

In pulsatile pipe flow, the laminar center-line velocity $U_c(t)$ and bulk velocity $u_b(t)$ are functions of time. While the bulk velocity is set by the pulsation, the evolution of $U_c(t)$ can be obtained from the NSE. The equation that gives the laminar SW profile can be written as:

$$\frac{\partial U_{SW}}{\partial t} = f_p(t) + F_{visc}(r,), \tag{7.1}$$

where,

$$F_{visc}(r) = \frac{1}{Re}\left(\frac{\partial^2 U_{SW}}{\partial r^2} + \frac{1}{r}\frac{\partial U_{SW}}{\partial r}\right). \tag{7.2}$$

At $r \to 0$,

$$F_{v_0}(t) = \lim_{r\to 0} F_{visc} = \lim_{r\to 0}\left[\frac{1}{Re}\left(\frac{\partial^2 U_{SW}}{\partial r^2} + \frac{1}{r}\frac{\partial U_{SW}}{\partial r}\right)\right]. \tag{7.3}$$

If one applies L'Hopital's rule to the above limit,

$$F_{v_0}(t) = \frac{2}{Re}\frac{\partial^2 U_{SW}}{\partial r^2}, \tag{7.4}$$

and, being $U_c(t) = U_{SW}(t, r=0)$,

$$\frac{\partial U_c}{\partial t} = f_p(t) + F_{v_0}(t). \tag{7.5}$$

The equilibrium of forces described in equation (7.5) must be included in the model in order to account for the time dependence of U_c. Thus, the original equation of the BM, eq. (A.3), is extended to:

$$\frac{\mathrm{d}u}{\mathrm{d}t} = g_{EBM}(q,u) = \epsilon\left(U_c(t) - u\right) + 2\epsilon\left(u_b(t) - u\right)q + f_p(t) + F_{v_0}(t), \tag{7.6}$$

where U_c, f_p and F_{v_0} are the corresponding laminar velocity, pressure gradient and the viscous force at the center line of the pipe. They can be precomputed by numerically integrating equation (7.5) for a given $u_b(t)$ bulk velocity.

7.2.2 Local dynamics of turbulence intensity

A time dependent control parameter $r_{EBM}(t) = r(Re) \cdot u_b(t+\phi)$ is considered, where r is calculated using the mean Re:

$$r = \frac{Re - R_0}{R_1 - R_0}, \tag{7.7}$$

and $u_b(t+\phi)$ is a time shifted bulk velocity. The phase lag ϕ models the time delay between the maximum integrated turbulence intensity $\langle q \rangle_{r,\theta,z}$ and the bulk velocity u_b, observed in DNS of pulsatile pipe flow, fig. 5.8. It is found that the phase lag $\phi(Wo)$ between the pressure gradient and laminar profile, first derived by Womersley [Wom55], is a good approximation to this phase difference:

$$\phi(Wo) \approx 32.34^\circ + 35.17^\circ \arctan(0.75(Wo - 2)) \tag{7.8}$$

As shown in Chapter 4, at certain $5 \lesssim Wo \lesssim 17$ and $A \gtrsim 0.5$, the laminar profile of pulsatile pipe flow is instantaneously unstable at certain phases of the period. In the EBM, the instantaneous stability of the mean shear is modeled by adding to the local dynamics of q in equation (A.4) the term $+\gamma\lambda_{\max}(t)\, q$. Here $\lambda_{\max}(t)$ represents how linearly unstable the instantaneous laminar profile is, and is always $\lambda_{\max} \geq 0$. When $\lambda_{\max} > 0$, it corresponds to the maximum eigenvalue of the instantaneous laminar profile, as described in §3.5. See a catalog of laminar profiles, with the corresponding eigenvalues in Appendix B. The parameter γ models the effect $\lambda_{\max}$ has on the growth of q. It represents the accuracy of the quasi-steady assumption used to compute $\lambda_{\max}$. It should scale with the length of the period in terms of advective time units $T = \frac{\pi Re}{2Wo^2}$. A good compromise is found by setting:

$$\gamma = \min(1, 0.28 \log(T)). \tag{7.9}$$

By introducing these changes to the model, the local dynamics of q in the EBM are described by the following ODE:

$$\frac{\mathrm{d}q}{\mathrm{d}t} = f_{EBM}(q,u) = q\left[r\, u_b(t+\phi) + \gamma\lambda_{\max}(t) + u - U_c(t) - (r\, u_b(t+\phi) + \delta)(q-1)^2\right]. \tag{7.10}$$

7.2.3 Spatially extended and stochastic model

In the case of the center-line velocity the spatially extended equation is:

$$\frac{\partial u}{\partial t} = -u\frac{\partial u}{\partial x} + g_{EBM}(q,u). \tag{7.11}$$

In the original BM, the velocity at which q is advected is equal to $u - \zeta$ where ζ acts as a correction parameter. In the case of pulsatile pipe flow, the advection velocity should also depend on the phase of the pulsation. This is modeled by correcting the velocity by $u - \zeta u_b(t)$:

$$\frac{\partial q}{\partial t} = -(u - \zeta u_b(t))\frac{\partial q}{\partial x} + f_{EBM}(q,u) + D_q\frac{\partial^2 q}{\partial x^2} + \sigma(Re)\,\tau(t,x)\,q, \tag{7.12}$$

Tab. 7.1.: BM parameters as described in [Bar+15] and the value of parameters used in the EBM.

	R_0	R_1	ζ	D_q	σ	δ	ϵ
BM	1920	2250	0.79	0.13	≤ 0.5	0.1	0.2
EBM	1920	2250	0.79	0.13	$0.2 \leq \sigma \leq 0.85$	0.1	0.1

Note that, in the EBM σ depends on Re, and is given as:

$$\sigma = \frac{6}{5} \cdot \frac{(Re - 1933)}{1000}, \tag{7.13}$$

with a lower limit of $\sigma \geq 0.2$, so there are always some stochastic behaviors in the model, and an upper limit of $\sigma \leq 0.85$, so the stochastic term is never dominant

7.2.4 Parameters of the EBM

The EBM parameters are fitted as in the original BM [Bar+15], see table 7.1, except for two exceptions. One, as described before, is σ, that is now a function of Re and not a constant. The other is ϵ that is changed from $\epsilon = 0.2$ to $\epsilon = 0.1$.

In the original work of Barkley, [Bar16], he suggests that ϵ should be inversely proportional to Re. But, since changing this parameter does not have a huge impact on turbulence front speeds and survival in the case of SSPF, he keeps it constant. In the case of pulsatile pipe flow, in order to find a better match with the DNS results, it should be slightly decreased. This is justified since, the maximum $Re_{\max} = (1 + A)\, Re$ is, in the worst case scenario considered here, two times the mean Re. Therefore ϵ is set to half its BM value in the EBM.

7.2.5 Time scale of the EBM

In §A.3.1 it is described how Barkley, [Bar+15], in order to compare the model and DNS/experiment front speeds, identifies that there is a:

$$\psi = 2\,(C_0 - C_1) = 0.28, \tag{7.14}$$

velocity scale difference between model and DNS/experiment results. This velocity scale difference can also be described as a time scale difference between model and DNS/experiments. In particular, an advective time unit (D/U) in DNS/experiments, corresponds to $\psi = 0.28$ time units in the model. This is of paramount importance in the EBM, as, a period of length $T = \frac{\pi Re}{2Wo^2}$, actually corresponds to a period of length $T^* = 0.28T$ in the model. This scaling is introduced in the model.

Equations (7.12) and (7.11) together with the local dynamics (7.10) and (7.6), the parameters defined in equations (7.9) and (7.13), and summarized in table 7.1, define the EBM. Note that, when $A = 0$ one recovers the original BM, since there is no oscillatory component in f_p, F_{v_0}, u_b or U_c; $f_p + F_{v_0} = 0$ and $\lambda_{\max} \equiv 0$.

7.3 Numerical methods

Equations (7.12) and (7.11) are integrated following Barkley *et al.* [Bar+15]. The second order derivatives are discretized with central finite differences of second order, and the first order deriva-

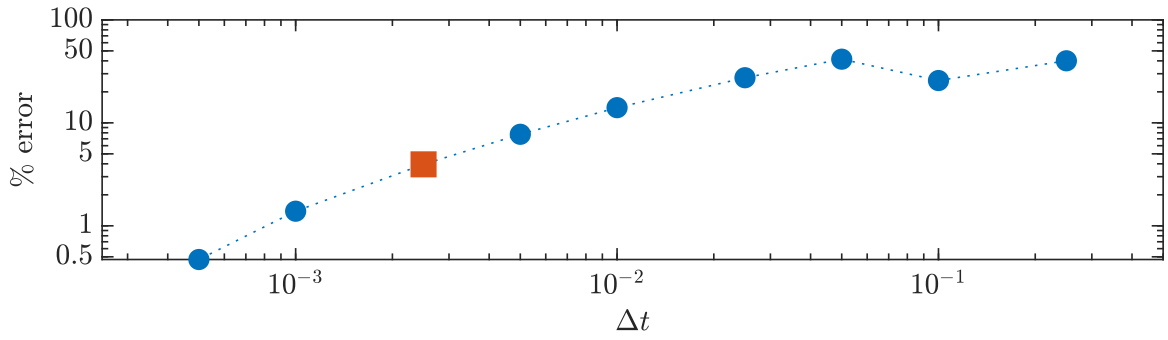

Fig. 7.1.: Grid convergence study of the integrator of the EBM. The figure shows the relative error between the resultant front speed, for different Δt compared to the fine case with $\Delta t = 5 \cdot 10^{-4}$. The results correspond to simulations at $Re = 2100$, $Wo = 11$, $A = 1$ and $\sigma = 0$ with a grid spacing Δx such that the CFL number $\text{CFL} = 4\frac{\Delta t}{\Delta x} = 0.2$ is the same for all the cases. With a red square find the case $\Delta t = 0.0025$ used in the rest of EBM simulations.

tives with a first order upwind scheme. Periodic boundary conditions are considered in x. The system is integrated using an explicit Euler method, with a time step size $\Delta t = 0.0025$. The results here correspond to a pipe of length $L = 100$ and a uniform grid spacing $\Delta x = 0.5$. The stochastic term is modeled as white Gaussian noise in space and time. All the EBM simulations are initialized with a localized 5 axial units long disturbance with magnitude $q \leq 0.5$ at initial time $t_0 = T^*/2$.

In order to validate the code, the EBM is integrated at $Re = 2100$, $Wo = 11$, $A = 1$ and $\sigma = 0$ with different Δt and Δx, see figure 7.1. The grid spacing Δx is changed according to the desired Δt to impose a constant $\text{CFL} = 4\frac{\Delta t}{\Delta x} = 0.2$. A good compromise between accuracy and computation time is found by setting $\Delta t = 0.0025$ and assuming an error of 5% in the front speeds.

In order to prepare all the variables needed to integrate the EBM the following algorithm has been implemented in a `MATLAB` code. After selecting the desired A, Re and Wo the code first numerically integrates the corresponding laminar profile to obtain all the time dependent parameters: u_b, U_c, f_p, F_{v_0} and $\lambda_{\max}$. It then computes the phase shift angle $\phi\,(Wo)$, the parameter σ using eq. (7.13) and scales the pulsation period to adapt it to the time scale of the model using equation (7.14). Finally it integrates the equations (7.12), (7.11), (7.10) and (7.6) to obtain u and q.

7.4 Results of the EBM

In this section the results obtained with the EBM, and their qualitative and quantitative comparison with DNS results are described. The cross section axial vorticity squared:

$$\langle \omega_x^2 \rangle_{r,\theta}\,(x,t) = \frac{1}{\pi R^2} \int_0^R \int_0^{2\pi} \omega_x^2\, r\, \mathrm{d}r\, \mathrm{d}\theta, \tag{7.15}$$

is used as an indicator of the existence and magnitude of turbulence in each axial x location in the DNS. Throughout this section this quantity and q are referred to as turbulent indicators in DNS and EBM respectively.

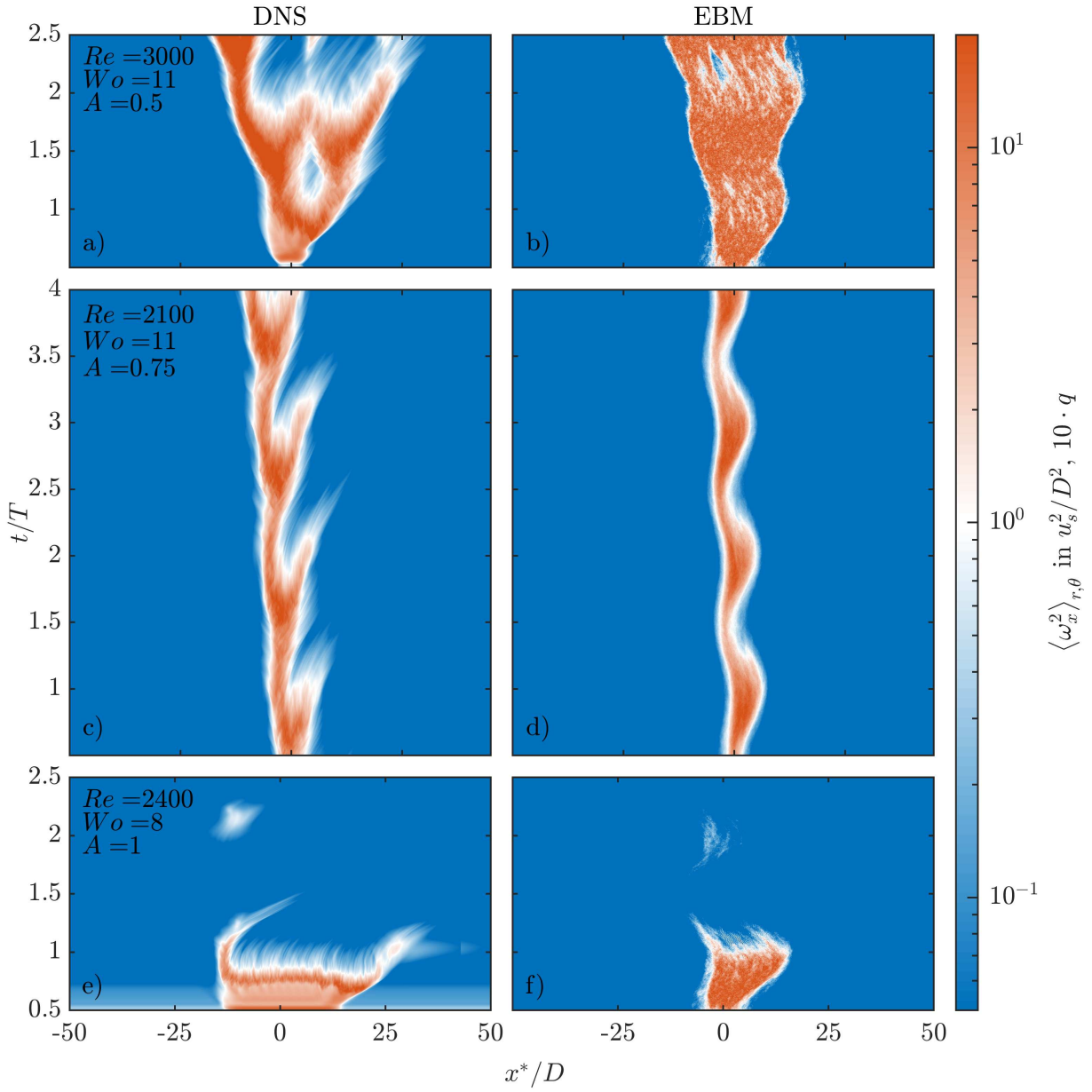

Fig. 7.2.: Space-time diagram of the cross section integral of axial vorticity squared (eq. (7.15)) of DNS (left plots: a, c, e) and $10 \cdot q$ of the model (right plots b, d, f). The results correspond to DNS and model simulations in a $L_x = 100D$ long pipe. The DNS are initialized with the optimal perturbation scaled to $|\boldsymbol{u}_0'| \approx 3e-2$ of magnitude and localized in a span of $5D$ [FMA21], while the model simulations with a localized puff of length $5D$. The figure is presented with respect to a moving frame x^*, moving with the bulk velocity u_b. a) and b) correspond to $Re = 3000$, $Wo = 11$, $A = 0.5$. c) and d) correspond to $Re = 2100$, $Wo = 11$, $A = 0.75$. e) and f) correspond to $Re = 2400$, $Wo = 8$, $A = 1$.

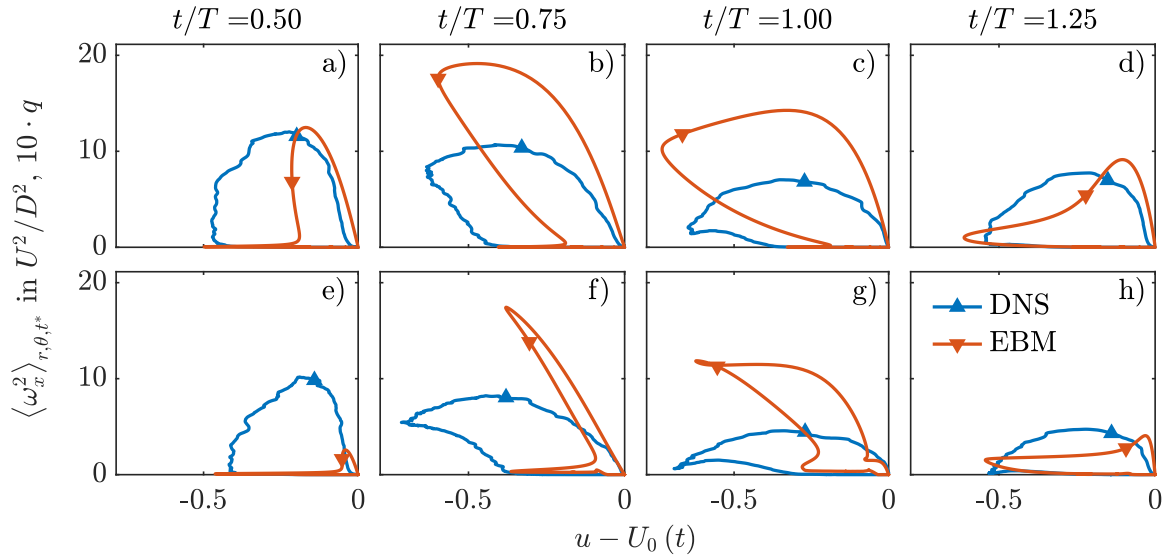

Fig. 7.3.: Turbulence indicator (cross section axial vorticity squared in DNS and $10 \cdot q$ in the EBM) with respect to the center-line velocity u at different pulsation phases. The results correspond to phase averaged DNS and EBM results at $Re = 2100$ and $Wo = 11$. Cases a)-d) are for $A = 0.5$, cases e)-h) for $A = 1$. The phase of each panel is indicated at the top of the corresponding panel column.

See in figure 7.2 three examples of DNS and model comparisons. The model is able to capture reasonably well the turbulent front speed and turbulence behaviour of all the cases, as seen qualitatively in figure 7.2.

See additional EBM results at the end of this chapter, in figure 7.6. There, 4 additional EBM results are shown. The parameters selected there correspond to the parameters shown in the DNS results in figure 5.3. By comparing model and DNS results, it becomes clear that the EBM is able to reproduce the 4 turbulent behaviors of puffs in pulsatile pipe flow described in Chapter 5.

7.4.1 Phase averaged puffs in pulsatile pipe flow

See in fig 7.3, phase averaged results of model and DNS. At $Re = 2100$, $Wo = 11$ and either $A = 0.5$ or $A = 1$. In these cases turbulence is localized and modulated by the pulsation as in the case shown in fig. 7.2c and d.

According to the local phase space in fig. 7.3 a, b, e and f, the structures at $t/T \approx 0.5$ and $t/T \approx 0.75$ are similar to localized turbulent slugs, see fig. A.2 [Son+17; Bar16]. According to the model, at $A = 1$, fig. 7.3f, turbulence elongates into a strong slug, while at $A = 0.5$, fig. 7.3b, the structure is more similar to a weak slug. As u_b^* decreases at $t/T = 1$, the magnitude q^* of slugs also decreases, fig. 7.3c and g. At $t/T \approx 1.25$ the slug shrinks to its minimum length and magnitude, becoming a turbulent puff, fig. 7.3d and h.

7.4.2 Effect of γ and $\lambda_{\max}$ in the EBM

In the EBM, there are two main sources of turbulent intensity production, see eq. (7.10). One is the time varying Re number that is modeled with the term $r\,u_b\,(t + \phi)$. The second one is the instability

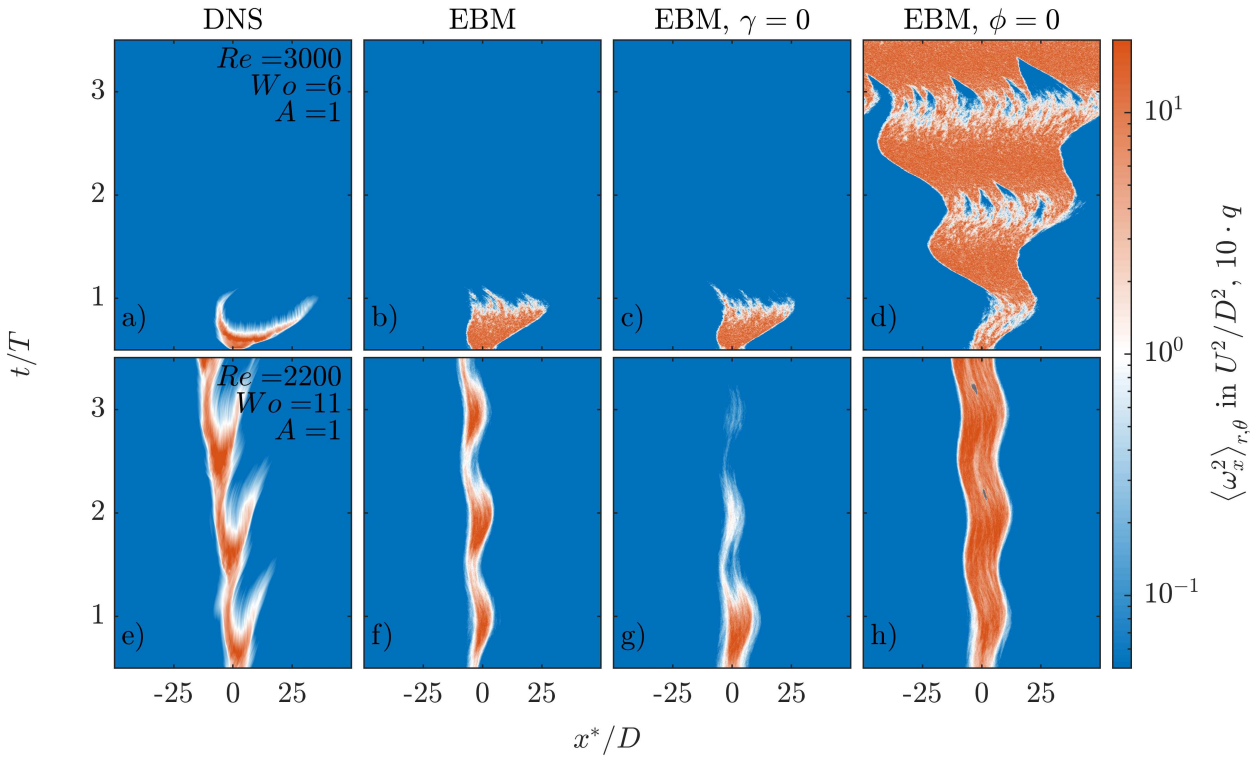

Fig. 7.4.: Space-time diagram of the cross section integral of axial vorticity squared of DNS (left plots: a, e) and $10 \cdot q$ of the EBM (right plots b, c, d, f, g, h). The results correspond to DNS and model simulations in a $100D$ long pipe at $A = 1$. The top panels (a,b,c,d) at $Re = 3000$ and $Wo = 6$. The bottom panels at $Re = 2200$ and $Wo = 11$. The DNS (a,e) are initialized with the optimal perturbation scaled to $|\boldsymbol{u}_0'| \approx 3e-2$ of magnitude and localized in a span of $5D$ [FMA21], while the model simulations with a localized puff of length $5D$. The figure is presented with respect to a moving frame x^*, moving with the bulk velocity u_b. Panels b, f correspond to EBM simulations with the parameters listed in table 7.1. Panels c, g correspond to EBM simulations with the parameters listed in table 7.1 but $\gamma = 0$. Panels d, h correspond to EBM simulations with the parameters listed in table 7.1 but $\phi = 0$.

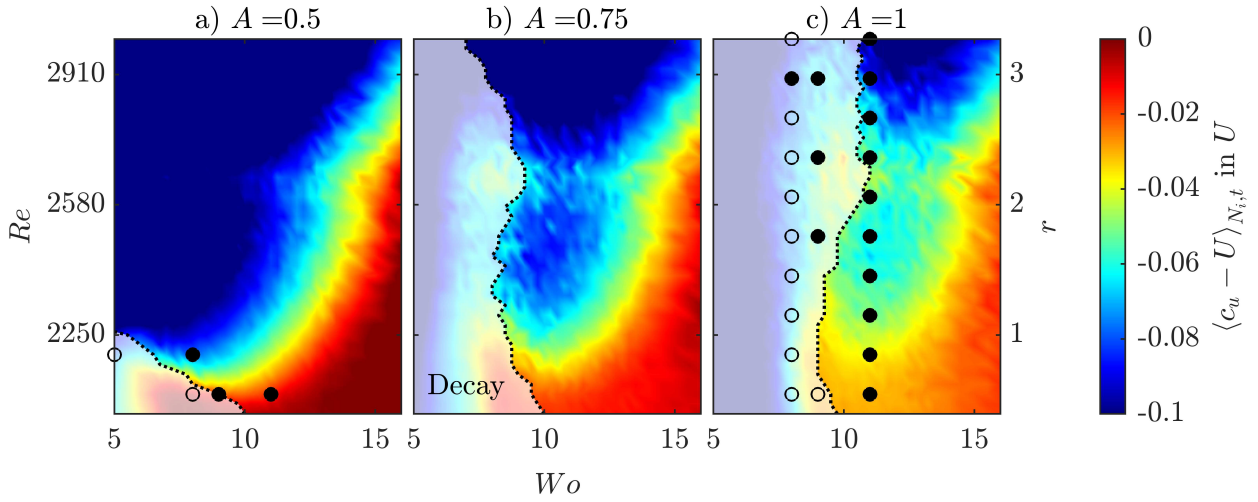

Fig. 7.5.: (With color) time and ensemble averaged upstream front speed of q according to simulations of the EBM at several Re and Wo for three different pulsation amplitudes. Note that the front speed has been transformed from model to U units to ease the comparison with figure 5.8b. The results correspond to the interpolated time and ensemble averaged front speed of 39×37 Re and Wo combinations, for $N_i = 50$ simulations each. In a) at $A = 0.5$, in b) at $A = 0.75$ in c) at $A = 1$. The dotted lines denote the threshold between Re and Wo cases where more than half of the N_i simulations show turbulence decay $q \leq 0.005$ before $t/T < 4$. With black dots we denote the observed survive/decay behaviors of different DNS at parameters close to the decay threshold. Filled dots correspond to simulations where turbulence survives for long times, or splits/elongates. Hollow points denote DNS where we observe turbulence decay at $t/T \leq 8$.

of the mean profile that is modeled by the product $\gamma\lambda_{\max}(t)$. Here the effects of ignoring ϕ or γ are shown.

See in figure 7.4 additional comparisons between DNS and EBM results. The figure also includes results of the EBM model for $\phi = 0$ or $\gamma = 0$. According to the results, if one does not consider the phase lag in the model, the results clearly diverge from the DNS ones at most flow parameters, see fig. 7.4d and h. This behaviour is also observed at other flow parameters. This confirms that turbulence perceives the pulsation at a certain phase lag, and that this phase lag can be modeled as a function of Wo alone.

Regarding the parameter γ, see fig. 7.4c and g, $Re = 3000$, $Wo = 6$ and $A = 1$, there is no apparent effect of ignoring the linear instability of the mean profile. At these flow parameters turbulence rapidly decays due to the effect of the pulsation, regardless of the presence of inflection points in the profile. However, at $Re = 2200$, $Wo = 11$ and $A = 1$, without the effect of the instantaneous linear instability, puffs quickly decay due to the effect of the pulsation.

7.4.3 *Parametric study using the EBM*

A huge number of simulations of the EBM were performed in a big Wo and Re parametric space for three different amplitudes. At each amplitude, 39 equispaced Re between $2050 \leq Re \leq 3000$ and 37 Wo between $5 \leq Wo \leq 16$ are considered. For each combination of Wo, Re and A; $N_i = 50$ EBM simulations for $t/T < 4$ are performed. The simulations are interrupted either at $t/T < 4$ or when turbulence decays in the whole domain $q \leq 0.005$.

See in figure 7.5 the time and ensemble averaged upstream front speed $\langle c_u \rangle_{t,N_i}$ together with an empiric threshold for turbulence decay of all the EBM simulations considered here. The threshold separates the parametric regions where more than half of the N_i simulations decay, at $t/T \leq 4$, from the rest. It can be understood as a critical $Re_c\,(Wo, A)$, up to which all puffs are more likely to decay than survive, split or elongate. This critical Re_c is a function of Wo and A. At low Wo, as the system becomes increasingly quasi-steady, puffs need of a higher mean Re to survive the phases of the period where $u_b\,(t+\phi) < U$. The amplitude A sets the minimum Re at each Wo. As A increases, this minimum Re increases. At $A = 1$, the EBM shows an asymptotic behavior at $Wo \approx 10$. Here, independently of the selected $Re \leq 3000$, puffs show a high chance to decay as soon as $Wo \leq 10$.

Regarding the upstream front speed, at high Wo and independently of the selected A, $\langle c_u \rangle_{t,N_i}$ decreases as Re increases. This is expected as the behaviour of puffs at high Wo is similar to the behaviour of puffs in SSPF. As shown in figure A.4, the upstream front speed of puffs in steady pipe flow, decreases for increasing Re.

As Wo decreases from $Wo < 20$, at $10 \lesssim Wo \lesssim 20$, $\langle c_u \rangle_{t,N_i}$ first decreases. At these frequencies, and specially at higher A, $\gamma\lambda_{\max} > 0$ for some phases of the period, which increases the overall turbulent production. This increase in turbulent production is analogous to an increase in Re, and therefore returns a lower averaged $\langle c_u \rangle_{t,N_i}$. At $Wo \approx 10$ the system is close to the decay threshold discussed above. Puffs tend to accelerate as they decay, which explains the increase of $\langle c_u \rangle_{t,N_i}$ at these Wo.

However the results show that, as Wo is further decreased, $\langle c_u \rangle_{t,N_i}$ decreases again. This is due to the way the EBM simulations are initialized. At $t_0 = T^*/2$ the puffs tend to elongate since $ru_b\,(t+\phi) \geq 0$ and $\gamma\lambda_{\max} \geq 0$. So during the initial phase of the EBM simulations at $Wo \lesssim 8$ puffs first rapidly elongate ($c_u < 0$), and then quickly decay when $u_b\,(t+\phi) < U$. Since the decay is faster than the elongation, the averaged front speed is $\langle c_u \rangle_{t,N_i} < 0$.

Comparison with DNS results

The EBM qualitatively captures the behavior of the upstream front speed observed in the DNS, as seen after comparing figure 7.5 with figure 5.8 (right). As in the DNS, the upstream front speed in the EBM decreases for increasing Re and A, and, at high Wo, it approaches the values of the upstream front speed of puffs in SSPF. The quantitative values of the upstream front speed of model and DNS are also similar.

In figure 7.5, the symbols represent the survival/decay behaviors of the DNS listed in table C.1, whose flow parameters are close to the decay thresholds of the EBM. Hollow symbols represent DNS where puffs decay at $t/T \leq 8$, and solid ones, DNS that show turbulence survival for long times. The model approximates relatively well the minimum Wo at each Re and A, where turbulence does not decay after a short number of pulsation periods. The match between EBM and DNS results is better at smaller A, like $A = 0.5$ than at higher A. At $A = 1$, while the model has a threshold to decay close to $Wo = 10$, in the DNS the threshold seems to be closer to $Wo = 8$, and slightly change as Re increases.

The observed discrepancies between model and DNS results are rooted in the limitations of the EBM. Some of them are described in the following section.

7.5 Limitations of the EBM

When correctly fitted, the EBM captures the dynamics of pulsatile pipe flow in a broad parametric regime, but it has some limitations that need to be mentioned. In this section these limitations are

described together with some suggestions on possible ways to improve the model in future analyses. The limitations are classified between limitations possibly inherited from the original BM, and those that are new to the EBM.

As a general comment, and different to the original BM, the EBM shows a much worse robustness with respect to the model parameters. Specially worrying are the dependence of the results to the noise intensity σ (from a qualitative point of view) and linear instability strength γ.

7.5.1 Limitations inherited from the original BM

The problem with parameter σ

In the original BM, the parameter σ was included in order to model puff decay, split and intermittency. As explained in Appendix A, the original BM fails to capture the intermittent behaviour of localized turbulence in steady pipe flow at $2250 \lesssim Re \lesssim 2500$. In this regime, according to the model, puffs elongate until they fill the whole domain with turbulence. However, according to DNS and experiments, at these Re, turbulent patches like puffs and slugs coexist with laminar regions of the flow, and elongate, split, decay in a highly intermittent way.

According to the DNS of pulsatile pipe flow, see Chapter 5, at these Re and $A > 0.5$, puffs remain localized at $6 \lesssim Wo \lesssim 12$. If the parameter σ is not scaled with Re, puffs at these flow parameters tend to elongate in the EBM.

The shape of elongated patches

The shape of the turbulent structures in the EBM do not perfectly match those observed in DNS, as seen in fig. 7.3f. The EBM clearly overestimates the ratio between the magnitude of q in the core of the turbulent patch. This was also observed in the case of slugs in the BM.

7.5.2 The problems with parameter γ

As described at the beginning of this chapter, the EBM was expected to work worse as A increases. At higher A, and $Wo > 5$, the laminar profile is very different to the simple parabolic profile of steady pipe flow, see Appendix B. In order to account for the shape of the pulsatile laminar profile, the instantaneous linear instability $\lambda_{\max}$, and the parameter γ are used. Both work reasonably well, as long as γ is correctly fitted. But as soon as γ is changed puffs either decay or elongate when they should not.

Also, due to the definition of γ the model overestimates the lifetime of puffs at certain flow parameters. In particular, according to the EBM, puffs at $10 \lesssim Wo \lesssim 15$, $A = 1$ and $1800 \lesssim Re \lesssim 2050$ survive the pulsation. This is obviously not observed in DNS of pulsatile pipe flow, where at $Re < 2050$ and $A = 1$ puffs tend to decay independently of the pulsation frequency. Moreover, at these flow parameters, the EBM is clearly dominated by the parameter $\lambda_{\max}$, and therefore by γ.

The EBM considers that, as long as $\lambda_{\max} > 0$, turbulence can always make use of the instantaneous linear instability to grow. However this may not be the case in a full DNS. At a given time step, the mean profile of a DNS can be highly perturbed. In this case, puffs do not have the chance to take advantage of the linear instability to grow.

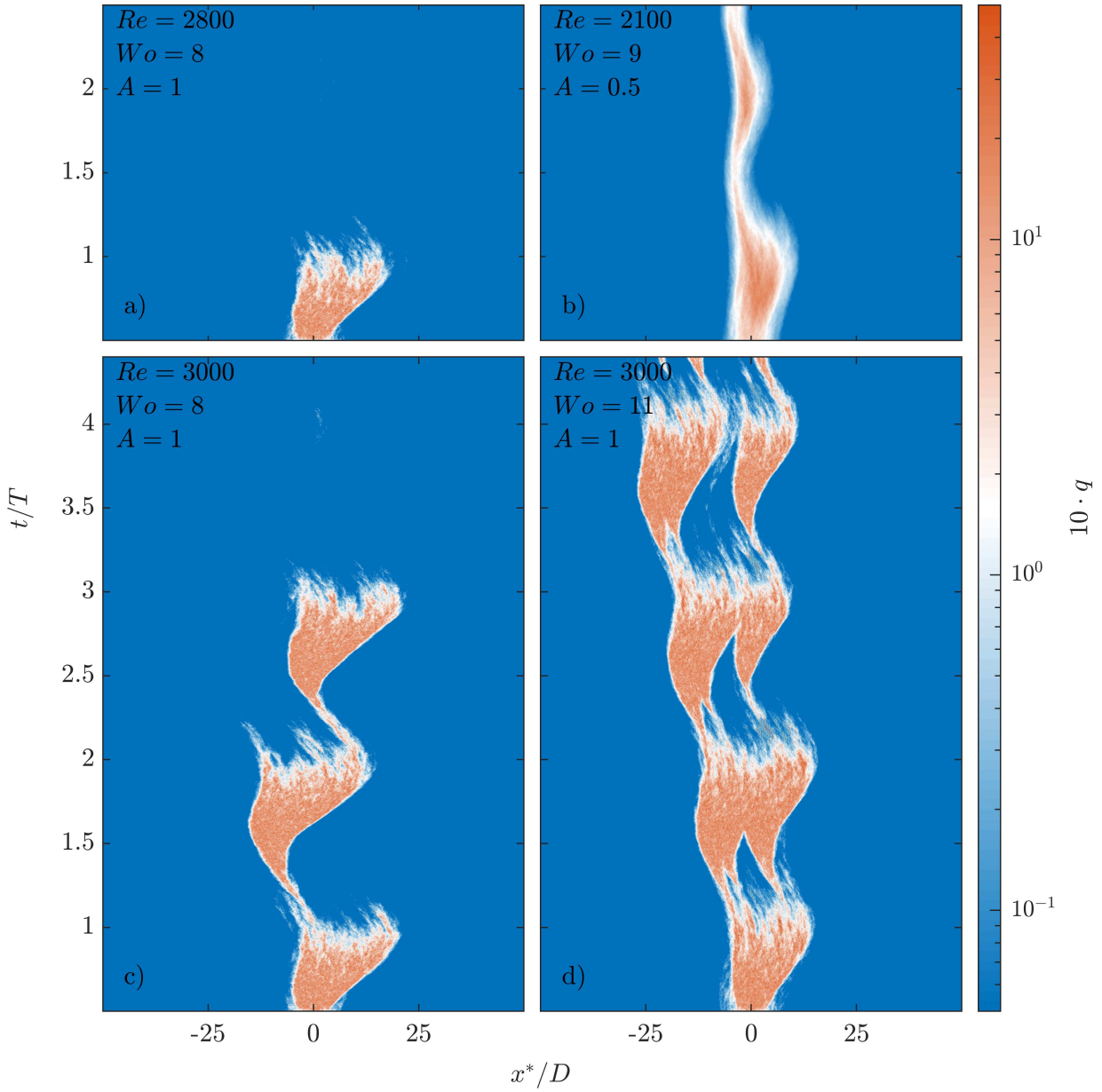

Fig. 7.6.: Space-time diagram of turbulence indicator of the EBM in a 100 axial units long domain. The model simulations are initialized with a localized q patch, in an axial span of 5 axial units. The diagrams are shown with respect to a moving frame x^*, moving with the bulk velocity $u_b\,(t)$. a) corresponds to $Re = 2800$, $Wo = 8$ and $A = 1$. b) corresponds to $Re = 2100$, $Wo = 9$ and $A = 0.5$. c) corresponds to $Re = 3000$, $Wo = 8$ and $A = 1$. d) corresponds to $Re = 3000$, $Wo = 11$ and $A = 1$.

7.6 Summary of the chapter

Here the BM is extended to the case of pulsatile pipe flow. By introducing a minimal number of changes in the BM, inspired by the physics discussed in Chapters 5 and 6, it is shown how the new EBM qualitatively and quantitatively agrees with DNS results of pulsatile pipe flow in a wide parametric regime.

8 Conclusions

In this thesis, the transition to turbulence, and the transitional regime, of pulsatile pipe flow at moderate-to-high amplitudes $A \geq 0.5$ have been studied. In particular, pulsatile pipe flows with non-reversal bulk velocities $u_b(t) \geq 0$, at pulsation frequencies of $3 \lesssim Wo \lesssim 21$ and mean Reynolds numbers $1000 \lesssim Re \lesssim 3000$ have been considered. This parameter regime is relevant for cardiovascular flows, particularly in the blood flow in the human aorta.

Two questions have been addressed:

1. How do pulsatile pipe flows transition to turbulence? And, corollary, how do the flow parameters affect this transition?
2. How does turbulence behave once triggered at these flow parameters?

In order to answer these questions, stability and transient growth analysis, together with direct numerical simulations, causal analysis and turbulence modeling were performed. The main conclusions are summarized in what follows.

Optimal perturbations

All the laminar pulsatile pipe flows studied here are susceptible to the transient growth of a pair of axially coherent stream-wise vortices. This perturbation is known to be the most amplified one for turbulence transition in steady pipe flow [SH94]. At certain flow parameters, however, pulsatile pipe flow is more susceptible to the growth of a new family of perturbations known as the helical perturbations [Xu+20]. In this thesis, it has been shown that these helical perturbations are linked to the instantaneous linear instability of the laminar velocity profile in pulsatile pipe flow. This instability emerges from the presence of inflection points in the laminar profile and their characteristics. Two requirements must be fulfilled for helical perturbations to grow.

The first one is that the flow is instantaneously unstable at some phases of the pulsation period. This instability occurs when inflection points in the laminar profile satisfy the Fjørtoft criterion. In general this is the case for $Re \gtrsim 800$, $Wo \gtrsim 3$ and $A \gtrsim 0.5$, although the precise dependence on Re, Wo and A is intricate.

The second requirement is that the laminar profile evolves much slower than the perturbations. The perturbations evolve in the advective time scale D/U, while the laminar profile evolves according to the pulsation period T. In advective time units, the period is equal to $T = \frac{\pi Re}{2Wo^2}$. As long as $T \gtrsim 10D/U$, the perturbations have enough time to take advantage of the inflection points to grow.

The waveform of the pulsation can change the lifetime, the radial span and the characteristics of these inflection points. For waveforms with longer low velocity phases, the inflection points remain a longer fraction of the period in the flow and give more time for the perturbations to grow on top

of them. Also, perturbations grow more, the more abrupt the acceleration and deceleration phases are. This means that, by just knowing the waveform and the flow parameters (Re and Wo), one can easily estimate the growth of perturbations for a given pulsatile pipe flow, without even performing stability or transient growth analysis (see eq. (4.8) in Chapter 4).

Transition to turbulence due to helical perturbations is not supercritical. Helical perturbations make use of linear instabilities to grow, but these instabilities are only present during some phases of the period. In fact, the net growth of helical perturbations, at these flow parameters, is always smaller than $G < 1$ after a sufficiently long time. That is the reason why Floquet analysis of pulsatile pipe flow at these flow parameters do not show the actual susceptibility to transition observed in the experiments [Tho+11]. In order for the helical perturbation to grow to a certain magnitude where it saturates, triggers non-linear effects and then triggers turbulence; it needs a sufficiently high initial magnitude. Therefore, the transition to turbulence via helical perturbations is subcritical.

It is worth noting that the (rare) existing measurements of the flow in models of the human aorta, primarily report helical flow patterns [Cor+21; Ha+16]. Coincidentally, the alignment of fibers in the tissue of cardiovascular vessels is helical [TKV13]. The fibers are believed to be aligned with the principal direction of wall shear stresses, which indirectly would confirm the presence of helical patterns in the flow. As it has been shown in this thesis, pulsatile pipe flows in rigid pipes driven with cardiovascular like waveforms are susceptible to the growth of helical perturbations. This would suggest that, the pulsatile nature of the flow alone, leads to the development of helical patterns. This hypothesis should be further studied, and compared to other cardiovascular flow features such as the inlet conditions or geometry of the aorta.

The rise of turbulence in pulsatile pipe flow

In order to understand how turbulence is triggered in pulsatile pipe flows, different DNS have been performed. All of them are initialized with the corresponding laminar profile, and on top of it, different disturbances are used to trigger turbulence. In a first group of simulations, the flow is constantly perturbed close to the pipe wall by a body force that models a localized geometric defect. In these simulations, at the flow parameters where the flow is susceptible to the growth of helical perturbations, turbulent patches are intermittently triggered every deceleration phase of the period. Turbulence may or may not survive the rest of the pulsation, but, what is important is that, at these flow parameters, the flow is highly susceptible to transition. This means that, when sufficiently perturbed, the flow is expected to have turbulent patches at least during some phases of the pulsation, as observed in experiments [Xu+20].

Other simulations are initialized with the helical perturbation, scaled to a small magnitude and localized in a short axial length. In these simulations, the initial helix grows in magnitude and axial length until it triggers localized turbulent patches. If the initial perturbation is not localized in the axial direction, the helical perturbation triggers turbulence in the whole domain. The turbulent patches require a certain distance with respect to one another to survive. If the initial perturbation is not localized, the turbulent patches that are created close to one another, tend to quickly decay [Hof+10].

In accordance with the energy growth predicted by the LSA and TGA, turbulence transition happens faster or slower depending on the waveform of the pulsation. Cases with longer low velocity phases and steeper acceleration/deceleration phases show higher initial peaks of turbulent fraction than cases with longer high velocity phases.

Turbulence in the transitional regime

Independently of the method used to trigger turbulence, at the flow parameters considered here, turbulence first appears in the form of localized turbulent patches. These turbulent patches are modulated in length and magnitude by the pulsation, and they are similar to the puffs and slugs found in SSPF. Depending on the flow parameters, they can have different behaviors, see §5.2. At some flow parameters (typically at $Wo \lesssim 8$), the structures decay after one, or a short number of, pulsation periods. These decay events happen always at the same phase of the period [XA18]. This means that decay events in pulsatile pipe flow are much more predictable than in SSPF. At higher pulsation frequencies, puffs either remain localized for asymptotically long times, or randomly split until the flow reaches a highly intermittent state, where localized turbulent patches split/decay in a quiescent laminar flow.

The waveform has also an effect on turbulence survival once turbulence is triggered. Opposite to what their effects on perturbation growth suggests, steeper acceleration/deceleration and longer low velocity phases, actually promote turbulence decay. This suggests that, in the non-linear regime, the waveform has additional effects.

It was observed that turbulent production of puffs in pulsatile pipe flow tends to localize radially close to the position of inflection points in the quiescent laminar profile. In order to further study the effects of inflection points on turbulence, a non-linear causal analysis was performed. The analysis systematically eliminates the inflection points from the laminar profile, while minimally affecting the state of the mean shear. According to the analysis, puffs actively make use of the inflection points in the quiescent laminar profile, and their corresponding instabilities, to survive the pulsation. This seems to contradict the results of Lozano *et al.* [LD+21], who determined that linear instabilities do not play an important role on turbulence survival. However, they considered fully turbulent flows, while I studied the case of localized turbulent patches in a quiescent laminar profile. My conclusion is that, as long as turbulence remains localized, it can make use of the surrounding laminar profile and its instantaneous instabilities to grow.

Using the lessons learned from the DNS results and the results of the causal analysis, a pre-existing model of puffs in SSPF developed by Barkley was adapted to pulsatile pipe flow. The extended model is able to reproduce reasonably well the behaviour of turbulent front speeds of puffs in pulsatile pipe flow, and their dependence on Re, A and Wo. It is also able to approximate the thresholds in terms of Re, A and Wo up to which rapid decay of turbulence is expected. According to the model at $A = 1$ and $2000 \lesssim Re \lesssim 3000$, any case with $Wo \lesssim 10$ is highly susceptible to relaminarization.

According to the DNS, causal analysis and extended model results, turbulence in pulsatile pipe flow, makes use of mainly two mechanisms to survive. The first mechanism is the turbulent production due to the mean shear, that is maximum in the phases of the period where the bulk velocity is high, $u_b\,(t + \phi) > U$. This production has a certain phase lag ϕ with respect to the pulsation, that is mainly set by Wo. The second mechanism is the instantaneous instability of the quiescent laminar flow. As long as puffs remain localized in pulsatile pipe flow, and surrounded by a quiescent laminar profile, they can take advantage of this instability to increase their turbulent production at certain phases of the period.

Outlook

This thesis mainly focuses on two particular questions regarding turbulence and turbulence transition, on a limited parametric space of pulsatile pipe flow. The results presented here suggest that the pulsatile driving of the flow alone is able to render the flow highly susceptible to transition. The question still remains on whether this effect is dominant for turbulence transition in cardiovascular flows or not, and if it is relevant at other flow parameters.

Future works should extend this analysis and consider additional blood flow characteristics, such as non-Newtonian effects, the effect of flexible walls or complex geometries. The inclusion of any of these features will result in laminar flows that are different to the Sexl-Womersley profile. This will have an impact on the presence and behavior of inflection points, and potentially reduce the growth of helical perturbations. For instance, the human aorta is obviously not straight, see fig. 1.10. The aortic arch can be modeled a $180°$ bend, while, although the descending aorta is almost straight, it still has some curvature. Both geometries will induce secondary flows that can disrupt the laminar profile and result in other types of instabilities and transition scenarios. In the case of flexible walls, fluid-structure interactions such as the Windkessel effect or wall oscillations, will have an impact on the laminar flow.

Different to the rest of the features, non-Newtonian effects are expected to be not so important in the larger arteries, except for the phases of the period where the bulk velocity is minimum. At these phases of the period, blood flow will experience a small mean shear, that could lead to the formation of red-blood cells structures like rouleaux, see fig. 1.2. The presence of these structures are usually modeled as a local increase in viscosity. This could have a detrimental effect on the growth of perturbations. Blood has other non-Newtonian features like shear-thinning and visco-elasticity. According to preliminary results, shear-thinning effects reduce the growth of helical perturbations, while visco-elastic effects enhance it. The former tend to radially move the inflection points closer to the wall, while the latter to the center-line. Some of these results are discussed in the Bachelor thesis of Laura Dot, see Appendix G. However more thorough analyses are needed in order to test these observations.

The additional features of cardiovascular flows will also have an impact on the behavior of turbulence once it is triggered. For instance, mild curvatures have been observed to delay transition and change the behavior of puffs and slugs in SSPF [RCS19]. It is expected that, the more pronounced curvatures of the aorta will have a bigger impact on the flow. Non-Newtonian effects also have an important effect on turbulence. In fact, if the visco-elastic effects are big enough, the flow reaches a new chaotic state known as Elasto-Inertial Turbulence, that shows different dynamics to turbulent flows [DTH23]. Perhaps the most critical feature is the effect of flexible walls. The expectation is that, stiffer walls promote turbulence, as they have been historically linked with cardiovascular diseases [Mal+16]. This has not been demonstrated yet, and the results of this thesis could serve as a nice starting point to study turbulence transition of pulsatile flows bounded by flexible walls.

In this thesis, in order to understand the behavior of turbulence in pulsatile pipe flow, a fairly new causal analysis was developed. This analysis can be used in the future, to study the behavior of localized turbulent structures in pipe, or in other set-ups like channel flows. Additionally, the EBM developed in this thesis could be used in future studies to quickly assess the behavior of puffs at different flow parameters, to investigate the interaction between several puffs in the same pipe, or the effect of suddenly changing the flow parameters. As it has been shown in this thesis, slight changes in the pulsation parameters, can result in big changes on the behavior of turbulence. Future analyses may be interested on designing control laws to manipulate the behavior of turbulence by changing the pulsation frequency or amplitude. They could use the EBM to, in a fast way, obtain preliminary control laws. All of these studies will need to, at some point, perform a big number of DNS. The `C-CUDA` code developed in this thesis, can aid in these analyses by performing fast and efficient simulations.

There are several fundamental questions regarding puffs in steady pipe flow that have not been answered yet, such as why puffs randomly decay at low Re and randomly split at higher Re. These behaviors are also observed in pulsatile pipe flow, but they take place in a more deterministic way. Puffs in pulsatile pipe flow tend to decay and/or split, only during concrete phases of the period and

not during others. A more thorough analysis of these behaviors may help explain the still unresolved dynamics of puffs in SSPF.

Bibliography

[AHA86] Farid Alavyoon, Dan S Henningson, and P Henrik Alfredsson. “Turbulent spots in plane Poiseuille flow–flow visualization”. In: *The Physics of fluids* 29.4 (1986), pp. 1328–1331 (cit. on p. 13).

[AO18] Ityona Amber and TS O’Donovan. “Natural convection induced by the absorption of solar radiation: A review”. In: *Renewable and Sustainable Energy Reviews* 82 (2018), pp. 3526–3545 (cit. on p. 2).

[Avi+11] Kerstin Avila, David Moxey, Alberto de Lozar, et al. “The onset of turbulence in pipe flow”. In: *Science* 333.6039 (2011), pp. 192–196 (cit. on pp. 7, 44).

[ABH23] Marc Avila, Dwight Barkley, and Björn Hof. “Transition to Turbulence in Pipe Flow”. In: *Annual Review of Fluid Mechanics* 55.1 (2023), null. eprint: `https://doi.org/10.1146/annurev-fluid-120720-025957` (cit. on pp. 2, 7, 13, 14).

[BS16] H. Babaee and T. P. Sapsis. “A minimization principle for the description of modes associated with finite-time instabilities”. In: *Proceedings of the Royal Society A: Mathematical, Physical and Engineering Sciences* 472.2186 (2016), p. 20150779. eprint: `https://royalsocietypublishing.org/doi/pdf/10.1098/rspa.2015.0779` (cit. on p. 11).

[BDT95] Jeffrey S Baggett, Tobin A Driscoll, and Lloyd N Trefethen. “A mostly linear model of transition to turbulence”. In: *Physics of Fluids* 7.4 (1995), pp. 833–838 (cit. on p. 15).

[BH98] Steven A Balbus and John F Hawley. “Instability, turbulence, and enhanced transport in accretion disks”. In: *Reviews of modern physics* 70.1 (1998), p. 1 (cit. on p. 2).

[Bar11a] Dwight Barkley. “Modeling the transition to turbulence in shear flows”. In: *Journal of Physics: Conference Series*. Vol. 318. 3. IOP Publishing. 2011, p. 032001 (cit. on pp. 15, 137).

[Bar11b] Dwight Barkley. “Simplifying the complexity of pipe flow”. In: *Physical Review E* 84.1 (2011), p. 016309 (cit. on pp. 15, 137).

[Bar16] Dwight Barkley. “Theoretical perspective on the route to turbulence in a pipe”. In: *Journal of Fluid Mechanics* 803 (2016), P1 (cit. on pp. 15, 104, 107, 137, 138, 142, 143).

[BBS08] Dwight Barkley, Hugh Maurice Blackburn, and Spencer J Sherwin. “Direct optimal growth analysis for timesteppers”. In: *International journal for numerical methods in fluids* 57.9 (2008), pp. 1435–1458 (cit. on pp. 11, 46).

[Bar+15] Dwight Barkley, Baofang Song, Vasudevan Mukund, et al. “The rise of fully turbulent flow”. In: *Nature* 526.7574 (2015), pp. 550–553 (cit. on pp. 15, 77, 80, 89, 104, 137, 139, 142).

[BT05] Dwight Barkley and Laurette S. Tuckerman. “Computational Study of Turbulent Laminar Patterns in Couette Flow”. In: *Physical review letters* 94 (1 2005), p. 014502 (cit. on p. 13).

[BG62] G. K. Batchelor and A. E. Gill. “Analysis of the stability of axisymmetric jets”. In: *Journal of Fluid Mechanics* 14.4 (1962), 529–551 (cit. on pp. 8, 61).

[Bäu+99] H Bäumler, B Neu, E Donath, and H Kiesewetter. “Basic phenomena of red blood cell rouleaux formation”. In: *Biorheology* 36.5-6 (1999), pp. 439–442 (cit. on p. 3).

[Ben+23] Miguel Beneitez, Yohann Duguet, Philipp Schlatter, and Dan S. Henningson. “Instability of the optimal edge trajectory in the Blasius boundary layer”. In: *Journal of Fluid Mechanics* 971 (2023), A42 (cit. on p. 11).

[Ber+21] Antony N Beris, Jeffrey S Horner, Soham Jariwala, Matthew J Armstrong, and Norman J Wagner. “Recent advances in blood rheology: A review”. In: *Soft Matter* 17.47 (2021), pp. 10591–10613 (cit. on p. 2).

[BCN82] Alan Bishop, David Campbell, and Basil Nicolaenko. *Nonlinear problems: present and future*. Elsevier, 1982 (cit. on p. 35).

[Blo18] Bloomberg. *This Physics Breakthrough Could Help Save the World*. `https://www.bloomberg.com/view/articles/2018-01-29/this-physics-breakthrough-could-help-save-the-world` [Accessed: 20/12/2023]. 2018 (cit. on p. 2).

[Boy01] John P Boyd. *Chebyshev and Fourier spectral methods*. Courier Corporation, 2001 (cit. on p. 28).

[BSH04] Luca Brandt, Philipp Schlatter, and Dan S. Henningson. “Transition in boundary layers subject to free-stream turbulence”. In: *Journal of Fluid Mechanics* 517 (2004), 167–198 (cit. on p. 8).

[BV18] Melissa C. Brindise and Pavlos P. Vlachos. “Pulsatile pipe flow transition: Flow waveform effects”. In: *Physics of Fluids* 30.1 (2018), p. 015111. eprint: `https://doi.org/10.1063/1.5021472` (cit. on pp. 16, 18, 63).

[BPK16] Steven L Brunton, Joshua L Proctor, and J Nathan Kutz. “Discovering governing equations from data by sparse identification of nonlinear dynamical systems”. In: *Proceedings of the national academy of sciences* 113.15 (2016), pp. 3932–3937 (cit. on p. 14).

[Bür+12] Jonas Bürk, Philipp Blanke, Zoran Stankovic, et al. “Evaluation of 3D blood flow patterns and wall shear stress in the normal and dilated thoracic aorta using flow-sensitive 4D CMR”. In: *Journal of cardiovascular magnetic resonance* 14.1 (2012), pp. 1–11 (cit. on pp. 2, 3, 23, 68, 84).

[CL13] Andres D Caballero and SJCE Laín. “A review on computational fluid dynamics modelling in human thoracic aorta”. In: *Cardiovascular Engineering and Technology* 4 (2013), pp. 103–130 (cit. on p. 3).

[Cha+16] George Chagelishvili, Jan-Niklas Hau, George Khujadze, and Martin Oberlack. “Mechanical picture of the linear transient growth of vortical perturbations in incompressible smooth shear flows”. In: *Physical Review Fluids* 1.4 (2016), p. 043603 (cit. on p. 11).

[Cha02] S. Jonathan Chapman. “Subcritical transition in channel flows”. In: *Journal of Fluid Mechanics* 451 (2002), 35–97 (cit. on p. 8).

[CXS22] Kaiwen Chen, Duo Xu, and Baofang Song. “Propagation speed of turbulent fronts in pipe flow at high Reynolds numbers”. In: *Journal of Fluid Mechanics* 935 (2022), A11 (cit. on pp. 15, 81, 89, 142).

[Che+11] Stefania Cherubini, Pietro De Palma, J-C Robinet, and Alessandro Bottaro. “The minimal seed of turbulent transition in the boundary layer”. In: *Journal of Fluid Mechanics* 689 (2011), pp. 221–253 (cit. on p. 10).

[CL16] Diana D Chin and David Lentink. “Flapping wing aerodynamics: from insects to vertebrates”. In: *Journal of Experimental Biology* 219.7 (2016), pp. 920–932 (cit. on p. 2).

[Col65] Donald Coles. “Transition in circular Couette flow”. In: *Journal of Fluid Mechanics* 21.3 (1965), pp. 385–425 (cit. on pp. 10, 13).

[Cor+21] Pascal Corso, Jonas Walheim, Hannes Dillinger, et al. “Toward an accurate estimation of wall shear stress from 4D flow magnetic resonance downstream of a severe stenosis”. In: *Magnetic Resonance in Medicine* 86.3 (2021), pp. 1531–1543. eprint: `https://onlinelibrary.wiley.com/doi/pdf/10.1002/mrm.28795` (cit. on pp. 2, 114).

[Cow87] Stephen J Cowley. “High frequency Rayleigh instability of Stokes layers”. In: *Stability of time dependent and spatially varying flows*. Springer, 1987, pp. 261–275 (cit. on pp. 18, 62).

[CG05] Kristopher S Cunningham and Avrum I Gotlieb. “The role of shear stress in the pathogenesis of atherosclerosis”. In: *Laboratory investigation* 85.1 (2005), pp. 9–23 (cit. on p. 2).

[DHB92] F. Daviaud, J. Hegseth, and P. Bergé. “Subcritical transition to turbulence in plane Couette flow”. In: *Physical review letters* 69 (17 1992), pp. 2511–2514 (cit. on p. 8).

[Dav15] Peter Alan Davidson. *Turbulence: an introduction for scientists and engineers*. Oxford university press, 2015 (cit. on pp. 1, 2, 5, 7, 12, 13).

[DTH23] Yves Dubief, Vincent E. Terrapon, and Björn Hof. “Elasto-Inertial Turbulence”. In: *Annual Review of Fluid Mechanics* 55.1 (2023), pp. 675–705. eprint: `https://doi.org/10.1146/annurev-fluid-032822-025933` (cit. on p. 116).

[Eck10] Michael Eckert. “The troublesome birth of hydrodynamic stability theory: Sommerfeld and the turbulence problem”. In: *The European Physical Journal H* 35.1 (2010), pp. 29–51 (cit. on p. 7).

[EP75] T. Ellingsen and E. Palm. “Stability of linear flow”. In: *The Physics of Fluids* 18.4 (Apr. 1975), pp. 487–488 (cit. on p. 10).

[EJ20] Miguel P Encinar and Javier Jiménez. “Momentum transfer by linearised eddies in turbulent channel flows”. In: *Journal of Fluid Mechanics* 895 (2020), A23 (cit. on pp. 14, 65).

[Eul52] Leonhard Euler. “Découverte d’un nouveau principe de mécanique”. In: *Mémoires de l’académie des sciences de Berlin* (1752), pp. 185–217 (cit. on p. 5).

[Fel+23] Daniel Feldmann, Daniel Borrero-Echeverry, Michael J Burin, Kerstin Avila, and Marc Avila. “Routes to turbulence in Taylor–Couette flow”. In: *Philosophical Transactions of the Royal Society A* 381.2246 (2023), p. 20220114 (cit. on p. 13).

[FMA21] Daniel Feldmann, Daniel Morón, and Marc Avila. “Spatiotemporal Intermittency in Pulsatile Pipe Flow”. In: *Entropy* 23.1 (2021) (cit. on pp. 73, 76, 77, 82, 106, 108, 167).

[Fjø50] Ragnar Fjørtoft. *Application of integral theorems in deriving criteria of stability for laminar flows and for the baroclinic circular vortex*. Vol. 17. Grøndahl & søns boktr., I kommisjon hos Cammermeyers boghandel Oslo, 1950 (cit. on p. 8).

[FBF20] Catarina G Fonseca, Pedro Barbacena, and Claudio A Franco. “Endothelial cells on the move: dynamics in vascular morphogenesis and disease”. In: *Vascular Biology* 2.1 (2020), H29–H43 (cit. on p. 3).

[For88] Bengt Fornberg. “Generation of Finite Difference Formulas on Arbitrarily Spaced Grids”. In: *Mathematics of Computation* 51.184 (1988), pp. 699–706 (cit. on p. 31).

[FH64] Edward D Freis and William C Heath. “Hydrodynamics of aortic blood flow”. In: *Circulation research* 14.2 (1964), pp. 105–116 (cit. on p. 2).

[FG22] Anna Frishman and Tobias Grafke. “Mechanism for turbulence proliferation in subcritical flows”. In: *Proceedings of the Royal Society A: Mathematical, Physical and Engineering Sciences* 478.2265 (2022), p. 20220218. eprint: https://royalsocietypublishing.org/doi/pdf/10.1098/rspa.2022.0218 (cit. on p. 15).

[FC80] Frederick N Fritsch and Ralph E Carlson. “Monotone piecewise cubic interpolation”. In: *SIAM Journal on Numerical Analysis* 17.2 (1980), pp. 238–246 (cit. on p. 24).

[GN10] Jonathan Golledge and Paul E Norman. *Atherosclerosis and abdominal aortic aneurysm: cause, response, or common risk factors?* 2010 (cit. on p. 2).

[Gül+18] Utku Gülan, Christelle Calen, Firat Duru, and Markus Holzner. “Blood flow patterns and pressure loss in the ascending aorta: a comparative study on physiological and aneurysmal conditions”. In: *Journal of Biomechanics* 76 (2018), pp. 152–159 (cit. on p. 2).

[Ha+16] Hojin Ha, Guk Bae Kim, Jihoon Kweon, et al. “The influence of the aortic valve angle on the hemodynamic features of the thoracic aorta”. In: *Scientific reports* 6.1 (2016), p. 32316 (cit. on pp. 3, 114).

[HW10] Georg Hager and Gerhard Wellein. *Introduction to high performance computing for scientists and engineers*. CRC Press, 2010 (cit. on p. 40).

[Hof+08] Björn Hof, Alberto De Lozar, Dirk Jan Kuik, and Jerry Westerweel. “Repeller or attractor? Selecting the dynamical model for the onset of turbulence in pipe flow”. In: *Physical review letters* 101.21 (2008), p. 214501 (cit. on p. 44).

[Hof+10] Björn Hof, Alberto de Lozar, Marc Avila, Xiaoyun Tu, and Tobias M. Schneider. “Eliminating Turbulence in Spatially Intermittent Flows”. In: *Science* 327.5972 (2010), pp. 1491–1494. eprint: https://www.science.org/doi/pdf/10.1126/science.1186091 (cit. on pp. 15, 101, 114, 139).

[HZ] Markus Holzner and Till Zeugin. *Fuid structure interaction in pulsatile flow*. https://www.slf.ch/de/projekte/fluid-structure-interaction-in-pulsatile-flow/. [Online; accessed 17-January-2024] (cit. on p. 3).

[HR98] Sandrine Hugues and Anthony Randriamampianina. “An improved projection scheme applied to pseudospectral methods for the incompressible Navier–Stokes equations”. In: *International Journal for Numerical Methods in Fluids* 28.3 (1998), pp. 501–521 (cit. on p. 51).

[Jim18] Javier Jiménez. “Coherent structures in wall-bounded turbulence”. In: *Journal of Fluid Mechanics* 842 (2018), P1 (cit. on p. 12).

[Jim13] Javier Jiménez. “How linear is wall-bounded turbulence?” In: *Physics of Fluids* 25.11 (2013) (cit. on p. 14).

[JM91] Javier Jiménez and Parviz Moin. “The minimal flow unit in near-wall turbulence”. In: *Journal of Fluid Mechanics* 225 (1991), pp. 213–240 (cit. on p. 13).

[JP99] Javier Jiménez and Alfredo Pinelli. “The autonomous cycle of near-wall turbulence”. In: *Journal of Fluid Mechanics* 389 (1999), pp. 335–359 (cit. on p. 13).

[Kar+14] Safoora Karimi, Mahsa Dabagh, Paritosh Vasava, et al. “Effect of rheological models on the hemodynamics within human aorta: CFD study on CT image-based geometry”. In: *Journal of Non-Newtonian Fluid Mechanics* 207 (2014), pp. 42–52 (cit. on p. 3).

[KD74] Christian Von Kerczek and Stephen H. Davis. “Linear stability theory of oscillatory Stokes layers”. In: *Journal of Fluid Mechanics* 62.4 (1974), 753–773 (cit. on p. 17).

[Ker+21] J Simon Kern, Miguel Beneitez, Ardeshir Hanifi, and Dan S Henningson. “Transient linear stability of pulsating Poiseuille flow using optimally time-dependent modes”. In: *Journal of Fluid Mechanics* 927 (2021), A6 (cit. on pp. 11, 18, 62).

[Ker18] Rich R. Kerswell. “Nonlinear Nonmodal Stability Theory”. In: *Annual Review of Fluid Mechanics* 50.1 (2018), pp. 319–345. eprint: `https://doi.org/10.1146/annurev-fluid-122316-045042` (cit. on p. 11).

[KS84] L. Kleiser and U. Schumann. “Spectral simulations of the laminar-turbulent transition process in plane Poiseuille flow”. In: *8th Internat.Conf.on Numerical Methods in Fluid Dynamics, Aachen, June 28 - July 2, 1982 Voigt, R.G. et al. [Hrsg.] Proc.of the Symp.on Spectral Methods for Partial Differential Equations, Hampton, Va., August 16-18, 1982 Philadelphia: SIAM 1984*. 1984, pp. 141–63 (cit. on p. 36).

[KS80] L. Kleiser and U. Schumann. “Treatment of Incompressibility and Boundary Conditions in 3-D Numerical Spectral Simulations of Plane Channel Flows”. In: *Proceedings of the Third GAMM — Conference on Numerical Methods in Fluid Mechanics: DFVLR, Cologne, October 10 to 12, 1979*. Ed. by E. H. Hirschel. Wiesbaden: Vieweg+Teubner Verlag, 1980, pp. 165–173 (cit. on p. 36).

[Küh+18] Jakob Kühnen, Baofang Song, Davide Scarselli, et al. “Destabilizing turbulence in pipe flow”. In: *Nature Physics* 14.4 (2018), pp. 386–390 (cit. on pp. 15, 91, 101, 139).

[Les+10] Andrea S Les, Shawn C Shadden, C Alberto Figueroa, et al. “Quantification of hemodynamics in abdominal aortic aneurysms during rest and exercise using magnetic resonance imaging and computational fluid dynamics”. In: *Annals of biomedical engineering* 38.4 (2010), pp. 1288–1313 (cit. on pp. 2, 20, 69).

[Liu+24] Xu Liu, Hongbo Zhu, Yan Bao, et al. “Time-delayed characteristics of turbulence in pulsatile pipe flow”. In: *Journal of Fluid Mechanics* 979 (2024), A24 (cit. on p. 78).

[Lor63] Edward N Lorenz. “Deterministic nonperiodic flow”. In: *Journal of atmospheric sciences* 20.2 (1963), pp. 130–141 (cit. on p. 14).

[LD+21] Adrián Lozano-Durán, Navid C. Constantinou, Marios-Andreas Nikolaidis, and Michael Karp. “Cause-and-effect of linear mechanisms sustaining wall turbulence”. In: *Journal of Fluid Mechanics* 914 (2021), A8 (cit. on pp. 14, 115).

[Ló+20] Jose Manuel López, Daniel Feldmann, Markus Rampp, et al. “nsCouette – A high-performance code for direct numerical simulations of turbulent Taylor–Couette flow”. In: *SoftwareX* 11 (2020), p. 100395 (cit. on p. 21).

[MAI99] Adel M Malek, Seth L Alper, and Seigo Izumo. “Hemodynamic shear stress and its role in atherosclerosis”. In: *Jama* 282.21 (1999), pp. 2035–2042 (cit. on p. 2).

[Mal+16] S Malik, P Bordei, A Rusali, and DM Iliescu. “The descending thoracic aorta morphological characteristics”. In: *ARS Medica Tomitana* 22.3 (2016), pp. 186–191 (cit. on pp. 3, 4, 116).

[Mar+20] Elena Marensi, Zijing Ding, Ashley P. Willis, and Rich R. Kerswell. “Designing a minimal baffle to destabilise turbulence in pipe flows”. In: *Journal of Fluid Mechanics* 900 (2020) (cit. on p. 24).

[MZJ18] Chiang C Mei, J Zhang, and HX Jing. “Fluid mechanics of Windkessel effect”. In: *Medical & biological engineering & computing* 56 (2018), pp. 1357–1366 (cit. on pp. 3, 4).

[Mes+09] Alvaro Meseguer, Fernando Mellibovsky, Marc Avila, and Francisco Marques. “Instability mechanisms and transition scenarios of spiral turbulence in Taylor-Couette flow”. In: *Physical Review E* 80.4 (2009), p. 046315 (cit. on p. 13).

[MT00] Alvaro Meseguer and Lloyd N Trefethen. “A spectral Petrov-Galerkin formulation for pipe flow I: Linear stability and transient growth”. In: (2000) (cit. on pp. 54, 55, 59).

[MT03] Alvaro Meseguer and Lloyd N Trefethen. “Linearized pipe flow to Reynolds number 107”. In: *Journal of Computational Physics* 186.1 (2003), pp. 178–197 (cit. on pp. 8, 54).

[Mia+17] JJ Miau, RH Wang, TW Jian, and YT Hsu. “An investigation into inflection-point instability in the entrance region of a pulsating pipe flow”. In: *Proceedings of the Royal Society A: Mathematical, Physical and Engineering Sciences* 473.2197 (2017), p. 20160590 (cit. on pp. 17, 61).

[MFE04] Jeff Moehlis, Holger Faisst, and Bruno Eckhardt. “A low-dimensional model for turbulent shear flows”. In: *New Journal of Physics* 6.1 (2004), p. 56 (cit. on p. 15).

[MFA22] Daniel Morón, Daniel Feldmann, and Marc Avila. “Effect of waveform on turbulence transition in pulsatile pipe flow”. In: *Journal of Fluid Mechanics* 948 (2022), A20 (cit. on pp. 57, 82, 94, 167).

[Neb19] Jonathan R. A. Nebauer. “On the stability and transition of time-periodic pipe flow”. PhD thesis. Monash University, 2019 (cit. on pp. 17, 18, 61, 62).

[Orr07] William M’F. Orr. “The Stability or Instability of the Steady Motions of a Perfect Liquid and of a Viscous Liquid. Part I: A Perfect Liquid”. In: *Proceedings of the Royal Irish Academy. Section A: Mathematical and Physical Sciences* 27 (1907), pp. 9–68 (cit. on p. 11).

[Pea+98] J Peacock, T Jones, C Tock, and R Lutz. “The onset of turbulence in physiological pulsatile flow in a straight tube”. In: *Experiments in fluids* 24.1 (1998), pp. 1–9 (cit. on p. 16).

[PHC78] WR Peltler, J Halle, and TL Clark. “The evolution of finite amplitude Kelvin-Helmholtz billows”. In: *Geophysical & Astrophysical Fluid Dynamics* 10.1 (1978), pp. 53–87 (cit. on p. 8).

[Pey02] Roger Peyret. *Spectral methods for incompressible viscous flow*. Vol. 148. Springer, 2002 (cit. on p. 26).

[PS17] Benoît Pier and Peter J. Schmid. “Linear and nonlinear dynamics of pulsatile channel flow”. In: *Journal of Fluid Mechanics* 815 (2017), 435–480 (cit. on p. 65).

[PS21] Benoît Pier and Peter J. Schmid. “Optimal energy growth in pulsatile channel and pipe flows”. In: *Journal of Fluid Mechanics* 926 (2021), A11 (cit. on p. 17).

[PT22] Carlos Plana Turmo. “Phase-field simulations of two-phase pipe flow”. PhD thesis. University of Bremen, 2022 (cit. on pp. 31, 36, 40).

[Pop00] Stephen B Pope. *Turbulent flows*. Cambridge university press, 2000 (cit. on pp. 1, 152).

[PK10] Chris CT Pringle and Rich R. Kerswell. “Using nonlinear transient growth to construct the minimal seed for shear flow turbulence”. In: *Physical review letters* 105.15 (2010), p. 154502 (cit. on p. 10).

[Ray95] Rayleigh. “On the stability or instability of certain fluid motions (iii.)” In: *Proceedings of the London Mathematical Society* 1.1 (1895), pp. 5–12 (cit. on p. 8).

[Rem06] Dietmar Rempfer. “On Boundary Conditions for Incompressible Navier-Stokes Problems”. In: *Applied Mechanics Reviews* 59.3 (May 2006), pp. 107–125. eprint: `https://asmedigitalcollection.asme.org/appliedmechanicsreviews/article-pdf/59/3/107/5441529/107\_1.pdf` (cit. on p. 36).

[Rey83] Osborne Reynolds. “An experimental investigation of the circumstances which determine whether the motion of water shall be direct or sinuous, and of the law of resistance in parallel channels”. In: *Philosophical Transactions of the Royal society of London* 174 (1883), pp. 935–982 (cit. on pp. 7, 10).

[RCS19] Enrico Rinaldi, Jacopo Canton, and Philipp Schlatter. “The vanishing of strong turbulent fronts in bent pipes”. In: *Journal of Fluid Mechanics* 866 (2019), 487–502 (cit. on p. 116).

[Rom+21] Francesco Romanò, Antoine Charles, François Dottori, and S. Amir Bahrani. “Transition to turbulence in a heated non-Newtonian pipe flow”. In: *Physics of Fluids* 33.9 (2021), p. 091702. eprint: `https://doi.org/10.1063/5.0064456` (cit. on p. 15).

[RB20] Marco E Rosti and Luca Brandt. “Low Reynolds number turbulent flows over elastic walls”. In: *Physics of Fluids* 32.8 (2020) (cit. on p. 2).

[Sar66] Turgut Sarpkaya. “Experimental Determination of the Critical Reynolds Number for Pulsating Poiseuille Flow”. In: *Journal of Basic Engineering* 88.3 (Sept. 1966), pp. 589–598 (cit. on pp. 16, 17).

[Sca+23] Davide Scarselli, JM Lopez, Atul Varshney, and Bjoern Hof. “Turbulence suppression by cardiac-cycle-inspired driving of pipe flow”. In: *Nature* 621.7977 (2023), pp. 71–74 (cit. on pp. 16, 18).

[Sch33] Herman Schlichting. “Berechnung der Anfachung kleiner Störungen bei der Plattenströmung”. In: *ZAMM* 13.171-174 (1933), p. 50 (cit. on p. 8).

[Sch10] Peter J. Schmid. “Dynamic mode decomposition of numerical and experimental data”. In: *Journal of Fluid Mechanics* 656 (2010), pp. 5–28 (cit. on p. 14).

[SH94] Peter J. Schmid and Dan S. Henningson. “Optimal energy density growth in Hagen–Poiseuille flow”. In: *Journal of Fluid Mechanics* 277 (1994), 197–225 (cit. on pp. 10, 17, 113).

[SH00] Peter J. Schmid and Dan S. Henningson. *Stability and Transition in Shear Flows*. Applied Mathematical Sciences. Springer New York, 2000 (cit. on pp. 8–10, 17, 61, 62).

[Sco+20] Michael B Scott, Hyungkyu Huh, Pim van Ooij, et al. “Impact of age, sex, and global function on normal aortic hemodynamics”. In: *Magnetic resonance in medicine* 84.4 (2020), pp. 2088–2102 (cit. on p. 3).

[Sex30] Theodor Sexl. “Über den von E. G. Richardson entdeckten "Annulareffekt"”. In: *Zeitschrift für Physik* 61.5-6 (1930), pp. 349–362 (cit. on pp. 16, 45).

[Son+17] Baofang Song, Dwight Barkley, Björn Hof, and Marc Avila. “Speed and structure of turbulent fronts in pipe flow”. In: *Journal of Fluid Mechanics* 813 (2017), 1045–1059 (cit. on pp. 13, 15, 77, 89, 107, 139, 140).

[Sta+11] Aurélien F Stalder, Alex Frydrychowicz, Max F Russe, et al. “Assessment of flow instabilities in the healthy aorta using flow-sensitive MRI”. In: *Journal of magnetic resonance imaging* 33.4 (2011), pp. 839–846 (cit. on pp. 2, 20, 69).

[SH86] J. C. Stettler and A. K. M. Fazle Hussain. “On transition of the pulsatile pipe flow”. In: *Journal of Fluid Mechanics* 170 (1986), 169–197 (cit. on pp. 16, 17).

[Stu82] J. T. Stuart. “Hydrodynamic Stability. By P. G. DRAZIN and W. H. REID. Cambridge University Press, 1981. 525 pp. £35 (hardback).” In: *Journal of Fluid Mechanics* 124 (1982), 529–532 (cit. on p. 17).

[Tho+11] Christian Thomas, Andrew P Bassom, PJ Blennerhassett, and Christopher Davies. “The linear stability of oscillatory Poiseuille flow in channels and pipes”. In: *Proceedings of the Royal Society A: Mathematical, Physical and Engineering Sciences* 467.2133 (2011), pp. 2643–2662 (cit. on pp. 17, 114).

[Tol35] W. Tollmien. *Ein allgemeines Kriterium der Instabilität laminarer Geschwindigkeitsverteilungen, aus dem Kaiser Wilhelm-Institut für Strömungsforschung, Göttingen, von ... W. Tollmien ... Vorgelegt von L. Prandtl in der Sitzung am 8. März 1935*. Weidmannsche Buchhandlung, 1935 (cit. on p. 8).

[Tow61] A. A. Townsend. “Equilibrium layers and wall turbulence”. In: *Journal of Fluid Mechanics* 11.1 (1961), 97–120 (cit. on p. 12).

[Tre00] Lloyd N Trefethen. *Spectral methods in MATLAB*. SIAM, 2000 (cit. on pp. 35, 50).

[Tri+12] R Trip, DJ Kuik, J Westerweel, and C Poelma. “An experimental study of transitional pulsatile pipe flow”. In: *Physics of fluids* 24.1 (2012), p. 014103 (cit. on pp. 16, 17).

[Tru06] Kai Elmar Truckenmüller. “Stabilitätstheorie für die oszillierende Rohrströmung”. Dissertation. Hamburg: Helmut-Schmidt-Universität, 2006 (cit. on p. 17).

[TKV13] Alkiviadis Tsamis, Jeffrey T Krawiec, and David A Vorp. “Elastin and collagen fibre microstructure of the human aorta in ageing and disease: a review”. In: *Journal of the royal society interface* 10.83 (2013), p. 20121004 (cit. on p. 114).

[TJ13] Florian Tuerke and Javier Jiménez. “Simulations of turbulent channels with prescribed velocity profiles”. In: *Journal of Fluid Mechanics* 723 (2013), 587–603 (cit. on p. 89).

[VM21] Alberto Vela-Martín. “The synchronisation of intense vorticity in isotropic turbulence”. In: *Journal of Fluid Mechanics* 913 (2021), R8 (cit. on p. 89).

[WBH16] Chenyang Weng, Susann Boij, and Ardeshir Hanifi. “Numerical and theoretical investigation of pulsatile turbulent channel flows”. In: *Journal of Fluid Mechanics* 792 (2016), 98–133 (cit. on p. 78).

[Wil17] Ashley P. Willis. “The Openpipeflow Navier–Stokes solver”. In: *SoftwareX* 6 (2017), pp. 124–127 (cit. on p. 36).

[Wom55] John Ronald Womersley. “Method for the calculation of velocity, rate of flow and viscous drag in arteries when the pressure gradient is known”. In: *The Journal of Physiology* 127.3 (Mar. 1955), pp. 553–563 (cit. on pp. 16, 45, 57, 80, 103).

[WC73] I. J. Wygnanski and F. H. Champagne. “On transition in a pipe. Part 1. The origin of puffs and slugs and the flow in a turbulent slug”. In: *Journal of Fluid Mechanics* 59.2 (1973), 281–335 (cit. on p. 13).

[XT10] Guanglei Xiong and Charles A. Taylor. “Influence of vessel roughness on wall shear stress in image-based blood flow modeling”. In: *2010 IEEE International Symposium on Biomedical Imaging: From Nano to Macro*. 2010, pp. 33–36 (cit. on p. 3).

[XA18] Duo Xu and Marc Avila. “The effect of pulsation frequency on transition in pulsatile pipe flow”. In: *Journal of Fluid Mechanics* 857 (2018), pp. 937–951 (cit. on pp. 16, 17, 72, 74, 78, 115).

[XSA21] Duo Xu, Baofang Song, and Marc Avila. “Non-modal transient growth of disturbances in pulsatile and oscillatory pipe flows”. In: *Journal of Fluid Mechanics* 907 (2021) (cit. on pp. 11, 17, 18, 50, 57, 58, 61, 62, 65, 94).

[Xu+20] Duo Xu, Atul Varshney, Xingyu Ma, et al. “Nonlinear hydrodynamic instability and turbulence in pulsatile flow”. In: *Proceedings of the National Academy of Sciences* 117.21 (2020), pp. 11233–11239 (cit. on pp. 17, 18, 57, 73, 113, 114).

[Xu+17] Duo Xu, Sascha Warnecke, Baofang Song, Xingyu Ma, and Björn Hof. “Transition to turbulence in pulsating pipe flow”. In: *Journal of Fluid Mechanics* 831 (2017), pp. 418–432 (cit. on pp. 16, 17).

List of Figures

List of Tables

List of Symbols

Non-dimensional numbers/parameters

$Re_{\max}$	Maximum Reynolds number
Re_τ	Shear Reynolds number
Re_c	Critical Reynolds number
$Re_i\,(t)$	Instantaneous Reynolds number
CFL	Courant number
a_n, b_n	Harmonics of the bulk velocity
F_t	Turbulence fraction in the pipe
M_θ	Number of azimuthal points after aliasing
M_x	Number of axial points after aliasing
N_θ	Half number of azimuthal modes
N_r	Number of radial points
N_x	Half number of axial modes
t_m, t_{ac}, t_{dc}	Parameters to define the waveform of the pulsation
A	Amplitude of pulsation
Re	Reynolds number
Wo	Womersley number

Greek Letters

α	Fourier axial wavenumber	$1/D$
β	Correction to the bulk velocity	
Δt	Time step size in simulations	D/U

Δt_i	Fraction of the pulsation period where the profile has one inflection point	T
Δt_u	Fraction of the pulsation period where the profile is unstable	T
δ	Parameter in the Barkley model	
ϵ	Parameter in the Barkley model (turbulence relaxation time)	
η	Kolmogorov length scale	
γ	Parameter of the EBM (intensity of linear instability term)	
λ_{max}	Maximum eigenvalue of the instantaneous laminar profile w.r.t. time	U/D
λ_i	Time weighted averaged eigenvalue (proxy)	U/D
λ_j	Eigenvalues of the instantaneous laminar profile	U/D
μ	Dynamic viscosity	kg/ms
ν	Kinematic viscosity	m^2/s
ϕ	Phase shift	rad
$\boldsymbol{\omega}(\boldsymbol{x}, t)$	Vorticity field	U/D
ψ	Time-scale correction between the EBM or BM; and DNS	
ρ_f	Fluid density	kg/m^3
σ	Parameter in the Barkley model (noise intensity term)	
τ	Mean puff lifetime	D/U
$\tau(x, t)$	White Gaussian noise in space and time of the BM and EBM	
τ_w	Wall shear stress	U^3/D
θ	Azimuthal direction	rad
ε	Turbulent dissipation	U^3/D
ζ	Parameter in the Barkley model (advective term)	
u_τ	Shear velocity	U

Latin Letters

$\boldsymbol{e}_x$	Unit axial vector	
$\boldsymbol{f}_b$	Body force	U^2/D
$\boldsymbol{u}(\boldsymbol{x}, t)$	Non-dimensional velocity field	U

$\boldsymbol{u}_0$	Initial velocity field	U
$\boldsymbol{x}$	Non-dimensional position in the flow	D
c_d	Downstream front speed	U
c_u	Upstream front speed	U
D	Pipe diameter	m
D_q	Parameter in the Barkley model	
E	Perturbation energy production	U^2
$E_L\,(t)$	Volume-averaged laminar axial kinetic energy	U^2
$E_M\,(t)$	Volume-averaged master axial kinetic energy	U^2
f	Pulsation frequency	$1/s$
f_p	Driving pressure gradient	U^2/D
$F_{v_0}\,(t)$	Center-line averaged viscous stresses	U/D^2
G	Maximal transient energy growth	
G_{LSA}	LSA energy growth	
G_{TGA}	TGA energy growth	
k	Axial Fourier wavenumber	
k_0	First axial harmonic	rad$/D$
L_x	Length of the pipe	D
m	Azimuthal Fourier wavenumber	
m_0	First azimuthal harmonic	
P	Turbulence (perturbation) energy production	U^3/D
$p\,(\boldsymbol{x}, t)$	Non-dimensional dynamic pressure field	U^2
Q	Condition for inviscid instability in cylindrical coordinates	U
$q\,(x, t)$	Turbulence intensity in the Barkley model	
R	Pipe radius	m
r	Control parameter in the Barkley model	
r	Radial (wall-normal) direction	D

T	Pulsation period	D/U
t	Time	D/U
t^*	Phase of the period	
U	Time-averaged bulk velocity	m/s
$u\,(x,t)$	Center-line velocity in the Barkley model	
$u_b\,(t)$	Bulk velocity	U
$U_c\,(t)$	Center-line velocity of the laminar profile	U
$U_{HP}\,(r)$	Hagen-Poiseuille velocity profile	U
$U_M\,(r,t)$	Master axial and azimuthal averaged (mean) axial velocity profile	U
$U_{SW}\,(r,t)$	Sexl-Womerlsey laminar profile	U
$U_S\,(r,t)$	Slave axial and azimuthal averaged (mean) axial velocity profile	U
V	Volume of the pipe	D^3
x	Axial (stream-wise) direction	D

Acronyms

BM	Barkley model
CFD	Computational Fluid Dynamics
DNS	Direct numerical simulation
EBM	Extended Barkley model
HP	Hagen-Poiseuille
LNSE	Linearized Navier–Stokes equations
LSA	Linear Stability Analysis
NSE	Navier–Stokes equations
SSPF	Statistically steady pipe flow
SW	Sexl-Womersley
TGA	Transient Growth Analysis

A Model for puffs and slugs in steady pipe flow

The model proposed by Barkley [Bar11a; Bar11b; Bar+15; Bar16] (here referred to as the Barkley Model BM) is able to reproduce the behavior of turbulent puffs and slugs in statistically steady pipe flow (SSPF). In this appendix the model is described in detail. Some important results of the BM and their comparison with DNS of SSPF are shown at the end. The main purpose of this appendix is to give an overview of the successful model by Barkley, that is extended to the case of puffs and slugs in pulsatile pipe flow in Chapter 7.

A.1 Derivation of the BM

In this section, the equations that describe the evolution of q and u in the BM are presented. The explanation follows the derivation presented by Barkley in [Bar16], and goes from the local (temporal) dynamics of q and u (§A.1.1), to the spatially extended model that includes advection and diffusion (§A.1.4). Finally, the need to use a stochastic term to better model the behavior of localized turbulence in statistically steady pipe flow is discussed (§A.1.6).

A.1.1 Local dynamics of the turbulence intensity in the BM

The local dynamics of q are described by the potential equation:

$$\frac{\mathrm{d}q}{\mathrm{d}t} = -\frac{\mathrm{d}V_q}{\mathrm{d}q} = f^*(q) = q\left[r - (r+\delta)(q-1)^2\right], \tag{A.1}$$

where r is a control parameter and δ a model parameter. The parameter r is proportional to the Reynolds number:

$$r = \frac{Re - R_0}{R_1 - R_0}, \tag{A.2}$$

being $R_0 = 1920$ and $R_1 = 2250$ for the case of pipe flow and $\delta = 0.1$ [Bar+15].

At low r, the potential V_q has a single minimum, meaning that, the local dynamics have a single equilibrium at $q = 0$ (laminar flow), see fig. A.1a. Hence any $q > 0$ quickly decays. At a certain $r > r_1$ the potential V_q presents a global and a local minimum, see fig. A.1b. The global minimum corresponds to $q = 0$, and the local minimum to a certain $q > 0$. At this r the local dynamics are

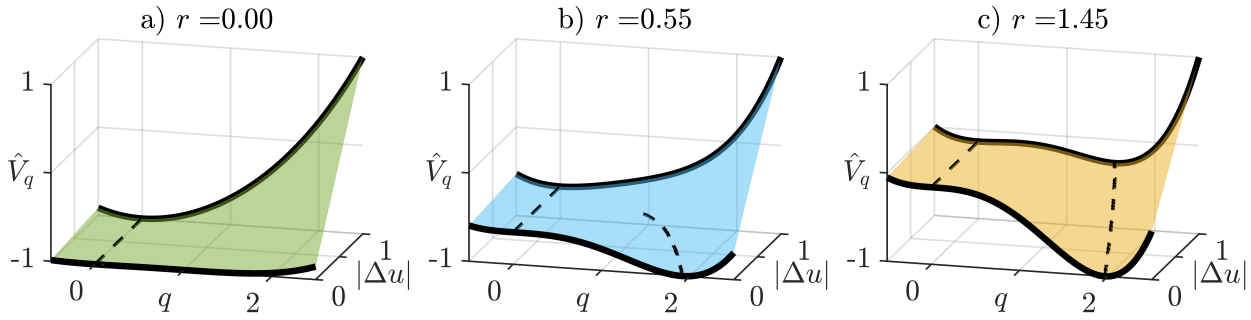

Fig. A.1.: Potential V_q in equation (A.4) as a function of turbulence intensity q and center-line velocity defect $\Delta u = U_c - u$ for three different r values. Find with dashed lines the local minimum of the function at each Δu. The potential V_q is normalized so it lays between $\hat{V}_q = -1$ and $\hat{V}_q = 1$, for the Δu and q considered here.

unconditionally stable for $q = 0$, and metastable for $q > 0$ (localized turbulence). As r further increases to $r > r_2$, $q = 0$ becomes a local minimum of the system, whereas $q > 0$ the global one, see fig. A.1c. In this case, the laminar profile is metastable, whereas the turbulent profile is unconditionally stable.

A.1.2 Local dynamics of the mean shear

The ordinary differential equation that describes the local dynamics of u reads:

$$\frac{\mathrm{d}u}{\mathrm{d}t} = g\,(q,u) = \epsilon\,(U_c - u) + 2\epsilon\,(u_b - u)\,q, \tag{A.3}$$

where ϵ is a model parameters.

According to equation (A.3), if there is no turbulence, $q = 0$, and $u < U_c$, the center-line velocity increases until it reaches the center-line velocity $U_c = 2$ of the laminar (parabolic) profile. The characteristic time of this viscous development of the laminar profile is set by the model parameter ϵ. According to Barkley, this parameter should be inversely proportional to the Reynolds number [Bar16], but it is fixed at $\epsilon = 0.2$ for all Re.

When the flow is locally turbulent $q > 0$ the center-line velocity decreases due to the effect of $q > 0$. The model assumes that the most disturbed mean shear possible is a plug like profile, where the center-line velocity equals the bulk velocity of SSPF $u = u_b = U = 1$. The parameter 2ϵ models the effect the turbulence intensity has on the mean shear.

A.1.3 Non-linear interactions in the local dynamics

As mentioned at the beginning of this appendix, the core idea of the BM is the non-linear interaction between q and u. The evolution of u, eq. (A.3), considers the effect q has on u. To model the effect u has on q, Barkley extends equation (A.1) to:

$$\frac{\mathrm{d}q}{\mathrm{d}t} = f\,(q,u) = q\left[r + u - U_c - (r+\delta)\,(q-1)^2\right]. \tag{A.4}$$

Note that if $u \equiv U_c$, one recovers equation (A.1).

The idea is that the growth of q is maximum when $u \equiv U_c$, when the mean profile is parabolic (laminar profile). When $u < U_c$, and therefore the profile is blunted, the growth of q is adversely affected. This is in line with direct numerical simulations and experiment results, where a blunter profile has been linked with a decrease in turbulence lifetime [Hof+10; Küh+18].

The non-linearly coupled ordinary differential equations (A.4) and (A.3) describe the local dynamics of q and u. After the model parameters δ, R_0, R_1 and ϵ are adjusted, the equations only depend on the control parameter r that is in turn set by Re. Importantly, r sets the equilibrium points of the equations: $\frac{\mathrm{d}q}{\mathrm{d}t} = \frac{\mathrm{d}u}{\mathrm{d}t} = 0$.

A.1.4 Spatially extended model

Puffs and slugs are localized structures that are advected by the flow and they move, elongate or shrink at certain front speeds. To model these dynamics the BM includes spatially extended features: advection and diffusion.

For the turbulence intensity, the equation reads

$$\frac{\partial q}{\partial t} = -\left(u - \zeta\right)\frac{\partial q}{\partial x} + f\left(q, u\right) + D_q \frac{\partial^2 q}{\partial x^2}, \tag{A.5}$$

where ζ and D_q are two additional model parameters. D_q represents the diffusion coefficient of q on the axial direction, whereas ζ corrects the mean advection velocity of q in the pipe.

The model assumes that the bulk of turbulent structures, q, is advected at a velocity close to, but smaller than, the center-line velocity. This was later confirmed in the DNS analysis of Song *et al.* [Son+17] where they identified that the mean advection speed of turbulent structures was $c_q \approx U_c\left(1 - (0.143 \pm 0.004)\right)$. The parameter ζ models this correction.

In the case of u, the equation reads

$$\frac{\partial u}{\partial t} = -u\frac{\partial u}{\partial x} + g\left(q, u\right). \tag{A.6}$$

A.1.5 About puffs and slugs in the BM

Equations (A.5) and (A.6) together with (A.4) and (A.3), define the deterministic version of the original Barkley Model. When its parameters, $(\delta,\ R_0,\ R_1,\ \epsilon,\ \zeta,\ D_q)$ are correctly fitted, the model is able to perfectly capture the front speeds of puffs and slugs in pipe and duct flows [Bar+15]. More importantly, the model allows to classify puffs and slugs as two distinct types of states/solutions.

At $r = r_1$, fig. A.2a, the system has a single point of equilibrium at $u = q = 0$ (laminar flow). However, at this r, when sufficiently perturbed, the system can have $q > 0$ during a certain time span before returning to $q = 0$. This corresponds to an excitable media, a system that has only one stable equilibrium point, but can be perturbed to an excitable state. Once excited the system takes a certain time to relax again to its equilibrium state, and then an additional time to be able to be excited again. This time is usually referred to as a refractory time. In spatially extended systems, this refractory time can be also understood as a refractory length. This is similar to the case of puffs, that can be triggered by exciting the laminar profile. Once a puff has been triggered, one needs to either wait a certain refractory time at a fixed location, or to move a given refractory length from the puff, to trigger a second one [Hof+10].

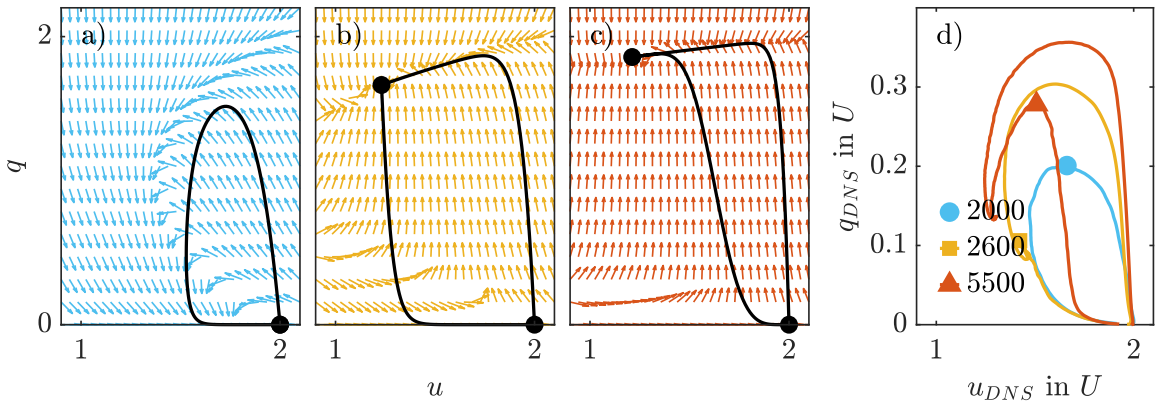

Fig. A.2.: Comparison between q and u trajectories according to equations (A.5) and (A.6) (a, b, c); and time averaged q_{DNS} and u_{DNS} (eq. (A.7)) trajectories in DNS (d). Model results correspond to BM simulations using the parameters listed in table A.1. The black lines correspond to the q and u trajectory according to the spatially extended equations (A.5) and (A.6); and the arrows represent the phase portrait computed using the local dynamics in equations (A.4) and (A.3). The black dots denote equilibrium points where $\frac{\mathrm{d}q}{\mathrm{d}t} = \frac{\mathrm{d}u}{\mathrm{d}t} = 0$. In a, at $Re = 2100$, $r = r_1 = 0.55$; in b, at $Re = 2400$, $r = r_2 = 1.46$ and in c, at $Re = 3000$, $r = r_3 = 3.27$. DNS results have been kindly lend by Prof. Baofang Song, from his results published in Song *et al.* [Son+17].

At $r = r_2, r_3 > r_1$ the system has two stable equilibrium points at $q = u = 0$ (laminar flow) and $q > 0$ $u < 2$ (turbulent flow), fig. A.2b and c. This corresponds to a bi-stable system where two different states can coexist in equilibrium. This is similar to the case of slugs, where a region of turbulent flow is stable. As shown below, the model is able to distinguish between weak and strong slugs. Weak slugs have a strong upstream front and a weak downstream font, see fig. A.2b, while strong slugs have only strong fronts, fig. A.2c.

When comparing q vs u in the BM, with the time averaged

$$q_{DNS} = \left\langle \sqrt{\langle u_r \rangle_{r,\theta}^2 + \langle u_\theta \rangle_{r,\theta}^2} \right\rangle_t \text{ vs } u_{DNS} = \langle u_x \left(r = 0\right) \rangle_t \,, \tag{A.7}$$

in the DNS, fig. A.2d, the model trajectories are qualitatively similar to the DNS results for the case of puffs, weak and strong slugs.

A.1.6 Stochastic model

Puffs and slugs are chaotic structures. Puffs can (randomly) decay, or split, and slugs present intermittent behaviors, with sudden changes of front speeds or relaminarization in some sections of their turbulent core. The BM only considers two variables, and it does not show any chaotic behavior for any value of r. In order to model these dynamics, Barkley considers a stochastic term. After including this last term the resultant stochastic-partial-differential equation of the turbulence intensity reads:

$$\frac{\partial q}{\partial t} = -\left(u - \zeta\right) \frac{\partial q}{\partial x} + f\left(q, u\right) + D_q \frac{\partial^2 q}{\partial x^2} + \sigma\tau\left(t, x\right) q, \tag{A.8}$$

being τ white Gaussian noise in space and time, and σ the strength of the noise.

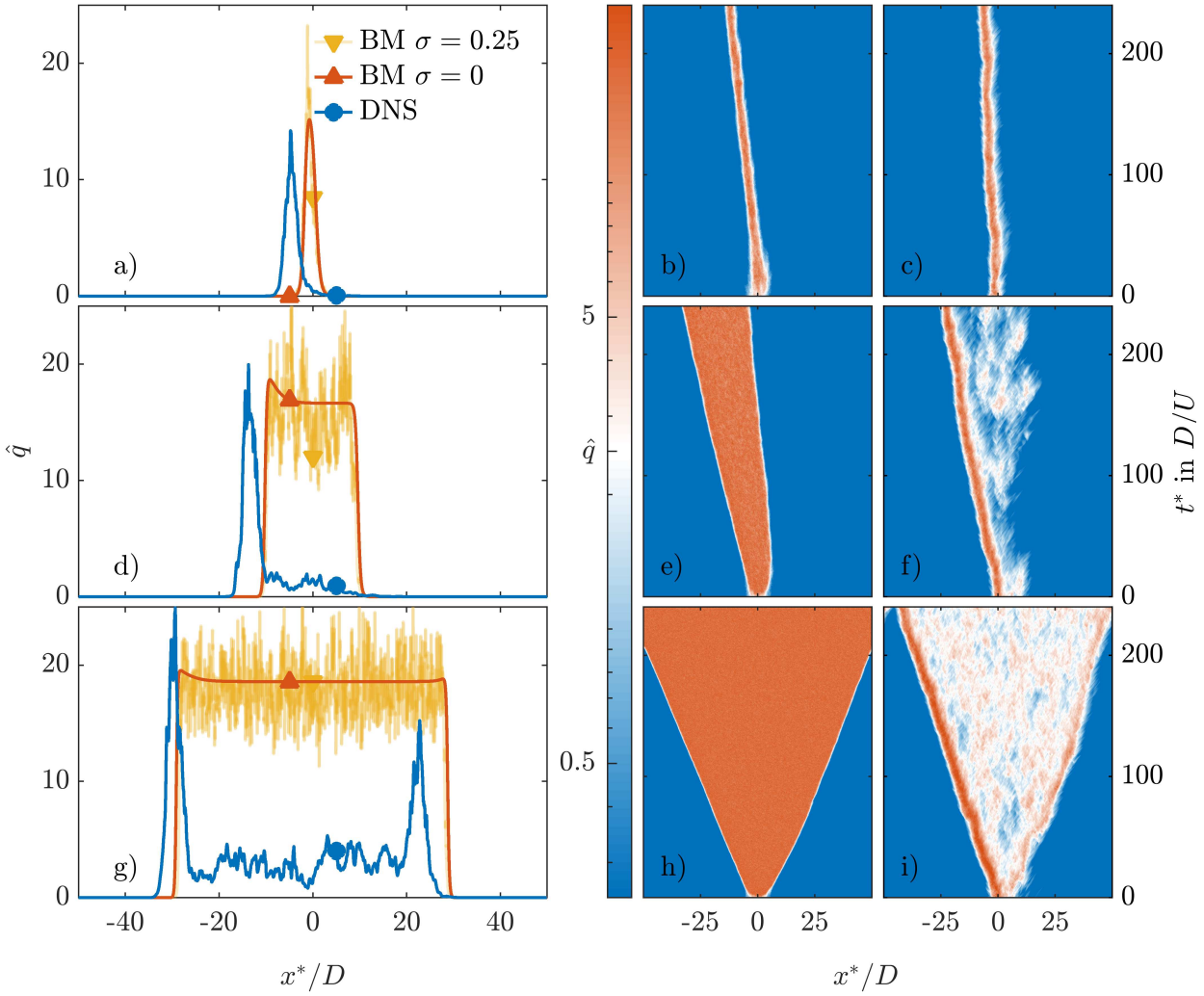

Fig. A.3.: Qualitative comparison between BM and DNS results of turbulence intensity $\hat{q}$, see eq (A.10), at different Re (or r, see eq. (A.2)). In a, b, c a puff at $Re = 2100$ $(r = 0.55)$; d, e, f a weak slug at $Re = 2400$ $(r = 1.46)$; g, h, i a strong slug at $Re = 3000$ $(r = 3.27)$. The BM simulations have been performed with the parameters listed in table A.1 and at either $\sigma = 0$ and $\sigma = 0.25$. Left subplots a, d, g compare the instantaneous $\hat{q}$ axial profiles of model and DNS at the same t^*. Here t^* is equal to the advective time scale in the DNS, and to the time scale of the model in the BM. The right subplots correspond to space-time diagrams of $\hat{q}$, of the BM (b, e, h) at $\sigma = 0.25$ and DNS (c, f, i). The results correspond to DNS and BM simulations in a $100D$ pipe, initialized with a localized puff of length $5D$. The figure is presented with respect to a moving frame x^*, moving with the bulk velocity u_b, and corresponding time scale t^*.

Tab. A.1.: BM fitted parameters [Bar+15].

R_0	R_1	ζ	D_q	σ	δ	ϵ
1920	2250	0.79	0.13	≤ 0.5	0.1	0.2

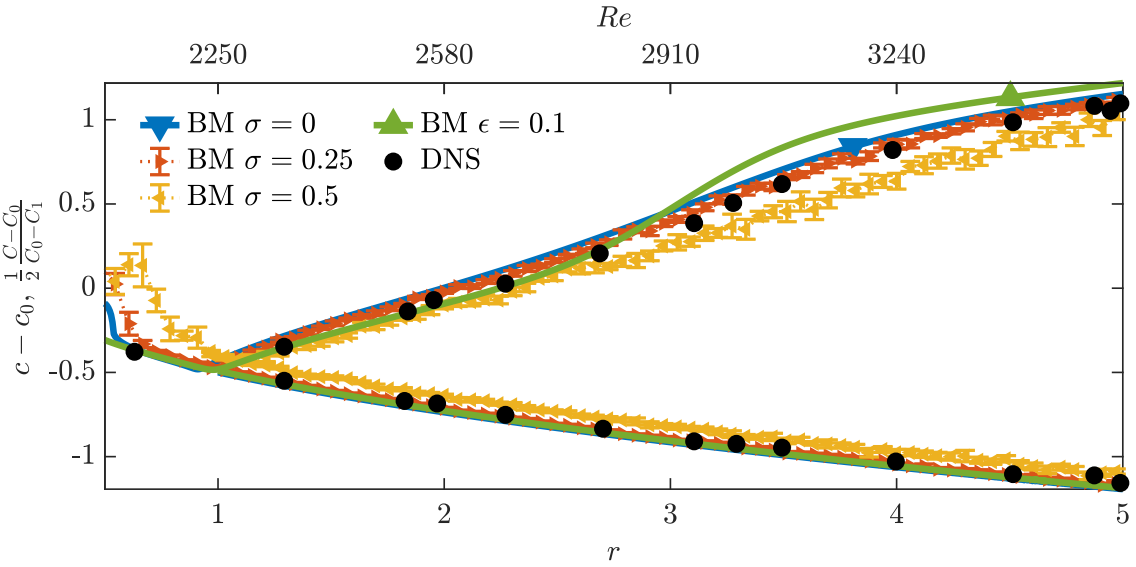

Fig. A.4.: Scaled front speeds c (C), see eq. (A.11), of puffs and slugs with respect to r (Re) according to the BM (DNS). The BM simulations are performed with the parameters listed in table A.1 unless stated otherwise in the corresponding legend item. The results of the BM are the mean front speed of $N_i = 100$ simulations, and corresponding 2 standard deviation errorbars at each r. The DNS results have been obtained from Barkley *et al.* [Bar+15].

Equations (A.8) and (A.6) together with (A.4) and (A.3), define the original BM.

A.2 Numerical methods

The second order derivatives are discretized with central finite-differences of second order, and the first-order derivatives with a first-order upwind scheme. Periodic boundary conditions are considered in x. The system is integrated using an explicit Euler method, with a time step size $\Delta t = 0.0025$. The pipe length is set to $L = 100$ and the grid spacing to a uniform $\Delta x = 0.5$. All the BM simulations are initialized with a localized 5 axial units long disturbance with magnitude $q \leq 0.5$.

A.3 Results of the model

After correctly fitting the model parameters, see table A.1, the BM can reproduce the front speeds of puffs and slugs for a wide range of Re [CXS22]. The front speeds measure the velocity at which the puffs and slugs are advected or elongated in pipe flow. In the case of puffs, the upstream c_u and downstream velocity c_d are equal, while for the case of slugs $c_d > c_u$. The case of a strong slug also satisfies $c_d \approx 2U - c_u$ [Bar16].

In figure A.4 the front speeds of the model are shown, compared with DNS results. The figure includes results of the model for three sets of parameters. Even after changing some parameters (ϵ, σ) the model returns front speeds remarkably close to those observed in DNS and experiments, highlighting its robustness.

Find in figure A.3 space time diagrams and instantaneous turbulence intensity axial profiles of DNS and BM results. The cross section axial vorticity squared is computed as:

$$\langle \omega_x^2 \rangle_{r,\theta}(x,t) = \frac{1}{\pi R^2} \int_0^R \int_0^{2\pi} \omega_x^2 \, r \, \mathrm{d}r \, \mathrm{d}\theta \tag{A.9}$$

and represents an indicator of the existence and magnitude of turbulence in each axial x location in the DNS. In this thesis, these indicator is chosen before q_{DNS}, eq. (A.7), since $10 \cdot q$ in the BM has a remarkably similar magnitude to it. The parameter $\hat{q}$ represents a general turbulent indicator and corresponds to eq. (A.9) for the DNS results, and $10 \cdot q$ for the BM results:

$$\hat{q} = \begin{cases} 10 \cdot q, & \text{BM} \\ \frac{1}{\pi R^2} \int_0^R \int_0^{2\pi} \omega_x^2 \, r \, \mathrm{d}r \, \mathrm{d}\theta, & \text{DNS} \end{cases} \tag{A.10}$$

As seen in figure A.3 the model is able to qualitatively capture the behaviour of turbulent fronts at all studied Re. However it does not capture the actual shape of slugs in steady pipe flow. See in figure A.3d and g a comparison of instantaneous slugs in DNS and on the model. The model overestimates the amplitude of q in the core of the slug. In the case of the DNS there is a clear difference between the turbulence magnitude in the upstream front and on the core. This was already noted by Barkley [Bar16]. This discrepancy is not important for the front speeds of the slugs in the model, when compared with those computed in the DNS, but results in qualitative differences between the axial behavior of $\hat{q}$ as seen in figures A.3 and A.5.

A.3.1 Time scale of the model

In order to compare the front speeds of the model c with the front speeds observed in DNS and experiments C, Barkley proposes the scaling:

$$c - c_0 = \frac{1}{2} \frac{C - C_1}{C_0 - C_1}. \tag{A.11}$$

Here C_0 is the front speed in advective units (U) at $Re = R_0$ and C_1 at $Re = R_1$. In the case of pipe flow $C_0 = 1.06U$ and $C_1 = 0.92U$. By setting this scaling, the front speeds calculated by the model almost perfectly match the front speeds observed in DNS and experiments.

Equation (A.11) indicates that the front speeds calculated with the BM, are scaled with a factor

$$\psi = 2\,(C_0 - C_1) = 0.28, \tag{A.12}$$

to the corresponding velocity of the actual puffs in pipe flow. This difference between velocity scales, can also be understood as a time scale difference between model and DNS/experiments. Note that the model has no units. In the rest of this thesis, it is assumed that an advective time unit (U/D) in DNS/experiments corresponds to 0.28 time units in the model.

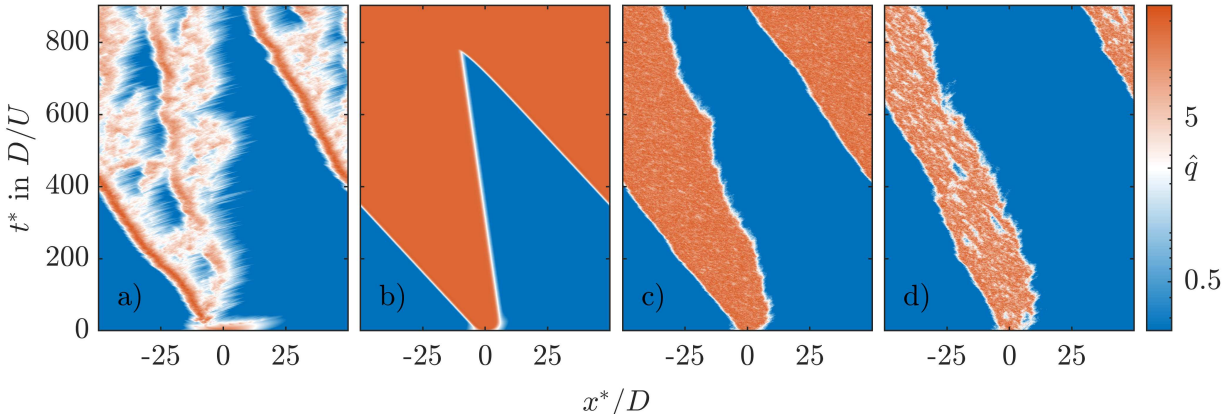

Fig. A.5.: Space-time diagram of the cross section integral of axial vorticity squared (eq. (A.9)) of DNS (a) and $10 \cdot q$ of the BM (b, c, d) with the parameters in table A.1. The results correspond to DNS and BM simulations in a $100D$ pipe, at $Re = 2400$, initialized with a localized puff of length $5D$. The figure is presented with respect to a moving frame x^*, moving with the bulk velocity u_b, and time t^* in advective time units for DNS, and model units for the BM. Subplot b) corresponds to a simulation of the BM with $\sigma = 0$; c) $\sigma = 0.5$ and d) $\sigma = 0.7$.

A.4 Limitations of the model

Despite being able to perfectly capture front speeds, the model has some limitations that are worth mentioning. The first big limitation is the aforementioned overestimation of the magnitude of q in the core of the slugs in the BM. Additionally, and as also previously noted, the model does not have clear physical units. This makes it difficult to compare with actual DNS or experimental results. Another source of concern is the long list of parameters of the model. In particular the model includes at least three different time rates ϵ, D_q and δ. This means that the model includes at least three different time scales, apart the time scale of the whole model.

Furthermore, the model does not capture the chaotic behaviors of localized turbulence in the Re regime $2250 \lesssim Re \lesssim 2500$. In this regime, according to the BM, puffs elongate into slugs filling the whole pipe with turbulence, as seen in figure A.5b, c and d and figure A.3e. However, in full DNS, puffs in this regime are observed to elongate and split in a highly intermittent manner. At these Re the flow usually reaches a highly heterogeneous state, where localized turbulent patches coexist with laminar flow patches, see fig. A.5a and A.3f. This behaviour can only be approximated by radically increasing the noise parameter σ in the model, see fig. A.5d, but at the same time loosing the good agreement between model and DNS/experiments front speeds.

B LSA and waveform

Find in this appendix a series of plots that are meant to represent a short catalog of pulsatile pipe flows at different flow parameters. The figures are equivalent to figure 4.4, and they show the laminar profile and its corresponding instantaneous maximum eigenvalue $\lambda_{\max}$. In yellow, the instantaneous laminar profiles U_{SW} of a single harmonic pulsation, at the indicated Re, Wo and A, and phase of the period. To not interfere with one another the profiles are scaled using a scalar with arbitrary units so the all time maximum is smaller than $t/T = 0.15$, since only the development of U_{SW} in time is of interest. With points, find the existence and position r_i of inflection points in the profile. Filled points correspond to inflection points that also satisfy the Fjørtoft criterion locally $\frac{\partial^2 U_{SW}}{\partial r^2}\left(U_{SW} - U_{SW}\left(r_i\right)\right) < 0$. In red, the maximum real component out of all the instantaneous eigenvalues of the laminar profile $\lambda_{\max}$, which are computed as described in §3.5. The areas (dc) and (ac) denote the deceleration $\left(\frac{\mathrm{d}u_b}{\mathrm{d}t} < 0\right)$ and acceleration $\left(\frac{\mathrm{d}u_b}{\mathrm{d}t} > 0\right)$ phases of the period.

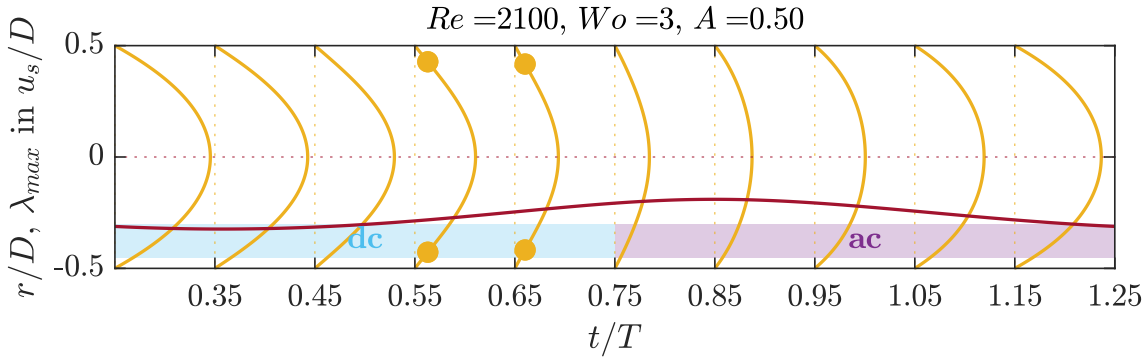

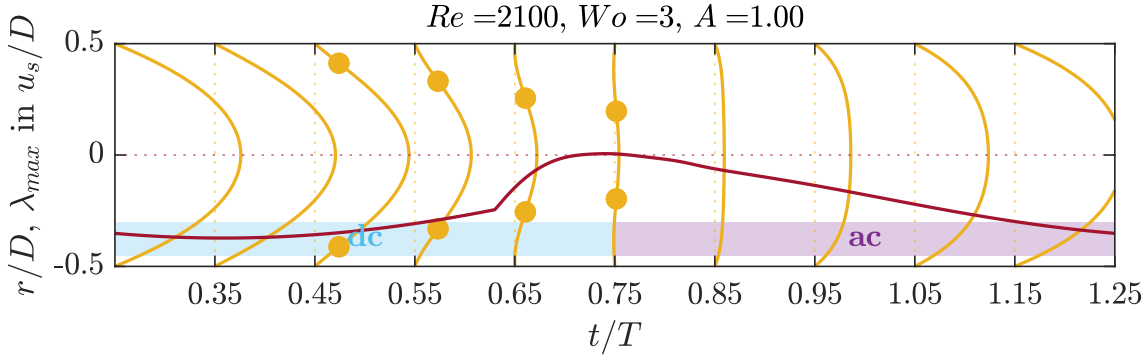

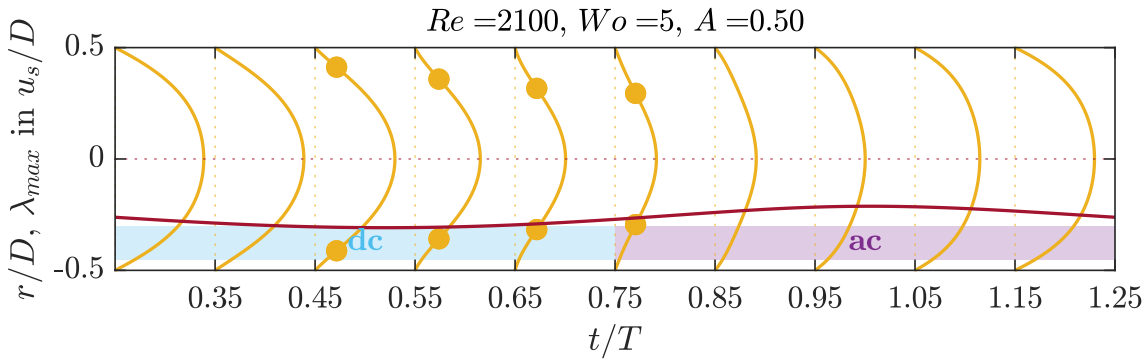
Re =2100, Wo =5, A =0.50
r/D, λ_{max} in u_s/D
0.5
0
-0.5
dc
ac
0.35 0.45 0.55 0.65 0.75 0.85 0.95 1.05 1.15 1.25
t/T

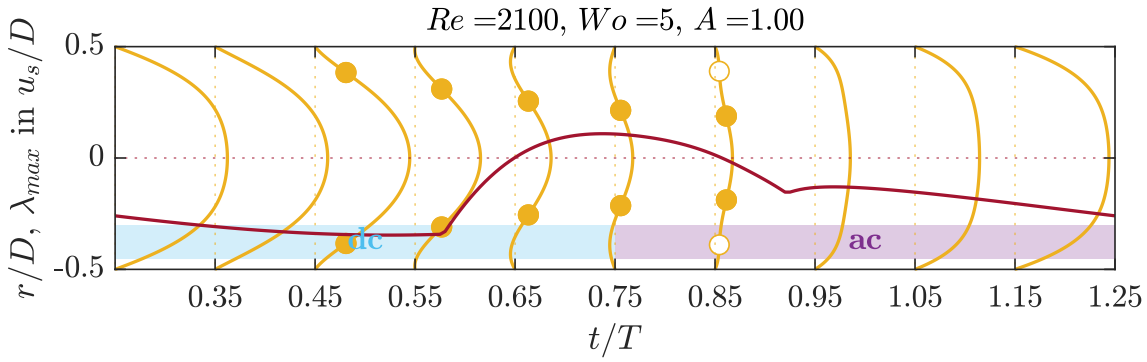
Re =2100, Wo =5, A =1.00
r/D, λ_{max} in u_s/D
0.5
0
-0.5
dc
ac
0.35 0.45 0.55 0.65 0.75 0.85 0.95 1.05 1.15 1.25
t/T

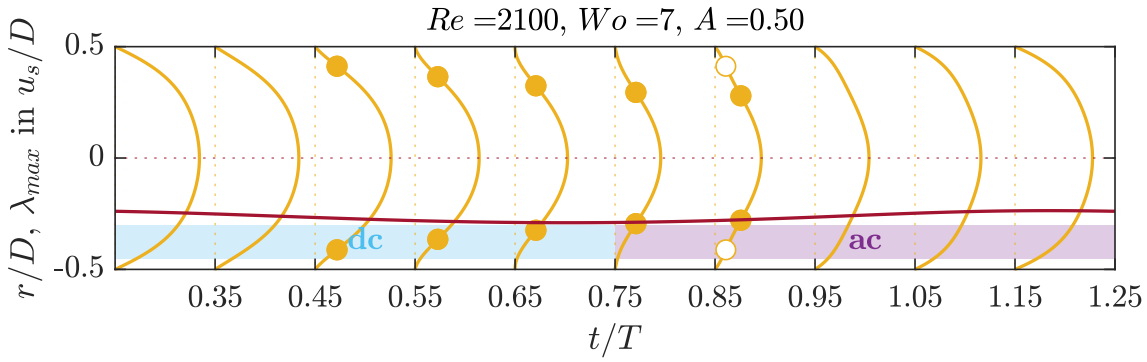
Re =2100, Wo =7, A =0.50
r/D, λ_{max} in u_s/D
0.5
0
-0.5
dc
ac
0.35 0.45 0.55 0.65 0.75 0.85 0.95 1.05 1.15 1.25
t/T

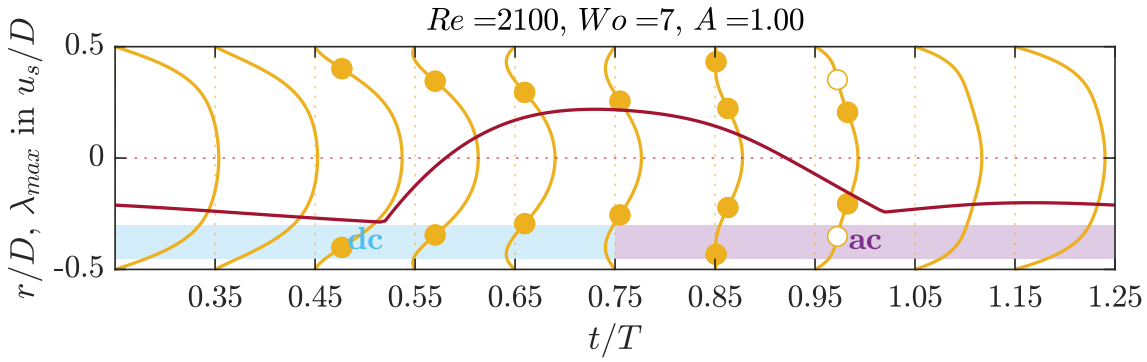
Re =2100, Wo =7, A =1.00
r/D, λ_{max} in u_s/D
0.5
0
-0.5
dc
ac
0.35 0.45 0.55 0.65 0.75 0.85 0.95 1.05 1.15 1.25
t/T

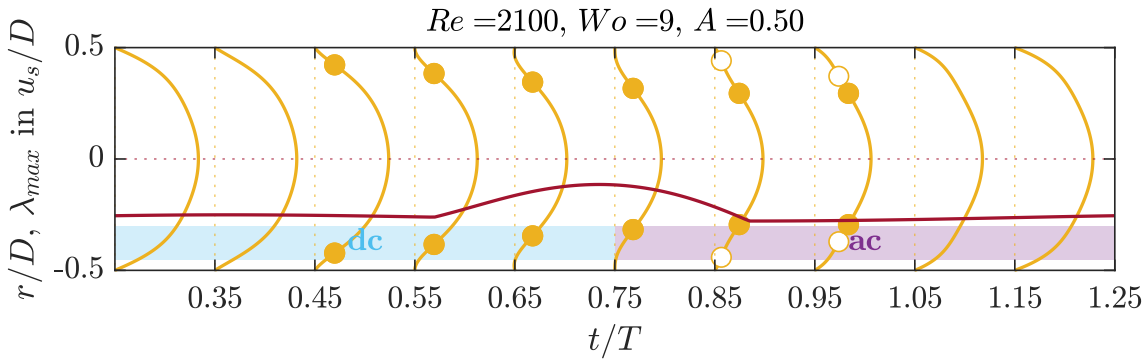
Re =2100, Wo =9, A =0.50
r/D, λmax in us/D
0.5
0
-0.5
dc
ac
0.35
0.45
0.55
0.65
0.75
0.85
0.95
1.05
1.15
1.25
t/T

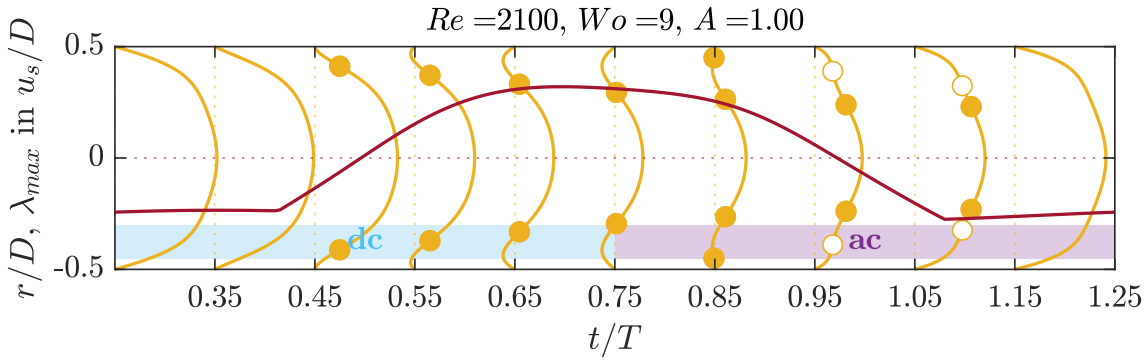
Re =2100, Wo =9, A =1.00
r/D, λmax in us/D
0.5
0
-0.5
dc
ac
0.35
0.45
0.55
0.65
0.75
0.85
0.95
1.05
1.15
1.25
t/T

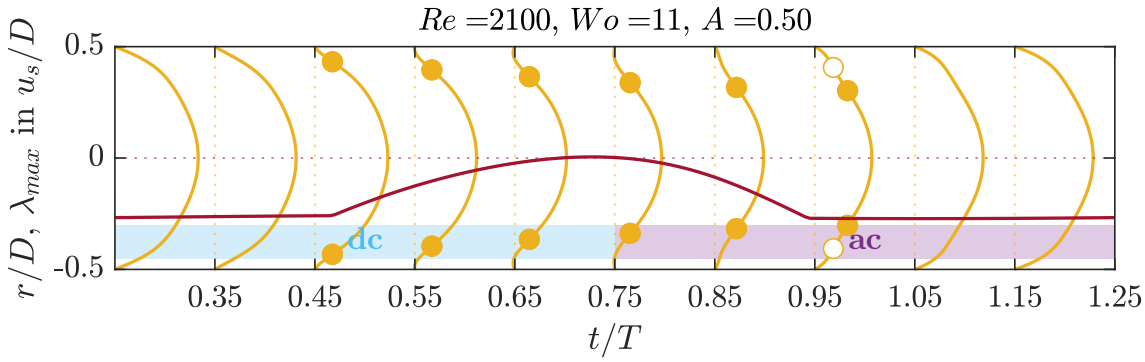
Re =2100, Wo =11, A =0.50
r/D, λmax in us/D
0.5
0
-0.5
dc
ac
0.35
0.45
0.55
0.65
0.75
0.85
0.95
1.05
1.15
1.25
t/T

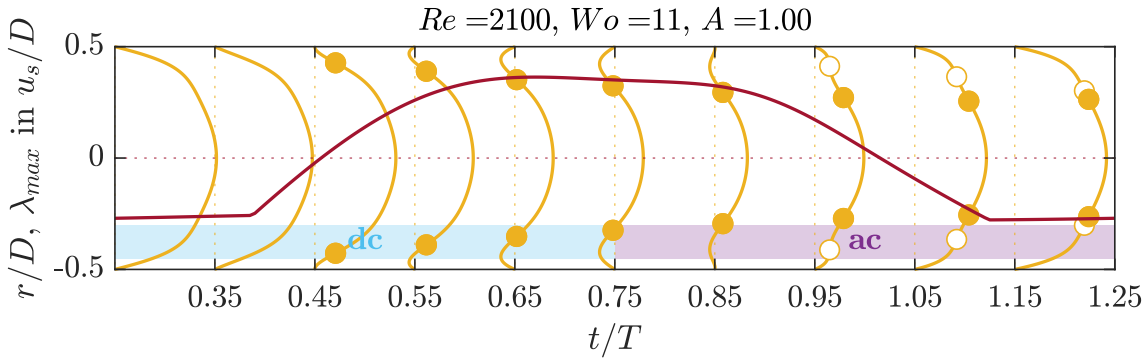
Re =2100, Wo =11, A =1.00
r/D, λmax in us/D
0.5
0
-0.5
dc
ac
0.35
0.45
0.55
0.65
0.75
0.85
0.95
1.05
1.15
1.25
t/T

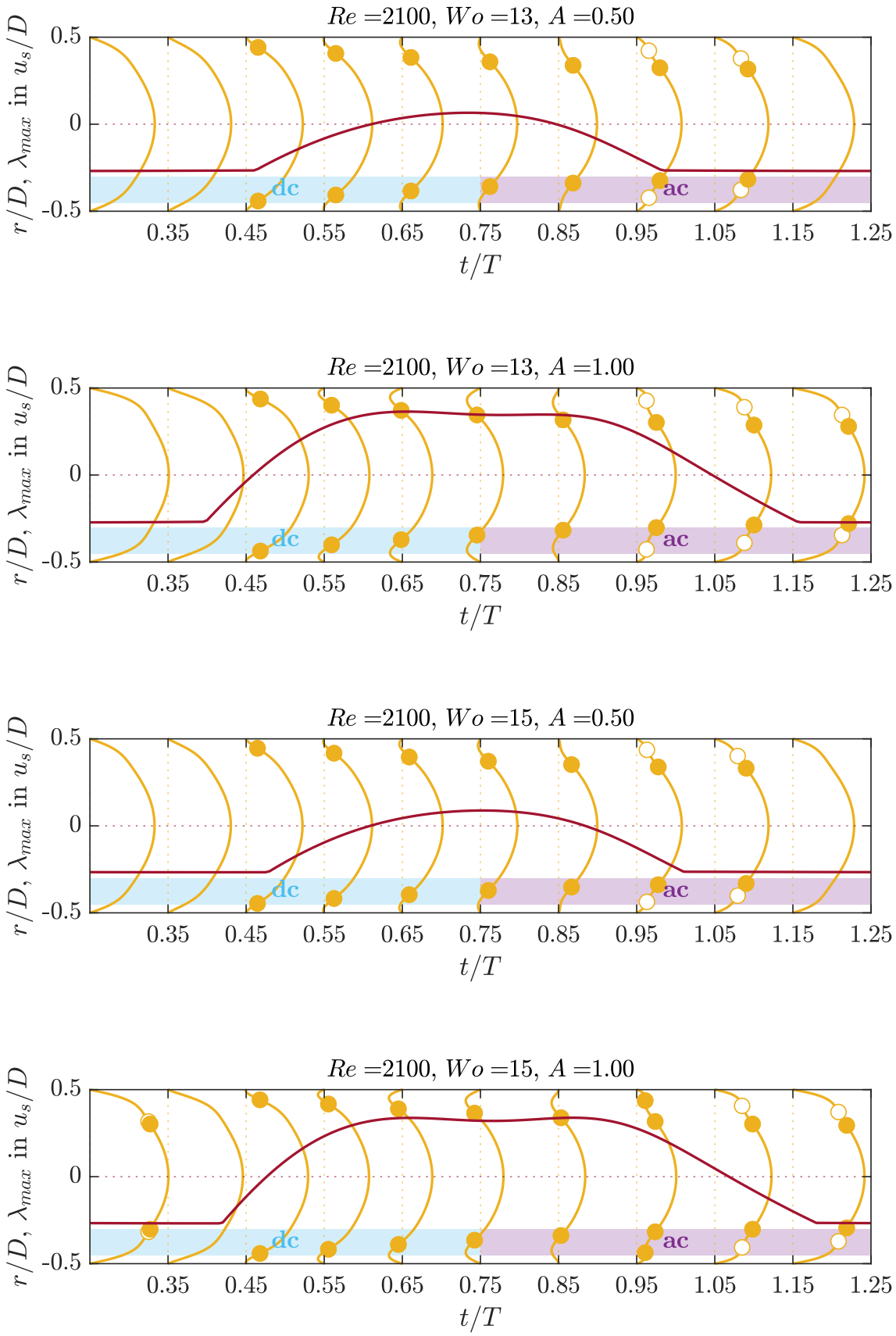
Re =2100, Wo =13, A =0.50
Re =2100, Wo =13, A =1.00
Re =2100, Wo =15, A =0.50
Re =2100, Wo =15, A =1.00
r/D, λmax in us/D
t/T
0.5
0
-0.5
0.35
0.45
0.55
0.65
0.75
0.85
0.95
1.05
1.15
1.25
dc
ac

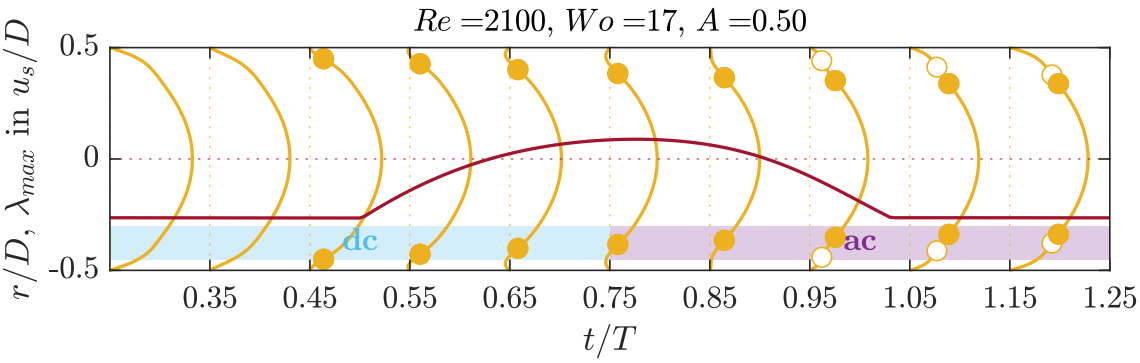
Re =2100, Wo =17, A =0.50
r/D, λmax in us/D
0.5
0
-0.5
dc
ac
0.35 0.45 0.55 0.65 0.75 0.85 0.95 1.05 1.15 1.25
t/T

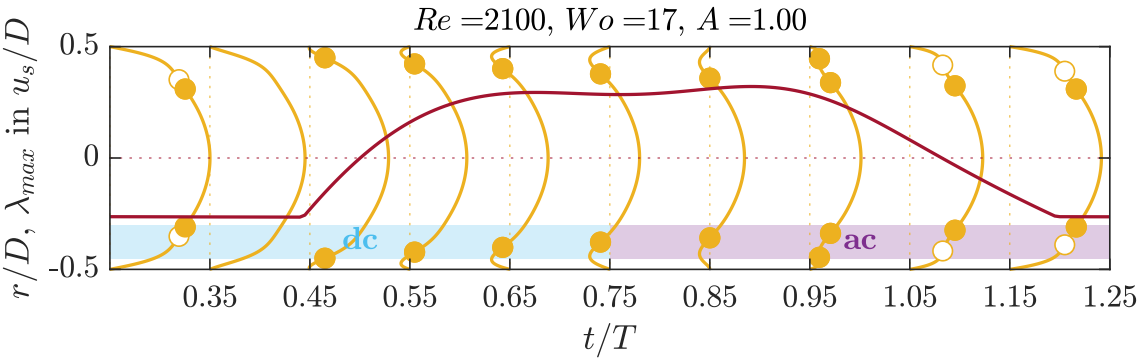
Re =2100, Wo =17, A =1.00
r/D, λmax in us/D
0.5
0
-0.5
dc
ac
0.35 0.45 0.55 0.65 0.75 0.85 0.95 1.05 1.15 1.25
t/T

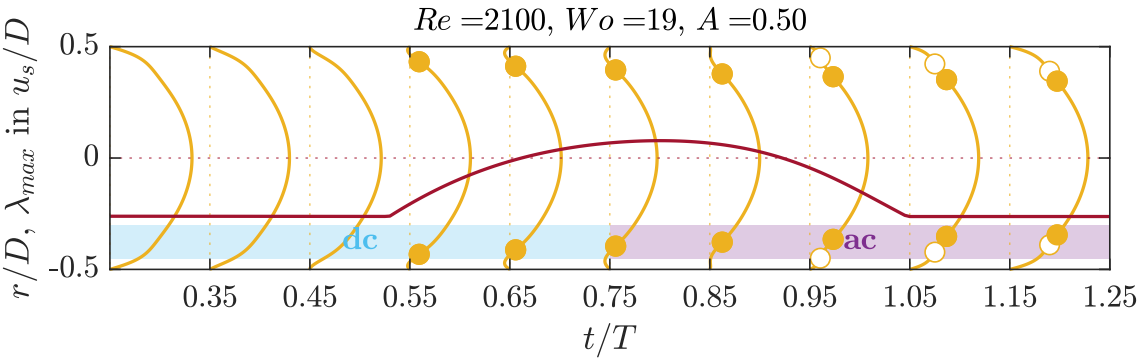
Re =2100, Wo =19, A =0.50
r/D, λmax in us/D
0.5
0
-0.5
dc
ac
0.35 0.45 0.55 0.65 0.75 0.85 0.95 1.05 1.15 1.25
t/T

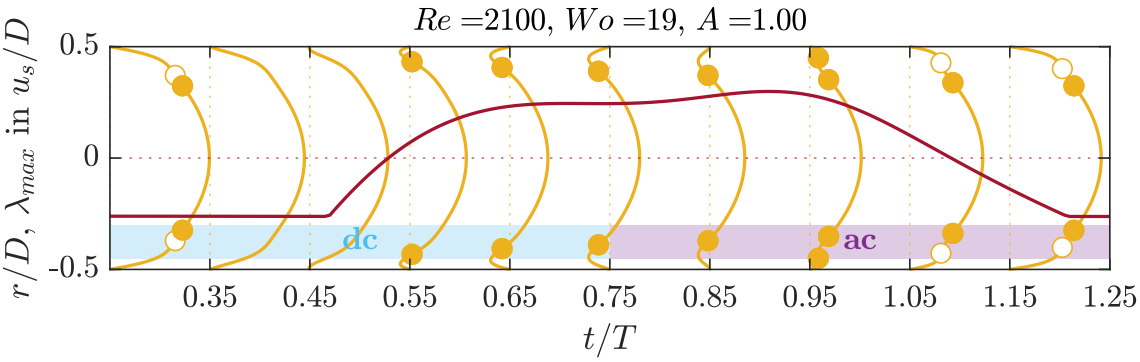
Re =2100, Wo =19, A =1.00
r/D, λmax in us/D
0.5
0
-0.5
dc
ac
0.35 0.45 0.55 0.65 0.75 0.85 0.95 1.05 1.15 1.25
t/T

C DNS grid and grid estimation

Find in this appendix a description of the way the grid resolution is estimated a priori, before running the DNS. The estimation is used as a guideline to define the final grid resolution of the simulations. Find at the end of the appendix tables with relevant data of all the single harmonic pulsatile pipe flow simulations performed in this work, both for individual DNS, see Chapter 5, and also for pairs of Master-Slave DNS, see Chapter 6. The tables gather the grid resolution of each case and the observed behaviour of turbulence in each simulation. For the case of Master-Slave pairs only the behaviour of turbulence in the Master simulation is shown.

C.1 Strategy to choose the grid resolution

In order to perform DNS of turbulent flows, the grid resolution must be fine enough so all the turbulent scales are well represented. There is a caveat however, one can only guess the size of the smallest scales before performing the simulation. Moreover it is of the best interest to keep the grid spacing as coarse as possible, in order to reduce the computation time. Thus, the goal is to make a good enough a priori estimation, that returns the minimal resolution possible that best represents the turbulent flow.

There are different methods to a priori estimate the size of the smallest scales and therefore of the minimum grid spacing beforehand. In this section a method proposed by Dr. Daniel Feldmann is explained. Note that the shear thickness is defined as $\delta_\nu = \nu/u_\tau = D/\left(2Re_\tau\right)$, where $u_\tau = \sqrt{\tau_w/\rho}$ is the shear velocity, τ_w is the magnitude of the average shear at the wall and $Re_\tau = u_\tau D/\left(2\nu\right)$ the shear Reynolds number.

C.1.1 Estimate the dissipation

First assume that the dissipation ε is equal to the volume (V) and time (t) averaged dissipation:

$$\varepsilon \approx \frac{1}{tV}\int_0^t \iiint_V \varepsilon\left(\boldsymbol{x},t\right)\mathrm{d}V, \tag{C.1}$$

at each point of the flow.

Secondly, assume that all the energy injected to the flow is dissipated by the dissipation. The energy injected by the flow is assumed to be equal, on average, to the axial pressure gradient $\left\langle \frac{\partial p}{\partial x} \right\rangle_t$ that drives the flow. Then:

$$\left\langle \frac{\partial p}{\partial x} \right\rangle_t \cdot U \approx \rho\varepsilon. \tag{C.2}$$

From the Reynolds Average Navier Stokes equations, one can obtain an equation for the pressure gradient as:

$$\left\langle \frac{\partial p}{\partial x} \right\rangle_t = \left\langle \frac{4\tau_w}{D} \right\rangle_t, \tag{C.3}$$

which in turn leads to:

$$\varepsilon \approx \frac{4u_\tau^2 U}{D}. \tag{C.4}$$

C.1.2 Estimate the shear at the wall

Here, fully turbulent flow is assumed. According to Blasius empirical resistance formula [Pop00], the shear stress is given as:

$$\frac{\tau_w}{\rho U^2} = \frac{1}{8}\frac{0.3164}{Re^{1/4}}. \tag{C.5}$$

This means that the shear velocity, u_τ can be computed as:

$$\frac{u_\tau}{U} = \sqrt{\frac{\tau_w}{\rho U^2}} = \sqrt{\frac{1}{8}\frac{0.3164}{Re^{1/4}}} \tag{C.6}$$

and the shear Reynolds number can then be written as a function of Re:

$$Re_\tau = \frac{u_\tau}{2U} Re = 0.099373 Re^{7/8}. \tag{C.7}$$

C.1.3 Estimate the Kolmogorov scale

An approximate Kolmogorov scale can be computed as:

$$\eta = \left(\frac{\nu^3}{\varepsilon}\right)^{1/4} \approx \left(\frac{D\nu^3}{4u_\tau^2 U}\right)^{1/4}. \tag{C.8}$$

In plus units, the Kolmogorov scale is then:

$$\eta^+ = \frac{\eta}{\delta_\nu} = \frac{\eta u_\tau}{\nu} \approx \left(\frac{D\nu^3 u_\tau^4}{4u_\tau^2 U\nu^4}\right)^{1/4} = \left(\frac{Du_\tau^2}{4U\nu}\right)^{1/4} = \left(\frac{u_\tau}{2U} Re_\tau\right)^{1/4}. \tag{C.9}$$

Invoking eq. (C.7), one finds:

$$\eta^+ \approx \left(\frac{Re_\tau^2}{Re}\right)^{1/4}. \tag{C.10}$$

With this definition, one can estimate the number of grid points needed for each coordinate.

C.1.4 Radial points

Here a uniform radial grid is assumed. Thus, the grid spacing in r is constant and equal to $\Delta r = \frac{D}{2N_r}$, where N_r are the radial points.

The radial grid spacing is chosen so, in the worst case scenario $\Delta r^+ \leq \eta^+$. This is a typical requirement in the simulation of shear flows.

One can obtain an expression for the required number of radial grid points as:

$$\Delta r^+ \leq \eta^+ \rightarrow \frac{Re_\tau}{N_r} \leq \eta^+ \rightarrow N_r \geq \frac{Re_\tau}{\eta^+}. \tag{C.11}$$

By invoking eq. (C.10) and eq. (C.7), one can write the number of radial points as a function of Re:

$$N_r \geq Re^{1/4} Re_\tau^{1/2} = 0.31532 Re^{7/16} Re^{1/4}, \text{ and find:} \tag{C.12}$$

$$N_r \geq 0.31523 Re^{11/16}. \tag{C.13}$$

C.1.5 Azimuthal points

Here a uniform azimuthal grid is assumed. The larger grid spacing of an azimuthal grid is found at the wall. There, the grid spacing is equal to $\Delta\theta = \frac{\pi D}{2N_\theta}$, where N_θ is half the total number of azimuthal Fourier modes.

The number of azimuthal grid points is chosen so, at the wall $\Delta\theta^+ \leq 4\eta^+$, which is the common spacing used in the span-wise direction of the simulations of shear flows.

With this requirement one can obtain an expression of the total number of azimuthal grid points as:

$$\Delta\theta^+ \leq 4\eta^+ \rightarrow \frac{2\pi Re_\tau}{2N_\theta} \leq 4\eta^+ \rightarrow 2N_\theta \geq \frac{\pi Re_\tau}{2\eta^+}. \tag{C.14}$$

By invoking equation (C.11) one finds:

$$2N_\theta \geq \frac{\pi}{2} N_r. \tag{C.15}$$

C.1.6 Axial points

A uniform axial grid is assumed. For a pipe length $L_x^* = L_x D$, the axial grid spacing is $\Delta x = \frac{L_x D}{2N_x}$, where N_x is half the total number of axial Fourier modes.

The number of axial grid points is chosen so: $\Delta x^+ \leq 8\eta^+$, which is the common spacing used in the stream-wise direction of simulations of shear flows.

With this requirement, one can obtain an expression of the total number of axial grid points as:

$$\Delta x^+ \leq 8\eta^+ \rightarrow \frac{2L_x Re_\tau}{2N_x} \leq 8\eta^+ \rightarrow 2N_x \geq \frac{L_x Re_\tau}{4\eta^+}. \tag{C.16}$$

By invoking the last equality in equation (C.11) one finds:

$$2N_x \geq \frac{L_x}{4} N_r. \tag{C.17}$$

C.1.7 Actual grid points

Equations (C.13), (C.15) and (C.17), represent a priori guesses of the grid resolution in pulsatile pipe flow DNS. In this thesis, instead of the mean Re, the maximum $Re_{\max} = (1 + A)\, Re$ is plugged in this equations when the number of points are estimated. This ensures that, at the time steps where the bulk velocity is maximum, the grid resolution is fine enough to represent the flow structures.

As a second requirement, the number of grid points are chosen so N_x and N_θ are powers of 2 when possible, and N_r a multiple of 4. The former is enforced, in order to ease the calculation of the FFT, and the latter for the parallelization of the `CPU` code. Note that this latter requirement is not needed for the `GPU` code.

C.2 Grid resolution in DNS

Tab. C.1.: Simulations in a $L_x = 100D$ long pipe of pulsatile pipe flow performed in this study. All of them are initialized with the corresponding SW profile, and the helical perturbation scaled in an axial length and in magnitude. In columns find the identification number of the simulation (Case); the flow parameters (Re, Wo, A); the radial points N_r and half the number of azimuthal and axial Fourier modes N_θ and N_x (the total number of points in physical space is $N_r \times 3N_\theta \times 3N_x$); the maximum Re_τ and grid discretization in $+$ units; the total number of periods run in the simulation NT and the behaviour of the simulation according to the description in §5.2: Rapid decay (RaD), Localized structures (Loc), Stochastic decay (StD) and Highly intermittent state (Int).

ID	Re	Wo	A	N_r	N_θ	N_x	Re_τ	$\Delta r^+_{\min}$	$\Delta r^+_{\max}$	$\Delta R\theta^+$	Δx^+	NT	Bhave
1	2100	8	0.50	96	80	1200	96.49	0.022	1.47	2.53	5.36	8.3	StD
2	2100	9	0.50	96	96	1600	99.52	0.023	1.52	2.17	4.15	12.4	Loc
3	2100	9	1.00	96	96	1536	123.55	0.028	1.89	2.70	5.36	23.0	StD
4	2100	11	0.50	96	80	1800	104.68	0.024	1.60	2.74	3.88	188.0	Loc
5	2100	11	0.75	96	80	1800	118.75	0.027	1.81	3.11	4.40	7.9	Loc
6	2100	11	1.00	96	80	1800	131.87	0.030	2.01	3.45	4.88	193.0	Loc
7	2100	15	0.50	96	80	1800	114.92	0.026	1.75	3.01	4.26	10.0	Loc
8	2100	15	1.00	96	80	1800	146.73	0.034	2.24	3.84	5.43	64.0	Loc
9	2100	17	0.50	96	80	1800	118.95	0.027	1.82	3.11	4.41	10.0	Loc
10	2100	17	1.00	96	80	1800	153.99	0.035	2.35	4.03	5.70	13.0	Loc
11	2200	5	0.50	96	80	1200	88.74	0.020	1.35	2.32	4.93	3.2	RaD
12	2200	8	0.50	96	80	1200	98.89	0.023	1.51	2.59	5.49	7.4	Loc
13	2200	8	1.00	96	80	1200	121.18	0.028	1.85	3.17	6.73	2.9	RaD
14	2200	9	0.50	96	80	1200	101.89	0.023	1.56	2.67	5.66	10.7	Loc
15	2200	11	0.50	96	96	1800	107.44	0.025	1.64	2.34	3.98	36.7	Loc
16	2200	11	1.00	96	96	1800	134.95	0.031	2.06	2.94	5.00	35.0	Loc
17	2400	8	0.50	96	96	2400	103.90	0.024	1.59	2.27	2.89	5.9	Loc
18	2400	8	1.00	96	96	2400	127.39	0.029	1.94	2.78	3.54	3.8	RaD
19	2500	8	1.00	96	80	1200	129.36	0.030	1.97	3.39	7.19	1.7	RaD
20	2500	9	1.00	96	80	1200	137.43	0.031	2.10	3.60	7.63	10.8	Int
21	2500	11	1.00	96	80	1200	147.43	0.034	2.25	3.86	8.19	12.5	Int
22	2600	8	1.00	96	80	1200	132.19	0.030	2.02	3.46	7.34	2.8	StD
23	2600	11	1.00	96	80	1200	148.81	0.034	2.27	3.90	8.27	11.6	Int
24	2700	8	1.00	128	96	1536	134.57	0.017	1.55	2.94	5.84	1.8	RaD
25	2700	9	1.00	128	96	1536	144.27	0.019	1.66	3.15	6.26	8.7	Int
26	2700	11	1.00	128	96	1536	154.13	0.020	1.77	3.36	6.69	9.2	Int
27	2800	8	1.00	128	96	1536	136.94	0.018	1.57	2.99	5.94	2.6	RaD
28	2800	11	1.00	128	96	1536	159.07	0.021	1.83	3.47	6.90	9.2	Int
29	2900	8	1.00	128	96	1536	143.55	0.019	1.65	3.13	6.23	6.5	Loc
30	2900	9	1.00	128	96	1536	150.14	0.019	1.73	3.28	6.52	8.3	Int
31	2900	11	1.00	128	96	1536	161.83	0.021	1.86	3.53	7.02	8.5	Int
32	3000	6	0.50	128	128	1536	114.48	0.015	1.32	1.87	4.97	3.5	Loc
33	3000	6	1.00	128	96	1536	129.97	0.017	1.49	2.84	5.64	1.5	RaD
34	3000	8	0.50	128	96	1536	118.80	0.015	1.37	2.59	5.16	4.0	Int
35	3000	8	1.00	128	96	1536	143.27	0.019	1.65	3.13	6.22	4.9	StD
36	3000	11	0.50	96	96	2800	136.95	0.031	2.09	2.99	3.26	4.6	Int
37	3000	11	1.00	128	96	1536	166.88	0.022	1.92	3.64	7.24	4.4	Int

Tab. C.2.: Simulations of pulsatile pipe flow using the master-slave method described in Chapter 6 performed in this study. All the simulations correspond to a $L_x = 100D$ long pipe. In columns find the identification number of the simulation (ID); the flow parameters (Re, Wo, A); the radial points N_r and half the number of azimuthal and axial Fourier modes N_θ and N_x (the total number of points in physical space is $N_r \times 3N_\theta \times 3N_x$); the maximum Re_τ and grid discretization in $+$ units; the total number of periods run in the simulation NT and the behaviour of the master simulation according to the description in §5.2: Rapid decay (RaD), Localized structures (Loc), Stochastic decay (StD) and Highly intermittent state (Int).

ID	Re	Wo	A	N_r	N_θ	N_x	Re_τ	$\Delta r^+_{\min}$	$\Delta r^+_{\max}$	$\Delta R\theta^+$	Δx^+	NT	Bhave
1	2100	9	0.50	80	64	1152	99.35	0.032	1.81	3.25	5.75	5.8	Loc
2	2100	9	0.70	80	64	1152	109.47	0.036	2.00	3.58	6.33	5.8	Loc
3	2100	9	0.90	80	64	1152	118.58	0.039	2.17	3.88	6.86	5.8	StD
4	2100	11	0.50	80	64	1152	104.55	0.034	1.91	3.42	6.05	6.0	Loc
5	2100	11	0.70	80	64	1152	116.35	0.038	2.12	3.81	6.73	7.8	Loc
6	2100	11	0.90	80	64	1152	126.71	0.041	2.31	4.15	7.33	6.0	Loc
7	2100	13	0.50	76	64	1152	109.68	0.039	2.10	3.59	6.35	9.6	Loc
8	2100	13	0.70	76	64	1152	122.38	0.044	2.35	4.01	7.08	9.6	Loc
9	2100	13	0.90	76	64	1152	133.99	0.048	2.57	4.38	7.75	9.6	Loc
10	2100	15	0.50	76	64	1152	114.47	0.041	2.19	3.75	6.62	13.6	Loc
11	2100	15	0.70	76	64	1152	128.50	0.046	2.46	4.21	7.44	13.6	Loc
12	2100	15	0.90	76	64	1152	140.92	0.051	2.70	4.61	8.16	13.6	Loc
13	2100	17	0.50	80	64	1152	119.02	0.039	2.17	3.89	6.89	11.0	Loc
14	2100	17	0.70	80	64	1152	134.08	0.044	2.45	4.39	7.76	11.0	Loc
15	2100	17	0.90	80	64	1152	147.39	0.048	2.69	4.82	8.53	11.0	Loc
16	2300	9	0.50	80	64	1152	104.52	0.034	1.91	3.42	6.05	4.8	Loc
17	2300	9	0.70	76	64	1152	114.97	0.041	2.20	3.76	6.65	4.8	Loc
18	2300	9	0.90	76	64	1152	124.75	0.045	2.39	4.08	7.22	4.8	StD
19	2300	11	0.50	80	64	1152	109.92	0.036	2.01	3.60	6.36	19.7	Loc
20	2300	11	0.70	80	64	1152	122.10	0.040	2.23	4.00	7.07	6.7	Loc
21	2300	11	0.90	80	64	1152	140.15	0.046	2.56	4.59	8.11	7.1	Loc
22	2300	13	0.50	80	64	1152	115.25	0.038	2.10	3.77	6.67	9.9	Loc
23	2300	13	0.70	80	64	1152	128.47	0.042	2.35	4.20	7.43	9.9	Loc
24	2300	13	0.90	80	64	1152	140.58	0.046	2.57	4.60	8.14	9.9	Loc
25	2300	15	0.50	80	64	1152	120.55	0.039	2.20	3.94	6.98	13.2	Int
26	2300	15	0.70	76	64	1152	134.89	0.048	2.59	4.41	7.81	13.2	Loc
27	2300	15	0.90	76	64	1152	148.14	0.053	2.84	4.85	8.57	14.8	Loc
28	2300	17	0.50	80	64	1152	125.86	0.041	2.30	4.12	7.28	20.0	Loc
29	2300	17	0.70	80	64	1152	141.07	0.046	2.58	4.62	8.16	20.0	Loc
30	2300	17	0.90	80	64	1152	154.80	0.050	2.83	5.07	8.96	16.0	Loc
31	2500	9	0.50	80	64	1152	109.47	0.036	2.00	3.58	6.34	4.9	Loc
32	2500	11	0.50	80	64	1152	115.18	0.038	2.10	3.77	6.67	5.8	Loc
33	2500	17	0.50	80	64	1152	133.98	0.044	2.45	4.38	7.75	17.5	Int
34	2500	17	0.70	80	64	1152	149.59	0.049	2.73	4.90	8.66	17.5	Int

D Master-Slave laminar profiles

Find in this appendix a series of plots that are meant to represent a short catalog of master-slave laminar profiles at different flow parameters. All the figures show in dashed lines the bulk velocities of slave and master laminar profiles. In solid lines, the instantaneous laminar profiles of master-slave cases at the indicated Re, Wo and A, and phase of the period. To not interfere with one another the profiles are scaled using a scalar with arbitrary units. In blue (right pointing triangles ▷) master bulk velocities/laminar profiles and in red (left pointing triangles ◁) slave bulk velocities/laminar profiles. Note that the slave laminar profiles have a monotonic decreasing shear from the wall to the center-line of the pipe. Note also that the slave bulk velocity deviates from the master one, specially at higher A and during the deceleration phase of the period.

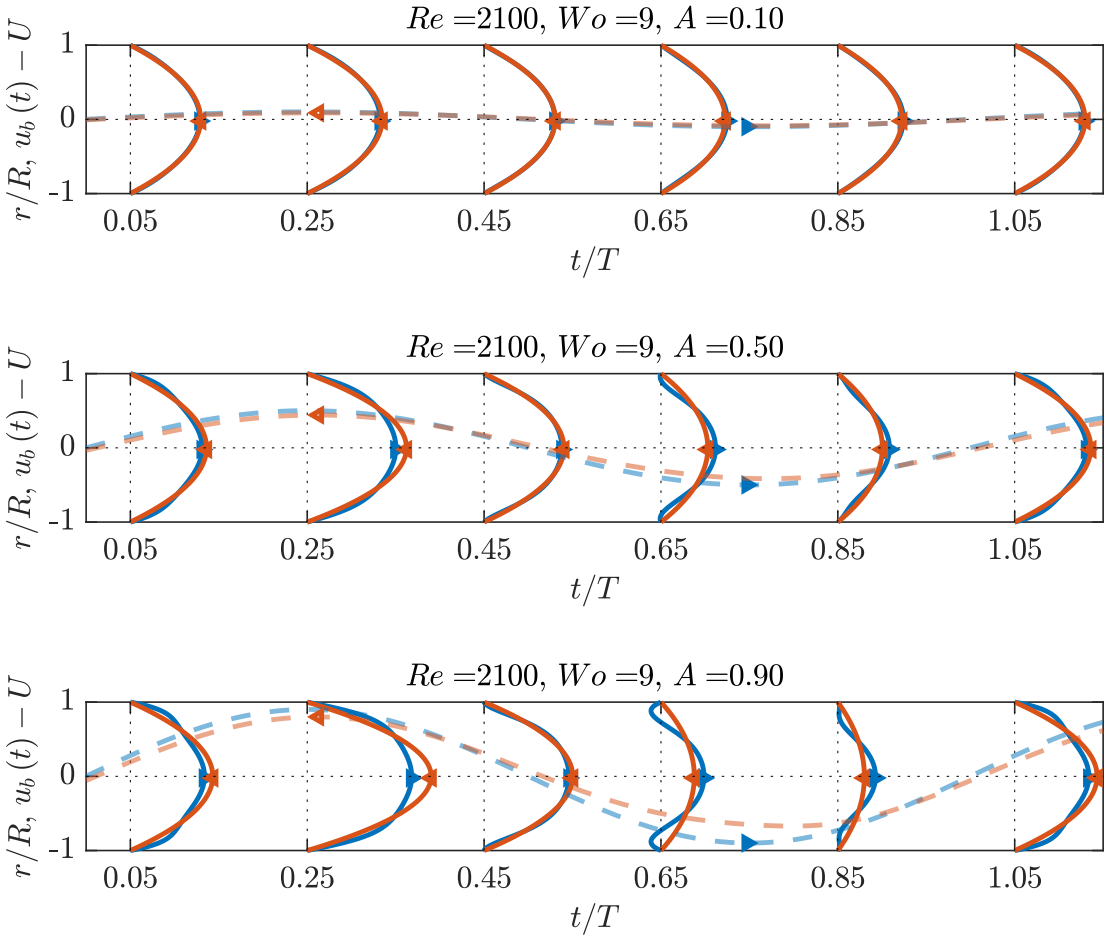

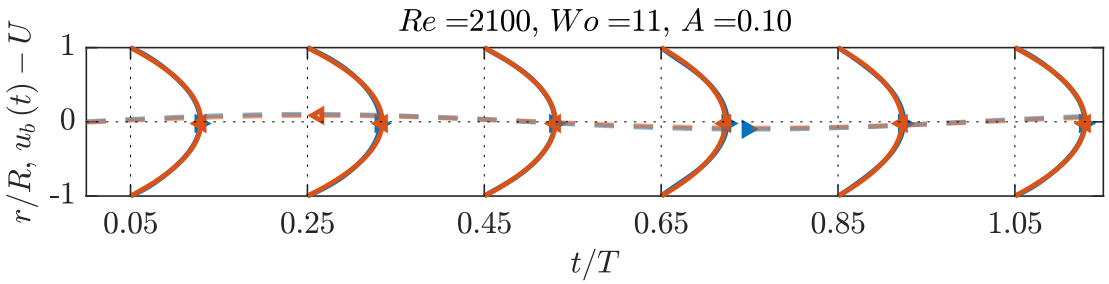
Re =2100, Wo =11, A =0.10
r/R, $u_b(t) - U$
1
0
-1
0.05
0.25
0.45
0.65
0.85
1.05
t/T

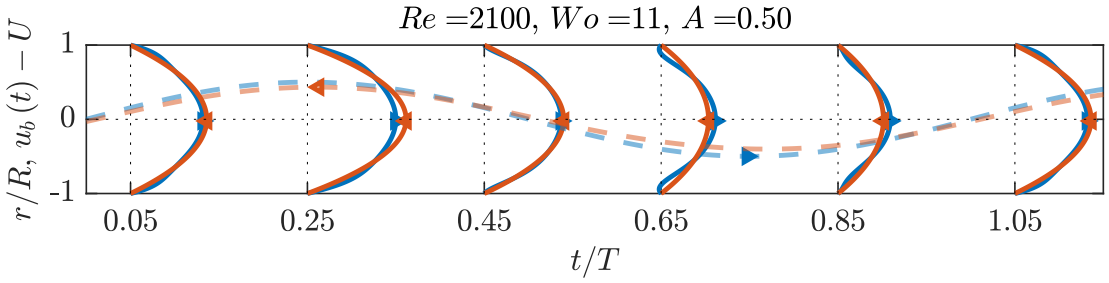
Re =2100, Wo =11, A =0.50
r/R, $u_b(t) - U$
1
0
-1
0.05
0.25
0.45
0.65
0.85
1.05
t/T

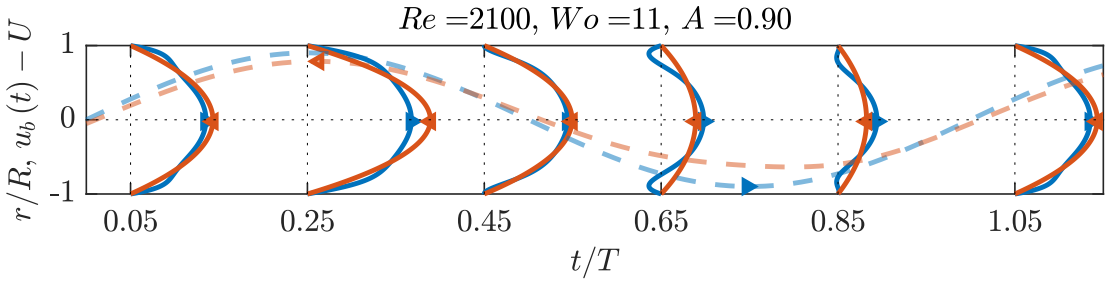
Re =2100, Wo =11, A =0.90
r/R, $u_b(t) - U$
1
0
-1
0.05
0.25
0.45
0.65
0.85
1.05
t/T

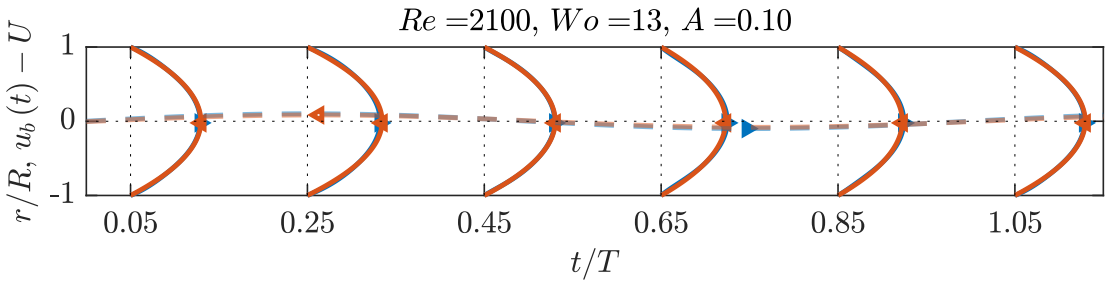
Re =2100, Wo =13, A =0.10
r/R, $u_b(t) - U$
1
0
-1
0.05
0.25
0.45
0.65
0.85
1.05
t/T

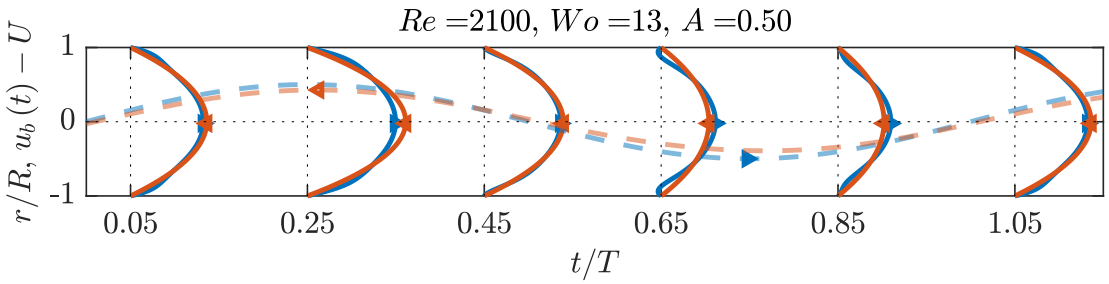
Re =2100, Wo =13, A =0.50
r/R, $u_b(t) - U$
1
0
-1
0.05
0.25
0.45
0.65
0.85
1.05
t/T

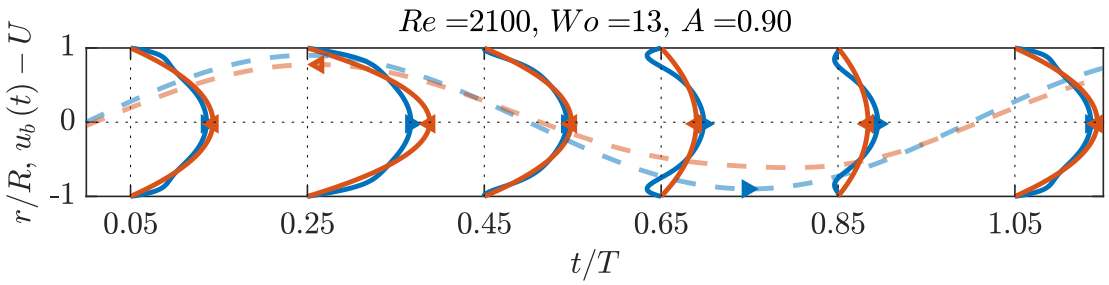
Re =2100, Wo =13, A =0.90
r/R, $u_b(t) - U$
1
0
-1
0.05
0.25
0.45
0.65
0.85
1.05
t/T

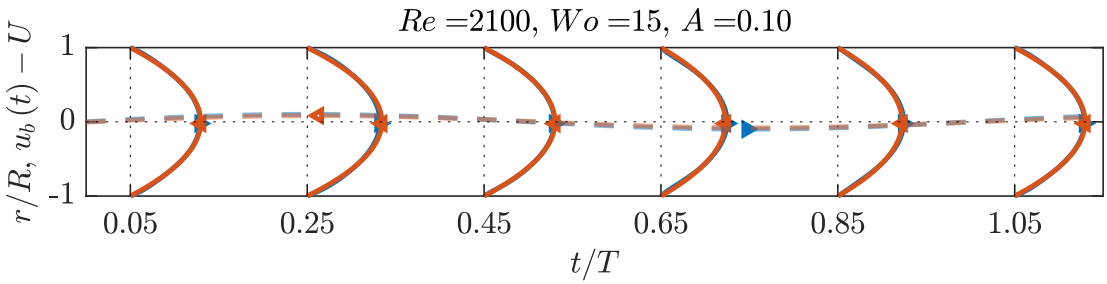
Re =2100, Wo =15, A =0.10
r/R, $u_b(t) - U$
1
0
-1
0.05
0.25
0.45
0.65
0.85
1.05
t/T

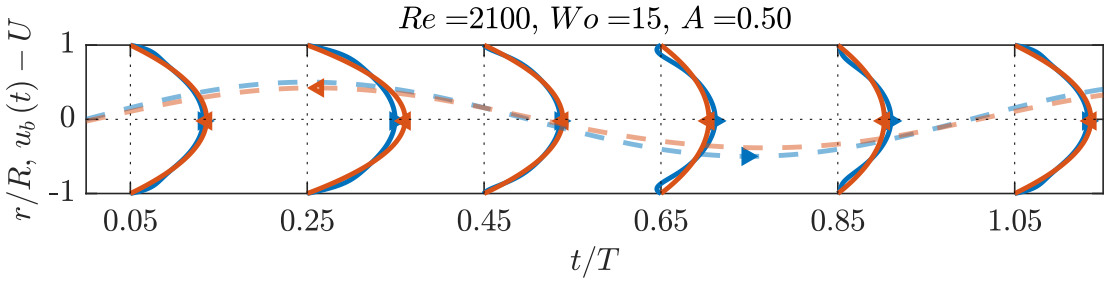
Re =2100, Wo =15, A =0.50
r/R, $u_b(t) - U$
1
0
-1
0.05
0.25
0.45
0.65
0.85
1.05
t/T

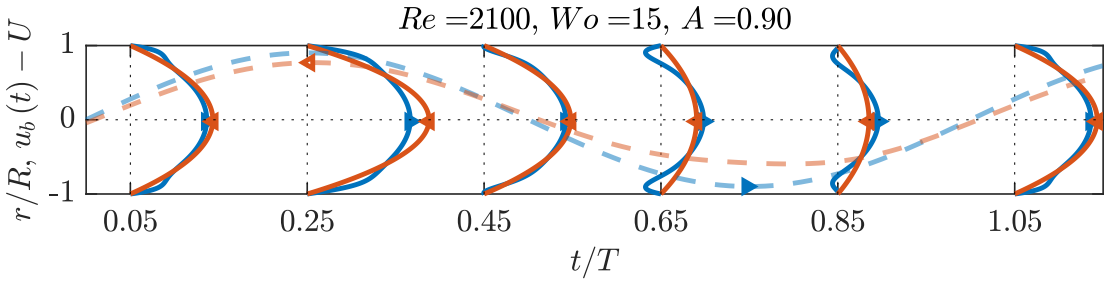
Re =2100, Wo =15, A =0.90
r/R, $u_b(t) - U$
1
0
-1
0.05
0.25
0.45
0.65
0.85
1.05
t/T

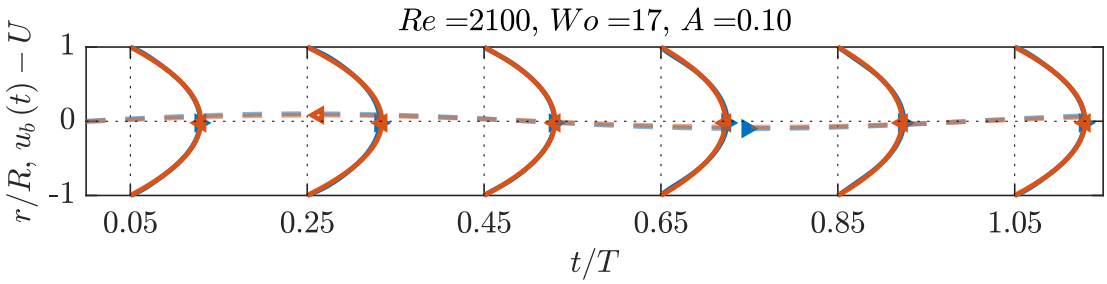
Re =2100, Wo =17, A =0.10
r/R, $u_b(t) - U$
1
0
-1
0.05
0.25
0.45
0.65
0.85
1.05
t/T

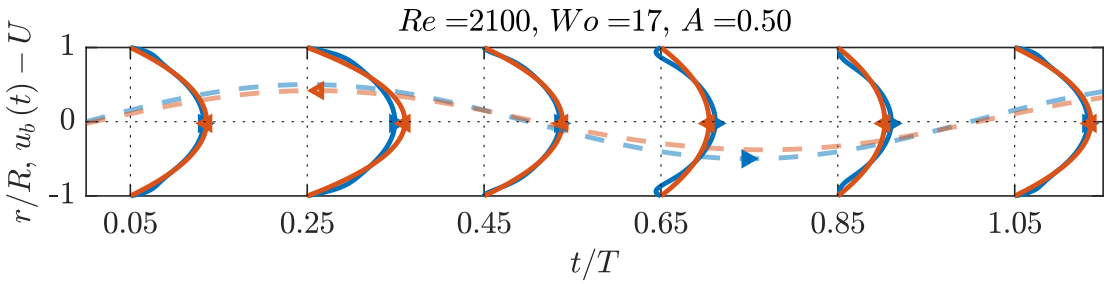
Re =2100, Wo =17, A =0.50
r/R, $u_b(t) - U$
1
0
-1
0.05
0.25
0.45
0.65
0.85
1.05
t/T

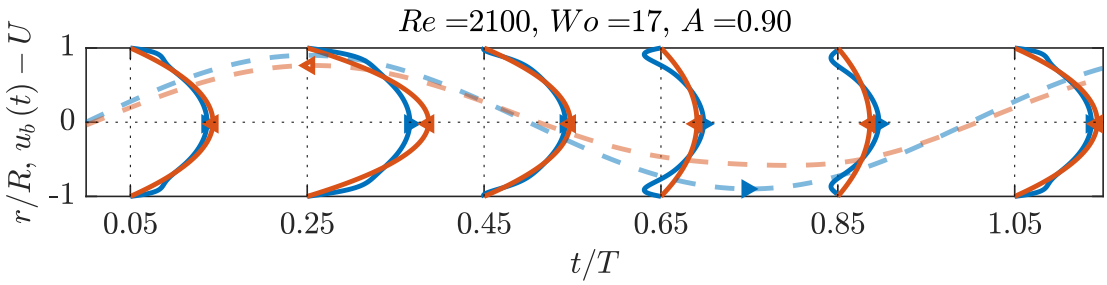
Re =2100, Wo =17, A =0.90
r/R, $u_b(t) - U$
1
0
-1
0.05
0.25
0.45
0.65
0.85
1.05
t/T

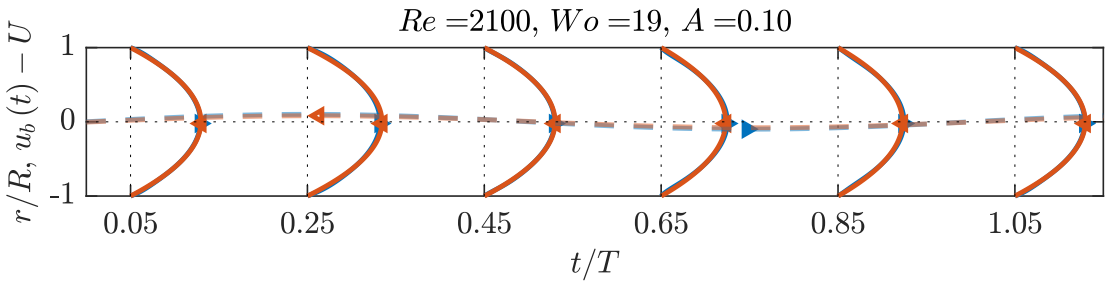
Re =2100, Wo =19, A =0.10
r/R, $u_b(t) - U$
1
0
-1
0.05
0.25
0.45
0.65
0.85
1.05
t/T

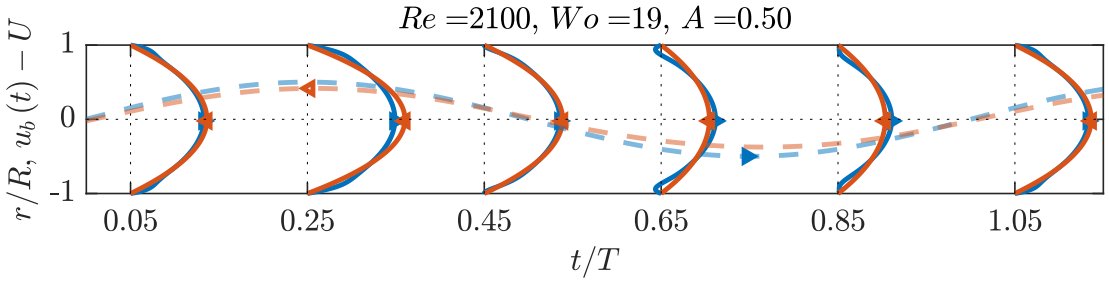
Re =2100, Wo =19, A =0.50
r/R, $u_b(t) - U$
1
0
-1
0.05
0.25
0.45
0.65
0.85
1.05
t/T

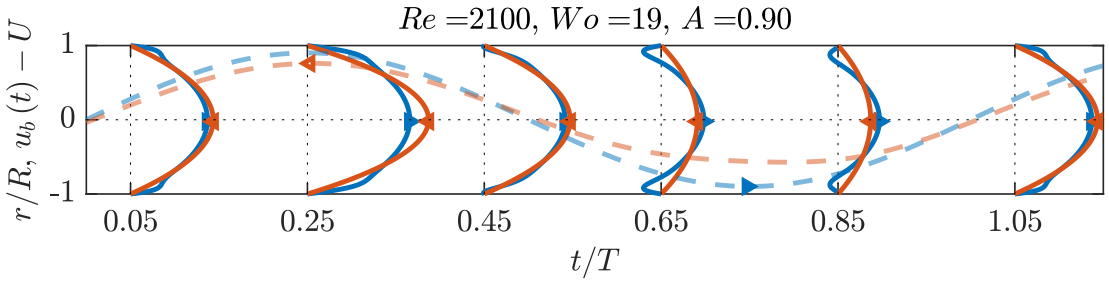
Re =2100, Wo =19, A =0.90
r/R, $u_b(t) - U$
1
0
-1
0.05
0.25
0.45
0.65
0.85
1.05
t/T

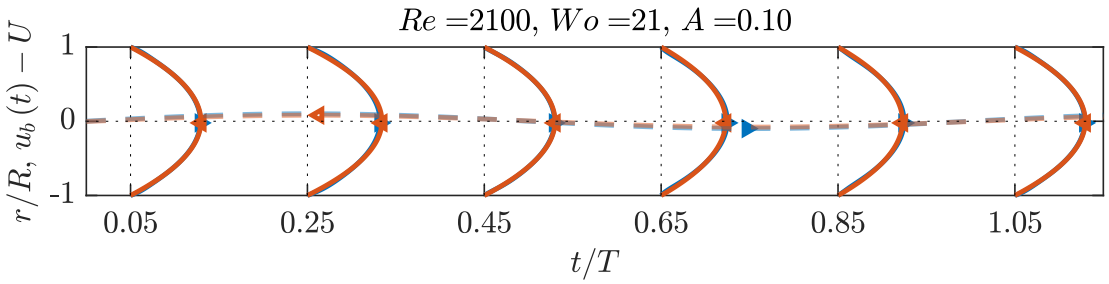
Re =2100, Wo =21, A =0.10
r/R, $u_b(t) - U$
1
0
-1
0.05
0.25
0.45
0.65
0.85
1.05
t/T

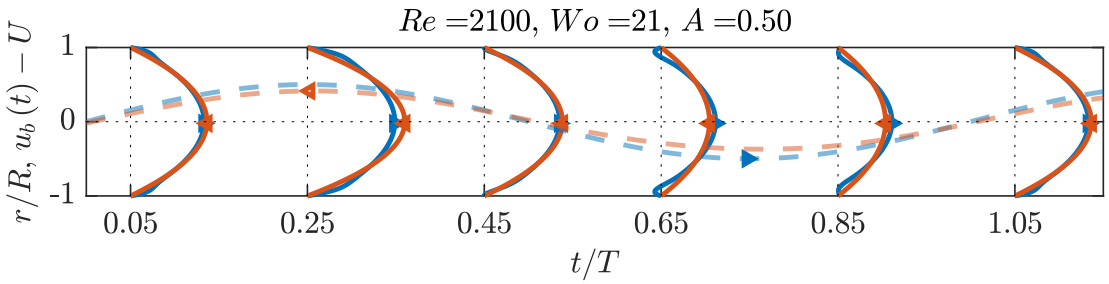
Re =2100, Wo =21, A =0.50
r/R, $u_b(t) - U$
1
0
-1
0.05
0.25
0.45
0.65
0.85
1.05
t/T

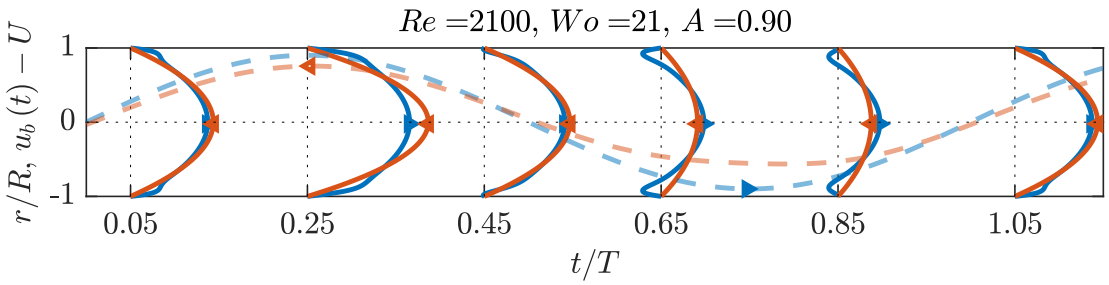
Re =2100, Wo =21, A =0.90
r/R, $u_b(t) - U$
1
0
-1
0.05
0.25
0.45
0.65
0.85
1.05
t/T

E Master-Slave additional results

Find in this appendix a series of plots that are meant to represent a short catalog of master-slave pairs of simulations. All the figures show space-time diagrams of the cross section integral of the cross section average cross section kinetic energy, in pairs of master-slave DNS at different Re, Wo and A. The results correspond to DNS in a $L_x = 100D$ long pipe initialized with a localized turbulent puff. The results are plotted with respect to a moving reference frame moving at the bulk velocity u_b. The left hand-side plots represent master DNS and the right hand side DNS to slave DNS. The figures are equivalent to fig. 6.6.

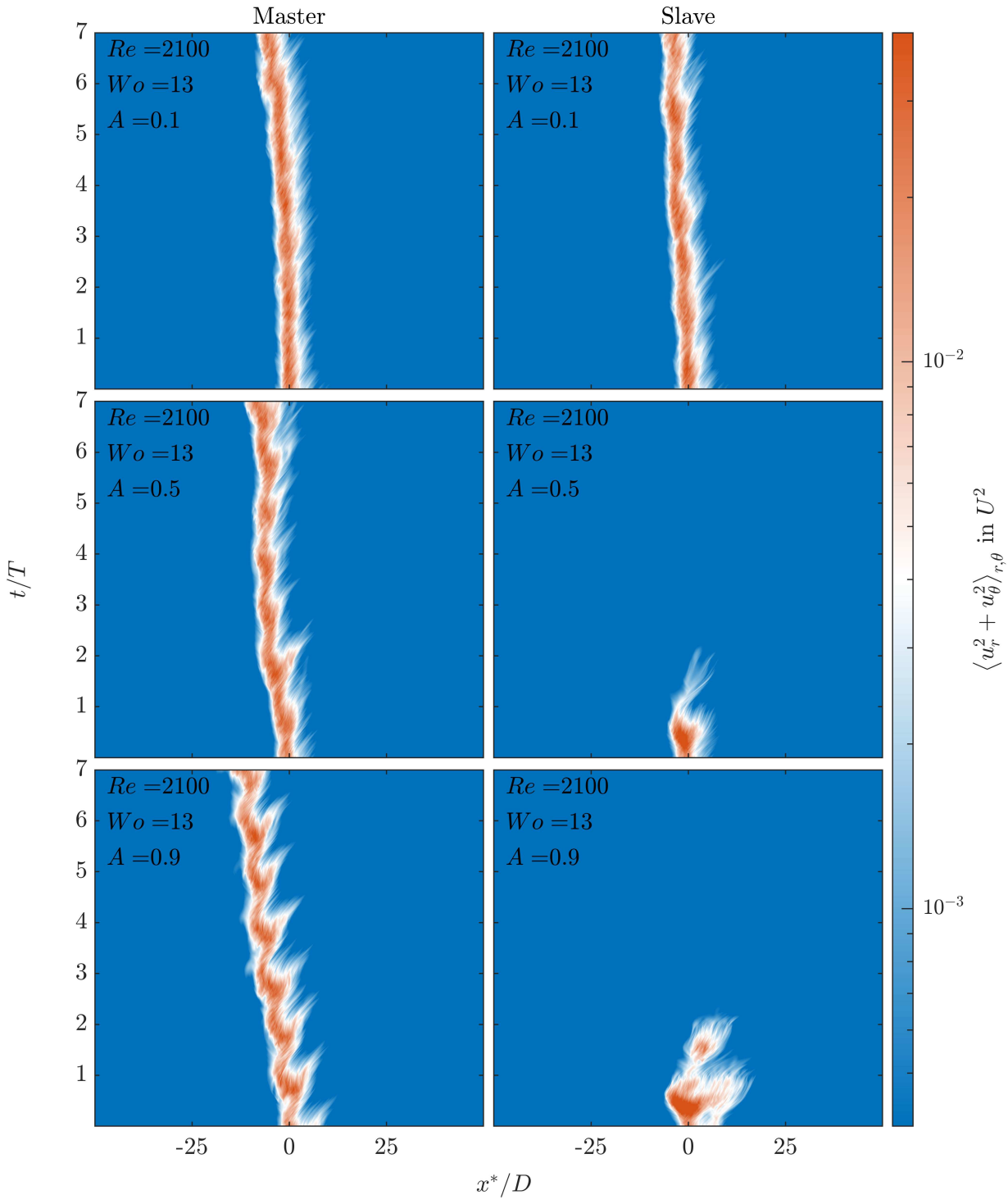
Master
Slave
Re =2100
Wo =13
A =0.1
Re =2100
Wo =13
A =0.5
Re =2100
Wo =13
A =0.9
t/T
x*/D
-25
0
25
1
2
3
4
5
6
7
10^-2
10^-3
⟨u_r^2 + u_θ^2⟩_{r,θ} in U^2

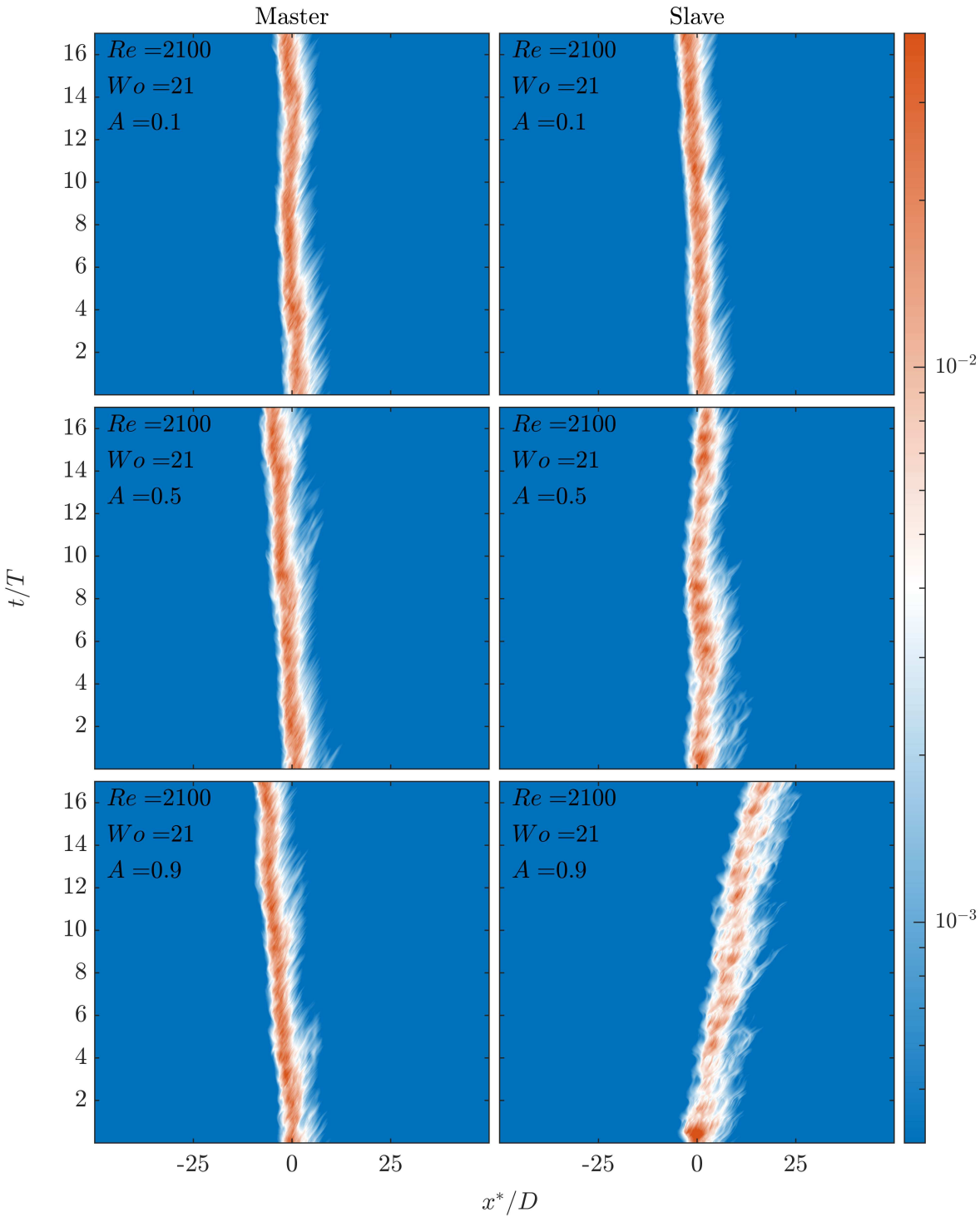
Master
Slave
Re =2100
Wo =21
A =0.1
Re =2100
Wo =21
A =0.5
Re =2100
Wo =21
A =0.9
t/T
x*/D
-25
0
25
2
4
6
8
10
12
14
16
10^-2
10^-3
⟨u_r^2 + u_θ^2⟩_{r,θ} in U^2

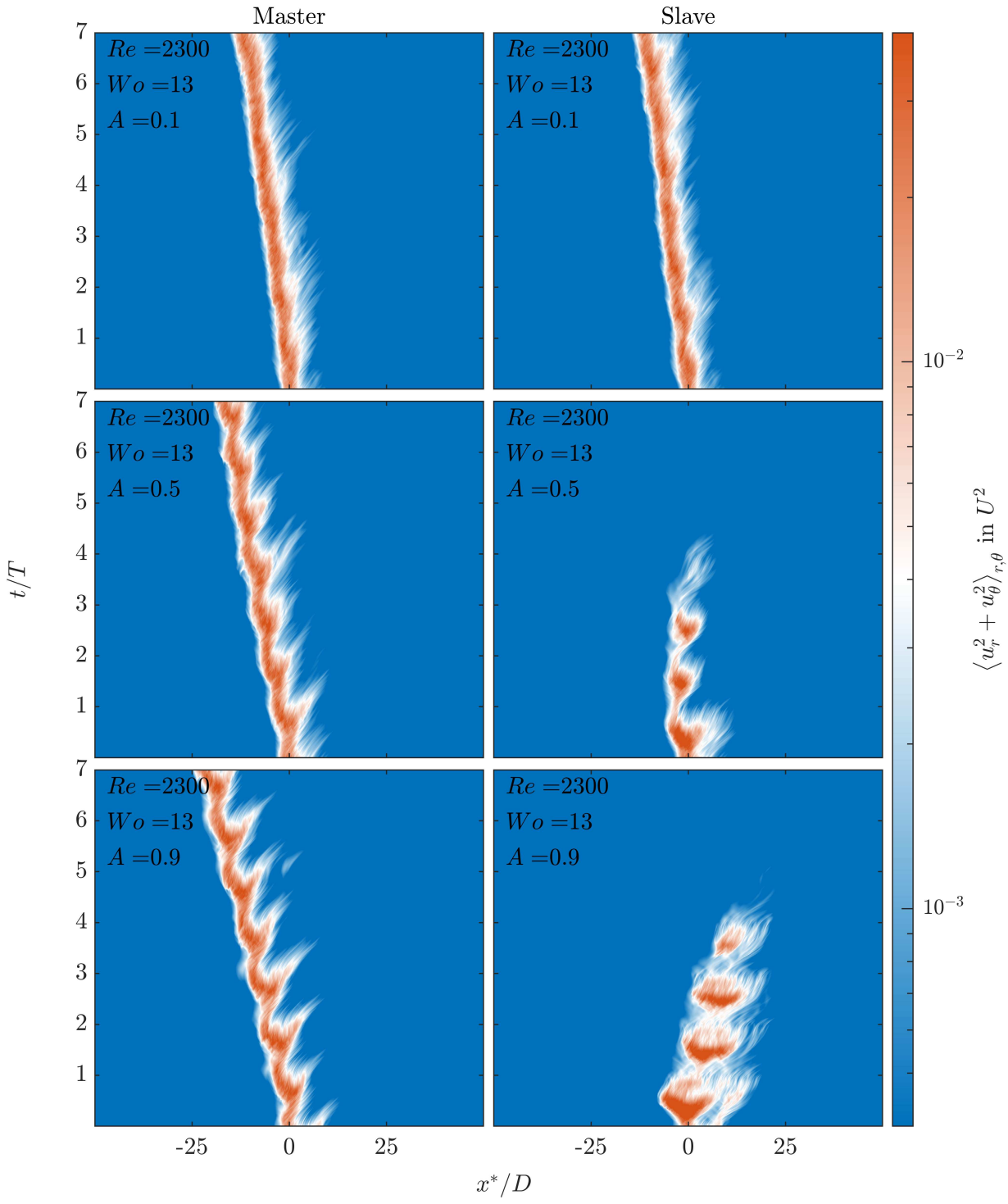
Master
Slave
Re =2300
Wo =13
A =0.1
A =0.5
A =0.9
t/T
x*/D
-25
0
25
1
2
3
4
5
6
7
10^-2
10^-3
⟨u_r^2 + u_θ^2⟩_{r,θ} in U^2

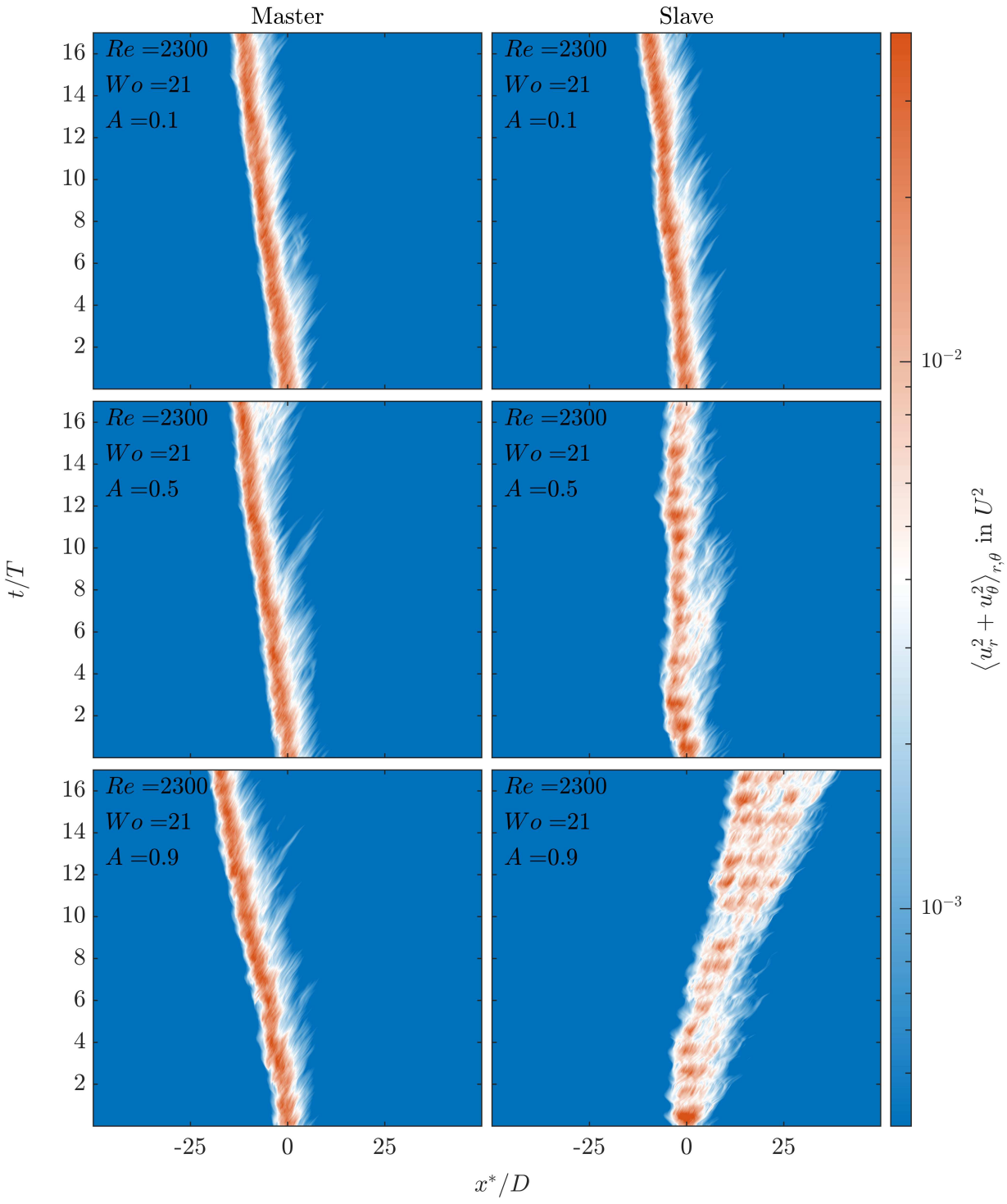
Master
Slave
Re =2300
Wo =21
A =0.1
Re =2300
Wo =21
A =0.5
Re =2300
Wo =21
A =0.9
t/T
x*/D
-25
0
25
2
4
6
8
10
12
14
16
10^-2
10^-3
⟨u_r^2 + u_θ^2⟩_{r,θ} in U^2

F Peer-Reviewed publications

The following published, peer-reviewed research papers are based on the results presented in this thesis:

[FMA21] Feldmann, D., Morón, D., & Avila, M. (2020). Spatiotemporal intermittency in pulsatile pipe flow. Entropy, 23(1), 46.

[MFA22] Morón, D., Feldmann, D., & Avila, M. (2022). Effect of waveform on turbulence transition in pulsatile pipe flow. Journal of Fluid Mechanics, 948, A20.

Morón, D. & Avila, M. (2024). Turbulent puffs in transitional pulsatile pipe flow at moderate pulsation amplitudes. *Accepted in Phys. Rev. Fluids.*

Morón, D. Vela-Martín, A., & Avila, M. (2024). Predictability of decay events in transitional wall-bounded flows. *Accepted in Journal of Physics: Conference Series*.

G Related students' work

In the dissertation the results from the supervision of the following students' works are included:

1. Dot Casadevall, Laura (2021). Turbulence transition in pulsating pipe flow: shear-thinning effects [Bachelor's thesis, UPC & Universität Bremen] `https://upcommons.upc.edu/handle/2117/355517`.
2. Cela París, José M. (2022). Assessing the physics of models for transition in pipe flow. [Bachelor's thesis, UPC & Universität Bremen] `https://upcommons.upc.edu/handle/2117/378144`.